



US010117707B2

(12) **United States Patent**  
**Garcia et al.**

(10) **Patent No.:** **US 10,117,707 B2**  
(45) **Date of Patent:** **Nov. 6, 2018**

(54) **SYSTEM AND METHOD FOR ESTIMATING TISSUE HEATING OF A TARGET ABLATION ZONE FOR ELECTRICAL-ENERGY BASED THERAPIES**

(58) **Field of Classification Search**  
CPC ..... A61B 18/1477; A61B 34/10; A61B 34/25; A61B 2034/104; A61B 2034/256;  
(Continued)

(71) Applicant: **Virginia Tech Intellectual Properties Inc.**, Blacksburg, VA (US)

(56) **References Cited**

U.S. PATENT DOCUMENTS

(72) Inventors: **Paulo A. Garcia**, Blacksburg, VA (US); **Christopher B. Arena**, Burlington, NC (US); **Michael B. Sano**, Durham, NC (US); **Rafael V. Davalos**, Blacksburg, VA (US)

1,653,819 A 12/1927 Northcott et al.  
3,730,238 A 5/1973 Butler  
(Continued)

FOREIGN PATENT DOCUMENTS

(73) Assignee: **Virginia Tech Intellectual Properties, Inc.**, Blacksburg, VA (US)

AU 2002315095 A1 12/2002  
AU 2003227960 A1 12/2003  
(Continued)

(\* ) Notice: Subject to any disclaimer, the term of this patent is extended or adjusted under 35 U.S.C. 154(b) by 441 days.

OTHER PUBLICATIONS

Beebe, S.J., et al., "Diverse effects of nanosecond pulsed electric fields on cells and tissues", *DNA and Cell Biology*, 22(12): 785-796 (2003).

(Continued)

(21) Appl. No.: **14/558,631**

*Primary Examiner* — Michael Peffley

(22) Filed: **Dec. 2, 2014**

(74) *Attorney, Agent, or Firm* — New River Valley IP Law, P.C.; Michele L. Mayberry; Timothy D. Nolan

(65) **Prior Publication Data**

US 2015/0088120 A1 Mar. 26, 2015

**Related U.S. Application Data**

(63) Continuation-in-part of application No. 14/012,832, filed on Aug. 28, 2013, now Pat. No. 9,283,051, (Continued)

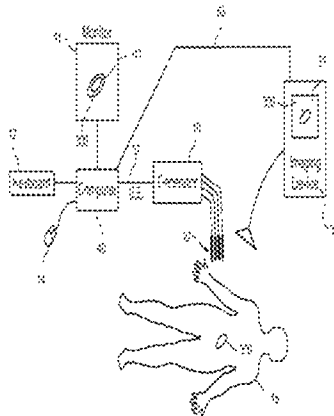
(51) **Int. Cl.**  
**A61B 18/14** (2006.01)  
**C12N 13/00** (2006.01)  
(Continued)

(57) **ABSTRACT**

Systems and methods are provided for modeling and for providing a graphical representation of tissue heating and electric field distributions for medical treatment devices that apply electrical treatment energy through one or a plurality of electrodes. In embodiments, methods comprise: providing one or more parameters of a treatment protocol for delivering one or more electrical pulses to tissue through a plurality of electrodes; modeling electric and heat distribution in the tissue based on the parameters; and displaying a graphical representation of the modeled electric and heat distribution. In another embodiment, a treatment planning module is adapted to generate an estimated target ablation zone based on a combination of one or more parameters for

(Continued)

(52) **U.S. Cl.**  
CPC ..... **A61B 18/1477** (2013.01); **A61B 34/10** (2016.02); **C12N 13/00** (2013.01);  
(Continued)



an irreversible electroporation protocol and one or more tissue-specific conductivity parameters.

### 21 Claims, 53 Drawing Sheets

#### Related U.S. Application Data

which is a continuation-in-part of application No. 12/491,151, filed on Jun. 24, 2009, now Pat. No. 8,992,517, which is a continuation-in-part of application No. 12/432,295, filed on Apr. 29, 2009, now Pat. No. 9,598,691.

- (60) Provisional application No. 61/694,144, filed on Aug. 28, 2012, provisional application No. 61/171,564, filed on Apr. 22, 2009, provisional application No. 61/167,997, filed on Apr. 9, 2009, provisional application No. 61/075,216, filed on Jun. 24, 2008, provisional application No. 61/125,840, filed on Apr. 29, 2008, provisional application No. 61/910,655, filed on Dec. 2, 2013.

#### (51) Int. Cl.

*A61B 18/00* (2006.01)  
*A61B 34/10* (2016.01)  
*A61B 34/00* (2016.01)  
*A61B 90/00* (2016.01)

#### (52) U.S. Cl.

CPC ..... *A61B 34/25* (2016.02); *A61B 90/37* (2016.02); *A61B 2018/0016* (2013.01); *A61B 2018/00613* (2013.01); *A61B 2018/00779* (2013.01); *A61B 2018/00875* (2013.01); *A61B 2018/00886* (2013.01); *A61B 2018/00892* (2013.01); *A61B 2018/1425* (2013.01); *A61B 2034/104* (2016.02); *A61B 2034/256* (2016.02)

#### (58) Field of Classification Search

CPC .. *A61B 2018/00613*; *A61B 2018/1425*; *A61B 2018/0016*; *A61B 2018/00892*; *A61B 2018/00875*; *A61B 2018/00886*; *A61B 2018/00779*; C12N 13/00

See application file for complete search history.

#### (56)

#### References Cited

##### U.S. PATENT DOCUMENTS

3,746,004 A	7/1973	Jankelson	4,672,969 A	6/1987	Dew
3,871,359 A	3/1975	Pacela	4,676,258 A	6/1987	Inokuchi et al.
4,016,886 A	4/1977	Doss et al.	4,676,782 A	6/1987	Yamamoto et al.
4,037,341 A	7/1977	Odle et al.	4,687,471 A	8/1987	Twardowski et al.
4,216,860 A	8/1980	Heimann	4,716,896 A	1/1988	Ackerman
4,226,246 A	10/1980	Fragnet	4,723,549 A	2/1988	Wholey et al.
4,262,672 A	4/1981	Kief	D294,519 S	3/1988	Hardy
4,267,047 A	5/1981	Henne et al.	4,756,838 A	7/1988	Veltman
4,278,092 A	7/1981	Borsanyi et al.	4,772,269 A	9/1988	Twardowski et al.
4,299,217 A	11/1981	Sagae et al.	4,798,585 A	1/1989	Inoue et al.
4,311,148 A	1/1982	Courtney et al.	4,810,963 A	3/1989	Blake-Coleman et al.
4,336,881 A	6/1982	Babb et al.	4,813,929 A	3/1989	Semrad
4,344,436 A	8/1982	Kubota	4,819,637 A	4/1989	Dormandy et al.
4,392,855 A	7/1983	Oreopoulos et al.	4,822,470 A	4/1989	Chang
4,406,827 A	9/1983	Carim	4,836,204 A	6/1989	Landymore et al.
4,407,943 A	10/1983	Cole et al.	4,840,172 A	6/1989	Augustine et al.
4,416,276 A	11/1983	Newton et al.	4,863,426 A	9/1989	Ferragamo et al.
4,447,235 A	5/1984	Clarke	4,885,003 A	12/1989	Hillstead
4,469,098 A	9/1984	Davi	4,886,496 A	12/1989	Conoscenti et al.
4,489,535 A	12/1984	Veltman	4,886,502 A	12/1989	Poirier et al.
4,512,765 A	4/1985	Muto	4,889,634 A	12/1989	El-Rashidy
4,580,572 A	4/1986	Granek et al.	4,907,601 A	3/1990	Frick
4,636,199 A	1/1987	Victor	4,919,148 A	4/1990	Muccio
			4,920,978 A	5/1990	Colvin
			4,921,484 A	5/1990	Hillstead
			4,946,793 A	8/1990	Marshall, III
			4,976,709 A	12/1990	Sand
			4,981,477 A	1/1991	Schon et al.
			4,986,810 A	1/1991	Semrad
			4,987,895 A	1/1991	Heimlich
			5,019,034 A	5/1991	Weaver et al.
			5,031,775 A	7/1991	Kane
			5,052,391 A	10/1991	Silberstone et al.
			5,053,013 A	10/1991	Ensminger et al.
			5,058,605 A	10/1991	Slovak
			5,071,558 A	12/1991	Itoh
			5,098,843 A	3/1992	Calvin
			5,122,137 A	6/1992	Lennox
			5,134,070 A	7/1992	Casnig
			5,137,517 A	8/1992	Loney et al.
			5,141,499 A	8/1992	Zappacosta
			D329,496 S	9/1992	Wotton
			5,156,597 A	10/1992	Verreet et al.
			5,173,158 A	12/1992	Schmukler
			5,186,715 A	2/1993	Phillips et al.
			5,186,800 A	2/1993	Dower
			5,188,592 A	2/1993	Hakki
			5,190,541 A	3/1993	Abele et al.
			5,192,312 A	3/1993	Orton
			5,193,537 A	3/1993	Freeman
			5,209,723 A	5/1993	Twardowski et al.
			5,215,530 A	6/1993	Hogan
			5,224,933 A	7/1993	Bromander
			5,227,730 A	7/1993	King et al.
			5,242,415 A	9/1993	Kantrowitz et al.
			5,273,525 A	12/1993	Hofmann
			D343,687 S	1/1994	Houghton et al.
			5,277,201 A	1/1994	Stern
			5,279,564 A	1/1994	Taylor
			5,281,213 A	1/1994	Milder
			5,283,194 A	2/1994	Schmukler
			5,290,263 A	3/1994	Wigness et al.
			5,308,325 A	5/1994	Quinn et al.
			5,308,338 A	5/1994	Helfrich
			5,318,543 A	6/1994	Ross et al.
			5,318,563 A	6/1994	Malis et al.
			5,328,451 A	7/1994	Davis et al.
			5,334,167 A	8/1994	Cocanower
			5,348,554 A	9/1994	Imran et al.
			D351,661 S	10/1994	Fischer
			5,383,917 A	1/1995	Desai et al.
			5,389,069 A	2/1995	Weaver
			5,391,158 A	2/1995	Peters
			5,403,311 A	4/1995	Abele et al.
			5,405,320 A	4/1995	Twardowski et al.
			5,425,752 A	6/1995	Vu Nguyen
			5,439,440 A	8/1995	Hofmann
			5,458,625 A	10/1995	Kendall
			5,484,400 A	1/1996	Edwards et al.

(56)

## References Cited

## U.S. PATENT DOCUMENTS

5,484,401	A	1/1996	Rodriguez et al.	6,050,994	A	4/2000	Sherman
5,533,999	A	7/1996	Hood et al.	6,055,453	A	4/2000	Hofmann et al.
5,536,240	A	7/1996	Edwards et al.	6,059,780	A	5/2000	Gough et al.
5,536,267	A	7/1996	Edwards et al.	6,066,134	A	5/2000	Eggers et al.
5,540,737	A	7/1996	Fenn	6,068,121	A	5/2000	McGlinch
5,546,940	A	8/1996	Panescu et al.	6,068,650	A	5/2000	Hofmann et al.
5,562,720	A	10/1996	Stern et al.	6,071,281	A	6/2000	Burnside et al.
5,575,811	A	11/1996	Reid et al.	6,074,374	A	6/2000	Fulton
D376,652	S	12/1996	Hunt et al.	6,074,389	A	6/2000	Levine et al.
5,582,588	A	12/1996	Sakurai et al.	6,085,115	A	7/2000	Weaver et al.
5,586,982	A	12/1996	Abela	6,090,016	A	7/2000	Kuo
5,588,424	A	12/1996	Insler et al.	6,090,105	A	7/2000	Zepeda et al.
5,588,960	A	12/1996	Edwards et al.	6,090,106	A	7/2000	Goble et al.
5,599,294	A	2/1997	Edwards et al.	D430,015	S	8/2000	Himbert et al.
5,599,311	A	2/1997	Raulerson	6,096,035	A	8/2000	Sodhi et al.
5,616,126	A	4/1997	Malekmehr et al.	6,102,885	A	8/2000	Bass
5,620,479	A	4/1997	Diederich	6,106,521	A	8/2000	Blewett et al.
5,626,146	A	5/1997	Barber et al.	6,109,270	A	8/2000	Mah et al.
D380,272	S	6/1997	Partika et al.	6,110,192	A	8/2000	Ravenscroft et al.
5,634,899	A	6/1997	Shapland et al.	6,113,593	A	9/2000	Tu et al.
5,643,197	A	7/1997	Brucker et al.	6,116,330	A	9/2000	Salyer
5,645,855	A	7/1997	Lorenz	6,122,599	A	9/2000	Mehta
5,672,173	A	9/1997	Gough et al.	6,123,701	A	9/2000	Nezhat
5,674,267	A	10/1997	Mir et al.	6,132,397	A	10/2000	Davis et al.
5,683,384	A	11/1997	Gough et al.	6,132,419	A	10/2000	Hofmann
5,687,723	A	11/1997	Avitall	6,134,460	A	10/2000	Chance
5,690,620	A	11/1997	Knott	6,139,545	A	10/2000	Utley et al.
5,697,905	A	12/1997	d'Ambrosio	6,150,148	A	11/2000	Nanda et al.
5,700,252	A	12/1997	Klingenstein	6,159,163	A	12/2000	Strauss et al.
5,702,359	A	12/1997	Hofmann et al.	6,178,354	B1	1/2001	Gibson
5,718,246	A	2/1998	Vona	D437,941	S	2/2001	Frattini
5,720,921	A	2/1998	Meserol	6,193,715	B1	2/2001	Wrublewski et al.
5,735,847	A	4/1998	Gough et al.	6,198,970	B1	3/2001	Freed et al.
5,752,939	A	5/1998	Makoto	6,200,314	B1	3/2001	Sherman
5,778,894	A	7/1998	Dorogi et al.	6,208,893	B1	3/2001	Hofmann
5,782,882	A	7/1998	Lerman et al.	6,210,402	B1	4/2001	Olsen et al.
5,800,378	A	9/1998	Edwards et al.	6,212,433	B1	4/2001	Behl
5,800,484	A	9/1998	Gough et al.	6,216,034	B1	4/2001	Hofmann et al.
5,807,272	A	9/1998	Kun et al.	6,219,577	B1	4/2001	Brown, III et al.
5,807,306	A	9/1998	Shapland et al.	D442,697	S	5/2001	Hajianpour
5,807,395	A	9/1998	Mulier et al.	6,233,490	B1	5/2001	Kasevich
5,810,742	A	9/1998	Pearlman	6,235,023	B1	5/2001	Lee et al.
5,810,762	A	9/1998	Hofmann	D443,360	S	6/2001	Haberland
5,830,184	A	11/1998	Basta	6,241,702	B1	6/2001	Lundquist et al.
5,836,897	A	11/1998	Sakurai et al.	6,241,725	B1	6/2001	Cosman
5,836,905	A	11/1998	Lemelson et al.	D445,198	S	7/2001	Frattini
5,843,026	A	12/1998	Edwards et al.	6,258,100	B1	7/2001	Alferness et al.
5,843,182	A	12/1998	Goldstein	6,261,831	B1	7/2001	Agee
5,865,787	A	2/1999	Shapland et al.	6,277,114	B1	8/2001	Bullivant et al.
5,868,708	A	2/1999	Hart et al.	6,278,895	B1	8/2001	Bernard
5,873,849	A	2/1999	Bernard	6,280,441	B1	8/2001	Ryan
5,904,648	A	5/1999	Arndt et al.	6,283,988	B1	9/2001	Laufer et al.
5,919,142	A	7/1999	Boone et al.	6,283,989	B1	9/2001	Laufer et al.
5,919,191	A	7/1999	Lennox et al.	6,284,140	B1	9/2001	Sommermeyer et al.
5,921,982	A	7/1999	Lesh et al.	6,287,293	B1	9/2001	Jones et al.
5,944,710	A	8/1999	Dev et al.	6,287,304	B1	9/2001	Eggers et al.
5,947,284	A	9/1999	Foster	6,296,636	B1	10/2001	Cheng et al.
5,947,889	A	9/1999	Hehrlein	6,298,726	B1	10/2001	Adachi et al.
5,951,546	A	9/1999	Lorentzen	6,299,633	B1	10/2001	Laufer
5,954,745	A	9/1999	Gertler et al.	6,300,108	B1	10/2001	Rubinsky et al.
5,957,919	A	9/1999	Laufer	D450,391	S	11/2001	Hunt et al.
5,957,963	A	9/1999	Dobak	6,312,428	B1	11/2001	Eggers et al.
5,968,006	A	10/1999	Hofmann	6,326,177	B1	12/2001	Schoenbach et al.
5,983,131	A	11/1999	Weaver et al.	6,327,505	B1	12/2001	Medhkour et al.
5,984,896	A	11/1999	Boyd	6,328,689	B1	12/2001	Gonzalez et al.
5,991,697	A	11/1999	Nelson et al.	6,347,247	B1	2/2002	Dev et al.
5,999,847	A	12/1999	Elstrom	6,349,233	B1	2/2002	Adams
6,004,339	A	12/1999	Wijay	6,351,674	B2	2/2002	Silverstone
6,009,347	A	12/1999	Hofmann	6,387,671	B1	5/2002	Rubinsky et al.
6,009,877	A	1/2000	Edwards	6,398,779	B1	6/2002	Buyse et al.
6,010,613	A	1/2000	Walters et al.	6,403,348	B1	6/2002	Rubinsky et al.
6,016,452	A	1/2000	Kasevich	6,405,732	B1	6/2002	Edwards et al.
6,029,090	A	2/2000	Herbst	6,411,852	B1	6/2002	Danek et al.
6,041,252	A	3/2000	Walker et al.	6,419,674	B1	7/2002	Bowser et al.
6,043,066	A	3/2000	Mangano et al.	6,443,952	B1	9/2002	Mulier et al.
				6,463,331	B1	10/2002	Edwards
				6,470,211	B1	10/2002	Ideker et al.
				6,482,221	B1	11/2002	Hebert et al.
				6,482,619	B1	11/2002	Rubinsky et al.

(56)

## References Cited

## U.S. PATENT DOCUMENTS

6,485,487	B1	11/2002	Sherman	7,012,061	B1	3/2006	Reiss et al.
6,488,673	B1	12/2002	Lauffer et al.	7,027,869	B2	4/2006	Danek et al.
6,488,678	B2	12/2002	Sherman	7,036,510	B2	5/2006	Zgoda et al.
6,488,680	B1	12/2002	Francischelli et al.	7,053,063	B2	5/2006	Rubinsky et al.
6,491,706	B1	12/2002	Alferness et al.	7,054,685	B2	5/2006	Dimmer et al.
6,493,589	B1	12/2002	Medhkour et al.	7,063,698	B2	6/2006	Whayne et al.
6,493,592	B1	12/2002	Leonard et al.	7,087,040	B2	8/2006	McGuckin et al.
6,500,173	B2	12/2002	Underwood et al.	7,097,612	B2	8/2006	Bertolero et al.
6,503,248	B1	1/2003	Levine	7,100,616	B2	9/2006	Springmeyer
6,506,189	B1	1/2003	Rittman et al.	7,113,821	B1	9/2006	Sun et al.
6,514,248	B1	2/2003	Eggers et al.	7,130,697	B2	10/2006	Chornenky et al.
6,520,183	B2	2/2003	Amar	7,211,083	B2	5/2007	Chornenky et al.
6,526,320	B2	2/2003	Mitchell	7,232,437	B2	6/2007	Berman et al.
D471,640	S	3/2003	McMichael et al.	7,250,048	B2	7/2007	Francischelli et al.
D471,641	S	3/2003	McMichael et al.	D549,332	S	8/2007	Matsumoto et al.
6,530,922	B2	3/2003	Cosman et al.	7,257,450	B2	8/2007	Auth et al.
6,533,784	B2	3/2003	Truckai et al.	7,264,002	B2	9/2007	Danek et al.
6,537,976	B1	3/2003	Gupta	7,267,676	B2	9/2007	Chornenky et al.
6,558,378	B2	5/2003	Sherman et al.	7,273,055	B2	9/2007	Danek et al.
6,562,604	B2	5/2003	Rubinsky et al.	7,291,146	B2	11/2007	Steinke et al.
6,569,162	B2	5/2003	He	7,331,940	B2	2/2008	Sommerich
6,575,969	B1	6/2003	Rittman et al.	7,331,949	B2	2/2008	Marisi
6,589,161	B2	7/2003	Corcoran	7,341,558	B2	3/2008	Torre et al.
6,592,594	B2	7/2003	Rimbaugh et al.	7,344,533	B2	3/2008	Pearson et al.
6,607,529	B1	8/2003	Jones et al.	D565,743	S	4/2008	Phillips et al.
6,610,054	B1	8/2003	Edwards et al.	D571,478	S	6/2008	Horacek
6,611,706	B2	8/2003	Avrahami et al.	7,387,626	B2	6/2008	Edwards et al.
6,613,211	B1	9/2003	Mccormick et al.	7,399,747	B1	7/2008	Clair et al.
6,616,657	B2	9/2003	Simpson et al.	D575,399	S	8/2008	Matsumoto et al.
6,627,421	B1	9/2003	Unger et al.	D575,402	S	8/2008	Sandor
D480,816	S	10/2003	McMichael et al.	7,419,487	B2	9/2008	Johnson et al.
6,634,363	B1	10/2003	Danek et al.	7,434,578	B2	10/2008	Dillard et al.
6,638,253	B2	10/2003	Breznock	7,449,019	B2	11/2008	Uchida et al.
6,653,091	B1	11/2003	Dunn et al.	7,451,765	B2	11/2008	Adler
6,666,858	B2	12/2003	Lafontaine	7,455,675	B2	11/2008	Schur et al.
6,669,691	B1	12/2003	Taimisto	7,476,203	B2	1/2009	DeVore et al.
6,673,070	B2	1/2004	Edwards et al.	7,520,877	B2	4/2009	Lee et al.
6,678,558	B1	1/2004	Dimmer et al.	7,533,671	B2	5/2009	Gonzalez et al.
6,689,096	B1	2/2004	Loubens et al.	D595,422	S	6/2009	Mustapha
6,692,493	B2	2/2004	McGovern et al.	7,544,301	B2	6/2009	Shah et al.
6,694,979	B2	2/2004	Deem et al.	7,549,984	B2	6/2009	Mathis
6,694,984	B2	2/2004	Habib	7,565,208	B2	7/2009	Harris et al.
6,695,861	B1	2/2004	Rosenberg et al.	7,571,729	B2	8/2009	Saadat et al.
6,697,669	B2	2/2004	Dev et al.	7,632,291	B2	12/2009	Stephens et al.
6,697,670	B2	2/2004	Chomenky et al.	7,655,004	B2	2/2010	Long
6,702,808	B1	3/2004	Kreindel	7,674,249	B2	3/2010	Ivorra et al.
6,712,811	B2	3/2004	Underwood et al.	7,680,543	B2	3/2010	Azure
D489,973	S	5/2004	Root et al.	D613,418	S	4/2010	Ryan et al.
6,753,171	B2	6/2004	Karube et al.	7,718,409	B2	5/2010	Rubinsky et al.
6,761,716	B2	7/2004	Kadhiresan et al.	7,722,606	B2	5/2010	Azure
D495,807	S	9/2004	Agbodoe et al.	7,742,795	B2	6/2010	Stone et al.
6,795,728	B2	9/2004	Chornenky et al.	7,765,010	B2	7/2010	Chornenky et al.
6,801,804	B2	10/2004	Miller et al.	7,771,401	B2	8/2010	Hekmat et al.
6,812,204	B1	11/2004	McHale et al.	RE42,016	E	12/2010	Chornenky et al.
6,837,886	B2	1/2005	Collins et al.	D630,321	S	1/2011	Hamilton
6,847,848	B2	1/2005	Sterzer et al.	D631,154	S	1/2011	Hamilton
6,860,847	B2	3/2005	Alferness et al.	RE42,277	E	4/2011	Jaafar et al.
6,865,416	B2	3/2005	Dev et al.	7,918,852	B2	4/2011	Tullis et al.
6,881,213	B2	4/2005	Ryan et al.	7,937,143	B2	5/2011	Demarais et al.
6,892,099	B2	5/2005	Jaafar et al.	7,938,824	B2	5/2011	Chornenky et al.
6,895,267	B2	5/2005	Panescu et al.	7,951,582	B2	5/2011	Gazit et al.
6,905,480	B2	6/2005	McGuckin et al.	7,955,827	B2	6/2011	Rubinsky et al.
6,912,417	B1	6/2005	Bernard et al.	RE42,835	E	10/2011	Chornenky et al.
6,927,049	B2	8/2005	Rubinsky et al.	D647,628	S	10/2011	Helfferen
6,941,950	B2	9/2005	Wilson et al.	8,048,067	B2*	11/2011	Davalos ..... A61B 18/12 606/32
6,942,681	B2	9/2005	Johnson	RE43,009	E	12/2011	Chornenky et al.
6,958,062	B1	10/2005	Gough et al.	8,109,926	B2	2/2012	Azure
6,960,189	B2	11/2005	Bates et al.	8,114,070	B2	2/2012	Rubinsky et al.
6,962,587	B2	11/2005	Johnson et al.	8,162,918	B2	4/2012	Ivorra et al.
6,972,013	B1	12/2005	Zhang et al.	8,187,269	B2	5/2012	Shaddock et al.
6,972,014	B2	12/2005	Eum et al.	8,221,411	B2	7/2012	Francischelli et al.
6,989,010	B2	1/2006	Francischelli et al.	8,231,603	B2	7/2012	Hobbs et al.
6,994,689	B1	2/2006	Zadno-Azizi et al.	8,240,468	B2	8/2012	Wilkinson et al.
6,994,706	B2	2/2006	Chornenky et al.	8,251,986	B2	8/2012	Chornenky et al.
7,011,094	B2	3/2006	Rapacki et al.	8,267,927	B2	9/2012	Dalal et al.
				8,267,936	B2	9/2012	Hushka et al.
				8,282,631	B2	10/2012	Davalos et al.
				8,298,222	B2	10/2012	Rubinsky et al.



(56)

## References Cited

## U.S. PATENT DOCUMENTS

8,348,921	B2	1/2013	Ivorra et al.	2003/0078490	A1	4/2003	Damasco et al.
D677,798	S	3/2013	Hart et al.	2003/0088189	A1	5/2003	Tu et al.
8,425,455	B2	4/2013	Nentwick	2003/0088199	A1	5/2003	Kawaji
8,425,505	B2	4/2013	Long	2003/0096407	A1	5/2003	Atala et al.
8,454,594	B2	6/2013	Demarais et al.	2003/0105454	A1	6/2003	Cucin
8,465,484	B2	6/2013	Davalos et al.	2003/0109871	A1	6/2003	Johnson et al.
8,511,317	B2	8/2013	Thapliyal et al.	2003/0127090	A1	7/2003	Gifford et al.
8,518,031	B2	8/2013	Boyden et al.	2003/0130711	A1	7/2003	Pearson et al.
8,562,588	B2	10/2013	Hobbs et al.	2003/0135242	A1	7/2003	Mongeon et al.
8,603,087	B2	12/2013	Rubinsky et al.	2003/0154988	A1	8/2003	DeVore et al.
8,632,534	B2	1/2014	Pearson et al.	2003/0159700	A1	8/2003	Laufer et al.
8,634,929	B2	1/2014	Chornenky et al.	2003/0166181	A1	9/2003	Rubinsky et al.
8,647,338	B2	2/2014	Chornenky et al.	2003/0170898	A1	9/2003	Gundersen et al.
8,715,276	B2	5/2014	Thompson et al.	2003/0194808	A1	10/2003	Rubinsky et al.
8,753,335	B2	6/2014	Moshe et al.	2003/0195385	A1	10/2003	DeVore
8,814,860	B2	8/2014	Davalos et al.	2003/0195406	A1	10/2003	Jenkins et al.
8,835,166	B2	9/2014	Phillips et al.	2003/0199050	A1	10/2003	Mangano et al.
8,845,635	B2	9/2014	Daniel et al.	2003/0208200	A1	11/2003	Palanker et al.
8,880,195	B2	11/2014	Azure	2003/0208236	A1	11/2003	Heil et al.
8,903,488	B2	12/2014	Callas et al.	2003/0212394	A1	11/2003	Pearson et al.
8,906,006	B2	12/2014	Chornenky et al.	2003/0212412	A1	11/2003	Dillard et al.
8,926,606	B2	1/2015	Davalos et al.	2003/0225360	A1	12/2003	Eppstein et al.
8,958,888	B2	2/2015	Chornenky et al.	2003/0228344	A1	12/2003	Fields et al.
8,968,542	B2	3/2015	Davalos et al.	2004/0009459	A1	1/2004	Anderson et al.
8,992,517	B2	3/2015	Davalos et al.	2004/0019371	A1	1/2004	Jaafar et al.
9,005,189	B2	4/2015	Davalos et al.	2004/0055606	A1	3/2004	Hendricksen et al.
9,078,665	B2	7/2015	Moss et al.	2004/0059328	A1	3/2004	Daniel et al.
9,149,331	B2	10/2015	Deem et al.	2004/0059389	A1	3/2004	Chornenky et al.
9,173,704	B2	11/2015	Hobbs et al.	2004/0068228	A1	4/2004	Cunningham
9,198,733	B2	12/2015	Neal, II et al.	2004/0116965	A1	6/2004	Falkenberg
9,283,051	B2	3/2016	Garcia et al.	2004/0133194	A1	7/2004	Eum et al.
9,598,691	B2	3/2017	Davalos	2004/0138715	A1	7/2004	Groeningen et al.
9,867,652	B2	1/2018	Sano et al.	2004/0146877	A1	7/2004	Diss et al.
2001/0039393	A1	11/2001	Mori et al.	2004/0153057	A1	8/2004	Davison
2001/0044596	A1	11/2001	Jaafar	2004/0176855	A1	9/2004	Badylak
2001/0046706	A1	11/2001	Rubinsky et al.	2004/0193097	A1	9/2004	Hofmann et al.
2001/0047167	A1	11/2001	Heggeness	2004/0199159	A1	10/2004	Lee et al.
2001/0051366	A1	12/2001	Rubinsky et al.	2004/0200484	A1	10/2004	Springmeyer
2002/0002393	A1	1/2002	Mitchell	2004/0206349	A1	10/2004	Alferness et al.
2002/0010491	A1	1/2002	Schoenbach et al.	2004/0210248	A1	10/2004	Gordon et al.
2002/0022864	A1	2/2002	Mahvi et al.	2004/0230187	A1	11/2004	Lee et al.
2002/0040204	A1	4/2002	Dev et al.	2004/0236376	A1	11/2004	Miklavcic et al.
2002/0049370	A1	4/2002	Laufer et al.	2004/0243107	A1	12/2004	Macoviak et al.
2002/0052601	A1	5/2002	Goldberg et al.	2004/0267189	A1	12/2004	Mavor et al.
2002/0055731	A1	5/2002	Atala et al.	2004/0267340	A1	12/2004	Cioanta et al.
2002/0065541	A1	5/2002	Fredricks et al.	2005/0010209	A1	1/2005	Lee et al.
2002/0072742	A1	6/2002	Schaefer et al.	2005/0010259	A1	1/2005	Gerber
2002/0077314	A1	6/2002	Falk et al.	2005/0013870	A1	1/2005	Freyman et al.
2002/0077676	A1	6/2002	Schroepel et al.	2005/0020965	A1	1/2005	Rioux et al.
2002/0082543	A1	6/2002	Park et al.	2005/0043726	A1	2/2005	Mchale et al.
2002/0099323	A1	7/2002	Dev et al.	2005/0049541	A1	3/2005	Behar et al.
2002/0111615	A1	8/2002	Cosman et al.	2005/0061322	A1	3/2005	Freitag
2002/0112729	A1	8/2002	DeVore et al.	2005/0066974	A1	3/2005	Fields et al.
2002/0115208	A1	8/2002	Mitchell et al.	2005/0143817	A1	6/2005	Hunter et al.
2002/0119437	A1	8/2002	Grooms et al.	2005/0165393	A1	7/2005	Eppstein
2002/0133324	A1	9/2002	Weaver et al.	2005/0171522	A1	8/2005	Christopherson
2002/0137121	A1	9/2002	Rubinsky et al.	2005/0171523	A1	8/2005	Rubinsky et al.
2002/0138075	A1	9/2002	Edwards et al.	2005/0171574	A1	8/2005	Rubinsky et al.
2002/0138117	A1	9/2002	Son	2005/0182462	A1	8/2005	Chornenky et al.
2002/0143365	A1	10/2002	Herbst	2005/0197619	A1	9/2005	Rule et al.
2002/0147462	A1	10/2002	Mair et al.	2005/0261672	A1	11/2005	Deem et al.
2002/0156472	A1	10/2002	Lee et al.	2005/0267407	A1	12/2005	Goldman
2002/0161361	A1	10/2002	Sherman et al.	2005/0282284	A1	12/2005	Rubinsky et al.
2002/0183684	A1	12/2002	Dev et al.	2005/0288684	A1	12/2005	Aronson et al.
2002/0183735	A1	12/2002	Edwards et al.	2005/0288702	A1	12/2005	McGurk et al.
2002/0183740	A1	12/2002	Edwards et al.	2005/0288730	A1	12/2005	Deem et al.
2002/0188242	A1	12/2002	Wu	2006/0004356	A1	1/2006	Bilski et al.
2002/0193784	A1	12/2002	McHale et al.	2006/0004400	A1	1/2006	McGurk et al.
2002/0193831	A1	12/2002	Smith	2006/0009748	A1	1/2006	Mathis
2003/0009110	A1	1/2003	Tu et al.	2006/0015147	A1	1/2006	Persson et al.
2003/0016168	A1	1/2003	Jandrell	2006/0020347	A1	1/2006	Barrett et al.
2003/0055220	A1	3/2003	Legrain	2006/0024359	A1	2/2006	Walker et al.
2003/0055420	A1	3/2003	Kadhiresan et al.	2006/0025760	A1	2/2006	Podhajsky
2003/0059945	A1	3/2003	Dzekunov et al.	2006/0074413	A1	4/2006	Behzadian
2003/0060856	A1	3/2003	Chornenky et al.	2006/0079838	A1	4/2006	Walker et al.
				2006/0079845	A1	4/2006	Howard et al.
				2006/0079883	A1	4/2006	Elmouelhi et al.
				2006/0085054	A1	4/2006	Zikorus et al.
				2006/0089635	A1	4/2006	Young et al.

(56)		References Cited						
		U.S. PATENT DOCUMENTS						
2006/0121610	A1	6/2006	Rubinsky et al.		2008/0249503	A1	10/2008	Fields et al.
2006/0142801	A1*	6/2006	Demarais .....	A61M 25/10	2008/0262489	A1	10/2008	Steinke
				607/2	2008/0269586	A1	10/2008	Rubinsky et al.
2006/0149123	A1	7/2006	Vidlund et al.		2008/0269838	A1	10/2008	Brighton et al.
2006/0173490	A1	8/2006	Lafontaine et al.		2008/0275465	A1	11/2008	Paul et al.
2006/0182684	A1	8/2006	Beliveau		2008/0281319	A1	11/2008	Paul et al.
2006/0195146	A1	8/2006	Tracey et al.		2008/0283065	A1	11/2008	Chang et al.
2006/0212032	A1	9/2006	Daniel et al.		2008/0288038	A1	11/2008	Paul et al.
2006/0212078	A1	9/2006	Demarais et al.		2008/0300589	A1	12/2008	Paul et al.
2006/0217703	A1	9/2006	Chornenky et al.		2008/0306427	A1	12/2008	Bailey
2006/0224188	A1	10/2006	Libbus et al.		2008/0312599	A1	12/2008	Rosenberg
2006/0235474	A1	10/2006	Demarais		2009/0018206	A1	1/2009	Barkan et al.
2006/0247619	A1	11/2006	Kaplan et al.		2009/0024075	A1	1/2009	Schroepfel et al.
2006/0264752	A1	11/2006	Rubinsky et al.		2009/0029407	A1	1/2009	Gazit et al.
2006/0264807	A1	11/2006	Westersten et al.		2009/0038752	A1	2/2009	Weng et al.
2006/0269531	A1	11/2006	Beebe et al.		2009/0062788	A1	3/2009	Long et al.
2006/0276710	A1	12/2006	Krishnan		2009/0062792	A1	3/2009	Vakharia et al.
2006/0283462	A1	12/2006	Fields et al.		2009/0081272	A1	3/2009	Clarke et al.
2006/0293713	A1	12/2006	Rubinsky et al.		2009/0105703	A1	4/2009	Shaddock
2006/0293725	A1	12/2006	Rubinsky et al.		2009/0114226	A1	5/2009	Deem et al.
2006/0293730	A1	12/2006	Rubinsky et al.		2009/0125009	A1	5/2009	Zikorus et al.
2006/0293731	A1	12/2006	Rubinsky et al.		2009/0138014	A1	5/2009	Bonutti
2006/0293734	A1	12/2006	Scott et al.		2009/0143705	A1	6/2009	Danek et al.
2007/0010805	A1	1/2007	Fedewa et al.		2009/0157166	A1	6/2009	Singhal et al.
2007/0016183	A1	1/2007	Lee et al.		2009/0163904	A1	6/2009	Miller et al.
2007/0016185	A1	1/2007	Tullis et al.		2009/0171280	A1	7/2009	Samuel et al.
2007/0021803	A1	1/2007	Deem et al.		2009/0177111	A1	7/2009	Miller et al.
2007/0025919	A1	2/2007	Deem et al.		2009/0186850	A1	7/2009	Kiribayashi et al.
2007/0043345	A1	2/2007	Davalos et al.		2009/0192508	A1	7/2009	Laufer et al.
2007/0060989	A1	3/2007	Deem et al.		2009/0198231	A1*	8/2009	Esser .....
2007/0078391	A1	4/2007	Wortley et al.					A61N 1/327
2007/0088347	A1	4/2007	Young et al.		2009/0228001	A1	9/2009	Pacey
2007/0093789	A1	4/2007	Smith		2009/0247933	A1	10/2009	Maor et al.
2007/0096048	A1	5/2007	Clerc		2009/0248012	A1	10/2009	Maor et al.
2007/0118069	A1	5/2007	Persson et al.		2009/0269317	A1	10/2009	Davalos
2007/0129711	A1	6/2007	Altshuler et al.		2009/0275827	A1	11/2009	Aiken et al.
2007/0129760	A1	6/2007	Demarais et al.		2009/0281477	A1	11/2009	Mikus et al.
2007/0156135	A1	7/2007	Rubinsky et al.		2009/0292342	A1	11/2009	Rubinsky et al.
2007/0191889	A1	8/2007	Lang		2009/0301480	A1	12/2009	Elsakka et al.
2007/0203486	A1	8/2007	Young		2009/0306544	A1	12/2009	Ng et al.
2007/0230757	A1	10/2007	Trachtenberg et al.		2009/0306545	A1	12/2009	Elsakka et al.
2007/0239099	A1	10/2007	Goldfarb et al.		2009/0318905	A1	12/2009	Bhargav et al.
2007/0244521	A1	10/2007	Bomzin et al.		2009/0326436	A1	12/2009	Rubinsky et al.
2007/0287950	A1	12/2007	Kjeken et al.		2009/0326570	A1	12/2009	Brown
2007/0295336	A1	12/2007	Nelson et al.		2010/0004623	A1	1/2010	Hamilton et al.
2007/0295337	A1	12/2007	Nelson et al.		2010/0023004	A1	1/2010	Franciscelli et al.
2008/0015571	A1	1/2008	Rubinsky et al.		2010/0030211	A1	2/2010	Davalos et al.
2008/0021371	A1	1/2008	Rubinsky et al.		2010/0049190	A1	2/2010	Long et al.
2008/0027314	A1	1/2008	Miyazaki et al.		2010/0057074	A1	3/2010	Roman et al.
2008/0027343	A1	1/2008	Fields et al.		2010/0069921	A1	3/2010	Miller et al.
2008/0033340	A1	2/2008	Heller et al.		2010/0087813	A1	4/2010	Long
2008/0033417	A1	2/2008	Nields et al.		2010/0130975	A1	5/2010	Long
2008/0045880	A1	2/2008	Kjeken et al.		2010/0152725	A1	6/2010	Pearson et al.
2008/0052786	A1	2/2008	Lin et al.		2010/0160850	A1	6/2010	Ivorra et al.
2008/0071262	A1	3/2008	Azure		2010/0168735	A1	7/2010	Deno et al.
2008/0097139	A1	4/2008	Clerc et al.		2010/0174282	A1	7/2010	Demarais et al.
2008/0097422	A1	4/2008	Edwards et al.		2010/0179530	A1	7/2010	Long et al.
2008/0103529	A1	5/2008	Schoenbach et al.		2010/0196984	A1	8/2010	Rubinsky et al.
2008/0121375	A1	5/2008	Richason et al.		2010/0204560	A1	8/2010	Salahieh et al.
2008/0125772	A1	5/2008	Stone et al.		2010/0204638	A1	8/2010	Hobbs et al.
2008/0132826	A1	6/2008	Shaddock et al.		2010/0222677	A1	9/2010	Placek et al.
2008/0132884	A1	6/2008	Rubinsky et al.		2010/0228247	A1	9/2010	Paul et al.
2008/0132885	A1	6/2008	Rubinsky et al.		2010/0241117	A1	9/2010	Paul et al.
2008/0140064	A1	6/2008	Vegesna		2010/0249771	A1	9/2010	Pearson et al.
2008/0146934	A1	6/2008	Czygan et al.		2010/0250209	A1	9/2010	Pearson et al.
2008/0154259	A1	6/2008	Gough et al.		2010/0255795	A1	10/2010	Rubinsky et al.
2008/0167649	A1	7/2008	Edwards et al.		2010/0256628	A1	10/2010	Pearson et al.
2008/0171985	A1	7/2008	Karakoca		2010/0256630	A1	10/2010	Hamilton, Jr. et al.
2008/0190434	A1	8/2008	Wai		2010/0261994	A1	10/2010	Davalos et al.
2008/0200911	A1	8/2008	Long		2010/0286690	A1	11/2010	Paul et al.
2008/0200912	A1	8/2008	Long		2010/0298823	A1	11/2010	Cao et al.
2008/0208052	A1	8/2008	LePivert et al.		2010/0331758	A1	12/2010	Davalos et al.
2008/0210243	A1	9/2008	Clayton et al.		2011/0017207	A1	1/2011	Hendricksen et al.
2008/0214986	A1	9/2008	Ivorra et al.		2011/0034209	A1	2/2011	Rubinsky et al.
2008/0236593	A1	10/2008	Nelson et al.		2011/0064671	A1	3/2011	Bynoe
					2011/0106221	A1	5/2011	Neal, II et al.
					2011/0112531	A1	5/2011	Landis et al.
					2011/0118727	A1	5/2011	Fish et al.

(56)

References Cited

U.S. PATENT DOCUMENTS

2011/0118732 A1\* 5/2011 Rubinsky ..... A6IN 1/0412  
606/41

2011/0130834 A1 6/2011 Wilson et al.  
2011/0144524 A1 6/2011 Fish et al.  
2011/0144635 A1 6/2011 Harper et al.  
2011/0144657 A1 6/2011 Fish et al.  
2011/0152678 A1 6/2011 Aljuri et al.  
2011/0202053 A1 8/2011 Moss et al.  
2011/0217730 A1 9/2011 Gazit et al.  
2011/0251607 A1 10/2011 Kruecker et al.  
2012/0034131 A1 2/2012 Rubinsky et al.  
2012/0059255 A1 3/2012 Paul et al.  
2012/0071872 A1 3/2012 Rubinsky et al.  
2012/0071874 A1 3/2012 Davalos et al.  
2012/0085649 A1 4/2012 Sano et al.  
2012/0089009 A1 4/2012 Omary et al.  
2012/0090646 A1 4/2012 Tanaka et al.  
2012/0095459 A1 4/2012 Callas et al.  
2012/0109122 A1 5/2012 Arena et al.  
2012/0130289 A1 5/2012 Demarais et al.  
2012/0150172 A1 6/2012 Ortiz et al.  
2012/0165813 A1 6/2012 Lee et al.  
2012/0179091 A1 7/2012 Ivorra et al.  
2012/0226218 A1 9/2012 Phillips et al.  
2012/0226271 A1 9/2012 Callas et al.  
2012/0265186 A1 10/2012 Burger et al.  
2012/0277741 A1 11/2012 Davalos et al.  
2012/0303020 A1 11/2012 Chornenky et al.  
2012/0310236 A1 12/2012 Placek et al.  
2013/0090646 A1 4/2013 Moss et al.  
2013/0108667 A1 5/2013 Soikum et al.  
2013/0110106 A1 5/2013 Richardson  
2013/0184702 A1 7/2013 Neal, II et al.  
2013/0196441 A1 8/2013 Rubinsky et al.  
2013/0197425 A1 8/2013 Golberg et al.  
2013/0202766 A1 8/2013 Rubinsky et al.  
2013/0218157 A1 8/2013 Callas et al.  
2013/0253415 A1 9/2013 Sano et al.  
2013/0281968 A1 10/2013 Davalos et al.  
2013/0345697 A1 12/2013 Garcia et al.  
2013/0345779 A1 12/2013 Maor et al.  
2014/0039489 A1 2/2014 Davalos et al.  
2014/0046322 A1 2/2014 Callas et al.  
2014/0081255 A1 3/2014 Johnson et al.  
2014/0088578 A1 3/2014 Rubinsky et al.  
2014/0121663 A1 5/2014 Pearson et al.  
2014/0163551 A1 6/2014 Maor et al.  
2014/0207133 A1 7/2014 Model et al.  
2014/0296844 A1 10/2014 Kevin et al.  
2014/0309579 A1 10/2014 Rubinsky et al.  
2014/0378964 A1 12/2014 Pearson  
2015/0088120 A1 3/2015 Garcia et al.  
2015/0088220 A1 3/2015 Callas et al.  
2015/0112333 A1 4/2015 Chorenky et al.  
2015/0126922 A1 5/2015 Willis  
2015/0164584 A1 6/2015 Davalos et al.  
2015/0173824 A1 6/2015 Davalos et al.  
2015/0201996 A1 7/2015 Rubinsky et al.  
2015/0265349 A1 9/2015 Moss et al.  
2015/0289923 A1 10/2015 Davalos et al.  
2015/0320488 A1 11/2015 Moshe et al.  
2015/0327944 A1\* 11/2015 Neal, II ..... C12N 13/00  
606/34

2016/0022957 A1 1/2016 Hobbs et al.  
2016/0066977 A1 3/2016 Neal et al.  
2016/0074114 A1 3/2016 Pearson et al.  
2016/0113708 A1 4/2016 Moss et al.  
2016/0143698 A1 5/2016 Garcia et al.  
2016/0235470 A1 8/2016 Callas et al.  
2016/0287313 A1 10/2016 Rubinsky et al.  
2016/0287314 A1 10/2016 Arena et al.  
2016/0338761 A1 11/2016 Chornenky et al.  
2016/0354142 A1 12/2016 Pearson et al.  
2017/0035501 A1 2/2017 Chornenky et al.  
2017/0189579 A1 7/2017 Davalos

2017/0209620 A1 7/2017 Davalos et al.  
2017/0266438 A1 9/2017 Sano  
2017/0360326 A1 12/2017 Davalos  
2018/0125565 A1 5/2018 Sano et al.  
2018/0161086 A1 6/2018 Davalos et al.

FOREIGN PATENT DOCUMENTS

AU 2005271471 A2 2/2006  
AU 2006321570 A1 6/2007  
AU 2006321574 A1 6/2007  
AU 2006321918 A1 6/2007  
CA 2297846 A1 2/1999  
CA 2378110 A1 2/2001  
CA 2445392 A1 11/2002  
CA 2458676 A1 3/2003  
CA 2487284 A1 12/2003  
CA 2575792 A1 2/2006  
CA 2631940 A1 6/2007  
CA 2631946 A1 6/2007  
CA 2632604 A1 6/2007  
CA 2751462 A1 11/2010  
CN 1525839 A 9/2004  
CN 101534736 A 9/2009  
CN 102238921 A 11/2011  
CN 102421386 A 4/2012  
DE 863111tr 1/1953  
DE 4000893tr 7/1991  
DE 60038026 2/2009  
EP 0218275 A1 4/1987  
EP 0339501 A2 11/1989  
EP 0378132 A 7/1990  
EP 0533511 A1 3/1993  
EP 0998235 A1 5/2000  
EP 0528891 B1 7/2000  
EP 1196550 A2 4/2002  
EP 1439792 A1 7/2004  
EP 1442765 A1 8/2004  
EP 1462065 A2 9/2004  
EP 1061983 B1 11/2004  
EP 1493397 A1 1/2005  
EP 1506039 A1 2/2005  
EP 0935482 B1 5/2005  
EP 1011495 B1 11/2005  
EP 1796568 A1 6/2007  
EP 1207797 B1 2/2008  
EP 1406685 B1 6/2008  
EP 1424970 B1 12/2008  
EP 2381829 A1 11/2011  
EP 2413833 A1 2/2012  
EP 1791485 B1 12/2014  
EP 2373241 B1 1/2015  
EP 1962710 B1 8/2015  
EP 1962708 B1 9/2015  
EP 1962945 B1 4/2016  
ES 2300272 6/2008  
ES 2315493 4/2009  
JP 2001510702 A 8/2001  
JP 2003505072 A 2/2003  
JP 2003506064 A 2/2003  
JP 2004203224 A 7/2004  
JP 2004525726 A 8/2004  
JP 2004303590 A 10/2004  
JP 2005501596 A 1/2005  
JP 2005526579 A 9/2005  
JP 2008508946 A 3/2008  
JP 4252316 B2 4/2009  
JP 2009518130 A 5/2009  
JP 2009518150 A 5/2009  
JP 2009518151 A 5/2009  
JP 2012510332 A 5/2012  
JP 2012521863 A 9/2012  
KR 101034682 A 5/2011  
WO 9104014 4/1991  
WO 9634571 11/1996  
WO 9639531 A 12/1996  
WO 9810745 3/1998  
WO 9814238 A 4/1998  
WO 9901076 1/1999

(56)

## References Cited

## FOREIGN PATENT DOCUMENTS

WO	9904710	2/1999
WO	0020554 A	4/2000
WO	0107583 A	2/2001
WO	0107584 A	2/2001
WO	0107585 A	2/2001
WO	0110319 A	2/2001
WO	0148153 A	7/2001
WO	2001048153 A1	7/2001
WO	0170114 A1	9/2001
WO	0181533 A	11/2001
WO	02078527 A	10/2002
WO	02089686 A	11/2002
WO	02100459 A	12/2002
WO	2003020144 A1	3/2003
WO	2003047684 A2	6/2003
WO	03099382 A	12/2003
WO	2004037341 A2	5/2004
WO	2004080347 A2	9/2004
WO	2005065284 A	7/2005
WO	2006017666 A2	2/2006
WO	2006031541 A1	3/2006
WO	2006130194 A2	12/2006
WO	2007067628 A1	6/2007
WO	2007067937 A2	6/2007
WO	2007067938 A2	6/2007
WO	2007067939 A2	6/2007
WO	2007067940 A2	6/2007
WO	2007067941 A2	6/2007
WO	2007067943 A2	6/2007
WO	2007070361 A2	6/2007
WO	2007123690 A2	11/2007
WO	2008063195 A1	5/2008
WO	2009046176 A1	4/2009
WO	2007137303	7/2009
WO	2009134876 A	11/2009
WO	2009135070 A1	11/2009
WO	2009137800 A2	11/2009
WO	2010064154 A1	6/2010
WO	2010117806 A1	10/2010
WO	2010118387 A	10/2010
WO	2010132472 A1	11/2010
WO	2010151277 A	12/2010
WO	2011047387 A	4/2011
WO	2011062653 A1	5/2011
WO	2011072221 A1	6/2011
WO	2012051433 A2	4/2012
WO	2012071526 A	5/2012
WO	2012088149 A	6/2012
WO	2015175570 A1	11/2015
WO	2016100325 A1	6/2016
WO	2016164930 A1	10/2016

## OTHER PUBLICATIONS

Chang, D.C., "Cell Poration and Cell-Fusion Using an Oscillating Electric-Field". *Biophysical Journal*, 56(4): p. 641-652 (1989).

Chen, M.T., et al., "Two-dimensional nanosecond electric field mapping based on cell electroporation", *PMC Biophys*, 2(1):9 (2009).

Co-pending U.S. Appl. No. 15/186,653, filed Jun. 20, 2016.

De Vuyst, E., et al., "In situ bipolar Electroporation for localized cell loading with reporter dyes and investigating gap junctional coupling", *Biophysical Journal*, 94(2): p. 469-479 (2008).

Esser, A.T., et al., "Towards solid tumor treatment by irreversible electroporation: intrinsic redistribution of fields and currents in tissue". *Technol Cancer Res Treat*, 6(4): p. 261-74 (2007).

Esser, A.T., et al., "Towards Solid Tumor Treatment by Nanosecond Pulsed Electric Fields". *Technology in Cancer Research & Treatment*, 8(4): p. 289-306 (2009).

Freeman, S.A., et al., Theory of Electroporation of Planar Bilayer-Membranes—Predictions of the Aqueous Area, Change in Capacitance, and Pore-Pore Separation. *Biophysical Journal*, 67(1):p. 42-56 (1994).

Gowrishankar T.R., et al., "Microdosimetry for conventional and supra-electroporation in cells with organelles". *Biochem Biophys Res Commun*, 341(4): p. 1266-76 (2006).

Kotnik, T. and D. Miklavcic, "Theoretical evaluation of the distributed power dissipation in biological cells exposed to electric fields", *Bioelectromagnetics*, 21(5): p. 385-394 (2000).

Kotnik, T., et al., "Cell membrane electroporation by symmetrical bipolar rectangular pulses. Part II. Reduced electrolytic contamination", *Bioelectrochemistry*, 54(1): p. 91-5 (2001).

Kotnik, T., et al., "Role of pulse shape in cell membrane electroporation", *Biochimica Et Biophysica Acta—Biomembranes*, 1614(2): p. 193-200 (2003).

Lackovic, I., et al., "Three-dimensional Finite-element Analysis of Joule Heating in Electrochemotherapy and in vivo Gene Electrotransfer", *Ieee Transactions on Dielectrics and Electrical Insulation*, 16(5): p. 1338-1347 (2009).

Long, G., et al., "Targeted Tissue Ablation With Nanosecond Pulses". *Ieee Transactions on Biomedical Engineering*, 58(8)(2011).

Nikolova, B., et al., "Treatment of Melanoma by Electroporation of Bacillus Calmette-Guerin". *Biotechnology & Biotechnological Equipment*, 25(3): p. 2522-2524 (2011).

Nuccitelli, R., et al., "A new pulsed electric field therapy for melanoma disrupts the tumor's blood supply and causes complete remission without recurrence", *Int J Cancer*, 125(2): p. 438-45 (2009).

PCT IPRP for PCT/US15/30429 (WO2015175570), dated Nov. 15, 2016.

Talele, S., et al., "Modelling single cell electroporation with bipolar pulse parameters and dynamic pore radii". *Journal of Electrostatics*, 68(3): p. 261-274 (2010).

Vernier, P.T., et al., "Nanosecond-pulse-driven membrane perturbation and small molecule permeabilization", *Bmc Cell Biology*, 7 (2006).

Weaver, J.C., "Electroporation of cells and tissues", *IEEE Transactions on Plasma Science*, 28(1): p. 24-33 (2000).

Sabuncu et al., "Dielectrophoretic separation of mouse melanoma clones." *Biomicrofluidics*, vol. 4, 7 pages (2010).

Salmanzadeh et al., "Investigating dielectric properties of different stages of syngeneic murine ovarian cancer cells" *Biomicrofluidics* 7, 011809 (2013), 12 pages.

Salmanzadeh et al., "Dielectrophoretic differentiation of mouse ovarian surface epithelial cells, macrophages, and fibroblasts using contactless dielectrophoresis." *Biomicrofluidics*, vol. 6, 13 Pages (2012).

Salmanzadeh et al., "Sphingolipid Metabolites Modulate Dielectric Characteristics of Cells in a Mouse Ovarian Cancer Progression Model." *Integr. Biol.*, 5(6), pp. 843-852 (2013).

Sano et al., "Contactless Dielectrophoretic Spectroscopy: Examination of the Dielectric Properties of Cells Found in Blood." *Electrophoresis*, 32, pp. 3164-3171, 2011.

Sano et al., "In-vitro bipolar nano- and microsecond electro-pulse bursts for irreversible electroporation therapies." *Bioelectrochemistry* vol. 100, pp. 69-79 (2014).

Sano et al., "Modeling and Development of a Low Frequency Contactless Dielectrophoresis (cDEP) Platform to Sort Cancer Cells from Dilute Whole Blood Samples." *Biosensors & Bioelectronics*, 8 pages (2011).

Saur et al., "CXCR4 expression increases liver and lung metastasis in a mouse model of pancreatic cancer." *Gastroenterology*, vol. 129, pp. 1237-1250 (2005).

Schoenbach et al., "Intracellular effect of ultrashort electrical pulses." *Bioelectromagnetics*, 22 (2001) pp. 440-448.

Seibert et al., "Clonal variation of MCF-7 breast cancer cells in vitro and in athymic nude mice." *Cancer Research*, vol. 43, pp. 2223-2239 (1983).

Seidler et al., "A Cre-IoxP-based mouse model for conditional somatic gene expression and knockdown in vivo by using avian retroviral vectors." *Proceedings of the National Academy of Sciences*, vol. 105, pp. 10137-10142 (2008).

Szot et al., "3D in vitro bioengineered tumors based on collagen I hydrogels." *Biomaterials* vol. 32, pp. 7905-7912 (2011).

(56)

## References Cited

## OTHER PUBLICATIONS

- Verbridge et al., "Oxygen-Controlled Three-Dimensional Cultures to Analyze Tumor Angiogenesis." *Tissue Engineering, Part A* vol. 16, pp. 2133-2141 (2010).
- Weaver et al., "A brief overview of electroporation pulse strength-duration space: A region where additional intracellular effects are expected." *Bioelectrochemistry* vol. 87, pp. 236-243 (2012).
- Yang et al., "Dielectric properties of human leukocyte subpopulations determined by electrorotation as a cell separation criterion." *Biophysical Journal*, vol. 76, pp. 3307-3314 (1999).
- Yao et al., "Study of transmembrane potentials of inner and outer membranes induced by pulsed-electric-field model and simulation." *IEEE Trans Plasma Sci*, 2007. 35(5): p. 1541-1549.
- Zhang, Y., et al., MR imaging to assess immediate response to irreversible electroporation for targeted ablation of liver tissues: preclinical feasibility studies in a rodent model. *Radiology*, 2010. 256(2): p. 424-32.
- Baptista et al., "The Use of Whole Organ Decellularization for the Generation of a Vascularized Liver Organoid," *Heptatology*, vol. 53, No. 2, pp. 604-617 (2011).
- Co-Pending U.S. Appl. No. 14/686,380, filed Apr. 14, 2015 and Published as US 2015/0289923 on Oct. 15, 2015.
- Co-pending U.S. Appl. No. 15/011,752, filed Feb. 1, 2016.
- Co-Pending Application No. PCT/US15/30429, International Search Report and Written Opinion dated Oct. 16, 2015, 19 pages.
- Co-Pending Application No. PCT/US2015/030429, Published on Nov. 19, 2015 as WO 2015/175570.
- Co-Pending U.S. Appl. No. 14/012,832, Response to Ex Parte Quayle Office Action dated Aug. 28, 2015, filed with RCE on Oct. 28, 2015, 9 pages.
- Corovic et al., "Analytical and numerical quantification and comparison of the local electric field in the tissue for different electrode configurations," *Biomed Eng Online*, 6, 14 pages, 2007.
- Cowley, Good News for Boomers, *Newsweek*, Dec. 30, 1996/Jan. 6, 1997.
- Cox, et al., Surgical Treatment of Atrial Fibrillation: A Review, *Europace* (2004) 5, S20-S-29.
- Crowley, Electrical Breakdown of Biomolecular Lipid Membranes as an Electromechanical Instability, *Biophysical Journal*, vol. 13, pp. 711-724, 1973.
- Daud, A.I., et al., "Phase I Trial of Interleukin-12 Plasmid Electroporation in Patients With Metastatic Melanoma," *Journal of Clinical Oncology*, 26, 5896-5903, Dec. 20, 2008.
- Davalos et al., "Electrical impedance tomography for imaging tissue electroporation," *IEEE Transactions on Biomedical Engineering*, 51, pp. 761-767, 2004.
- Davalos et al., "Theoretical analysis of the thermal effects during in vivo tissue electroporation." *Bioelectrochemistry*, vol. 61(1-2): pp. 99-107, 2003.
- Davalos et al., "Tissue ablation with irreversible electroporation." *Annals of Biomedical Engineering*, 3(2), pp. 223-231 (2005).
- Davalos, et al., A Feasibility Study for Electrical Impedance Tomography as a Means to Monitor Tissue Electroporation for Molecular Medicine, *IEEE Transactions on Biomedical Engineering*, vol. 49, No. 4, Apr. 2002.
- Davalos, R. V. & Rubinsky, B. Temperature considerations during irreversible electroporation. *International Journal of Heat and Mass Transfer* 51, 5617-5622, doi:10.1016/j.ijheatmasstransfer.2008.04.046 (2008).
- Davalos, Real-Time Imaging for Molecular Medicine through Electrical Impedance Tomography of Electroporation, Dissertation for Ph.D. in Engineering—Mechanical Engineering, Graduate Division of University of California, Berkeley, 2002.
- Dean, Nonviral Gene Transfer to Skeletal, Smooth, and Cardiac Muscle in Living Animals, *Am J. Physiol Cell Physiol* 289: 233-245, 2005.
- Demirbas, M. F., "Thermal Energy Storage and Phase Change Materials: An Overview" *Energy Sources Part B* 1(1), 85-95 (2006).
- Dev, et al., Medical Applications of Electroporation, *IEEE Transactions of Plasma Science*, vol. 28, No. 1, pp. 206-223, Feb. 2000.
- Dev, et al., Sustained Local Delivery of Heparin to the Rabbit Arterial Wall with an Electroporation Catheter, *Catheterization and Cardiovascular Diagnosis*, Nov. 1998, vol. 45, No. 3, pp. 337-343.
- Duraiswami, et al., Boundary Element Techniques for Efficient 2-D and 3-D Electrical Impedance Tomography, *Chemical Engineering Science*, vol. 52, No. 13, pp. 2185-2196, 1997.
- Duraiswami, et al., Efficient 2D and 3D Electrical Impedance Tomography Using Dual Reciprocity Boundary Element Techniques, *Engineering Analysis with Boundary Elements* 22, (1998) 13-31.
- Duraiswami, et al., Solution of Electrical Impedance Tomography Equations Using Boundary Element Methods, *Boundary Element Technology XII*, 1997, pp. 226-237.
- Edd et al., "Mathematical modeling of irreversible electroporation for treatment planning." *Technology in Cancer Research and Treatment*, vol. 6, No. 4, pp. 275-286 (2007).
- Edd, J. et al., In-Vivo Results of a New Focal Tissue Ablation Technique: Irreversible Electroporation, *IEEE Trans. Biomed. Eng.* 53 (2006) p. 1409-1415.
- Ellis TL, Garcia PA, Rossmeisl JH, Jr., Henao-Guerrero N, Robertson J, et al., "Nonthermal irreversible electroporation for intracranial surgical applications. Laboratory investigation", *J Neurosurg* 114: 681-688 (2011).
- Erez, et al., Controlled Destruction and Temperature Distributions in Biological Tissues Subjected to Monoactive Electrocoagulation, *Transactions of the ASME: Journal of Mechanical Design*, vol. 102, Feb. 1980.
- Extended European Search Report, May 11, 2012. PCT/US2009042100 from EP 09739678.2.
- Faroja, M., et al., "Irreversible Electroporation Ablation: Is the entire Damage Nonthermal?", *Radiology*, 266(2), 462-470 (2013).
- Foster RS, "High-intensity focused ultrasound in the treatment of prostatic disease", *European Urology*, 1993, vol. 23 Suppl 1, pp. 29-33.
- Foster, R.S., et al., Production of Prostatic Lesions in Canines Using Transrectally Administered High-Intensity Focused Ultrasound. *Eur. Urol.*, 1993; 23: 330-336.
- Fox, et al., Sampling Conductivity Images via MCMC, Mathematics Department, Auckland University, New Zealand, May 1997.
- Garcia et al., "Irreversible electroporation (IRE) to treat brain cancer." ASME Summer Bioengineering Conference, Marco Island, FL, Jun. 25-29, 2008, 2 pages.
- Garcia et al., "Non-thermal irreversible electroporation (N-TIRE) and adjuvant fractionated radiotherapeutic multimodal therapy for intracranial malignant glioma in a canine patient," *Technol Cancer Res Treat*, 10, pp. 73-83, 2011.
- Garcia et al., "Towards a Predictive Model of Electroporation-Based Therapies using Pre-Pulse Electrical Measurements" Abstract presented in the IEEE Engineering in Medicine and Biology Conference in Aug. 28, 2012 in San Diego, California, 4 pages.
- Garcia P.A., et al., "7.0-T Magnetic Resonance Imaging Characterization of Acute Blood-Brain-Barrier Disruption Achieved with Intracranial Irreversible Electroporation", *PLOS One*, Nov. 2012, 7:11, e50482.
- Garcia P.A., et al., "Pilot study of irreversible electroporation for intracranial surgery", *Conf Proc IEEE Eng Med Biol Soc*, 2009:6513-6516, 2009.
- Garcia, et al. "A Parametric Study Delineating Irreversible Electroporation from Thermal Damage Based on a Minimally Invasive Intracranial Procedure," *Biomed Eng Online*, vol. 10:34, 22 pages, 2011.
- Garcia, P. et al. Intracranial nonthermal irreversible electroporation: in vivo analysis. *J Membr Biol* 236, 127-136 (2010).
- Gauger, et al., A Study of Dielectric Membrane Breakdown in the Fucus Egg, *J. Membrane Biol.*, vol. 48, No. 3, pp. 249-264, 1979.
- Gehl, et al. In Vivo Electroporation of Skeletal Muscle: Threshold, Efficacy and Relation to Electric Field Distribution, *Biochimica et Biophysica Acta* 1428, 1999, pp. 233-240.
- Gençer, et al., Electrical Impedance Tomography: Induced-Current Imaging Achieved with a Multiple Coil System, *IEEE Transactions on Biomedical Engineering*, vol. 43, No. 2, Feb. 1996.
- Gilbert, et al., Novel Electrode Designs for Electrochemotherapy, *Biochimica et Biophysica Acta* 1334, 1997, pp. 9-14.

(56)

## References Cited

## OTHER PUBLICATIONS

- Gilbert, et al., The Use of Ultrasound Imaging for Monitoring Cryosurgery, Proceedings 6th Annual Conference, IEEE Engineering in Medicine and Biology, 107-111, 1984.
- Gilbert, T. W., et al., "Decellularization of tissues and organs", Biomaterials, Elsevier Science Publishers, Barking, GB, vol. 27, No. 19, Jul. 1, 2006, pp. 3675-3683.
- Glidewell, et al., The Use of Magnetic Resonance Imaging Data and the Inclusion of Anisotropic Regions in Electrical Impedance Tomography, Biomed. Sci. Instrum. 1993; 29: 251-7.
- Golberg, A. and Rubinsky, B., "A statistical model for multidimensional irreversible electroporation cell death in tissue." Biomed Eng Online, 9, 13 pages, 2010.
- Gothelf, et al., Electrochemotherapy: Results of Cancer Treatment Using Enhanced Delivery of Bleomycin by Electroporation, Cancer Treatment Reviews 2003; 29: 371-387.
- Griffiths, et al., A Dual-Frequency Electrical Impedance Tomography System, Phys. Med. Biol., 1989, vol. 34, No. 10, pp. 1465-1476.
- Griffiths, The Importance of Phase Measurement in Electrical Impedance Tomography, Phys. Med. Biol., 1987, vol. 32, No. 11, pp. 1435-1444.
- Griffiths, Tissue Spectroscopy with Electrical Impedance Tomography: Computer Simulations, IEEE Transactions on Biomedical Engineering, vol. 42, No. 9, Sep. 1995.
- Gumerov, et al., The Dipole Approximation Method and Its Coupling with the Regular Boundary Element Method for Efficient Electrical Impedance Tomography, Boundary Element Technology XIII, 1999.
- Hapala, Breaking the Barrier: Methods for Reversible Permeabilization of Cellular Membranes, Critical Reviews in Biotechnology, 17(2): 105-122, 1997.
- Heller, et al., Clinical Applications of Electrochemotherapy, Advanced Drug Delivery Reviews, vol. 35, pp. 119-129, 1999.
- Hjouj, M., et al., "Electroporation-Induced BBB Disruption and Tissue Damage Depicted by MRI", Neuro-Oncology 13: Issue suppl 3, abstract ET-32 (2011).
- Hjouj, M., et al., "MRI Study on Reversible and Irreversible Electroporation Induced Blood Brain Barrier Disruption", PLOS One, Aug. 2012, 7:8, e42817.
- Ho, et al., Electroporation of Cell Membranes: A Review, Critical Reviews in Biotechnology, 16(4): 349-362, 1996.
- Holder, et al., Assessment and Calibration of a Low-Frequency System for Electrical Impedance Tomography (EIT), Optimized for Use in Imaging Brain Function in Ambulant Human Subjects, Annals of the New York Academy of Science, vol. 873, Issue 1, Electrical BI, pp. 512-519, 1999.
- Huang, et al., Micro-Electroporation: Improving the Efficiency and Understanding of Electrical Permeabilization of Cells, Biomedical Microdevices, vol. 2, pp. 145-150, 1999.
- Hughes, et al., An Analysis of Studies Comparing Electrical Impedance Tomography with X-Ray Videofluoroscopy in the Assessment of Swallowing, Physiol. Meas. 15, 1994, pp. A199-A209.
- Issa, et al., The TUNA Procedure for BPH: Review of the Technology: The TUNA Procedure for BPH: Basic Procedure and Clinical Results, Reprinted from Infections in Urology, Jul./Aug. 1998 and Sep./Oct. 1998.
- Ivanuša, et al., MRI Macromolecular Contrast Agents as Indicators of Changed Tumor Blood Flow, Radiol. Oncol. 2001; 35(2): 139-47.
- J.F. Edd and R.V. Davalos, "Mathematical modeling of irreversible electroporation for treatment planning," Technology in Cancer Research and Treatment, 6, pp. 275-286, 2007.
- Jaroszkeski, et al., In Vivo Gene Delivery by Electroporation, Advanced Drug Delivery Review, vol. 35, pp. 131-137, 1999.
- Jossinet et al., Electrical Impedance Endo-Tomography: Imaging Tissue From Inside, IEEE Transactions on Medical Imaging, vol. 21, No. 6, Jun. 2002, pp. 560-565.
- Kinosita, et al., Hemolysis of Human Erythrocytes by a Transient Electric Field, Proc. Natl. Acad. Sci. USA, vol. 74, No. 5, pp. 1923-1927, 1977.
- Lee, E. W. et al. Advanced Hepatic Ablation Technique for Creating Complete Cell Death : Irreversible Electroporation. Radiology 255, 426-433, doi:10.1148/radiol.10090337 (2010).
- Lee, E.W., et al., "Imaging guided percutaneous irreversible electroporation: ultrasound and immunohistological correlation", Technol Cancer Res Treat 6: 287-294 (2007).
- Li, W., et al., "The Effects of Irreversible Electroporation (IRE) on Nerves" PLoS One, Apr. 2011, 6(4), e18831.
- Liu, et al., Measurement of Pharyngeal Transit Time by Electrical Impedance Tomography, Clin. Phys. Physiol. Meas., 1992, vol. 13, Suppl. A, pp. 197-200.
- Lundqvist, et al., Altering the Biochemical State of Individual Cultured Cells and Organelles with Ultramicroelectrodes, Proc. Natl. Acad. Sci. USA, vol. 95, pp. 10356-10360, Sep. 1998.
- Lurquin, Gene Transfer by Electroporation, Molecular Biotechnology, vol. 7, 1997.
- Lynn, et al., A New Method for the Generation and Use of Focused Ultrasound in Experimental Biology, The Journal of General Physiology, vol. 26, 179-193, 1942.
- M. Marty et al., "Electrochemotherapy—An easy, highly effective and safe treatment of cutaneous and subcutaneous metastases: Results of ESOPE (European Standard Operating Procedures of Electrochemotherapy) study," European Journal of Cancer Supplements, 4, pp. 3-13, 2006.
- Mahmood, F., et al., "Diffusion-Weighted MRI for Verification of Electroporation-Based Treatments", Journal of Membrane Biology 240: 131-138 (2011).
- Mahnich-Kalamiza, et al., "Educational application for visualization and analysis of electric field strength in multiple electrode electroporation," BMC Med Educ, vol. 12:102, 13 pages, 2012.
- Maor et al., The Effect of Irreversible Electroporation on Blood Vessels, Tech. in Cancer Res. and Treatment, vol. 6, No. 4, Aug. 2007, pp. 307-312.
- Maor, E., A. Ivorra, and B. Rubinsky, Non Thermal Irreversible Electroporation: Novel Technology for Vascular Smooth Muscle Cells Ablation, PLoS One, 2009, 4(3): p. e4757.
- Maor, E., A. Ivorra, J. Leor, and B. Rubinsky, Irreversible electroporation attenuates neointimal formation after angioplasty, IEEE Trans Biomed Eng, Sep. 2008, 55(9): p. 2268-74.
- Miklavcic et al., "A validated model of in vivo electric field distribution in tissues for electrochemotherapy and for DNA electrotransfer for gene therapy," Biochimica et Biophysica Acta, 1523, pp. 73-83, 2000.
- Miklavčič, et al., The Importance of Electric Field Distribution for Effective in Vivo Electroporation of Tissues, Biophysical Journal, vol. 74, May 1998, pp. 2152-2158.
- Miller, L., et al., Cancer cells ablation with irreversible electroporation, Technology in Cancer Research and Treatment 4 (2005) 699-706.
- Mir et al., "Mechanisms of Electrochemotherapy" Advanced Drug Delivery Reviews 35:107-118 (1999).
- Mir, et al., Effective Treatment of Cutaneous and Subcutaneous Malignant Tumours by Electrochemotherapy, British Journal of Cancer, vol. 77, No. 12, pp. 2336-2342, 1998.
- Mir, et al., Electrochemotherapy Potentiation of Antitumor Effect of Bleomycin by Local Electric Pulses, European Journal of Cancer, vol. 27, No. 1, pp. 68-72, 1991.
- Mir, et al., Electrochemotherapy, a Novel Antitumor Treatment: First Clinical Trial, C.R. Acad. Sci. Paris, Ser. III, vol. 313, pp. 613-618, 1991.
- Mir, L.M. and Orlowski, S., The basis of electrochemotherapy, in Electrochemotherapy, electrogenotherapy, and transdermal drug delivery: electrically mediated delivery of molecules to cells, M.J. Jaroszkeski, R. Heller, R. Gilbert, Editors, 2000, Humana Press, p. 99-118.
- Mir, L.M., et al., Electric Pulse-Mediated Gene Delivery to Various Animal Tissues, in Advances in Genetics, Academic Press, 2005, p. 83-114.
- Mir, Therapeutic Perspectives of In Vivo Cell Electroporation, Bioelectrochemistry, vol. 53, pp. 1-10, 2000.
- Narayan, et al., Establishment and Characterization of a Human Primary Prostatic Adenocarcinoma Cell Line (ND-1), The Journal of Urology, vol. 148, 1600-1604, Nov. 1992.

(56)

## References Cited

## OTHER PUBLICATIONS

- Naslund, Cost-Effectiveness of Minimally Invasive Treatments and Transurethral Resection (TURP) in Benign Prostatic Hyperplasia (BPH), (Abstract), Presented at 2001 AUA National Meeting Anaheim, CA, Jun. 5, 2001.
- Naslund, Michael J., Transurethral Needle Ablation of the Prostate, *Urology*, vol. 50, No. 2, Aug. 1997.
- Neal II et al., "A Case Report on the Successful Treatment of a Large Soft-Tissue Sarcoma with Irreversible Electroporation," *Journal of Clinical Oncology*, 29, pp. 1-6, 2011.
- Neal II et al., "Experimental Characterization and Numerical Modeling of Tissue Electrical Conductivity during Pulsed Electric Fields for Irreversible Electroporation Treatment Planning," *Biomedical Engineering, IEEE Transactions on Biomedical Engineering*, vol. 59, pp. 1076-1085, 2012.
- Neal II, R. E., et al., "Successful Treatment of a Large Soft Tissue Sarcoma with Irreversible Electroporation", *Journal of Clinical Oncology*, 29:13, e372-e377 (2011).
- Neal II, Robert E. and R.V. Davalos, The Feasibility of Irreversible Electroporation for the Treatment of Breast Cancer and Other Heterogeneous Systems, *Ann Biomed Eng.*, 2009, 37(12): p. 2615-2625.
- Neumann, et al., Gene Transfer into Mouse Lyoma Cells by Electroporation in High Electric Fields, *J. Embo.*, vol. 1, No. 7, pp. 841-845, 1982.
- Neumann, et al., Permeability Changes Induced by Electric Impulses in Vesicular Membranes, *J. Membrane Biol.*, vol. 10, pp. 279-290, 1972.
- Okino, et al., Effects of High-Voltage Electrical Impulse and an Anticancer Drug on in Vivo Growing Tumors, *Japanese Journal of Cancer Research*, vol. 78, pp. 1319-1321, 1987.
- Onik, et al., Sonographic Monitoring of Hepatic Cryosurgery in an Experimental Animal Model, *AJR American J. of Roentgenology*, vol. 144, pp. 1043-1047, May 1985.
- Onik, et al., Ultrasonic Characteristics of Frozen Liver, *Cryobiology*, vol. 21, pp. 321-328, 1984.
- Organ, L.W., Electrophysiological principles of radiofrequency lesion making, *Apply. Neurophysiol.*, 1976. 39: p. 69-76.
- Ott, H. C., et al., "Perfusion-decellularized matrix: using nature's platform to engineer a bioartificial heart", *Nature Medicine, Nature Publishing Group, New York, NY, US*, vol. 14, No. 2, Feb. 1, 2008, pp. 213-221.
- Pavselj, et al., "The course of tissue permeabilization studied on a mathematical model of a subcutaneous tumor in small animals," *IEEE Trans Biomed Eng.* vol. 52, pp. 1373-1381, 2005.
- Phillips, M., Maor, E. & Rubinsky, B. Non-Thermal Irreversible Electroporation for Tissue Decellularization. *J. Biomech. Eng.* doi:10.1115/1.4001882 (2010).
- Piñero, et al., Apoptotic and Necrotic Cell Death Are Both Induced by Electroporation in HL60 Human Promyeloid Leukaemia Cells, *Apoptosis*, vol. 2, No. 3, 330-336, Aug. 1997.
- Precision Office TUNA System, When Patient Satisfaction is Your Goal, *VidaMed* 2001.
- Rajagopal, V. and S.G. Rockson, Coronary restenosis: a review of mechanisms and management, *The American Journal of Medicine*, 2003, 115(7): p. 547-553.
- Rols, M.P., et al., Highly Efficient Transfection of Mammalian Cells by Electric Field Pulses: Application to Large Volumes of Cell Culture by Using a Flow System, *Eur. J. Biochem.* 1992, 206, pp. 115-121.
- Rubinsky, B., "Irreversible Electroporation in Medicine", *Technology in Cancer Research and Treatment*, vol. 6, No. 4, Aug. 1, 2007, pp. 255-259.
- Rubinsky, B., ed, *Cryosurgery. Annu Rev. Biomed. Eng.* vol. 2 2000. 157-187.
- Rubinsky, B., et al., "Irreversible Electroporation: A New Ablation Modality—Clinical Implications" *Technol. Cancer Res. Treatment* 6(1), 37-48 (2007).
- Salford, L.G., et al., "A new brain tumour therapy combining bleomycin with in vivo electroporation", *Biochem. Biophys. Res. Commun.*, 194(2): 938-943 (1993).
- Sang, M. B., et al., "Towards the creation of decellularized organ constructs using irreversible electroporation and active mechanical perfusion", *Biomedical Engineering Online, Biomed Central LTD, London, GB*, vol. 9, No. 1, Dec. 10, 2010, p. 83.
- Schmukler, *Impedance Spectroscopy of Biological Cells, Engineering in Medicine and Biology Society, Engineering Advances: New Opportunities for Biomedical Engineers, Proceedings of the 16th Annual Internal Conference of the IEEE*, vol. 1, p. A74, downloaded from IEEE Xplore website, 1994.
- Sel, D., Lebar, A. M. & Miklavcic, D. Feasibility of employing model-based optimization of pulse amplitude and electrode distance for effective tumor electroporation. *IEEE Trans Biomed Eng* 54, 773-781 (2007).
- Sel, et al., "Sequential finite element model of tissue electroporation." *IEEE Trans Biomed Eng.* vol. 52, pp. 816-827, 2005.
- Sersa, et al., Reduced Blood Flow and Oxygenation in SA-1 Tumours after Electrochemotherapy with Cisplatin, *British Journal of Cancer*, 87, 1047-1054, 2002.
- Sersa, et al., Tumour Blood Flow Modifying Effects of Electrochemotherapy: a Potential Vascular Targeted Mechanism, *Radiol. Oncol.*, 37(1): 43-8, 2003.
- Sharma, A., et al., "Review on Thermal Energy Storage with Phase Change Materials and Applications", *Renewable Sustainable Energy Rev.* 13(2), 318-345 (2009).
- Sharma, et al., Poloxamer 188 Decreases Susceptibility of Artificial Lipid Membranes to Electroporation, *Biophysical Journal*, vol. 71, No. 6, pp. 3229-3241, Dec. 1996.
- Shiina, S., et al, Percutaneous ethanol injection therapy for hepatocellular carcinoma: results in 146 patients. *AJR*, 1993, 160: p. 1023-8.
- Tekle, Ephrem, R. Dean Astumian, and P. Boon Chock, Electroporation by using bipolar oscillating electric field: An improved method for DNA transfection of NIH 3T3 cells, *Proc. Natl. Acad. Sci.*, vol. 88, pp. 4230-4234, May 1991, *Biochemistry*.
- Thompson, et al., To determine whether the temperature of 2% lignocaine gel affects the initial discomfort which may be associated with its instillation into the male urethra, *BJU International* (1999), 84, 1035-1037.
- Thomson et al., "Investigation of the safety of irreversible electroporation in humans." *J Vasc Intery Radiol*, 22, pp. 611-621, 2011.
- TUNA—Suggested Local Anesthesia Guidelines, no date available.
- Vidamed, Inc., Transurethral Needle Ablation (TUNA): Highlights from Worldwide Clinical Studies, Vidamed's Office TUNA System, 2001.
- Weaver, Electroporation: A General Phenomenon for Manipulating Cells and Tissues, *Journal of Cellular Biochemistry*, 51: 426-435, 1993.
- Weaver, et al., Theory of Electroporation: A Review, *Bioelectrochemistry and Bioenergetics*, vol. 41, pp. 136-160, 1996.
- Weaver, J. C., Electroporation of biological membranes from multicellular to nano scales, *IEEE Trns. Dielectr. Electr. Insul.* 10, 754-768 (2003).
- Weisstein: Cassini Ovals. From MathWorld—A. Wolfram Web Resource; Apr. 30, 2010; <http://mathworld.wolfram.com/> (updated May 18, 2011).
- Zimmermann, et al., Dielectric Breakdown of Cell Membranes, *Biophysical Journal*, vol. 14, No. 11, pp. 881-899, 1974.
- Zlotta, et al., Long-Term Evaluation of Transurethral Needle Ablation of the Prostate (TUNA) for Treatment of Benign Prostatic Hyperplasia (BPH): Clinical Outcome After 5 Years. (Abstract) Presented at 2001 AUA National Meeting, Anaheim, CA—Jun. 5, 2001.
- Zlotta, et al., Possible Mechanisms of Action of Transurethral Needle Ablation of the Prostate on Benign Prostatic Hyperplasia Symptoms: a Neurohistochemical Study, Reprinted from *Journal of Urology*, vol. 157, No. 3, Mar. 1997, pp. 894-899.
- Co-Pending Application No. PCT/US15/30429, filed May 12, 2015.
- PCT International Preliminary Report on Patentability of Corresponding International Application No. PCT/2011/062067, dated May 28, 2013.

(56)

## References Cited

## OTHER PUBLICATIONS

- PCT International Preliminary Report on Patentability of Corresponding International Application No. PCT/2011/066239, dated Jun. 25, 2013.
- PCT International Search Report (dated Aug. 2, 2011), Written Opinion (dated Aug. 2, 2011), and International Preliminary Report on Patentability (dated Apr. 17, 2012) of PCT/US10/53077.
- PCT International Search Report (dated Aug. 22, 2012), and Written Opinion (dated Aug. 22, 2012) of PCT/US11/66239.
- PCT International Search Report (dated Aug. 26, 2005), Written Opinion (dated Aug. 26, 2005), and International Preliminary Report on Patentability (dated Jun. 26, 2006) of PCT/US2004/043477.
- PCT International Search Report (dated Jan. 19, 2010), Written Opinion (dated Jan. 19, 2010), and International Preliminary Report on Patentability (dated Jan. 4, 2010) of PCT/US09/62806, 15 pgs.
- PCT International Search Report (dated Jul. 15, 2010), Written Opinion (dated Jul. 15, 2010), and International Preliminary Report on Patentability (dated Oct. 11, 2011) from PCT/US2010/030629.
- PCT International Search Report (dated Jul. 9, 2009), Written Opinion (dated Jul. 9, 2009), and International Preliminary Report on Patentability (dated Nov. 2, 2010) of PCT/US2009/042100.
- PCT International Search Report and Written Opinion (dated Jul. 25, 2012) of PCT/US2011/062067.
- PCT International Search Report, 4 pgs, (dated Jul. 30, 2010), Written Opinion, 7 pgs, (dated Jul. 30, 2010), and International Preliminary Report on Patentability, 8 pgs, (dated Oct. 4, 2011) from PCT/US2010/029243.
- Co-Pending U.S. Appl. No. 14/940,863, filed Nov. 13, 2015 and Published as US 2016/0066977 on Mar. 10, 2016.
- Hjouj, Mohammad et al., "Electroporation-Induced BBB Disruption and Tissue Damage Depicted by MRI," Abstracts from 16th Annual Scientific Meeting of the Society for Neuro-Oncology in Conjunction with the AANS/CNS Section on Tumors, Nov. 17-20, 2011, Orange County California, Neuro-Oncology Supplement, vol. 13, Supplement 3, p. iii114.
- Ivorra et al., "In vivo electric impedance measurements during and after electroporation of rat live." *Bioelectrochemistry*, vol. 70, pp. 287-295 (2007).
- Ivorra et al., "In vivo electrical conductivity measurements during and after tumor electroporation: conductivity changes reflect the treatment outcome." *Physics in Medicine and Biology*, vol. 54, pp. 5949-5963 (2009).
- Ivorra, "Bioimpedance monitoring for physicians: an overview." *Biomedical Applications Group*, 35 pages (2002).
- Laufer et al., "Electrical impedance characterization of normal and cancerous human hepatic tissue." *Physiological Measurement*, vol. 31, pp. 995-1009 (2010).
- Reberšek, M. and D. Miklavčič, "Advantages and Disadvantages of Different Concepts of Electroporation Pulse Generation," *Automatika* 52(2011) 1, 12-19.
- A.I. Daud et al., "Phase I Trial of Interleukin-12 Plasmid Electroporation in Patients With Metastatic Melanoma," *Journal of Clinical Oncology*, 26, pp. 5896-5903, 2008.
- Agerholm-Larsen, B., et al., "Preclinical Validation of Electrochemotherapy as an Effective Treatment for Brain Tumors", *Cancer Research* 71: 3753-3762 (2011).
- Al-Sakere et al., "Tumor ablation with irreversible electroporation," *PLoS One*, 2, e1135, 2007, 8 pages.
- Amasha, et al., "Quantitative Assessment of Impedance Tomography for Temperature Measurements in Microwave Hyperthermia," *Clin. Phys. Physiol. Meas.*, 1998, Suppl. A, 49-53.
- Andreason, "Electroporation as a Technique for the Transfer of Macromolecules into Mammalian Cell Lines," *J. Tiss. Cult. Meth.*, 15:56-62, 1993.
- Arena, Christopher B., et al., "Towards the development of latent heat storage electrodes for electroporation-based therapies", *Applied Physics Letters*, 101, 083902 (2012).
- Arena, Christopher B., et al., "Phase Change Electrodes for Reducing Joule Heating During Irreversible Electroporation". Proceedings of the ASME 2012 Summer Bioengineering Conference, SBC2012, Jun. 20-23, 2012, Fajardo, Puerto Rico.
- Bagla, S. and Papadouris, D., "Percutaneous Irreversible Electroporation of Surgically Unresectable Pancreatic Cancer: A Case Report" *J. Vascular Int. Radiol.* 23(1), 142-145 (2012).
- Baker, et al., "Calcium-Dependent Exocytosis in Bovine Adrenal Medullary Cells with Leaky Plasma Membranes," *Nature*, vol. 276, pp. 620-622, 1978.
- Bancroft, et al., "Design of a Flow Perfusion Bioreactor System for Bone Tissue-Engineering Applications," *Tissue Engineering*, vol. 9, No. 3, 2003, p. 549-554.
- Barber, "Electrical Impedance Tomography Applied Potential Tomography," *Advances in Biomedical Engineering*, Beneken and Thevenin, eds., IOS Press, pp. 165-173, 1993.
- Beebe, S.J., et al., "Nanosecond pulsed electric field (nsPEF) effects on cells and tissues: apoptosis induction and tumor growth inhibition." *PPPS-2001 Pulsed Power Plasma Science 2001*, 28th IEEE International Conference on Plasma Science and 13th IEEE International Pulsed Power Conference, Digest of Technical Papers (Cat. No. 01CH37251). IEEE, Part vol. 1, 2001, pp. 211-215, vol. I, Piscataway, NJ, USA.
- Ben-David, et al., "Characterization of Irreversible Electroporation Ablation in Vivo Porcine Liver," *Am J Roentgenol*, vol. 198, pp. W62-W68, 2012.
- Blad, et al., "Impedance Spectra of Tumour Tissue in Comparison with Normal Tissue; a Possible Clinical Application for Electrical Impedance Tomography," *Physiol. Meas.* 17 (1996) A105-A115.
- Bolland, F., et al., "Development and characterisation of a full-thickness acellular porcine bladder matrix for tissue engineering", *Biomaterials*, Elsevier Science Publishers, Barking, GB, vol. 28, No. 6, Nov. 28, 2006, pp. 1061-1070.
- Boone, K., Barber, D. & Brown, B. Review—Imaging with electricity: report of the European Concerted Action on Impedance Tomography. *J. Med. Eng. Technol.* 21, 201-232 (1997).
- BPH Management Strategies: Improving Patient Satisfaction, *Urology Times*, May 2001, vol. 29, Supplement 1.
- Brown, et al., "Blood Flow Imaging Using Electrical Impedance Tomography," *Clin. Phys. Physiol. Meas.*, 1992, vol. 13, Suppl. A, 175-179.
- Brown, S.G., "Phototherapy of tumors." *World J. Surgery*, 1983, 7: p. 700-9.
- Cemazar M, Parkins CS, Holder AL, Chaplin DJ, Tozer GM, et al., "Electroporation of human microvascular endothelial cells: evidence for an anti-vascular mechanism of electrochemotherapy", *Br J Cancer* 84: 565-570 (2001).
- Chandrasekar, et al., "Transurethral Needle Ablation of the Prostate (TUNA)—a Prospective Study, Six Year Follow Up, (Abstract), Presented at 2001 National Meeting, Anaheim, CA, Jun. 5, 2001.
- Coates, C.W., et al., "The Electrical Discharge of the Electric Eel, *Electrophorus Electricus*," *Zoologica*, 1937, 22(1), pp. 1-32.
- Cook, et al., "ACT3: A High-Speed, High-Precision Electrical Impedance Tomograph," *IEEE Transactions on Biomedical Engineering*, vol. 41, No. 8, Aug. 1994.
- Co-pending U.S. Appl. No. 10/571,162, filed Oct. 18, 2006 (published as 2007/0043345 on Feb. 22, 2007).
- Co-Pending U.S. Appl. No. 12/432,295, filed Apr. 29, 2009.
- Co-Pending U.S. Appl. No. 12/609,779, filed Oct. 30, 2009.
- Co-pending U.S. Appl. No. 12/751,826, filed Mar. 31, 2010 (published as 2010/0250209 on Sep. 30, 2010).
- Co-pending U.S. Appl. No. 12/751,854, filed Mar. 31, 2010 (published as 2010/0249771 on Sep. 30, 2010).
- Co-Pending U.S. Appl. No. 12/757,901, filed Apr. 9, 2010.
- Co-Pending U.S. Appl. No. 12/906,923, filed Oct. 18, 2010.
- Co-Pending Application No. PCT/US04/43477, filed Dec. 21, 2004.
- Co-Pending Application No. PCT/US09/42100, filed Apr. 29, 2009.
- Co-Pending Application No. PCT/US09/62806, filed Oct. 30, 2009.
- Co-Pending Application No. PCT/US10/30629, filed Apr. 9, 2010.
- Co-Pending Application No. PCT/US10/53077, filed Oct. 18, 2010.
- Co-Pending Application No. PCT/US11/62067, filed Nov. 23, 2011.
- Co-Pending Application No. PCT/US11/66239, filed Dec. 20, 2011.
- Co-pending Application No. PCT/US2010/029243, filed Mar. 30, 2010, published as WO 2010/117806 on Oct. 14, 2010.
- Co-Pending U.S. Appl. No. 12/491,151, filed Jun. 24, 2009.



(56)

## References Cited

## OTHER PUBLICATIONS

- Co-Pending U.S. Appl. No. 13/332,133, filed Dec. 20, 2011.  
 Co-Pending U.S. Appl. No. 13/550,307, filed Jul. 16, 2012.  
 Co-Pending U.S. Appl. No. 13/919,640, filed Jun. 17, 2013.  
 Co-Pending U.S. Appl. No. 13/958,152, filed Aug. 2, 2013.  
 Co-Pending U.S. Appl. No. 13/989,175, filed May 23, 2013.  
 Co-Pending U.S. Appl. No. 14/012,832, filed Aug. 28, 2013.  
 Co-Pending U.S. Appl. No. 14/017,210, filed Sep. 3, 2013.  
 Co-Pending U.S. Appl. No. 14/627,046, filed Feb. 20, 2015.  
 Co-Pending U.S. Appl. No. 14/686,380, filed Apr. 14, 2015.  
 Co-pending European Application No. 10 824 248.8, Invitation Pursuant to rule 62a(1) EPC (Sep. 25, 2013).  
 Alberts et al., "Molecular Biology of the Cell," 3rd edition, Garland Science, New York, 1994, 1 page.  
 Arena et al. "High-Frequency Irreversible Electroporation (H-FIRE) for Non-thermal Ablation without Muscle Contraction." *Biomed. Eng. Online*, vol. 10, 20 pages (2011).  
 Arena, C.B., et al., "A three-dimensional in vitro tumor platform for modeling therapeutic irreversible electroporation." *Biophysical Journal*, 2012.103(9): p. 2033-2042.  
 Asami et al., "Dielectric properties of mouse lymphocytes and erythrocytes." *Biochimica et Biophysica Acta (BBA)—Molecular Cell Research*, 1010 (1989) pp. 49-55.  
 Ball, C., K.R. Thomson, and H. Kavnoudias, "Irreversible electroporation: a new challenge in "out of-operating theater" anesthesia." *Anesth Analg*, 2010. 110(5): p. 1305-9.  
 Bower et al., "Irreversible electroporation of the pancreas: definitive local therapy without systemic effects." *Journal of surgical oncology*, 2011. 104(1): p. 22-28.  
 Cannon et al., "Safety and early efficacy of irreversible electroporation for hepatic tumors in proximity to vital structures." *Journal of Surgical Oncology*, 6 pages (2012).  
 Carpenter A.E. et al., "CellProfiler: image analysis software for identifying and quantifying cell phenotypes." *Genome Biol.* 2006; 7(10): R100. Published online Oct. 31, 2006, 11 pages.  
 Charpentier, K.P., et al., "Irreversible electroporation of the pancreas in swine: a pilot study." *HPB: the official journal of the International Hepato Pancreato Biliary Association*, 2010. 12(5): p. 348-351.  
 Chen et al., "Classification of cell types using a microfluidic device for mechanical and electrical measurement on single cells." *Lab on a Chip*, vol. 11, pp. 3174-3181 (2011).  
 Clark et al., "The electrical properties of resting and secreting pancreas." *The Journal of Physiology*, vol. 189, pp. 247-260 (1967).  
 Co-Pending U.S. Appl. No. 14/808,679, filed Jul. 24, 2015.  
 Co-Pending U.S. Appl. No. 14/012,832, Ex Parte Quayle Office Action dated Aug. 28, 2015, 6 pages.  
 Dahl et al., "Nuclear shape, mechanics, and mechanotransduction." *Circulation Research* vol. 102, pp. 1307-1318 (2008).  
 Eppich et al., "Pulsed electric fields for selection of hematopoietic cells and depletion of tumor cell contaminants." *Nature Biotechnology* 18, pp. 882-887 (2000).  
 Ermolina et al., "Study of normal and malignant white blood cells by time domain dielectric spectroscopy." *IEEE Transactions on Dielectrics and Electrical Insulation*, 8 (2001) pp. 253-261.  
 Fischbach et al., "Engineering tumors with 3D scaffolds." *Nat Meth* 4, pp. 855-860 (2007).  
 Flanagan et al., "Unique dielectric properties distinguish stem cells and their differentiated progeny." *Stem Cells*, vol. 26, pp. 656-665 (2008).  
 Fong et al., "Modeling Ewing sarcoma tumors in vitro with 3D scaffolds." *Proceedings of the National Academy of Sciences* vol. 110, pp. 6500-6505 (2013).  
 Gascoyne et al., "Membrane changes accompanying the induced differentiation of Friend murine erythroleukemia cells studied by dielectrophoresis." *Biochimica et Biophysica Acta (BBA)—Biomembranes*, vol. 1149, pp. 119-126 (1993).  
 Gimsa et al., "Dielectric spectroscopy of single human erythrocytes at physiological ionic strength: dispersion of the cytoplasm." *Biophysical Journal*, vol. 71, pp. 495-506 (1996).  
 Helczynska et al., "Hypoxia promotes a dedifferentiated phenotype in ductal breast carcinoma in situ." *Cancer Research*, vol. 63, pp. 1441-1444 (2003).  
 Ibey et al., "Selective cytotoxicity of intense nanosecond-duration electric pulses in mammalian cells." *Biochimica Et Biophysica Acta—General Subjects*, vol. 1800, pp. 1210-1219 (2010).  
 Jarm et al., "Antivascular effects of electrochemotherapy: implications in treatment of bleeding metastases." *Expert Rev Anticancer Ther.* vol. 10, pp. 729-746 (2010).  
 Jensen et al., "Tumor volume in subcutaneous mouse xenografts measured by microCT is more accurate and reproducible than determined by 18FFDG-microPET or external caliper." *BMC medical Imaging* vol. 8:16, 9 Pages (2008).  
 Kingham et al., "Ablation of perivascular hepatic malignant tumors with irreversible electroporation." *Journal of the American College of Surgeons*, 2012. 215(3), p. 379-387.  
 Kinoshita and Tsong, "Formation and resealing of pores of controlled sizes in human erythrocyte membrane." *Nature*, vol. 268 (1977) pp. 438-441.  
 Kinoshita and Tsong, "Voltage-induced pore formation and hemolysis of human erythrocytes." *Biochimica et Biophysica Acta (BBA)—Biomembranes*, 471 (1977) pp. 227-242.  
 Kinoshita et al., "Electroporation of cell membrane visualized under a pulsed-laser fluorescence microscope." *Biophysical Journal*, vol. 53, pp. 1015-1019 (1988).  
 Kirson et al., "Alternating electric fields arrest cell proliferation in animal tumor models and human brain tumors." *Proceedings of the National Academy of Sciences* vol. 104, pp. 10152-10157 (2007).  
 Kotnik and Miklavcic, "Theoretical evaluation of voltage induction on internal membranes of biological cells exposed to electric fields." *Biophysical Journal*, vol. 90(2), pp. 480-491 (2006).  
 Labeed et al., "Differences in the biophysical properties of membrane and cytoplasm of apoptotic cells revealed using dielectrophoresis." *Biochimica et Biophysica Acta (BBA)—General Subjects*, vol. 1760, pp. 922-929 (2006).  
 Lebar et al., "Inter-pulse interval between rectangular voltage pulses affects electroporation threshold of artificial lipid bilayers." *IEEE Transactions on NanoBioscience*, vol. 1 (2002) pp. 116-120.  
 Maček Lebar and Miklavcic, "Cell electroporation to small molecules in vitro: control by pulse parameters." *Radiology and Oncology*, vol. 35(3), pp. 193-202 (2001).  
 Malpica et al., "Grading ovarian serous carcinoma using a two-tier system." *The American Journal of Surgical Pathology*, vol. 28, pp. 496-504 (2004).  
 Marszalek et al., "Schwan equation and transmembrane potential induced by alternating electric field." *Biophysical Journal*, vol. 58, pp. 1053-1058 (1990).  
 Martin, n.R.C.G., et al., "Irreversible electroporation therapy in the management of locally advanced pancreatic adenocarcinoma." *Journal of the American College of Surgeons*, 2012. 215(3): p. 361-369.  
 Mulhall et al., "Cancer, pre-cancer and normal oral cells distinguished by dielectrophoresis." *Analytical and Bioanalytical Chemistry*, vol. 401, pp. 2455-2463 (2011).  
 Neal II, R.E. et al., "Treatment of breast cancer through the application of irreversible electroporation using a novel minimally invasive single needle electrode." *Breast Cancer Research and Treatment*, 2010. 123(1): p. 295-301.  
 Nesin et al., "Manipulation of cell volume and membrane pore comparison following single cell permeabilization with 60- and 600-ns electric pulses." *Biochimica et Biophysica Acta (BBA)—Biomembranes*, vol. 1808, pp. 792-801 (2011).  
 O'Brien et al., "Investigation of the Alamar Blue (resazurin) fluorescent dye for the assessment of mammalian cell cytotoxicity." *European Journal of Biochemistry*, vol. 267, pp. 5421-5426 (2000).  
 Onik, G. and B. Rubinsky, eds. "Irreversible Electroporation: First Patient Experience Focal Therapy of Prostate Cancer. Irreversible Electroporation", ed. B. Rubinsky 2010, Springer Berlin Heidelberg, pp. 235-247.  
 Onik, G., P. Mikus, and B. Rubinsky, "Irreversible electroporation: implications for prostate ablation." *Technol Cancer Res Treat.* 2007. 6(4): p. 295-300.  
 Paszek et al., "Tensional homeostasis and the malignant phenotype." *Cancer Cell*, vol. 8, pp. 241-254 (2005).

(56)

**References Cited**

## OTHER PUBLICATIONS

Polak et al., "On the Electroporation Thresholds of Lipid Bilayers: Molecular Dynamics Simulation Investigations." *The Journal of Membrane Biology*, vol. 246, pp. 843-850 (2013).

Pucihar et al., "Numerical determination of transmembrane voltage induced on irregularly shaped cells." *Annals of Biomedical Engineering*, vol. 34, pp. 642-652 (2006).

Ron et al., "Cell-based screening for membranar and cytoplasmatic markers using dielectric spectroscopy." *Biophysical chemistry*, 135 (2008) pp. 59-68.

Rossmeisil et al., "Pathology of non-thermal irreversible electroporation (N-TIRE)-induced ablation of the canine brain." *Journal of Veterinary Science* vol. 14, pp. 433-440 (2013).

Rossmeisil, "New Treatment Modalities for Brain Tumors in Dogs and Cats." *Veterinary Clinics of North America: Small Animal Practice* 44, pp. 1013-1038 (2014).

Rubinsky et al., "Optimal Parameters for the Destruction of Prostate Cancer Using Irreversible Electroporation." *The Journal of Urology*, 180 (2008) pp. 2668-2674.

Co-Pending U.S. Appl. No. 12/906,923, File History Jul. 2017, 55 pages.

Co-Pending U.S. Appl. No. 14/808,679, Preliminary Amendment, filed Jul. 27, 2015, 9 pages.

Co-pending U.S. Appl. No. 15/011,752 Preliminary Amendment, filed Feb. 2, 2016, 6 pages.

Co-pending U.S. Appl. No. 15/423,986, filed Feb. 3, 2017.

Co-pending U.S. Appl. No. 15/424,335, filed Feb. 3, 2017.

Co-Pending U.S. Appl. No. 15/310,114, filed Nov. 10, 2016.

Co-Pending U.S. Appl. No. 15/310,114, Preliminary Amendment filed Nov. 10, 2016, 9 pages.

Co-Pending U.S. Appl. No. 13/550,307, Final Office Action dated Aug. 26, 2016, 12 pages.

Co-Pending U.S. Appl. No. 13/550,307, Final Office Action dated May 23, 2017, 13 pages.

Co-Pending U.S. Appl. No. 13/550,307, Final Office Action dated Oct. 23, 2015, 10 pages.

Co-Pending U.S. Appl. No. 13/550,307, Interview Summary and Misc. Internal Document dated Dec. 23, 2016, 4 pages.

Co-Pending U.S. Appl. No. 13/550,307, Non-Final Office Action dated Apr. 15, 2015, 10 pages.

Co-Pending U.S. Appl. No. 13/550,307, Non-Final Office Action dated Aug. 26, 2016, 12 pages.

Co-Pending U.S. Appl. No. 13/550,307, Response to Aug. 26, 2016 Non-Final Office Action, filed Nov. 28, 2016, 14 pages.

Co-Pending U.S. Appl. No. 13/550,307, Response to Final Office Action filed Feb. 23, 2016, 9 pages.

Co-Pending U.S. Appl. No. 13/550,307, Response to May 23, 2017 Final Office Action dated Aug. 23, 2017, 11 pages.

Co-Pending U.S. Appl. No. 13/550,307, Reponse to Non-Final Office Action filed Jul. 15, 2015, 9 pages.

Co-Pending U.S. Appl. No. 13/550,307, Response to Restriction Requirement filed Mar. 9, 2015, 3 pages.

Co-Pending U.S. Appl. No. 13/550,307, Restriction Requirement dated Jan. 7, 2015, 8 pages.

Co-Pending U.S. Appl. No. 13/550,307, Supplemental Amendment filed Dec. 21, 2016, 9 pages.

Co-Pending U.S. Appl. No. 14/017,210, Final Office Action dated Aug. 30, 2016, 11 pages.

Co-Pending U.S. Appl. No. 14/017,210, Final Office Action dated May 1, 2017, 11 pages.

Co-Pending U.S. Appl. No. 14/017,210, Non-Final Office Action dated Dec. 15, 2016, 8 pages.

Co-Pending U.S. Appl. No. 14/017,210, Non-Final Office Action dated Oct. 25, 2017, 9 pages.

Co-Pending U.S. Appl. No. 14/017,210, Non-Final Office Action, dated Sep. 8, 2015, 8 pages.

Co-Pending U.S. Appl. No. 14/017,210, Priority Petition dated Dec. 11, 2015, 5 pages.

Co-Pending U.S. Appl. No. 14/017,210, RCE filed Aug. 1, 2017, 13 pages.

Co-Pending U.S. Appl. No. 14/017,210, Response to Aug. 30, 2016 Final Office Action, dated Nov. 30, 2016, 10 pages.

Co-Pending U.S. Appl. No. 14/017,210, Response to Dec. 15, 2016 Non-Final Office Action dated Mar. 20, 2017, 9 pages.

Co-Pending U.S. Appl. No. 14/017,210, Response to Sep. 8, 2015 Non-Final Office Action, dated Mar. 8, 2016, 57 pages.

Co-Pending U.S. Appl. No. 14/686,380, Non-Final Office Action dated Nov. 22, 2017, 11 pages.

Co-Pending U.S. Appl. No. 14/686,380, Response to Jul. 19, 2017 Restriction Requirement, dated Sep. 15, 2017, 2 pages.

Co-Pending U.S. Appl. No. 14/686,380, Restriction Requirement dated Jul. 19, 2017, 7 pages.

Garcia, Paulo A., Robert E. Neal II and Rafael V. Davalos, Chapter 3, Non-Thermal Irreversible Electroporation for Tissue Ablation, In: *Electroporation in Laboratory and Clinical Investigations* ISBN 978-1-61668-327-6 Editors: Enrico P. Spugnini and Alfonso Baldi, 2010, 22 pages.

Wimmer, Thomas, et al., "Planning Irreversible Electroporation (IRE) in the Porcine Kidney: Are Numerical Simulations Reliable for Predicting Empiric Ablation Outcomes?", *Cardiovasc Intervent Radiol.* Feb. 2015 ; 38(1): 182-190. doi:10.1007/s00270-014-0905-2.

Co-Pending U.S. Appl. No. 15/843,888, filed Dec. 15, 2017.

Co-Pending U.S. Appl. No. 15/881,414, filed Jan. 26, 2018.

Co-Pending U.S. Appl. No. 13/550,307, Non-Final Office Action dated Mar. 14, 2018, 18 pages.

Co-Pending U.S. Appl. No. 14/017,210, Response to Oct. 25, 2017 Non-Final Office Action dated Jan. 25, 2018, 11 pages.

Neal RE II, et al. (2013) Improved Local and Systemic Anti-Tumor Efficacy for Irreversible Electroporation in Immunocompetent versus Immunodeficient Mice. *PLoS One* 8(5): e64559. <https://doi.org/10.1371/journal.pone.0064559>.

Co-Pending U.S. Appl. No. 14/940,863, Notice of Allowance dated May 25, 2018, 9 pages.

Co-Pending U.S. Appl. No. 15/011,752 Non-Final Office Action dated May 11, 2018, 11 pages.

Co-Pending U.S. Appl. No. 14/017,210, Final Office Action dated Apr. 11, 2018, 10 pages.

Co-Pending U.S. Appl. No. 14/686,380, Final Office Action dated May 9, 2018, 14 pages.

Co-Pending U.S. Appl. No. 14/686,380, Response to Nov. 22, 2017 Non-Final Office Action dated Mar. 28, 2018, 11 pages.

Kotnik et al., "Sensitivity of transmembrane voltage induced by applied electric fields—A theoretical analysis", *Bioelectrochemistry and Bioenergetics*, vol. 43, Issue 2, 1997, pp. 285-291.

\* cited by examiner

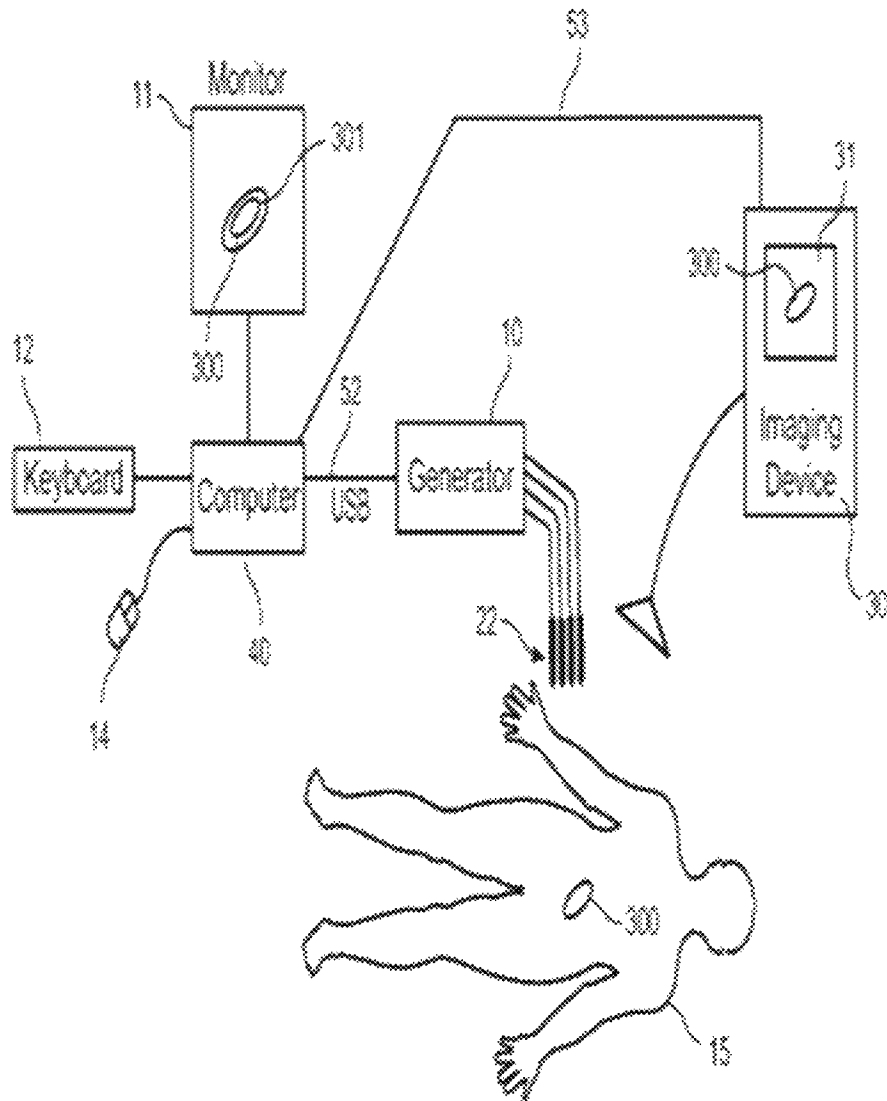


FIG. 1

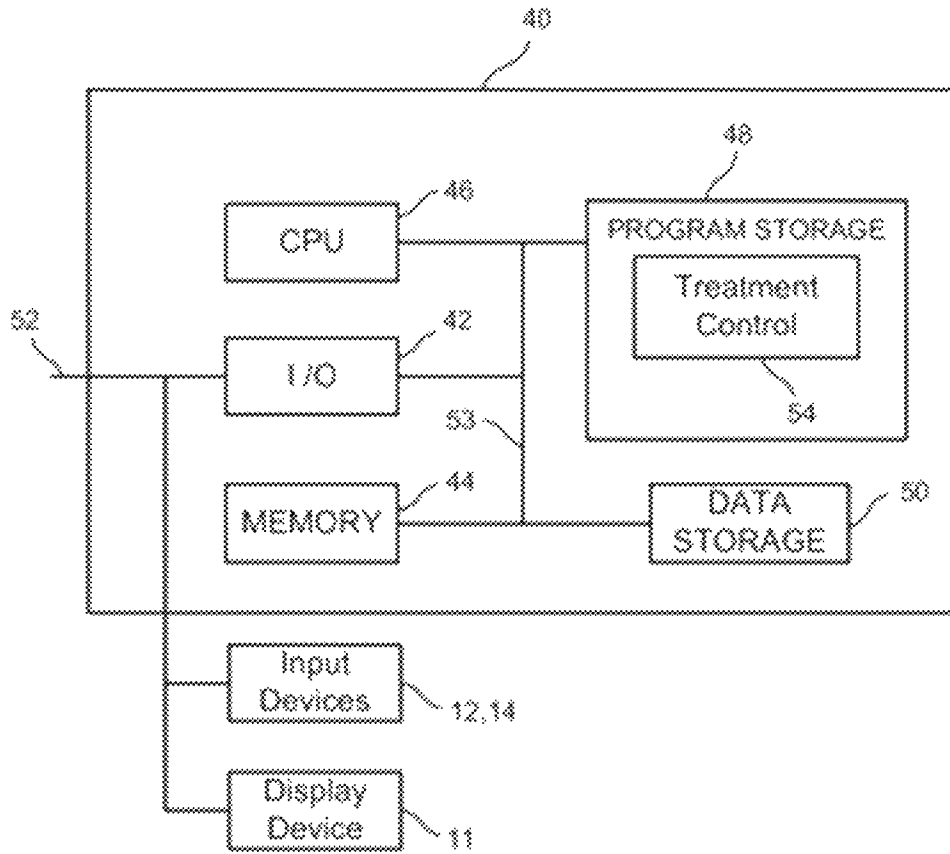


FIG. 2

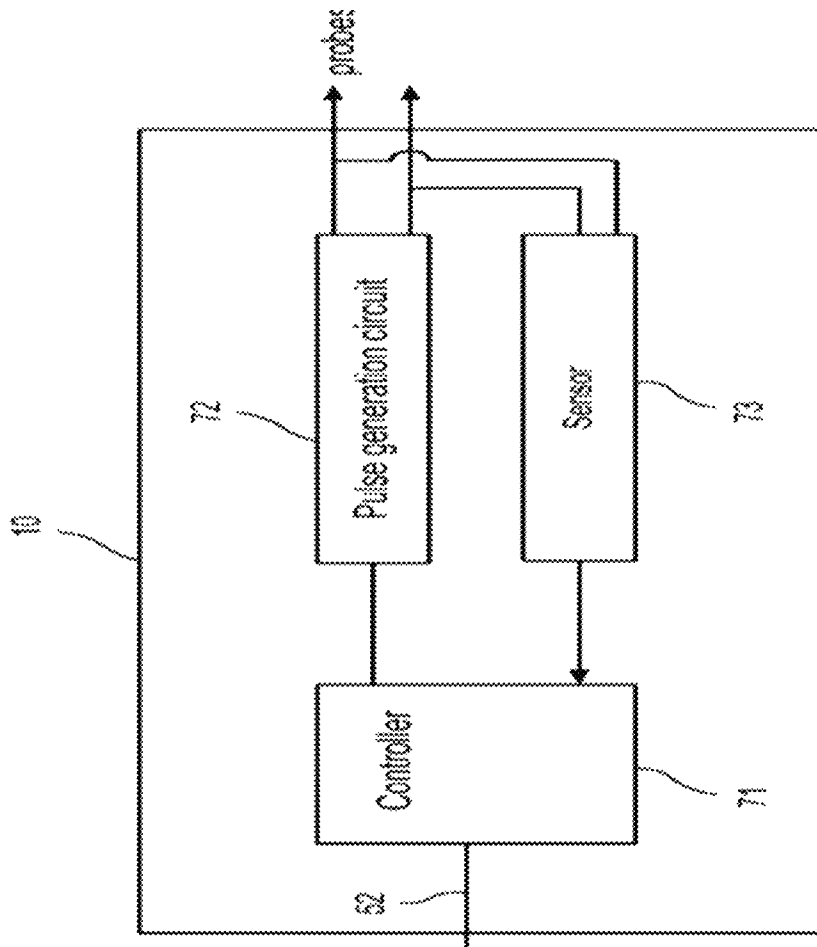


FIG. 3

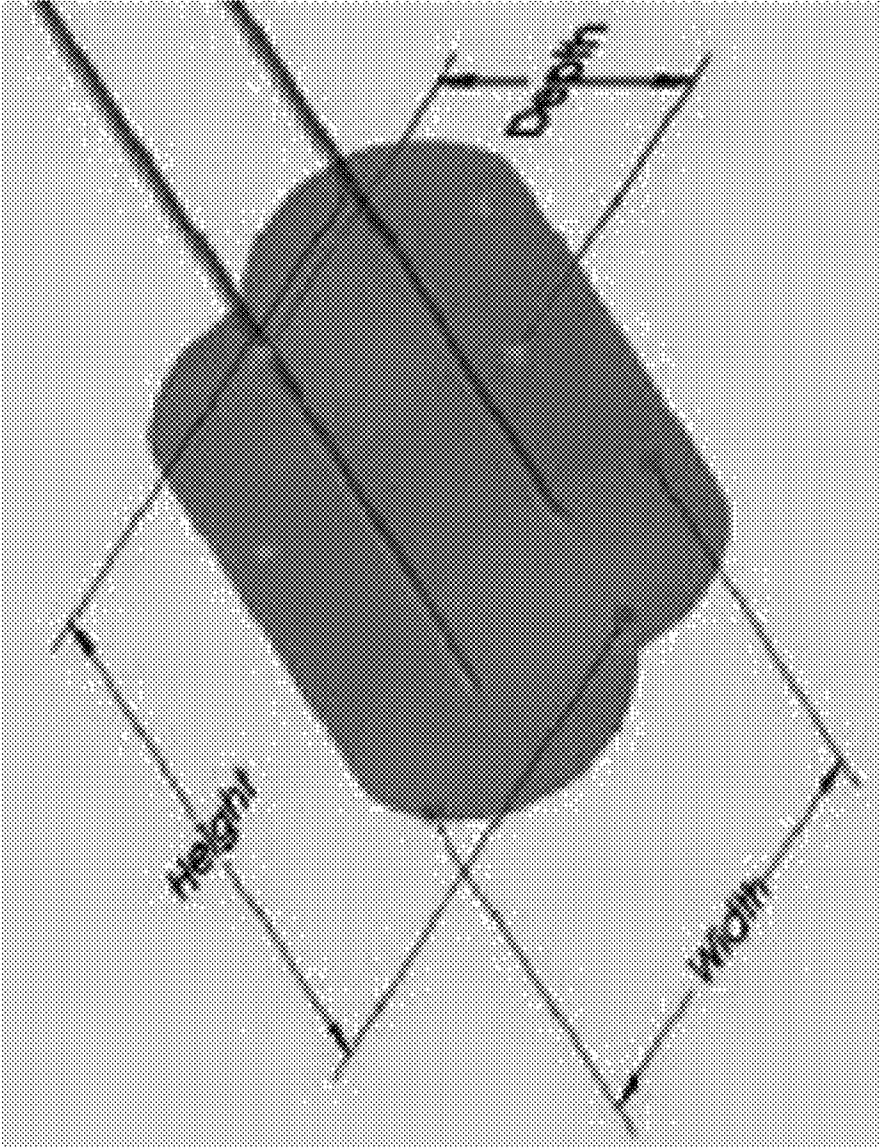


FIG. 4

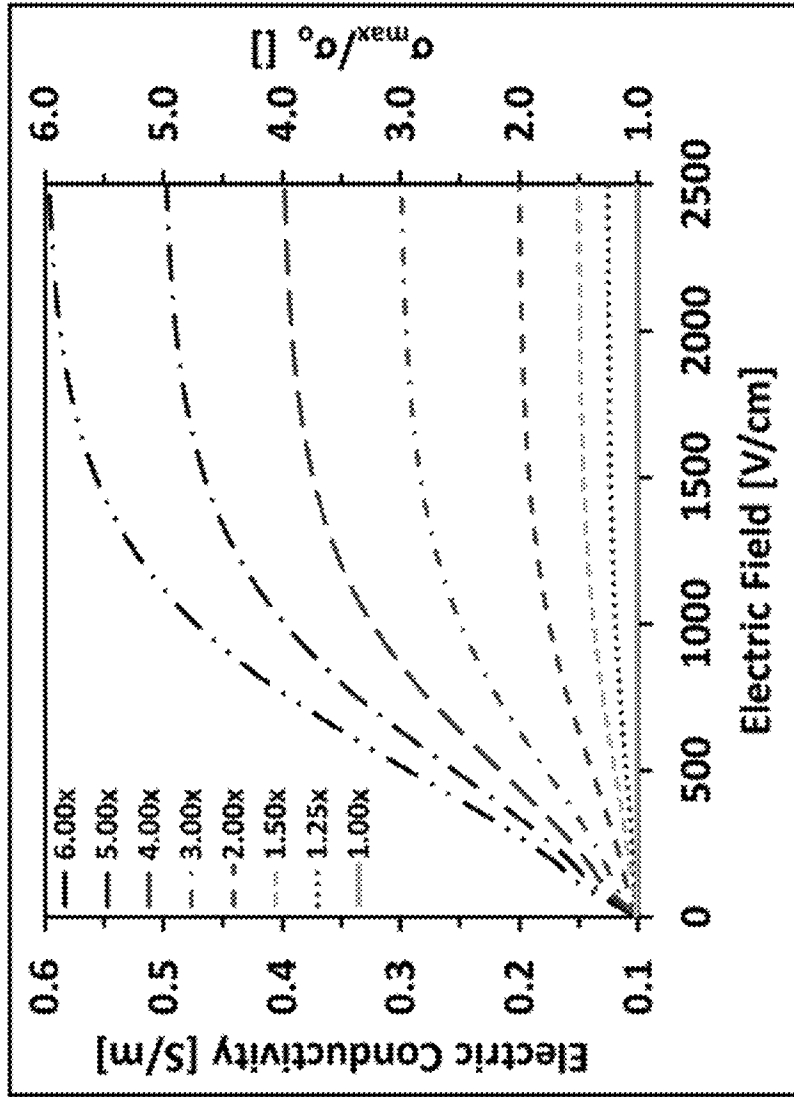


FIG. 5

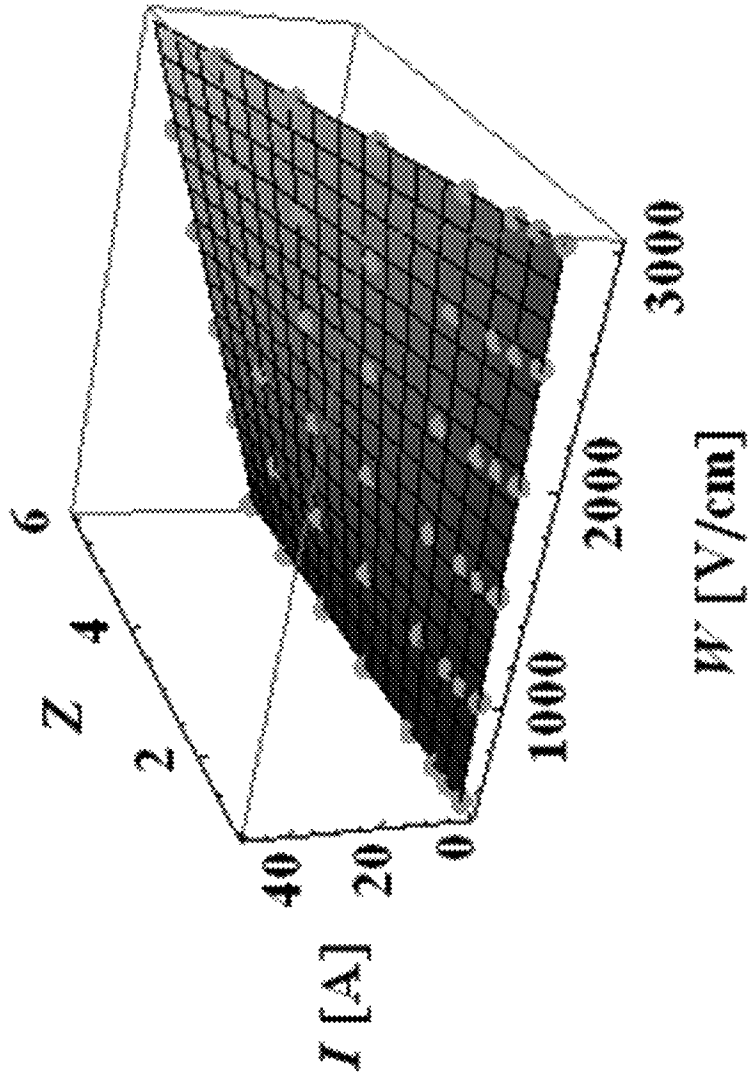


FIG. 6



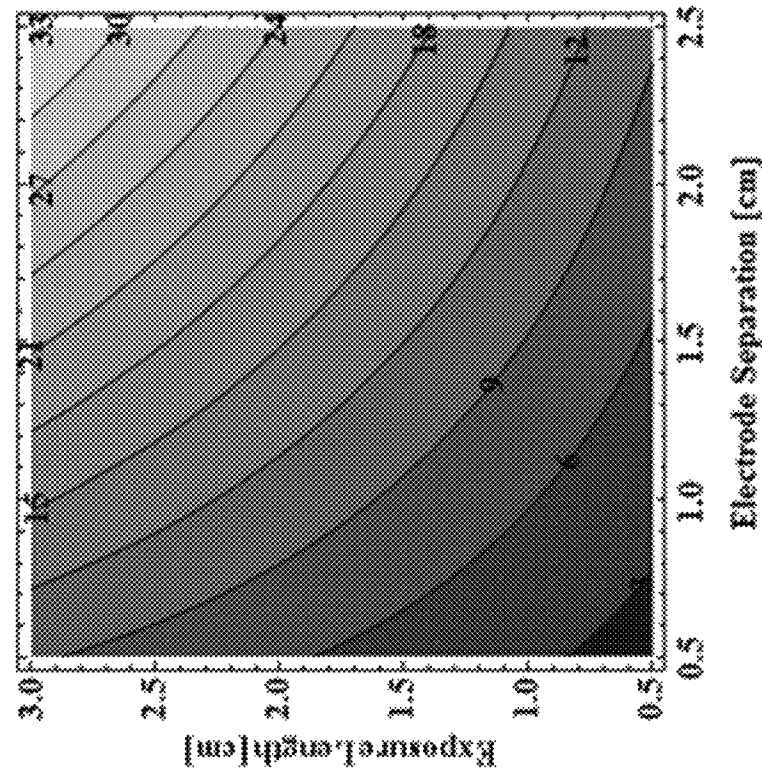


FIG. 7A

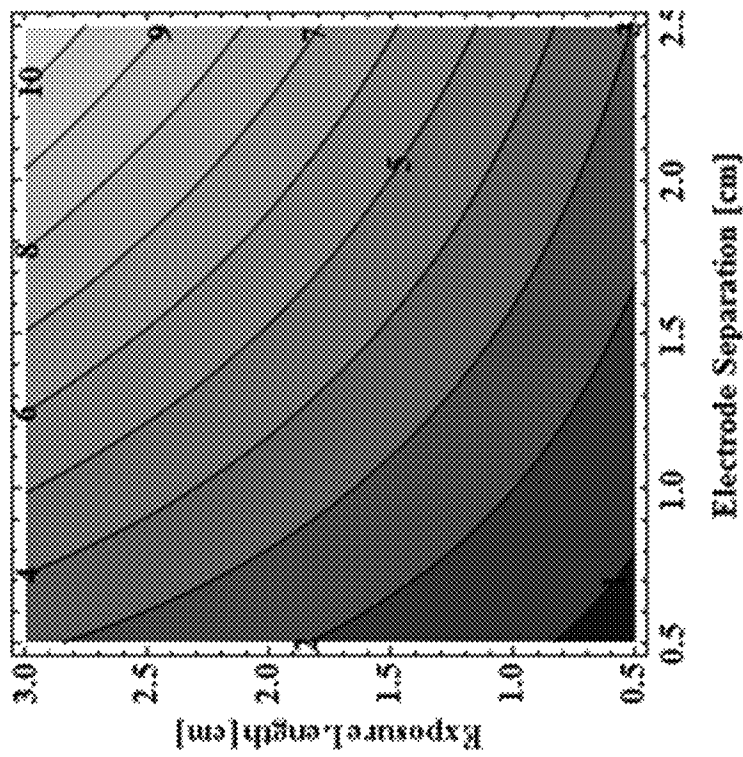


FIG. 7B

**Response Current (A)**  
**Whole Model**  
**Parameter Estimates**

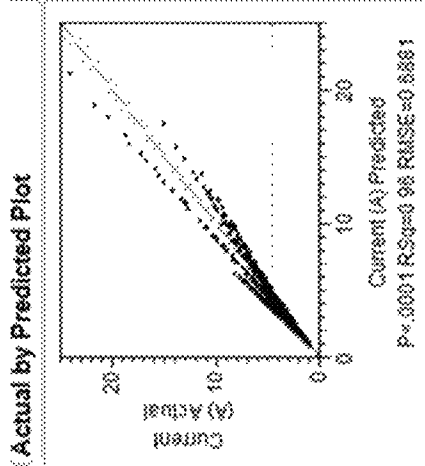
Term	Estimate	Std Error	t Ratio	Prob >  t
Intercept	-1.428927	0.1150684	-13.90	< .0001*
Cap (mm)	-0.3389848	0.0028208	-69.79	< .0001*
Radius (mm)	2.1298809	0.1299271	16.42	< .0001*
Exposure (mm)	0.2191464	0.0030903	69.88	< .0001*
F factor	1.1118276	0.1447111	7.55	< .0001*
Cap (mm)*Radius (mm)*F	-0.1163882	0.0117965	-8.49	< .0001*
Cap (mm)*Exposure (mm)*F	-0.0191131	0.0029425	-7.38	< .0001*
Radius (mm)*Exposure (mm)*F	-0.0812908	0.0028283	-32.38	< .0001*
Cap (mm)*F	0.0822293	0.0147111	5.59	< .0001*
Radius (mm)*F	0.4354413	0.0230771	18.86	< .0001*
Exposure (mm)*F	0.0469314	0.0011783	39.83	< .0001*
Cap (mm)*Radius (mm)	-0.0081994	0.0020268	-2.89	0.0038*
Cap (mm)*Exposure (mm)	0.0165327	0.005844	1.98	0.0507
Radius (mm)*Exposure (mm)	-0.0033861	0.0005284	-15.85	< .0001*
Cap (mm)*F*Exposure (mm)	-0.041393	0.010192	-4.05	< .0001*
Cap (mm)*Radius (mm)*Exposure (mm)	-0.0020342	0.0011984	-1.71	0.0878

FIG. 8A

**Effect Tests**

Source	DF	Sum of Squares	F Ratio	Prob > F
Cap (mm)	1	1027.5188	2170.425	< .0001*
Radius (mm)	1	138.4796	288.1906	< .0001*
Exposure (mm)	1	1315.6881	4997.319	< .0001*
F factor	1	2782.2793	5798.019	< .0001*
Cap (mm)*Radius (mm)	1	19.82881	42.1885	< .0001*
Cap (mm)*Exposure (mm)	1	209.4149	598.0843	< .0001*
Cap (mm)*F factor	1	494.8241	1043.528	< .0001*
Radius (mm)*Exposure (mm)	1	14.8143	31.2918	< .0001*
Radius (mm)*F factor	1	17.3917	36.6734	< .0001*
Exposure (mm)*F factor	1	388.8384	818.8387	< .0001*
Cap (mm)*Radius (mm)*Exposure (mm)	1	4.6748	9.8078	0.0035*
Radius (mm)*Exposure (mm)*F factor	1	1.9146	1.8328	0.0667
Cap (mm)*Exposure (mm)*F factor	1	118.9035	251.1195	< .0001*
Cap (mm)*Radius (mm)*F factor	1	1.7742	16.4215	< .0001*
Cap (mm)*Radius (mm)*Exposure (mm)*F factor	1	1.3858	2.9268	0.0878

FIG. 8B



**Summary of Fit**

RSquare	0.957568
RSquare Adj	0.956864
Root Mean Square Error	0.888054
Mean of Response	4.608821
Observations (or Sum Wgts)	720

**Analysis of Variance**

Source	DF	Squares	Mean Square	F Ratio	Prob > F
Model	15	7521.2186	501.421	1059.150	< .0001*
Error	704	333.2884	0.473		
C. Total	719	7854.5070			

FIG. 8C

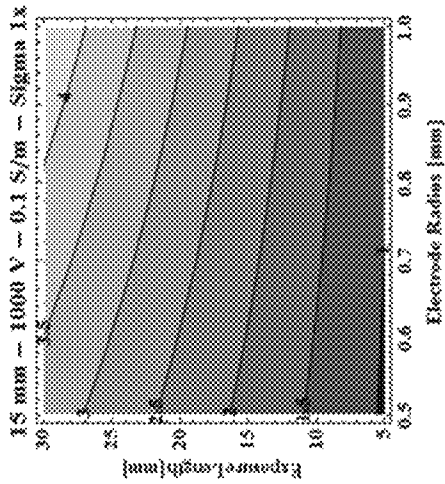


FIG. 9A

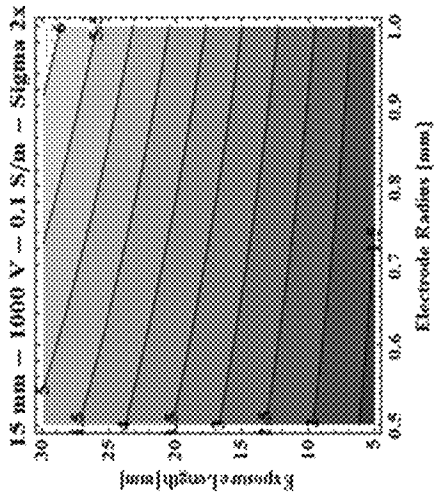


FIG. 9B

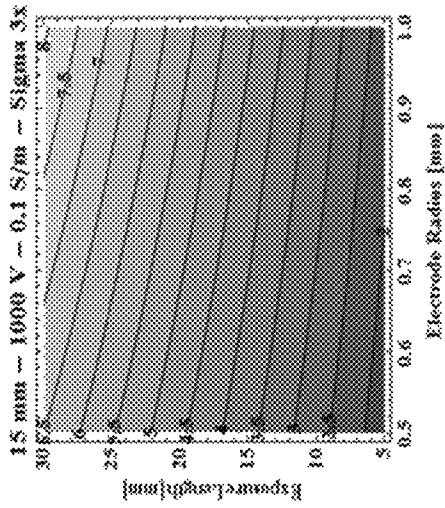


FIG. 9C

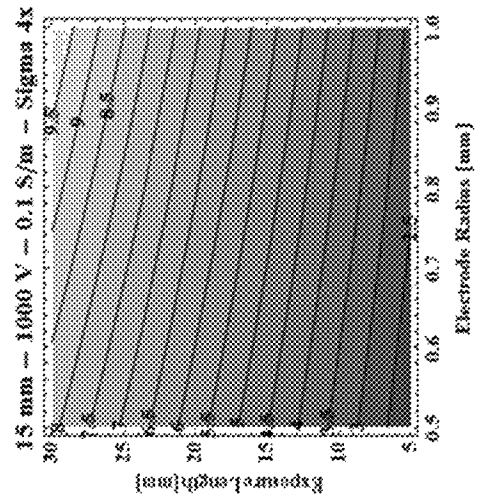


FIG. 9D

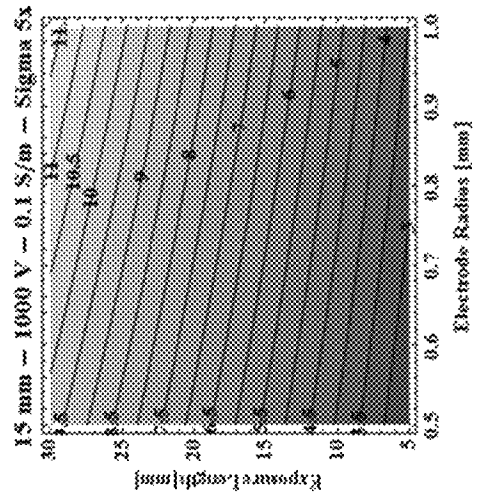


FIG. 9E

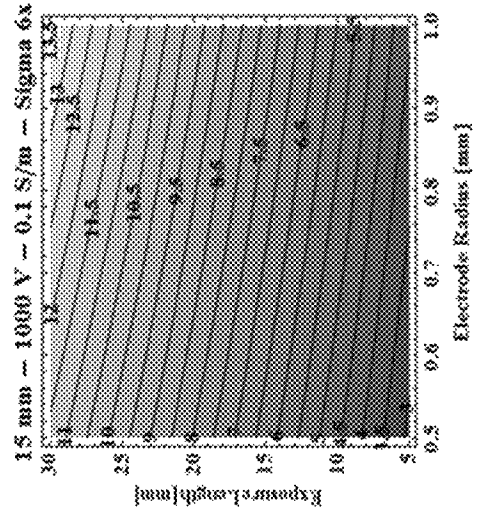


FIG. 9F

Timing	Voltage (V)	Current (A)	$\sigma$ (\$/m)	$\sigma$ (\$/m)	$\sigma$ (\$/m)	$\sigma$ (\$/m)	$\sigma$ (\$/m)	$\sigma_{\text{max}}/\sigma_{\text{min}}$	$\sigma_{\text{max}}/\sigma_{\text{min}}$	$\sigma_{\text{max}}/\sigma_{\text{min}}$	$\sigma_{\text{max}}/\sigma_{\text{min}}$	$\sigma_{\text{max}}/\sigma_{\text{min}}$	$\sigma_{\text{max}}/\sigma_{\text{min}}$
Pre-IRE	24	-	0.018	-	0.021	-	0.020	-	1.0	-	-	-	1.0
Pre-IRE	48	-	0.036	-	0.021	-	0.020	-	1.0	-	-	-	1.0
Pre-IRE	72	-	0.061	-	0.023	-	0.023	-	1.1	-	-	-	1.2
Pre-IRE	96	0.108	0.126	0.031	0.036	0.034	0.041	1.5	1.7	1.7	1.7	1.7	2.1
Pre-IRE	123	0.165	0.232	0.037	0.052	0.043	0.063	1.8	2.5	2.5	2.1	2.1	3.2
IRE	984	15.4 (1 <sup>st</sup> )	19.2 (90 <sup>th</sup> )	0.430	0.536	0.589	0.737	20.9	26.0	26.0	29.5	29.5	36.9
Post-IRE	24	0.384	0.348	0.440	0.399	0.602	0.545	21.3	19.3	19.3	30.2	30.2	27.3
Post-IRE	48	0.78	0.72	0.447	0.412	0.612	0.564	21.7	20.0	20.0	30.6	30.6	28.2
Post-IRE	72	1.2	1.14	0.458	0.435	0.628	0.596	22.2	21.1	21.1	31.4	31.4	29.8
Post-IRE	96	1.54	1.48	0.441	0.424	0.604	0.580	21.4	20.6	20.6	30.2	30.2	29.0
Post-IRE	120	1.92	1.86	0.440	0.426	0.602	0.583	21.3	20.7	20.7	30.2	30.2	29.2

FIG. 10A

Timing	Voltage (V)	Current (A)	Current (A)	$\sigma$ (S/m)	$\sigma$ (S/m)	$\sigma$ (S/m)	$\sigma$ (S/m)	$\sigma$ (S/m)	$\sigma$ (S/m)	$\sigma$ (S/m)	$\sigma$ (S/m)	$\sigma$ (S/m)	$\sigma$ (S/m)	$\sigma$ (S/m)	$\sigma$ (S/m)	$\sigma$ (S/m)	$\sigma$ (S/m)
Pre-IRE	21	-	0.018	-	0.024	-	0.023	-	1.0	-	1.0	-	-	-	-	-	1.0
Pre-IRE	48	-	0.036	-	0.021	-	0.020	-	0.9	-	0.9	-	-	-	-	-	0.8
Pre-IRE	72	0.071	0.079	0.027	0.030	0.026	0.029	1.2	1.3	1.2	1.2	1.2	1.2	1.2	1.2	1.2	1.4
Pre-IRE	96	0.134	0.17	0.038	0.049	0.043	0.058	1.6	2.1	1.6	1.6	1.6	1.6	1.6	1.6	1.6	2.5
Pre-IRE	120	0.24	0.336	0.055	0.077	0.066	0.097	2.3	3.3	2.3	2.3	2.3	2.3	2.3	2.3	2.3	4.2
IRE	996	14.6 (1 <sup>st</sup> )	19 (90 <sup>th</sup> )	0.403	0.524	0.550	0.719	17.1	22.3	17.1	17.1	17.1	17.1	17.1	17.1	17.1	31.5
Post-IRE	24	0.4	0.36	0.458	0.412	0.527	0.563	19.4	17.5	19.4	19.4	19.4	19.4	19.4	19.4	19.4	24.7
Post-IRE	48	0.79	0.74	0.452	0.424	0.619	0.579	19.2	18.0	19.2	19.2	19.2	19.2	19.2	19.2	19.2	25.4
Post-IRE	72	1.15	1.11	0.439	0.424	0.600	0.579	18.6	18.0	18.6	18.6	18.6	18.6	18.6	18.6	18.6	25.4
Post-IRE	96	1.6	1.52	0.458	0.435	0.627	0.595	19.4	18.5	19.4	19.4	19.4	19.4	19.4	19.4	19.4	26.0
Post-IRE	123	1.96	1.92	0.498	0.429	0.599	0.586	18.6	18.2	18.6	18.6	18.6	18.6	18.6	18.6	18.6	25.7

FIG. 10B

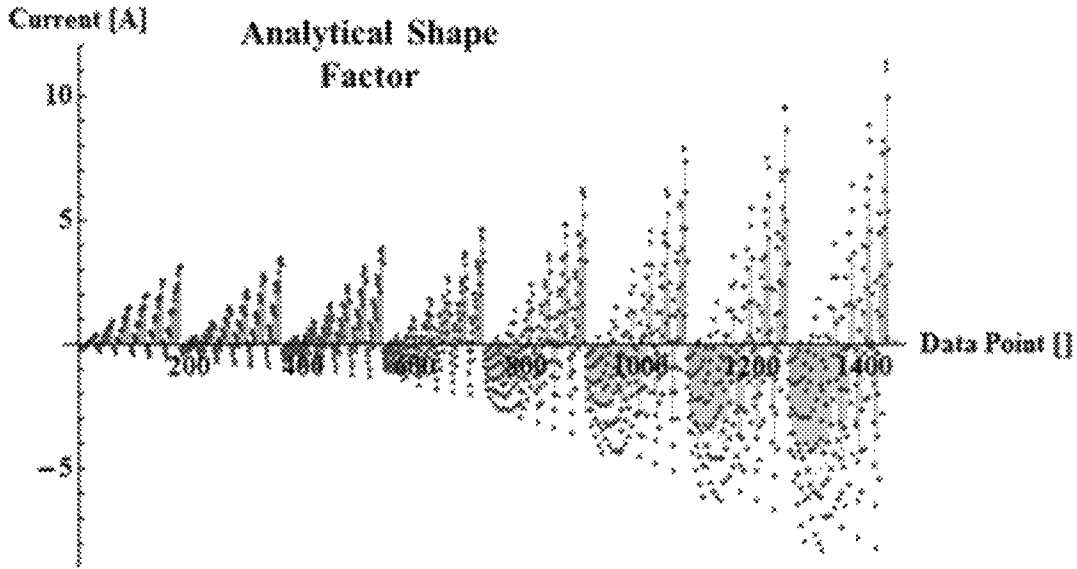


FIG. 11A

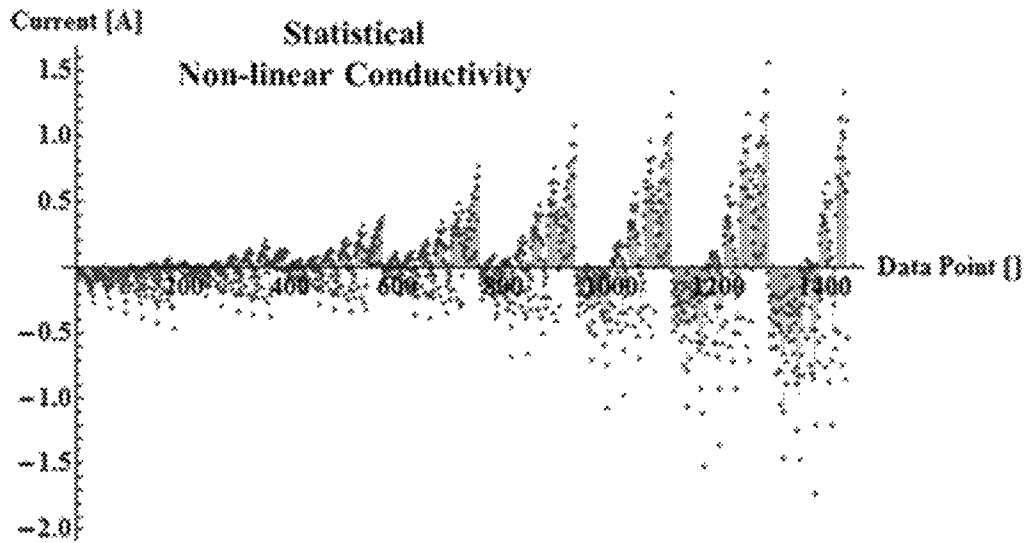


FIG. 11B

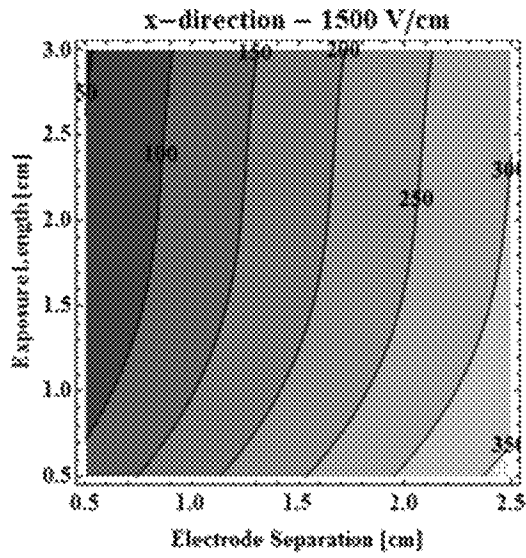


FIG. 12A

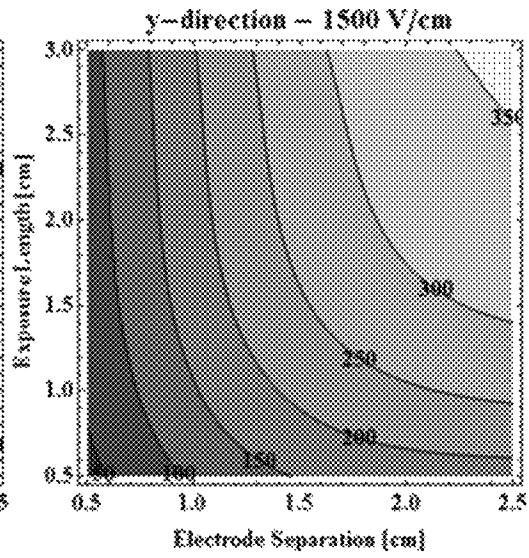


FIG. 12B

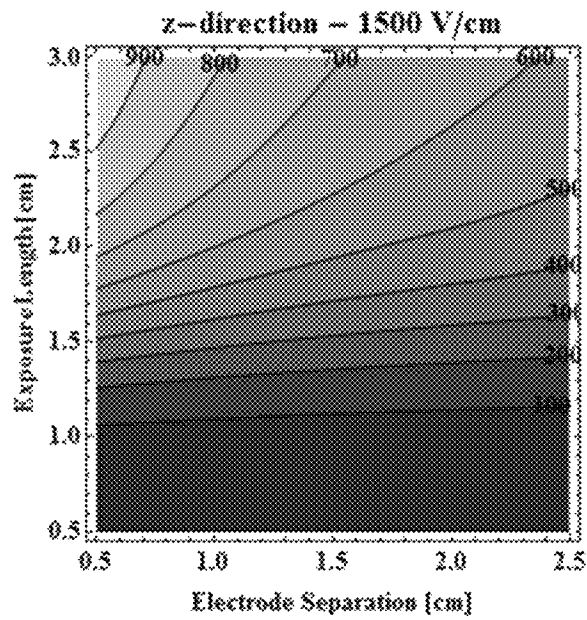


FIG. 12C

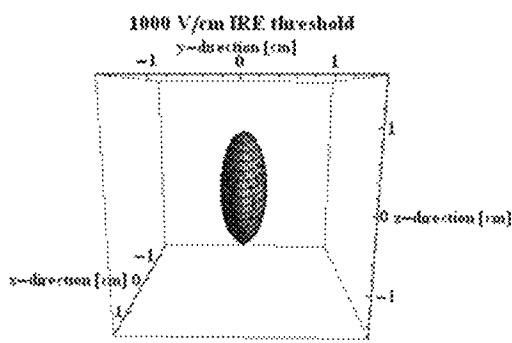


FIG. 13A

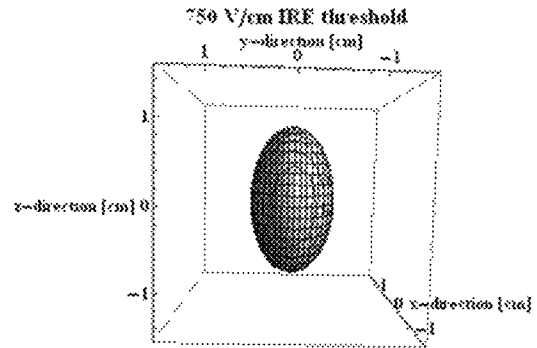


FIG. 13B

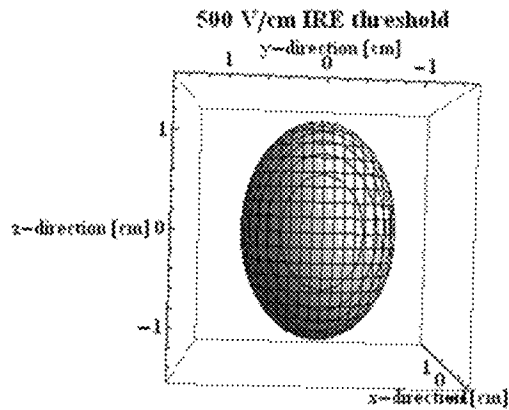


FIG. 13C



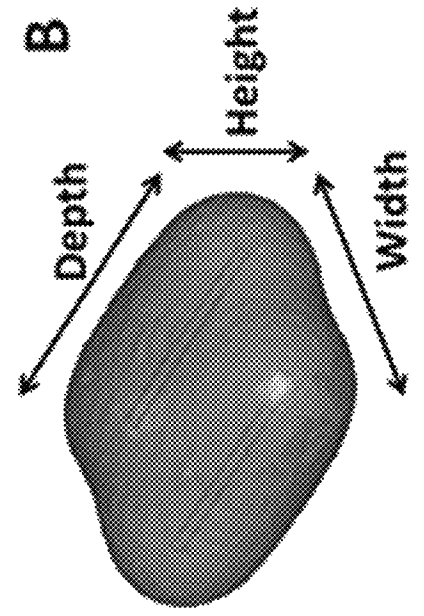


FIG. 14B

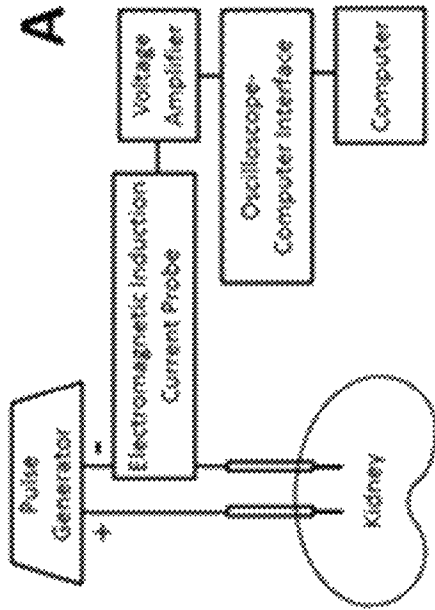


FIG. 14A

FIG. 14D

FIG. 14C

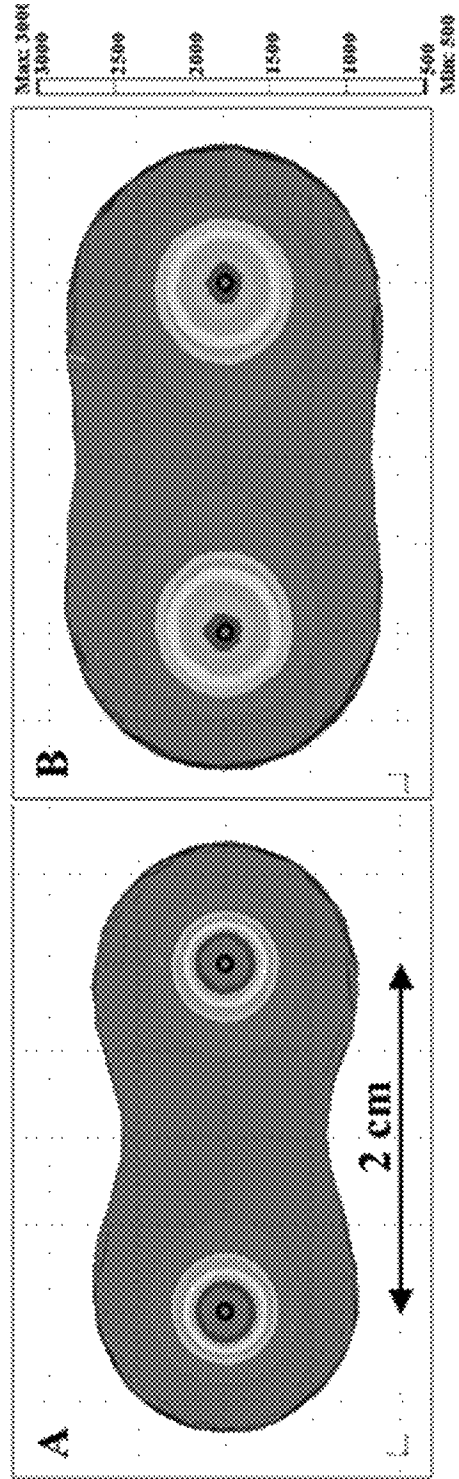


FIG. 15B

FIG. 15A

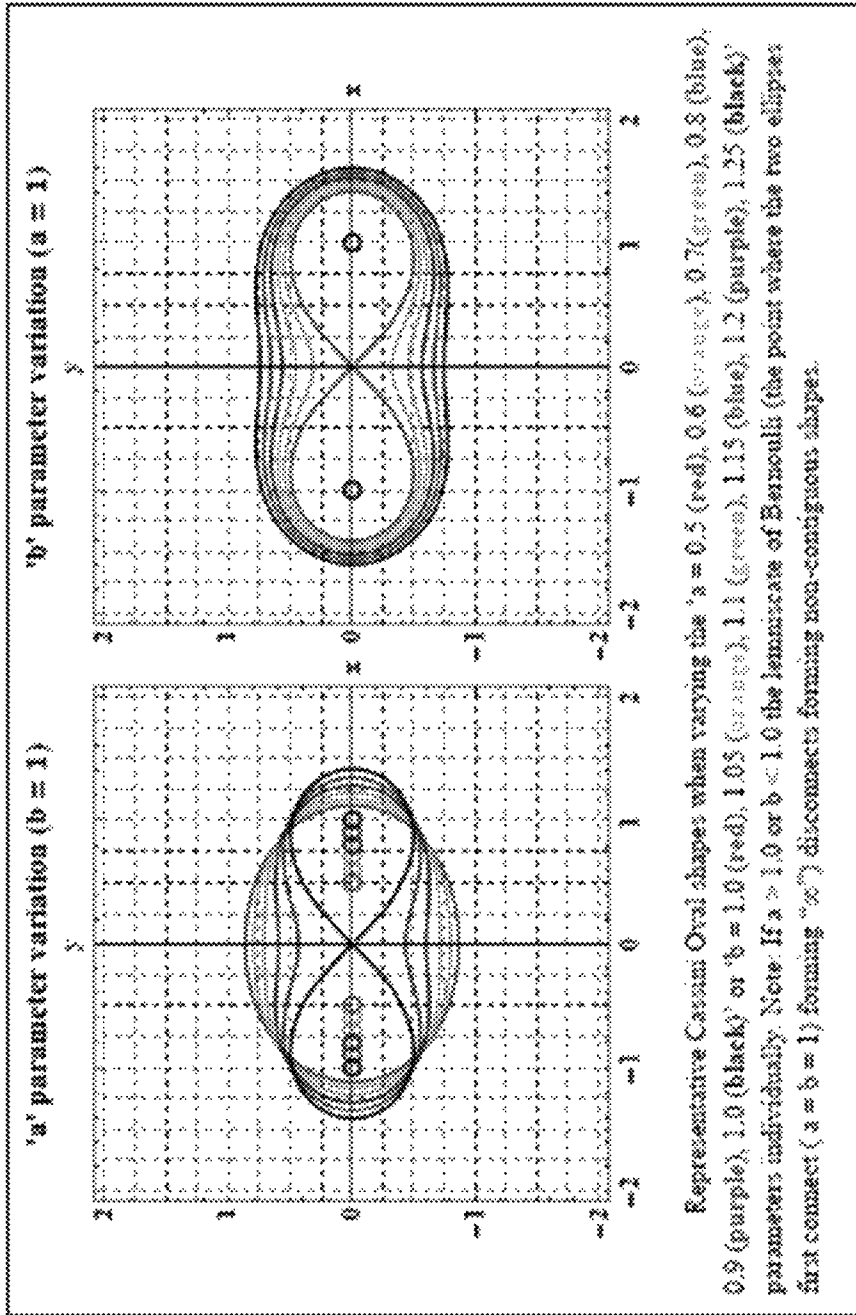


FIG. 16A

FIG. 16B

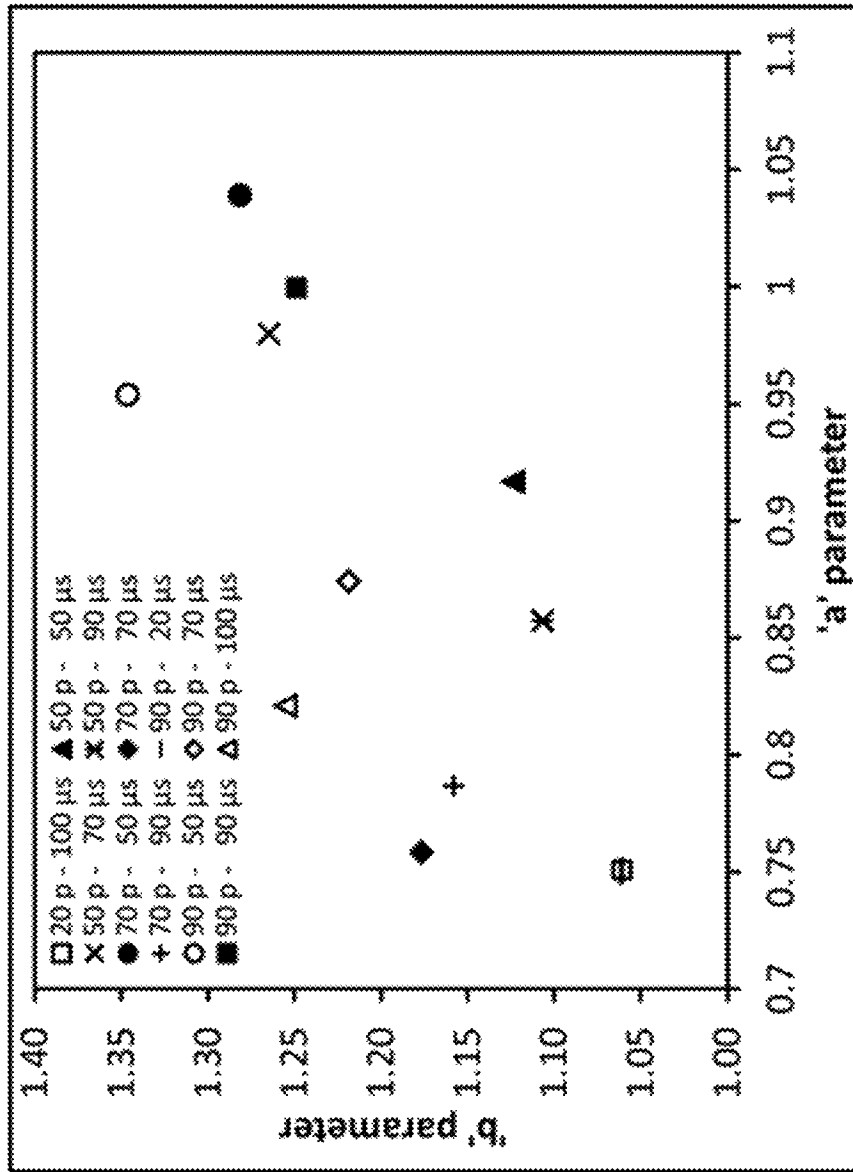


FIG. 17

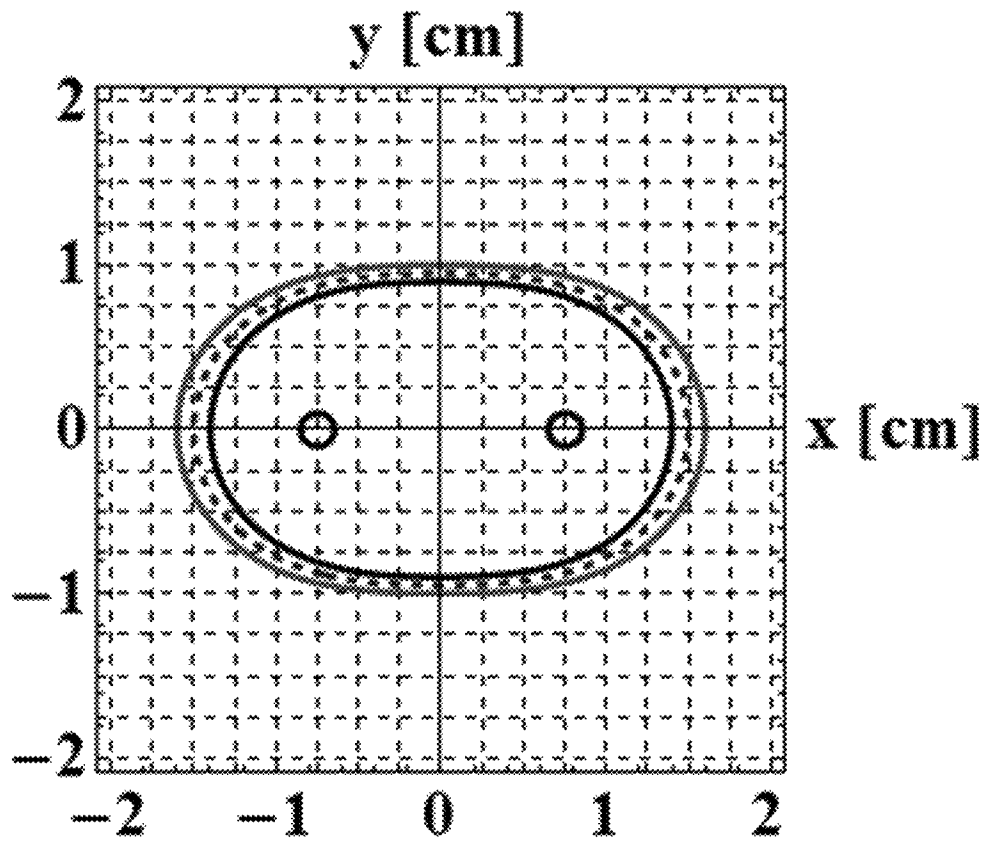


FIG. 18

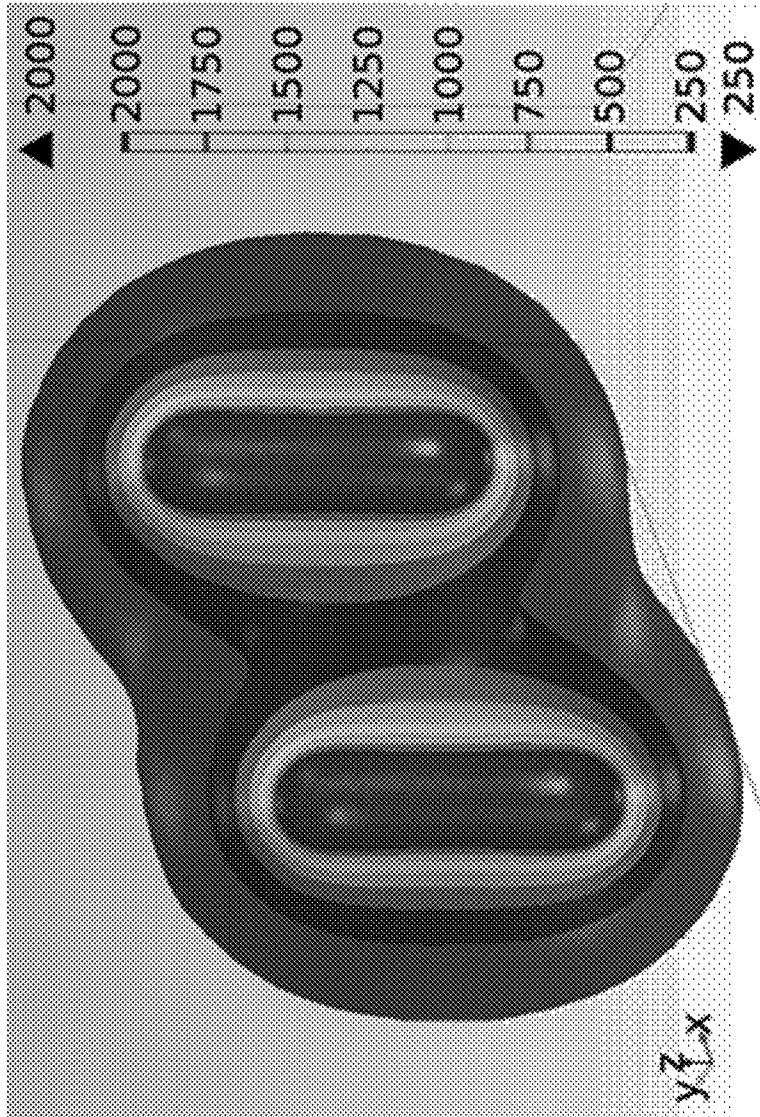


FIG. 19

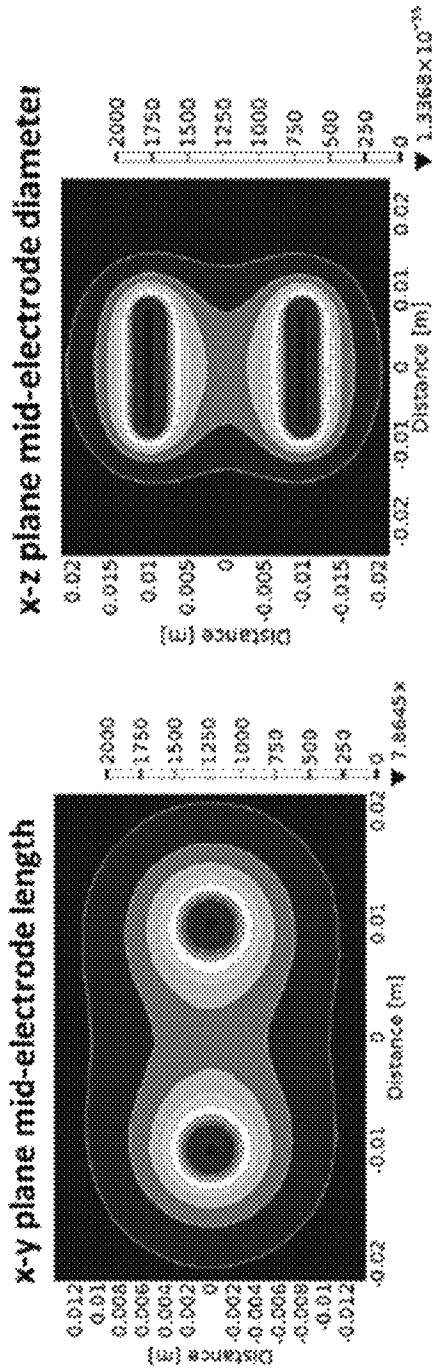


FIG. 20A

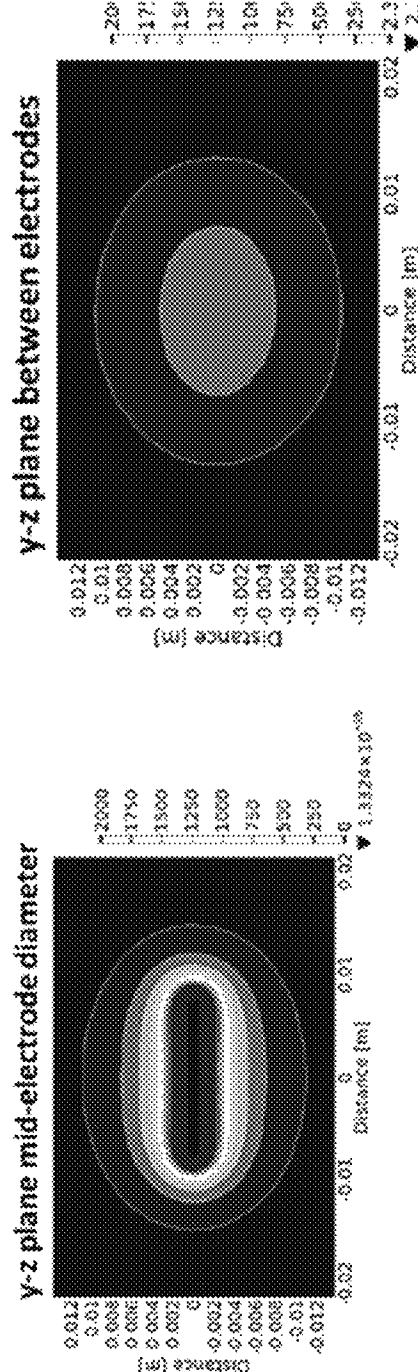


FIG. 20B

FIG. 20C

FIG. 20D

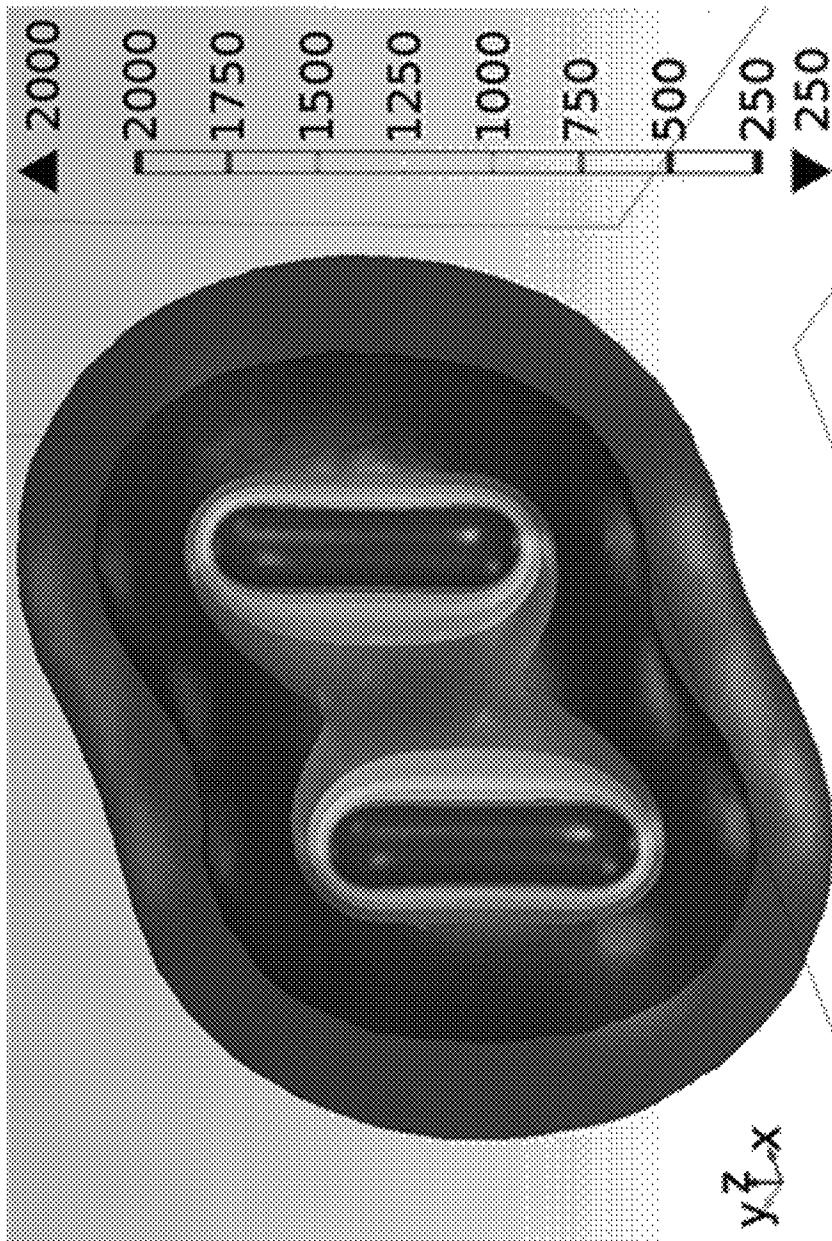


FIG. 21



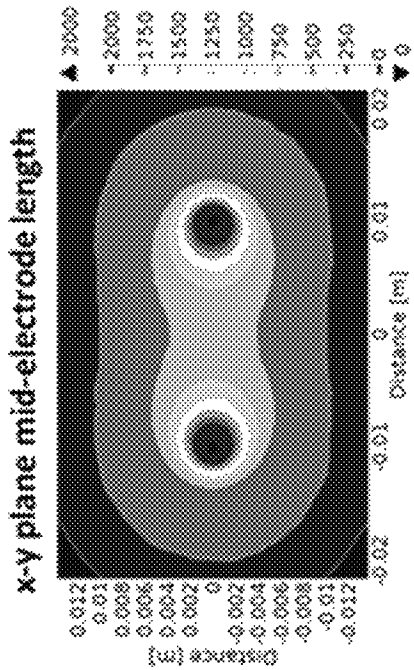


FIG. 22A

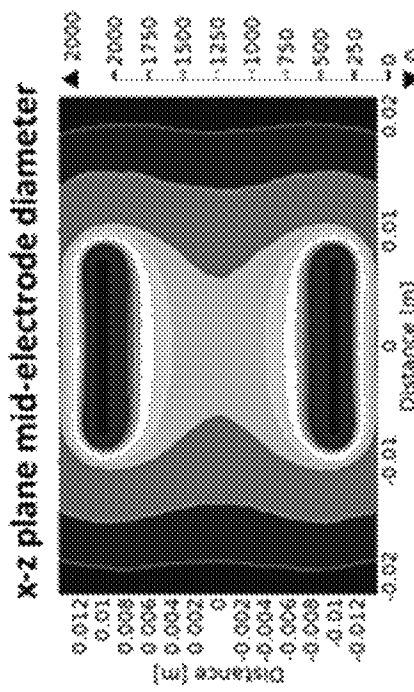


FIG. 22B

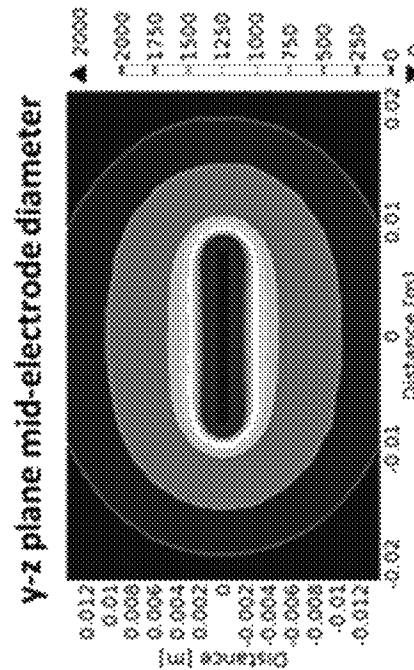


FIG. 22C

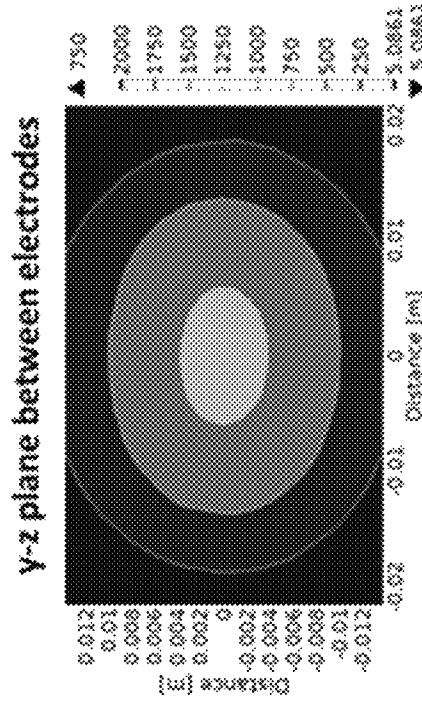


FIG. 22D

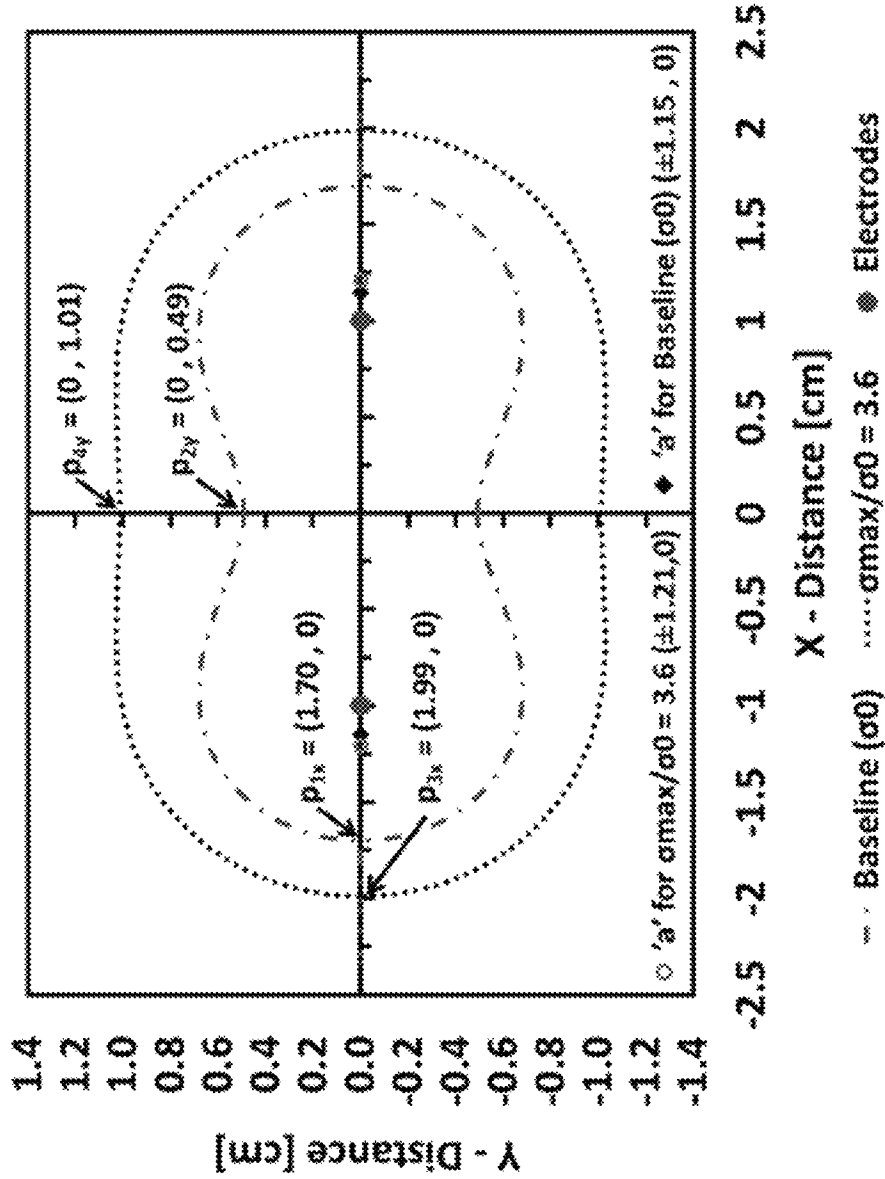
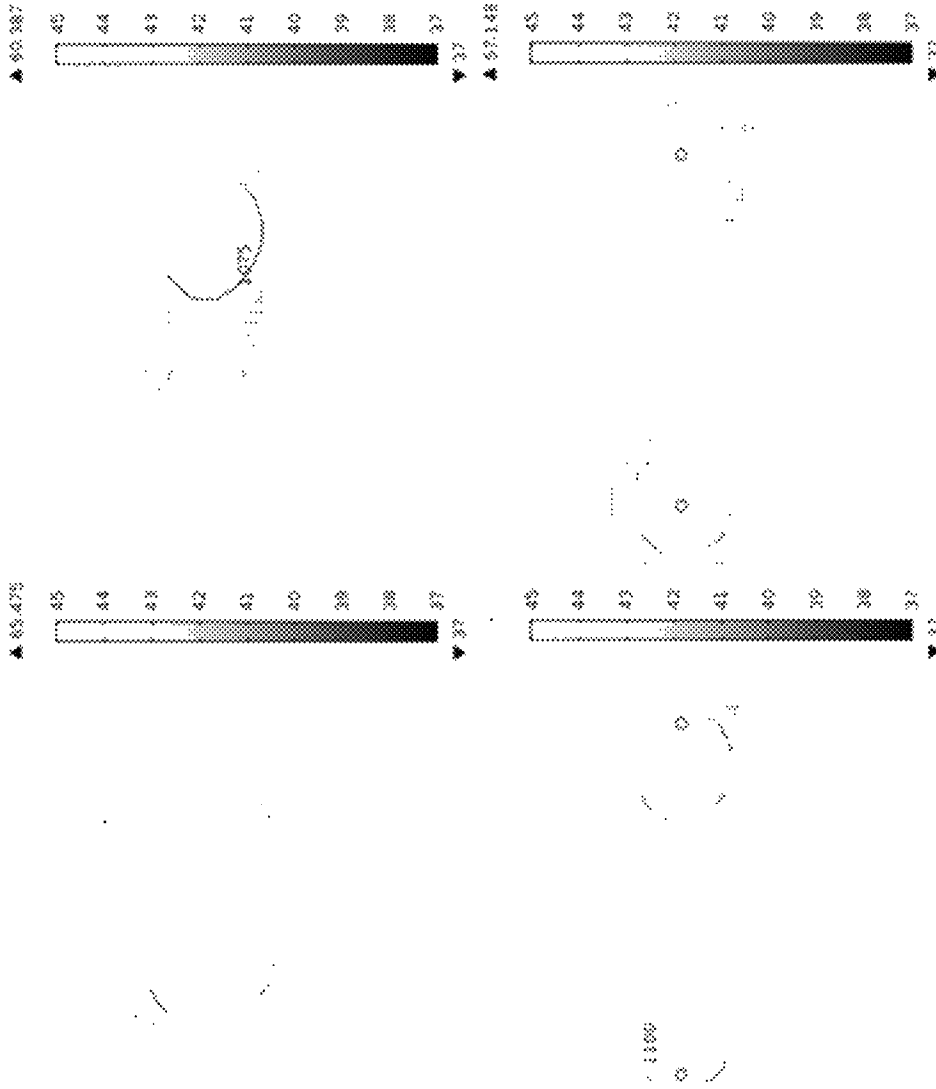
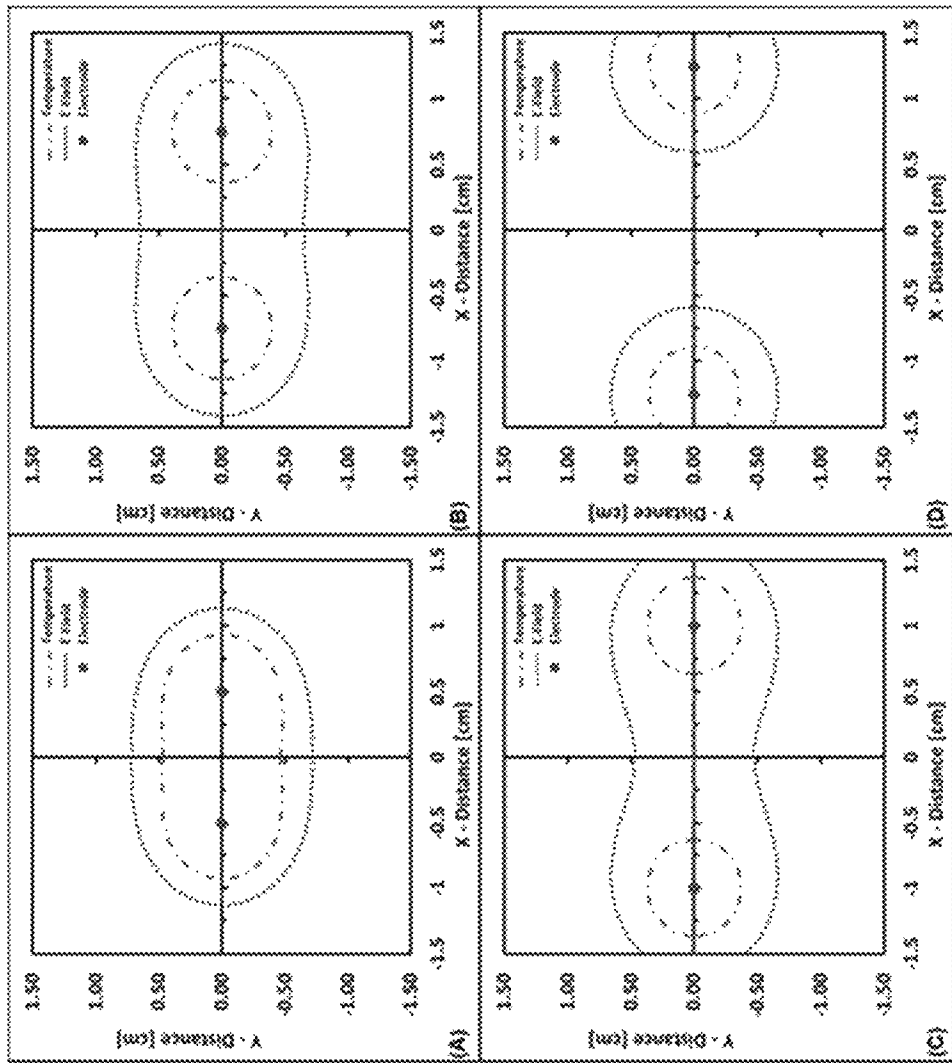


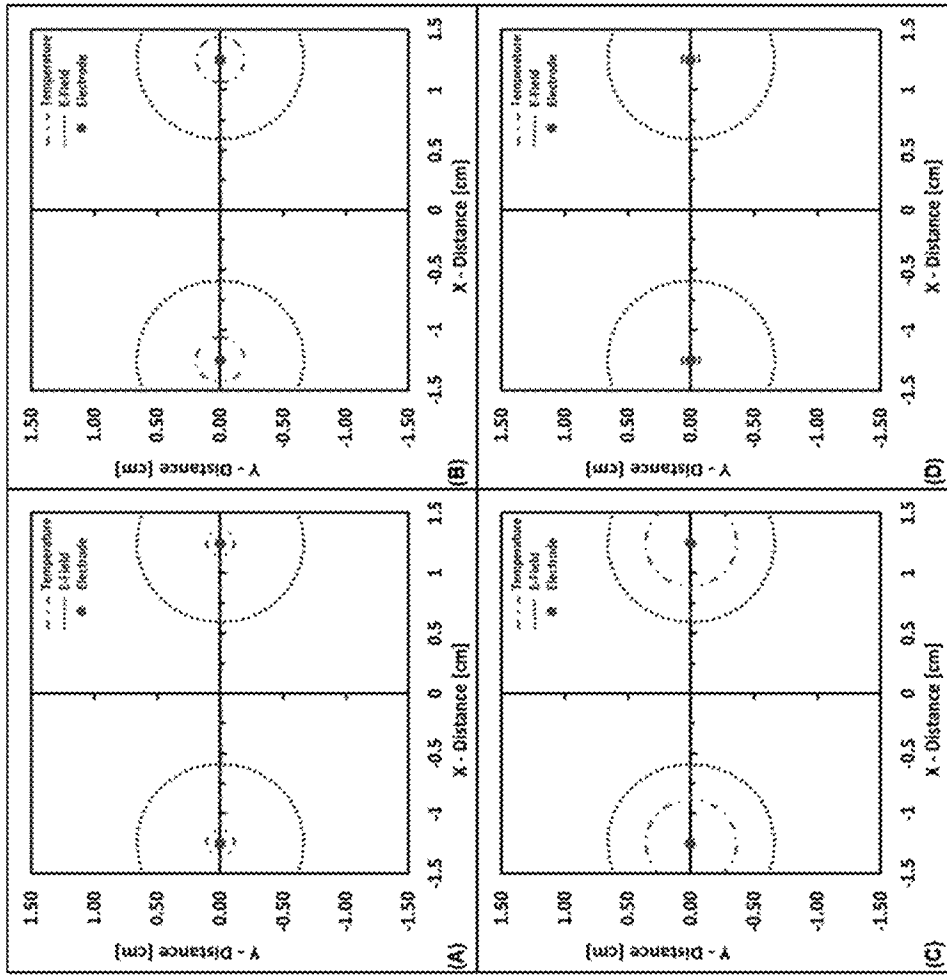
FIG. 23



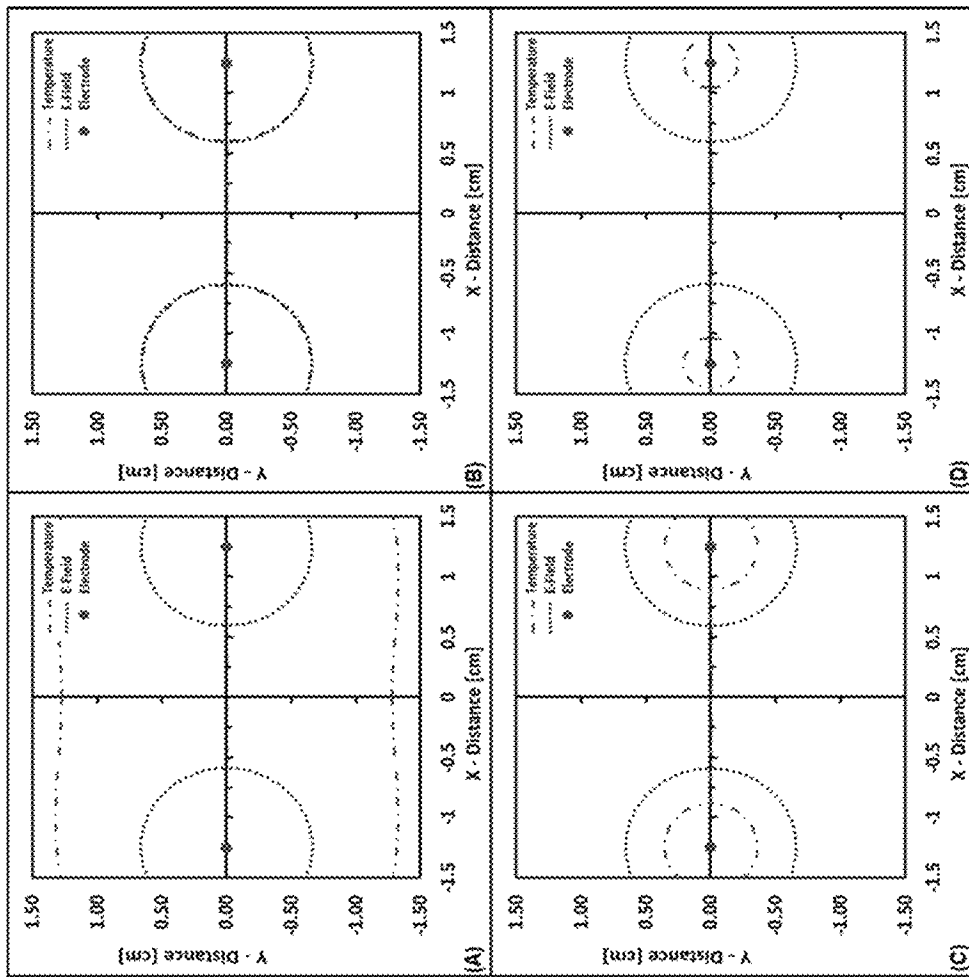
FIGS. 24A-D



FIGS. 25A-D



FIGS. 26A-D



FIGS. 27A-D

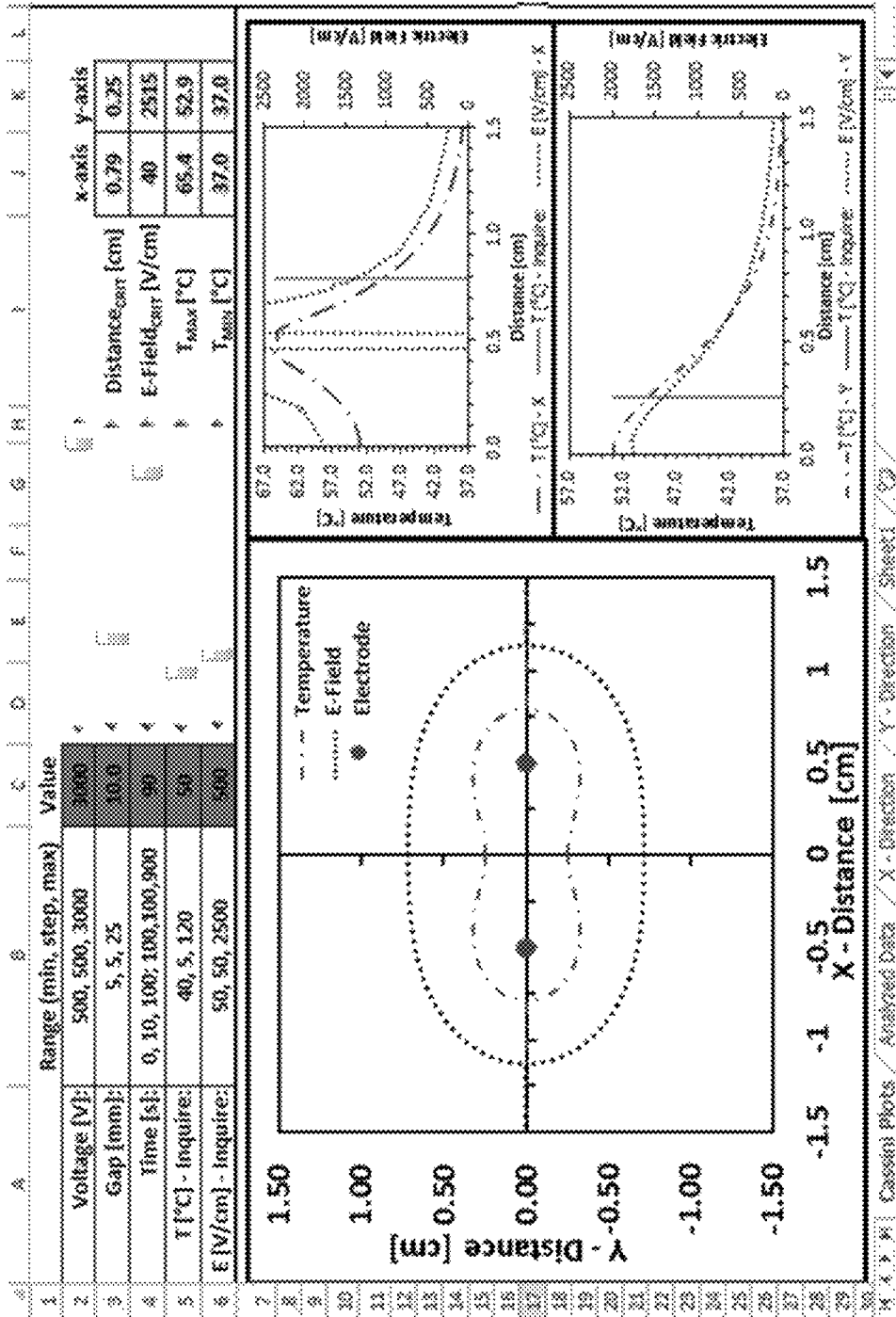


FIG. 28

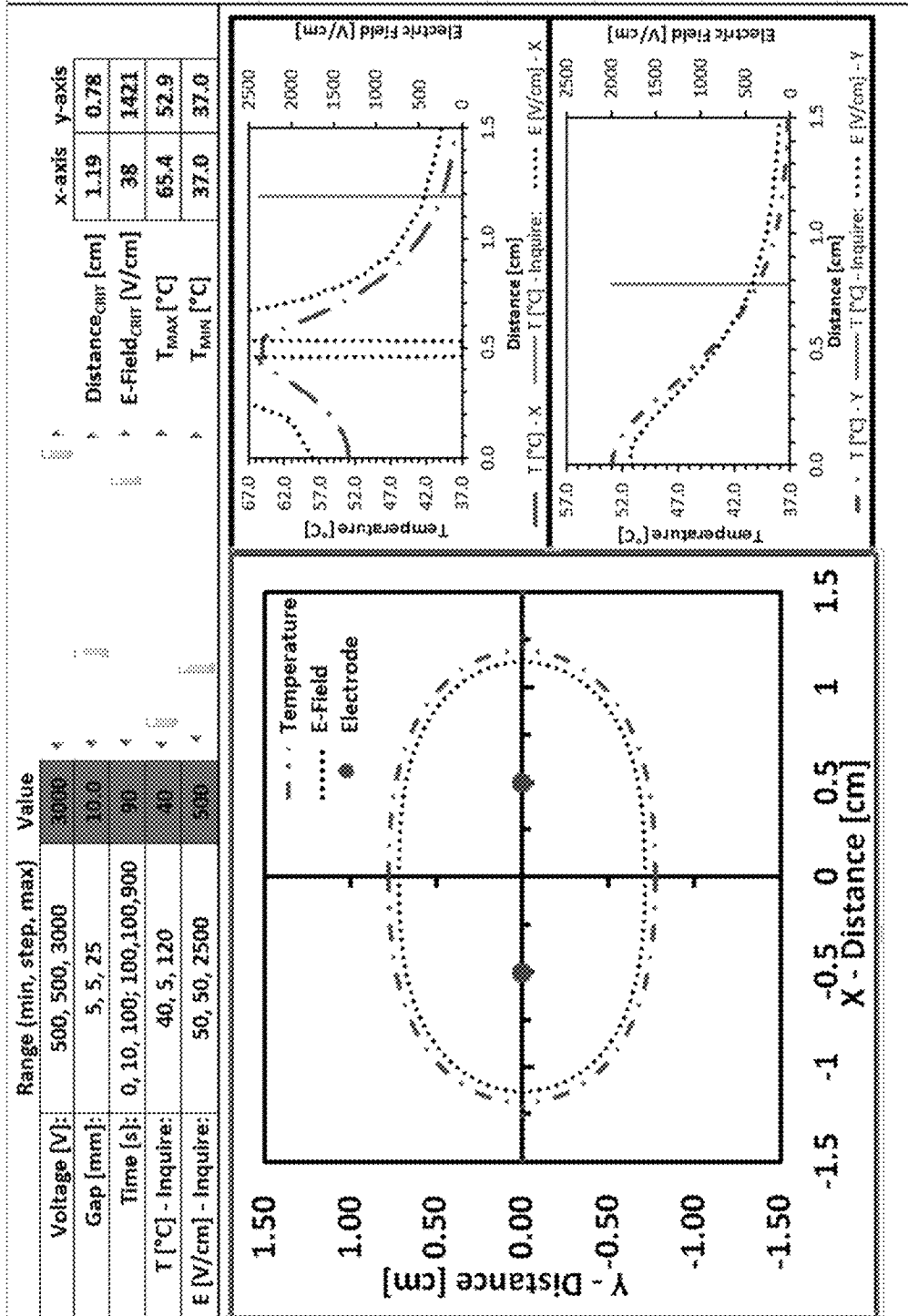


FIG. 29



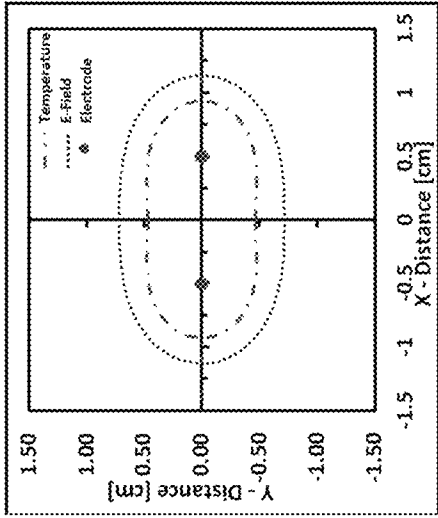


FIG. 30B

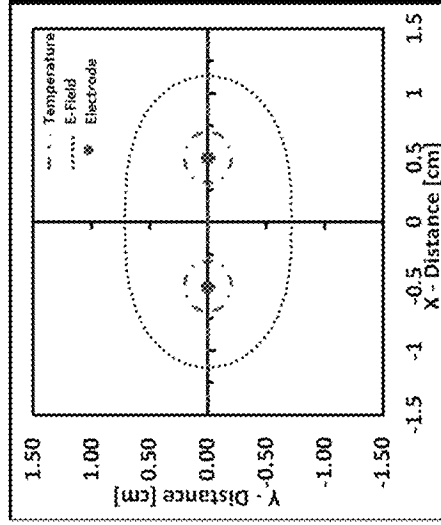


FIG. 30D

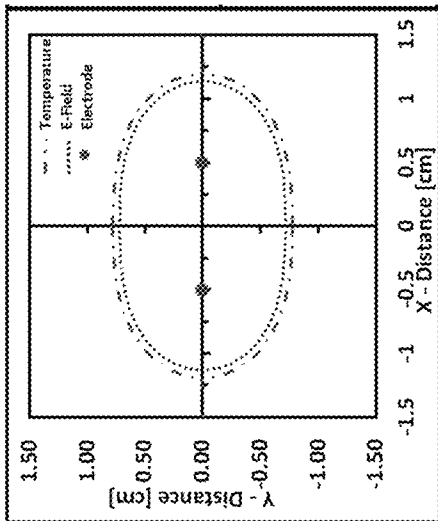


FIG. 30A

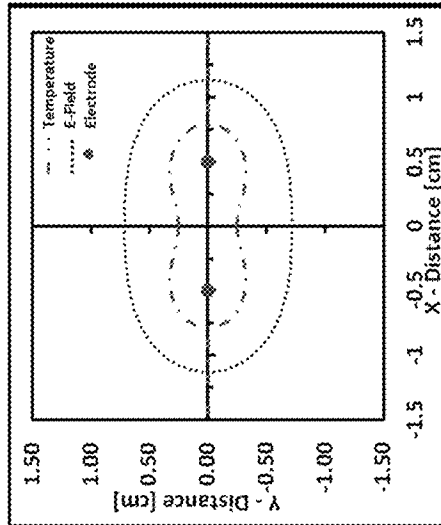


FIG. 30C

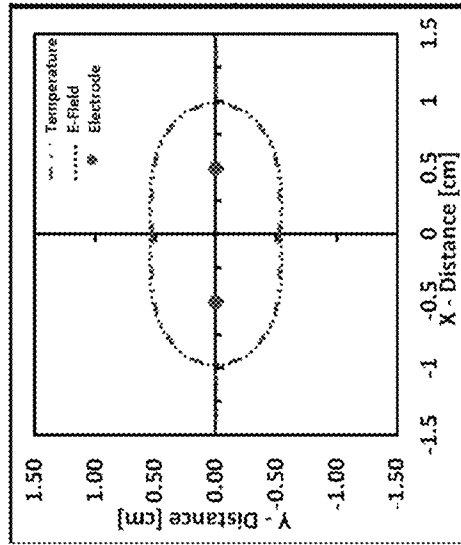


FIG. 31A

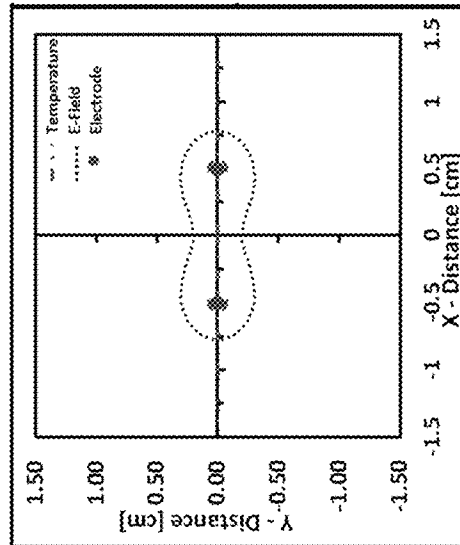


FIG. 31B

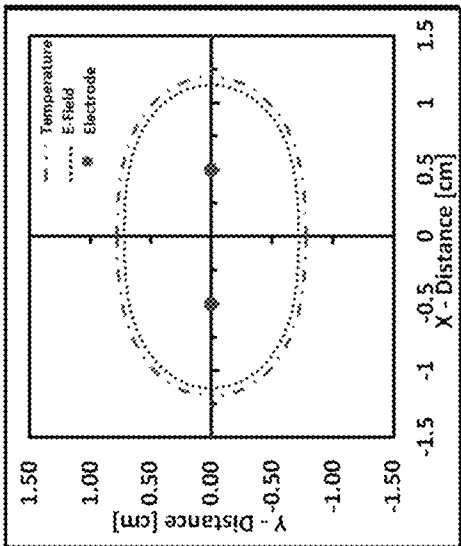


FIG. 31C

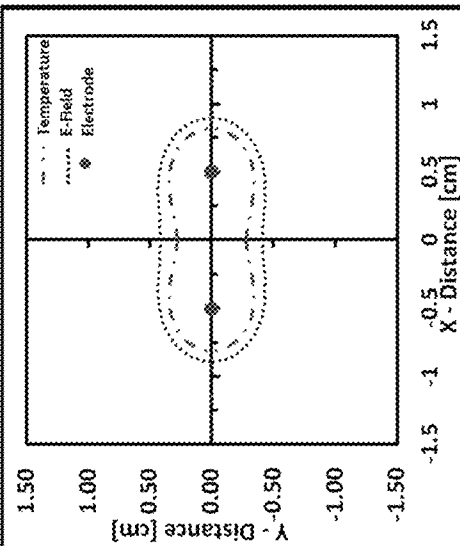


FIG. 31D

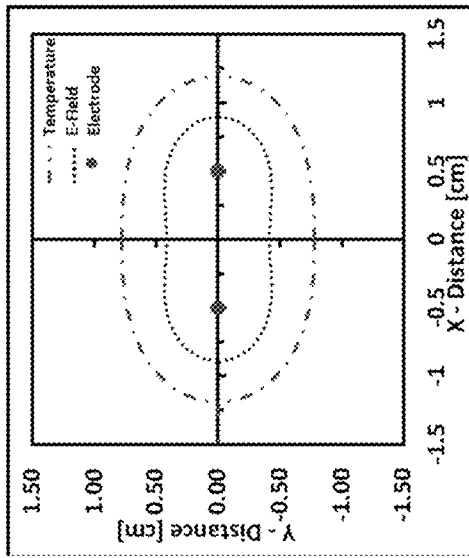


FIG. 32A

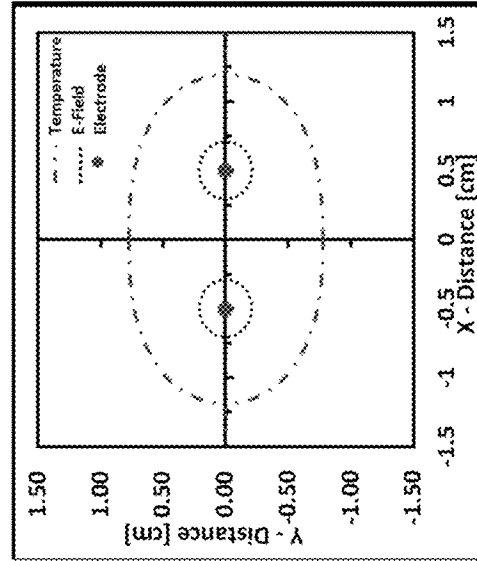


FIG. 32B

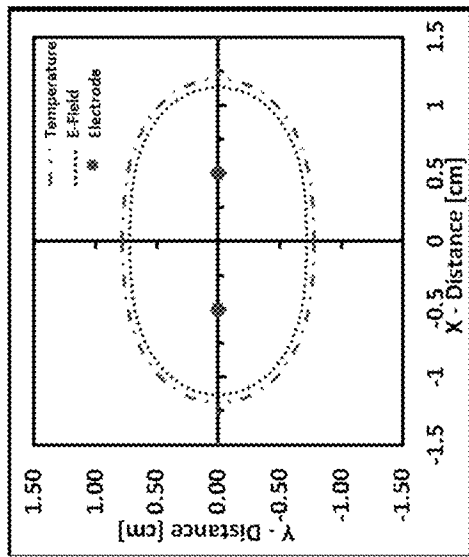


FIG. 32C

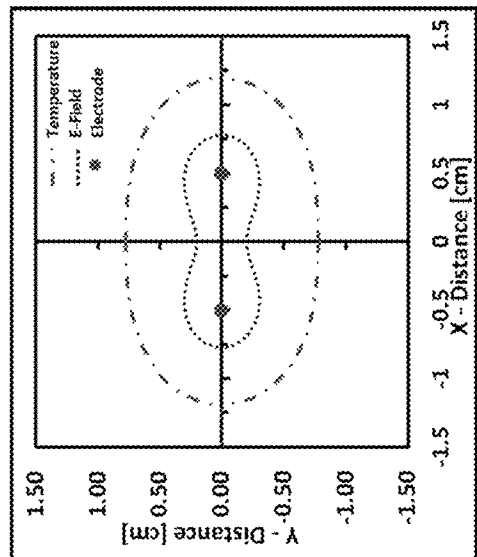


FIG. 32D

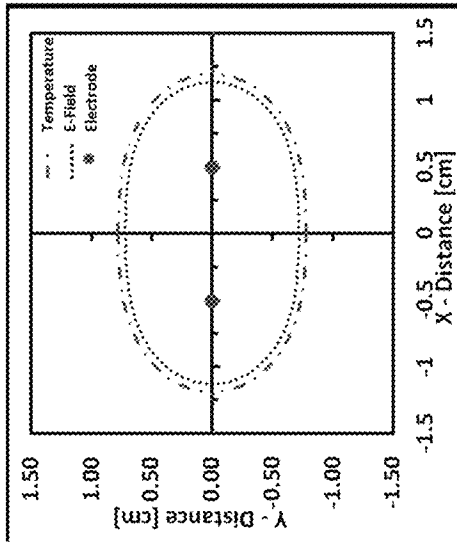


FIG. 33A

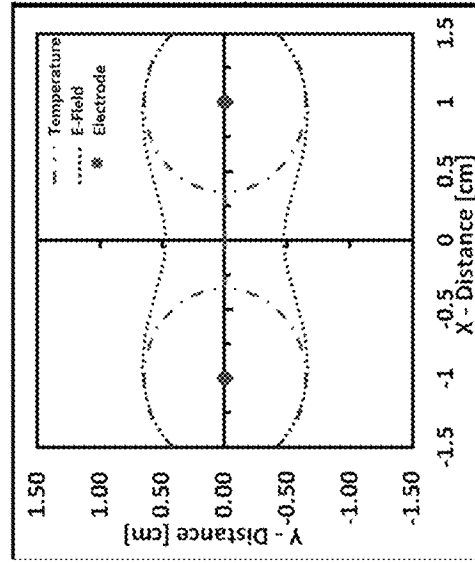


FIG. 33B

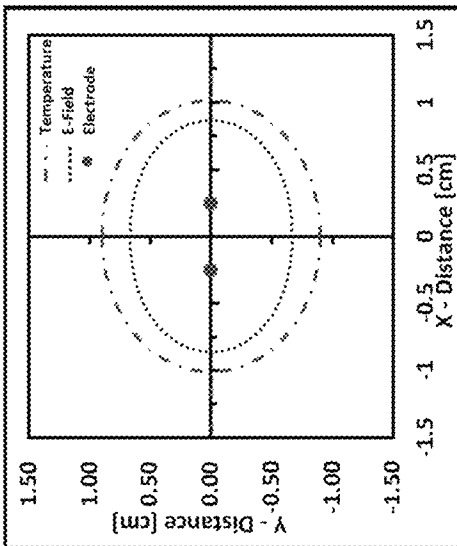


FIG. 33C

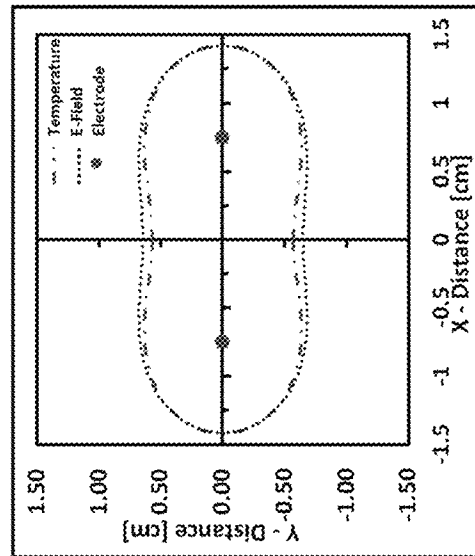


FIG. 33D

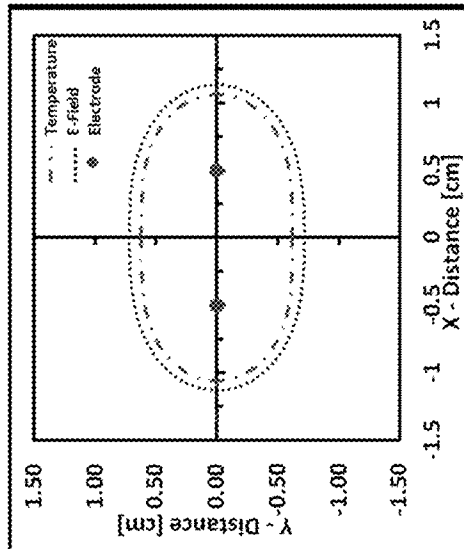


FIG. 34B

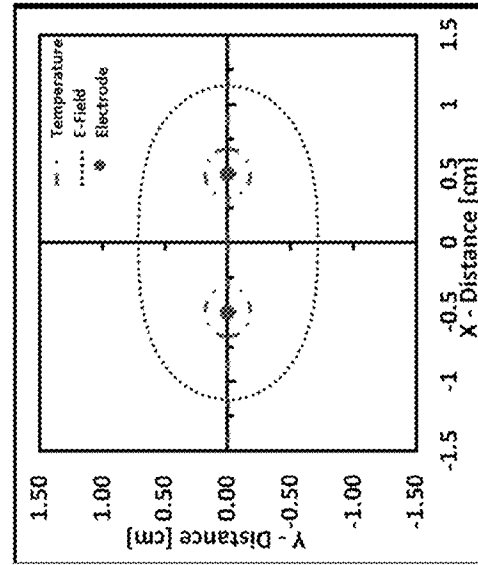


FIG. 34D

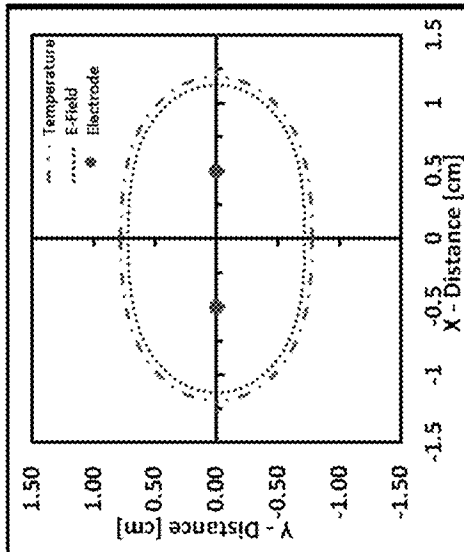


FIG. 34A

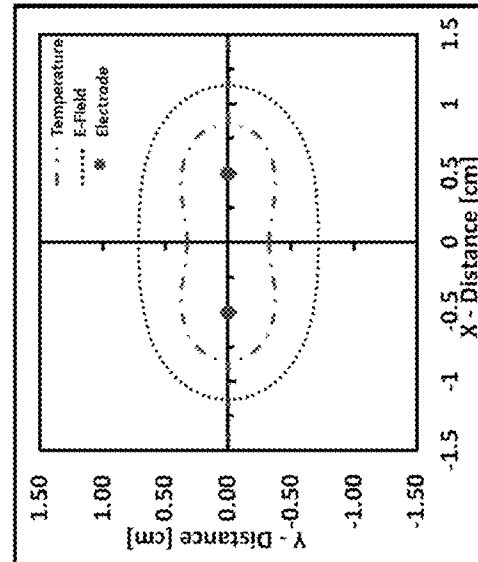


FIG. 34C

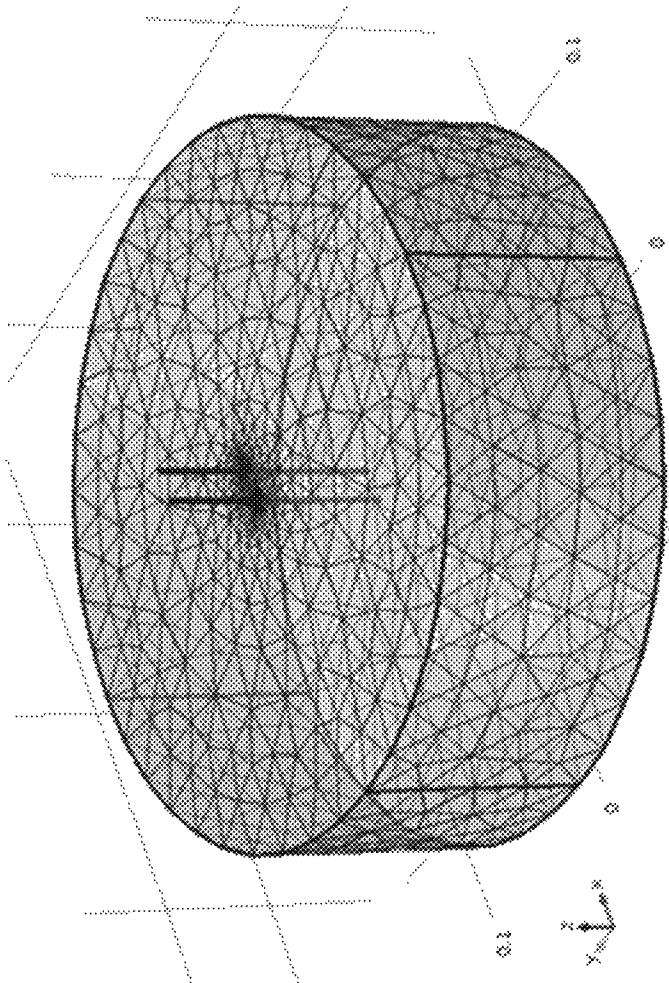


FIG. 35

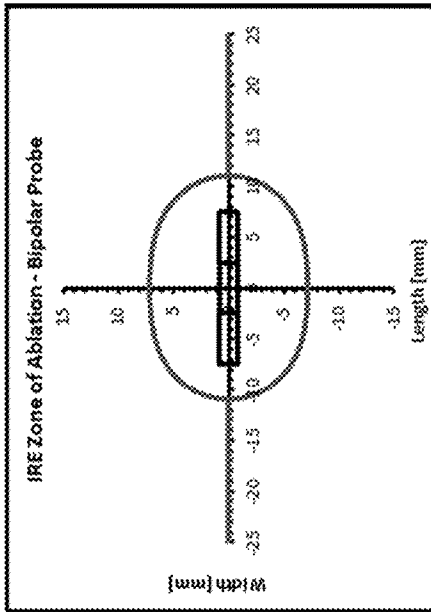


FIG. 36A

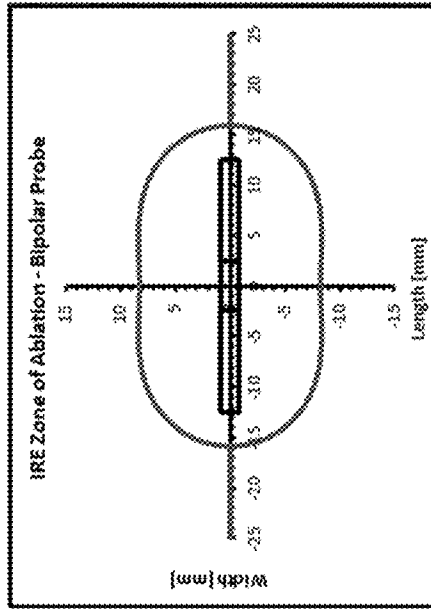


FIG. 36B

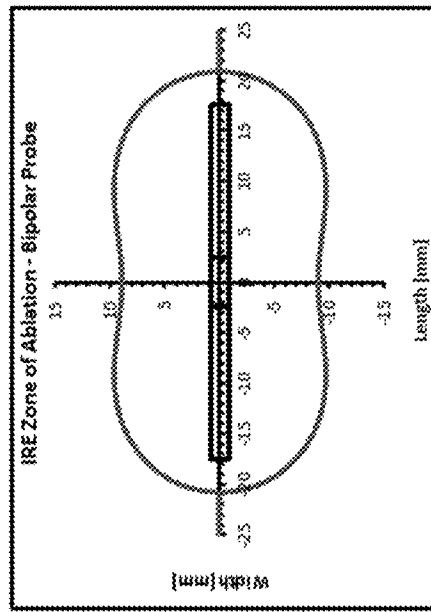


FIG. 36C

Voltage (V)	Electrode (mm)	Insulation (mm)	Run
3000	5.0	5.0	7
3000	10.0	5.0	8
3000	15.0	5.0	9

FIG. 36D

Lesion Statistics (650 V/cm @ 3000 V)				
Run	Width	Length	W/L Ratio	Max field
7	14.3	22.0	0.65	5545.9
8	16.5	31.8	0.52	4686.8
9	17.7	41.8	0.42	4139.9

FIG. 36E

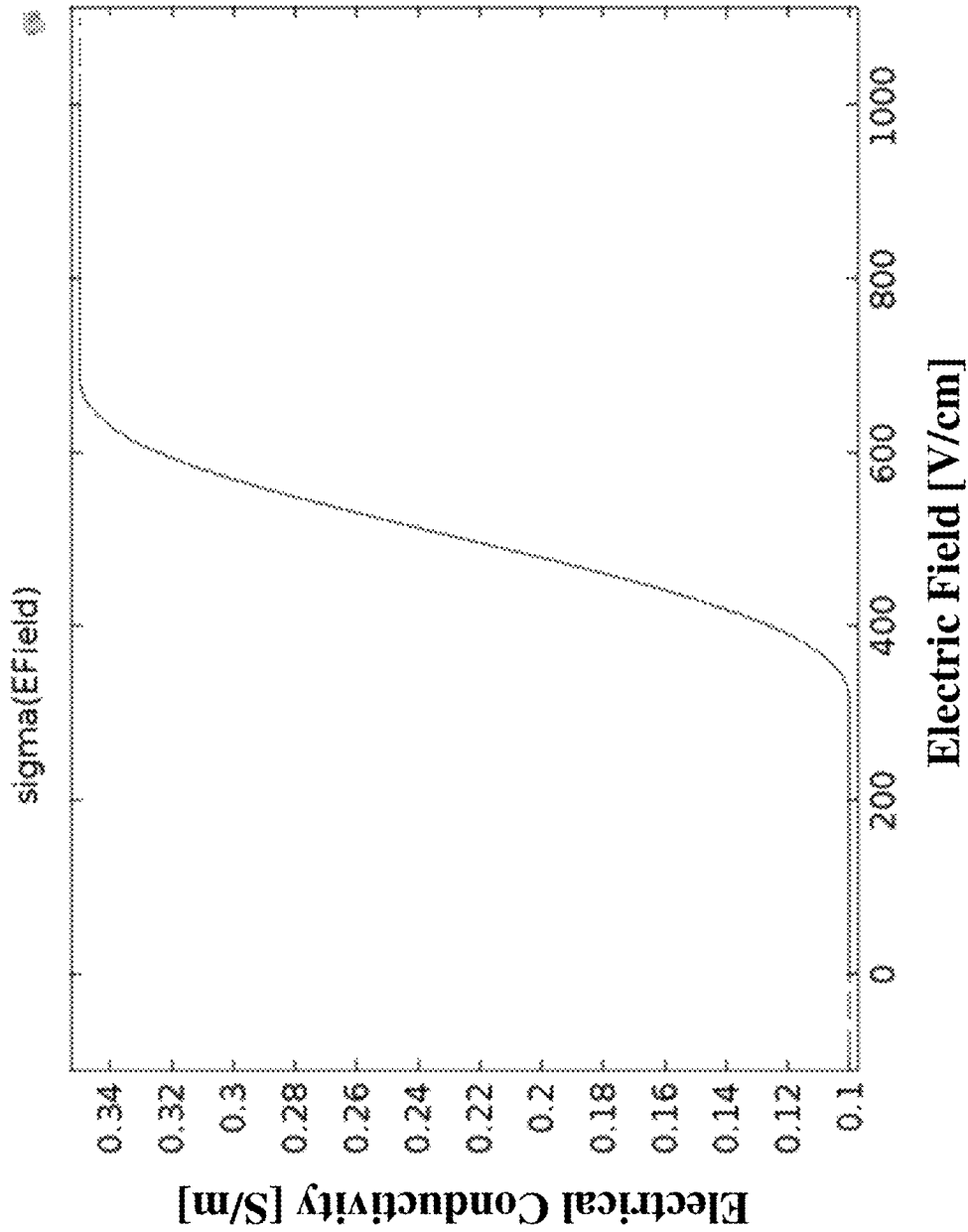


FIG. 37



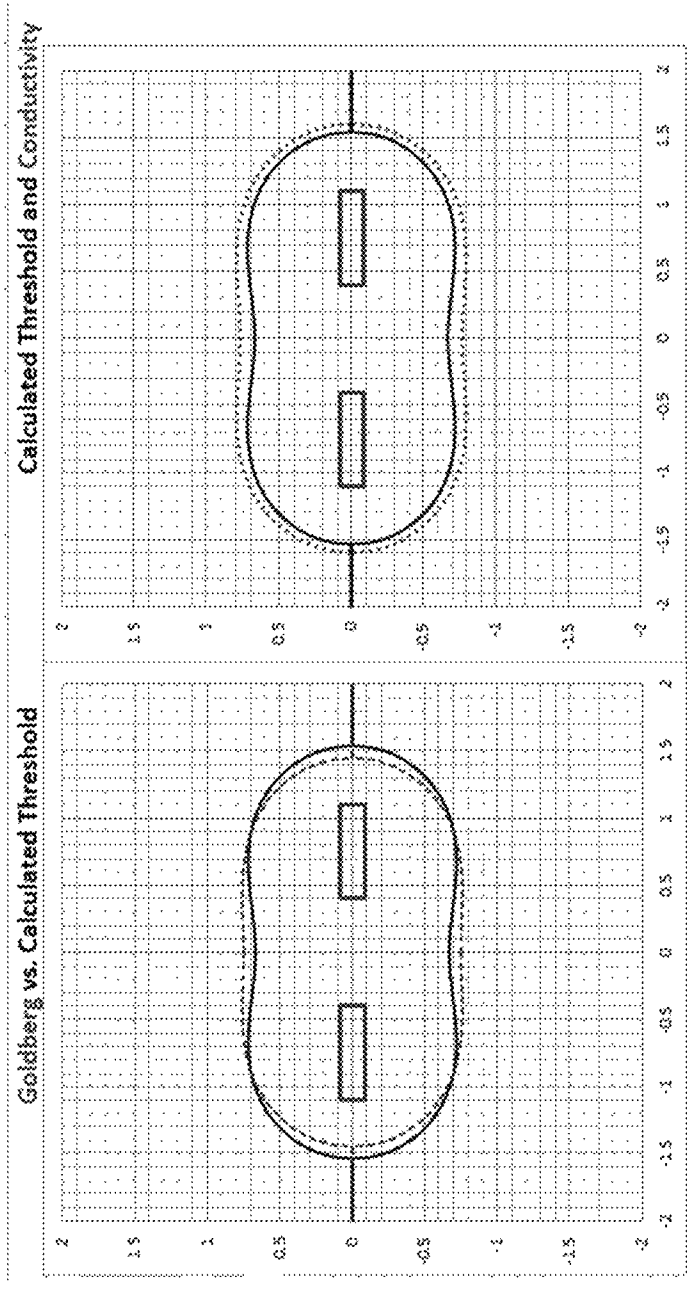


FIG. 38B

FIG. 38A

IRE Threshold [V/cm]	500
Transition Zone	0.2
Conductivity Multiplier	2
Voltage	2700
E-Field [V/cm]	500
Sigma [S/m]	0.1

FIG. 38C

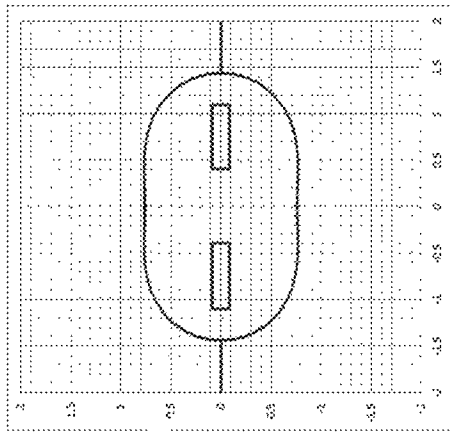


FIG. 39A

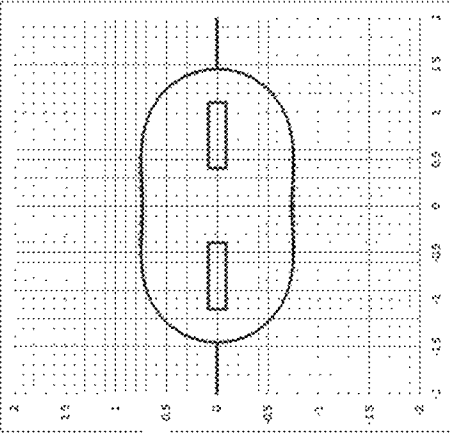


FIG. 39B

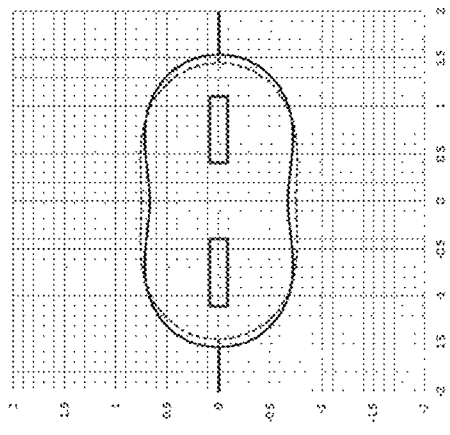


FIG. 39C

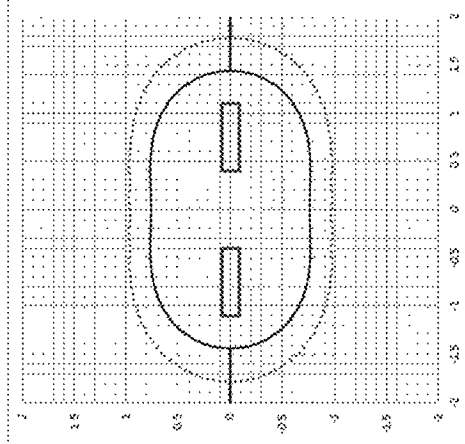


FIG. 39D

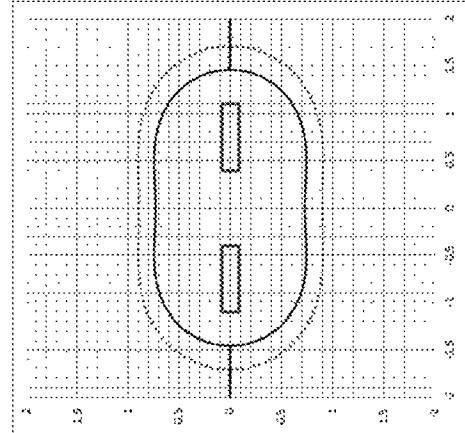


FIG. 39E

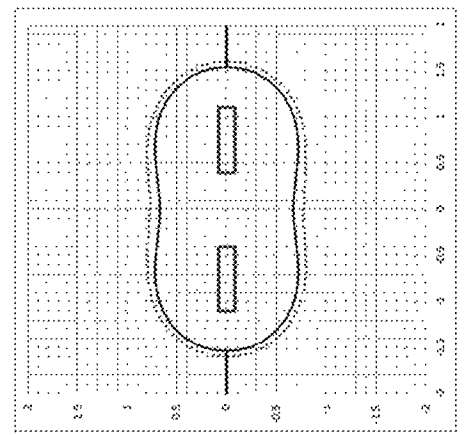


FIG. 39F

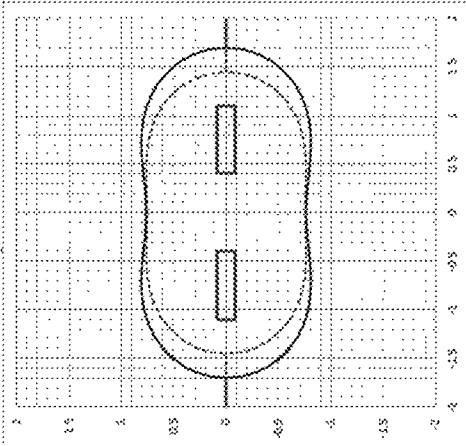


FIG. 40A

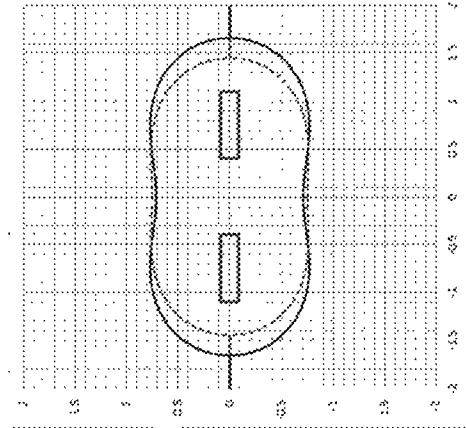


FIG. 40B

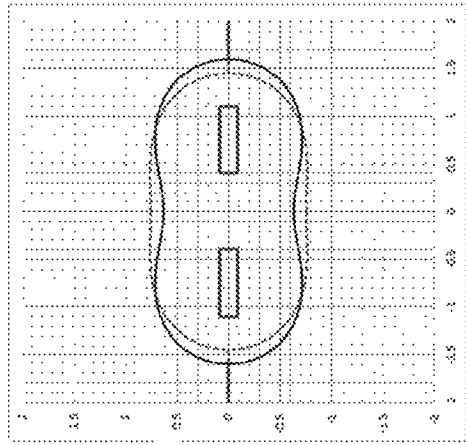


FIG. 40C

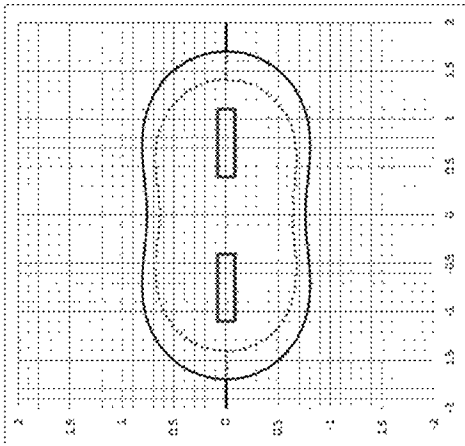


FIG. 40D

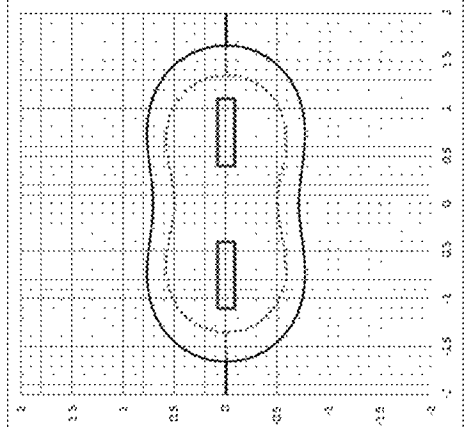


FIG. 40E

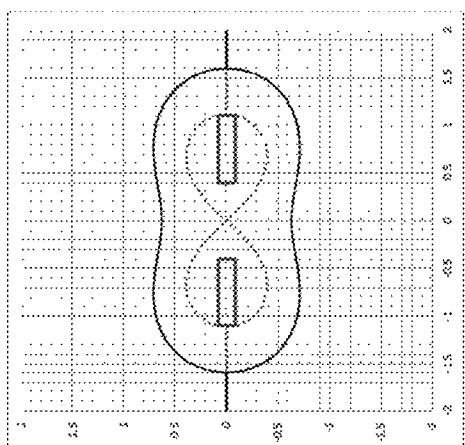


FIG. 40F

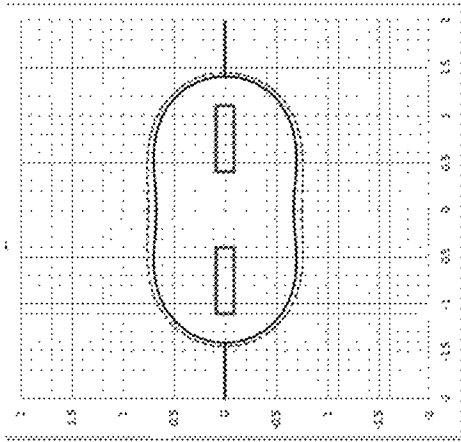


FIG. 41A

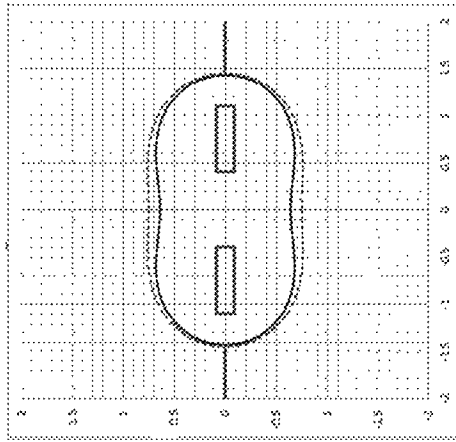


FIG. 41B

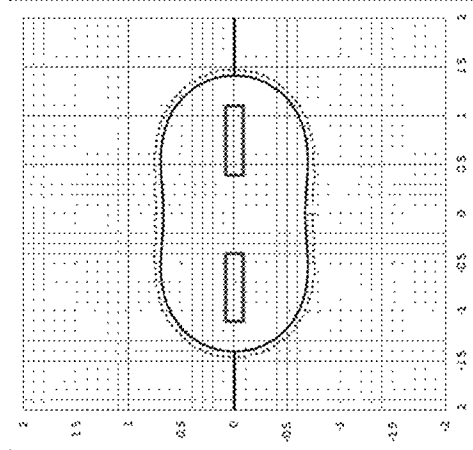


FIG. 41C

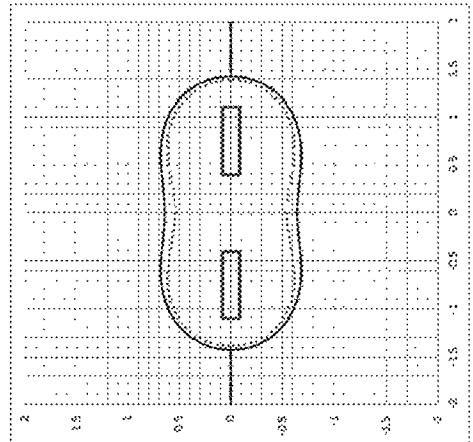


FIG. 41E

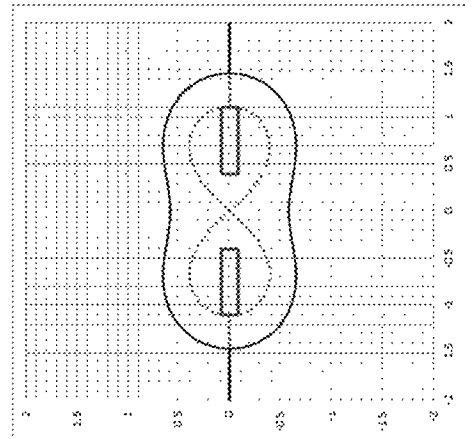


FIG. 41D

FIG. 41F

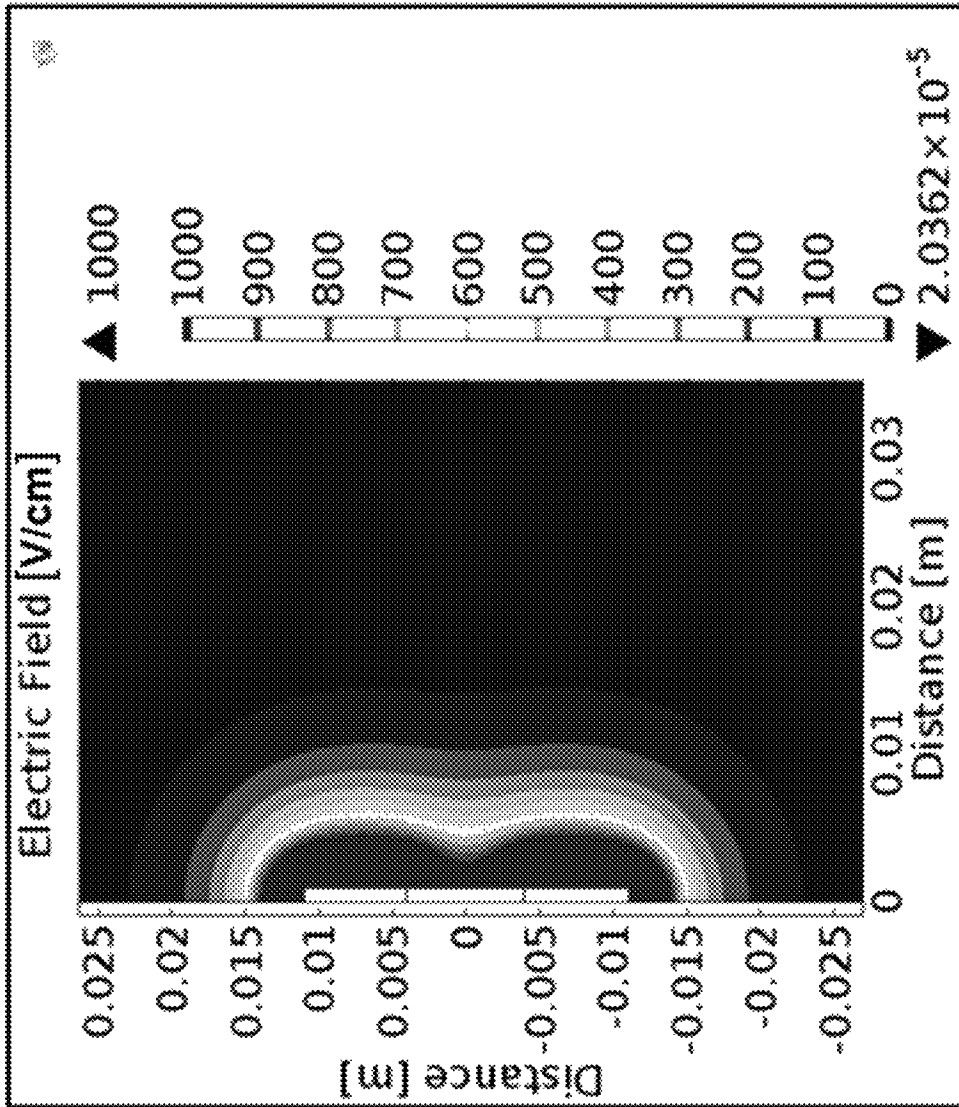
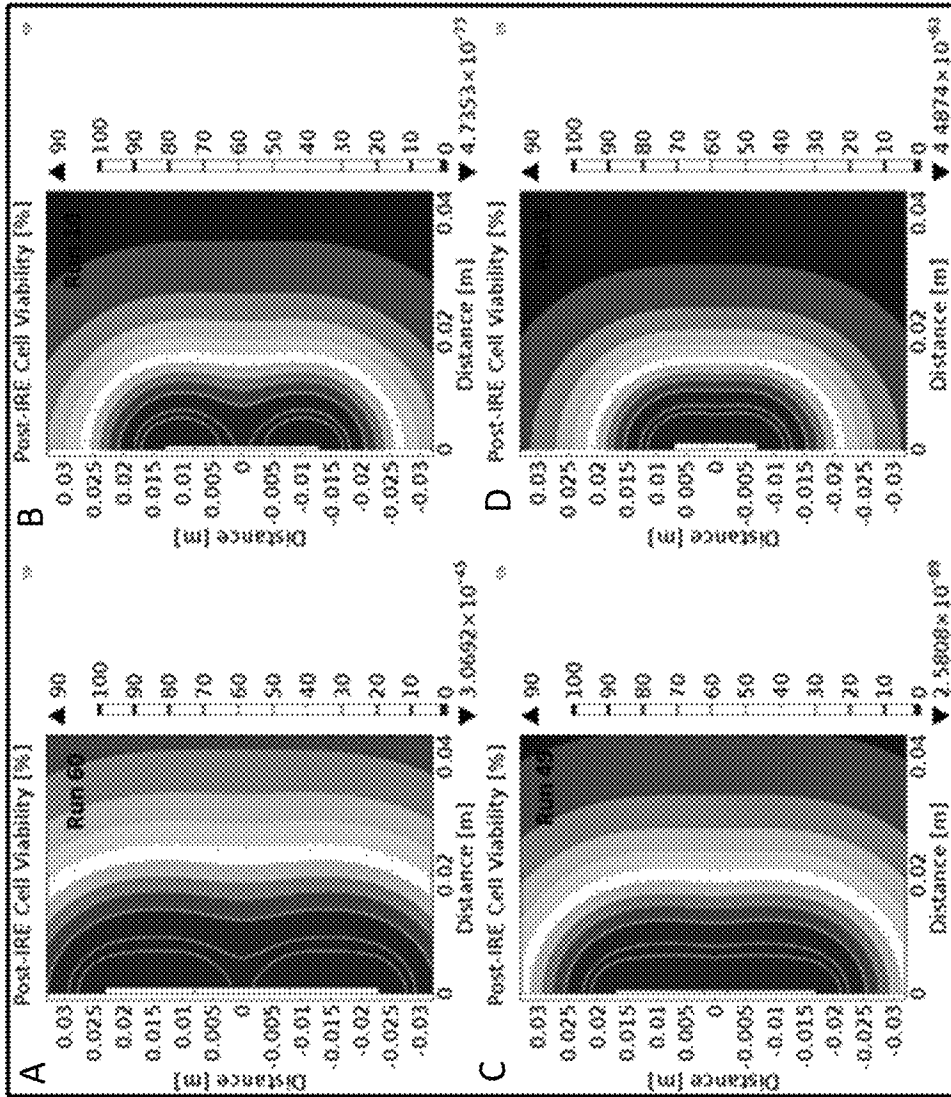


FIG. 42



FIGS. 43A-D

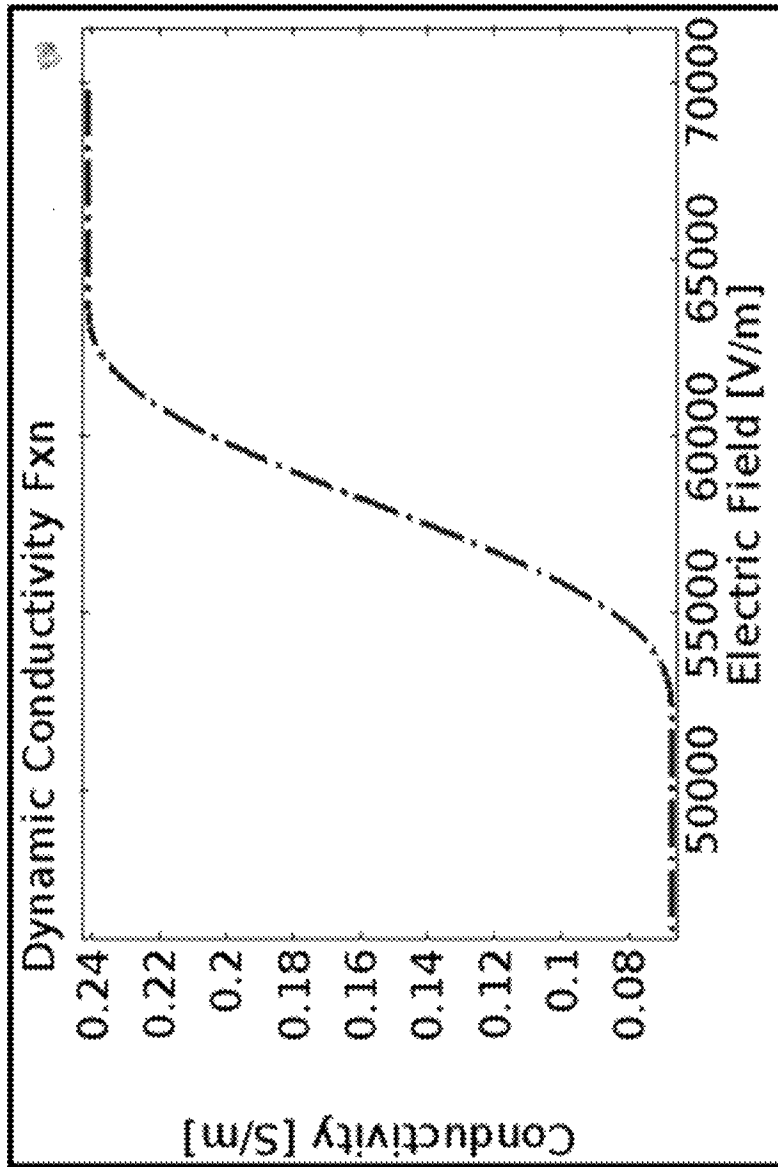


FIG. 44

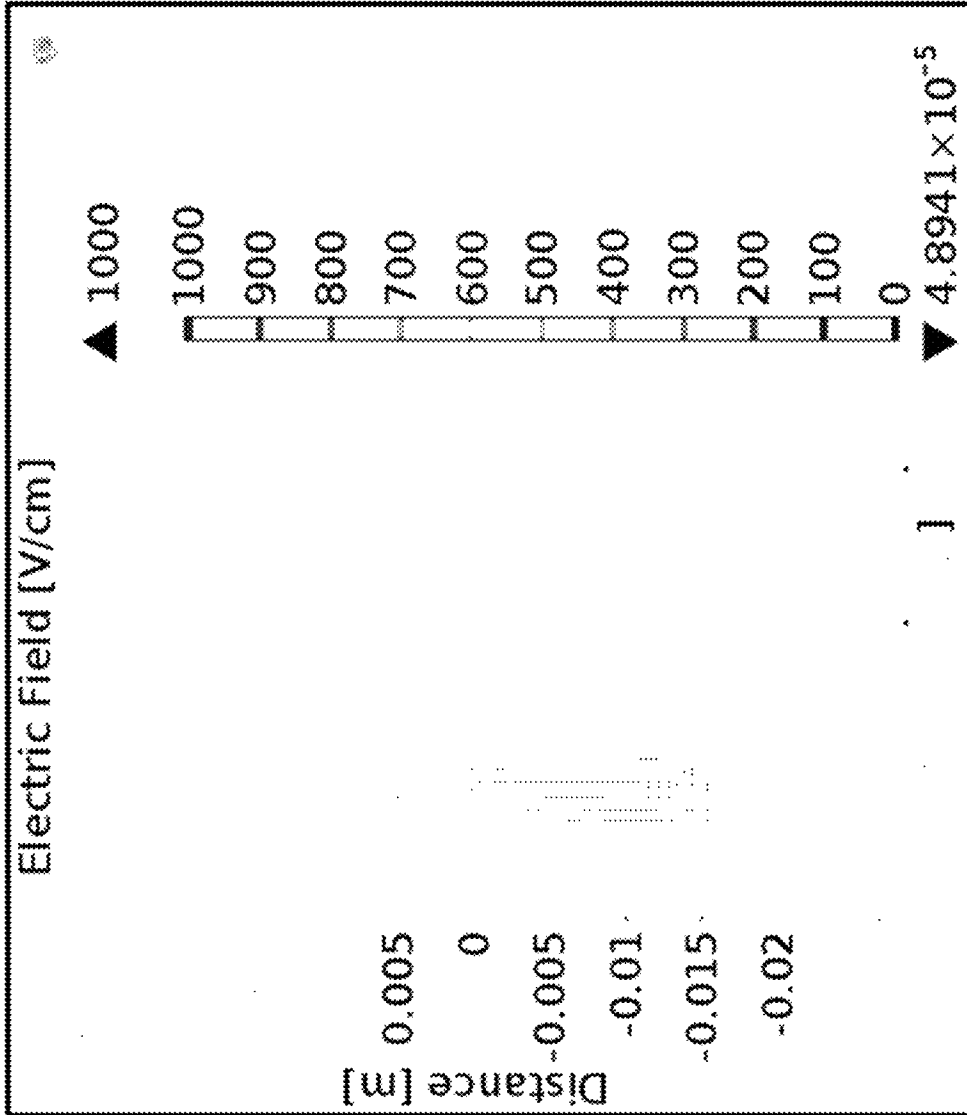
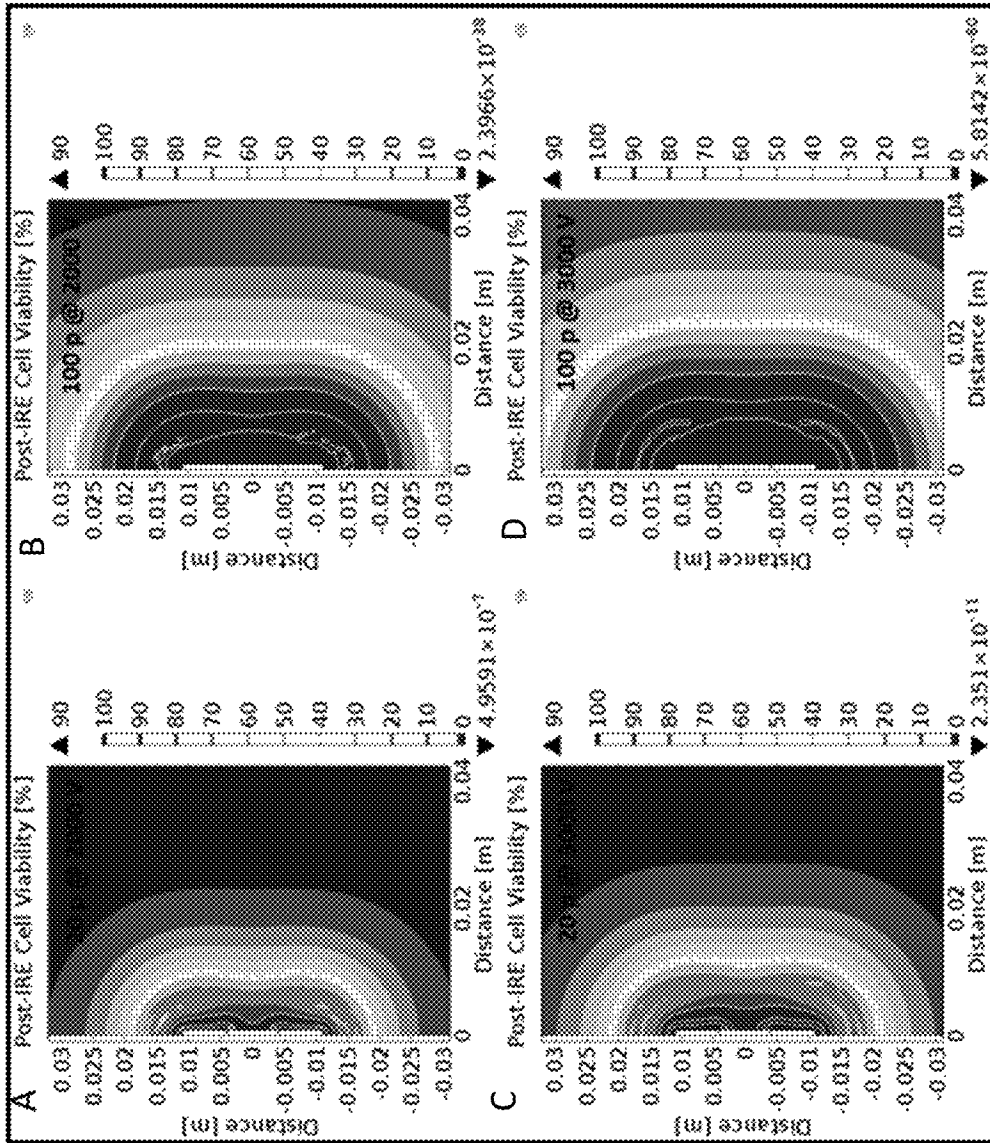


FIG. 45





FIGS. 46A-D

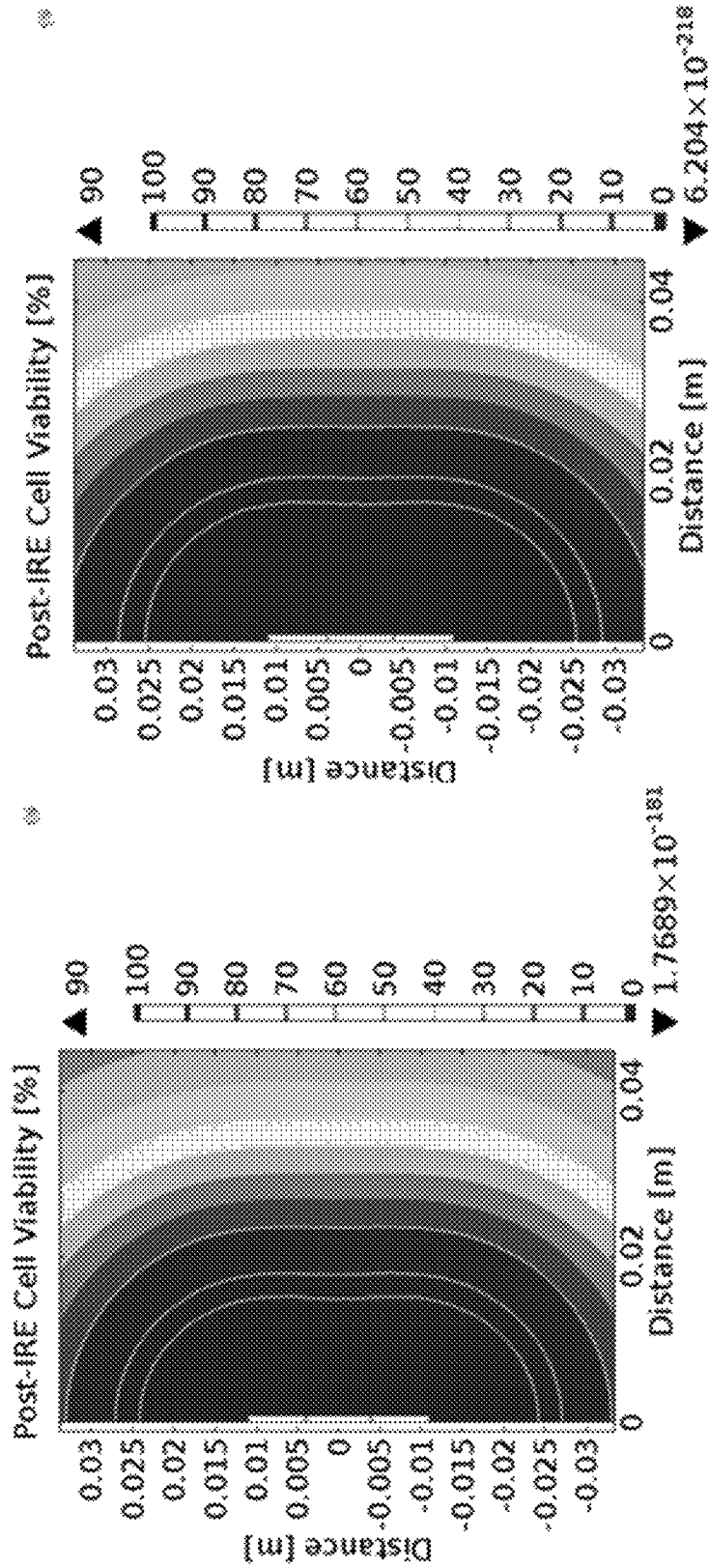


FIG. 47A

FIG. 47B

Parametric study on bipolar electrode configuration as a function of electrode length, separation distance, and diameter in the resulting IRE area and volume.

Number	Electrode Length (mm)	Insulation Length (mm)	Diameter (mm)	IRE Area (cm <sup>2</sup> )	IRE Volume (cm <sup>3</sup> )
1	5.00	4.00	1.27	0.943	1.590
2	5.00	4.00	1.65	1.025	1.880
3	5.00	4.00	2.11	1.120	2.241
4	5.00	8.00	1.27	1.100	1.844
5	5.00	8.00	1.65	1.199	2.204
6	5.00	8.00	2.11	1.309	2.645
7	5.00	12.00	1.27	1.116	1.792
8	5.00	12.00	1.65	1.253	2.208
9	5.00	12.00	2.11	1.395	2.721
10	5.00	16.00	1.27	1.042	1.689
11	5.00	16.00	1.65	1.160	2.058
12	5.00	16.00	2.11	1.283	2.493
13	7.50	4.00	1.27	1.274	2.346
14	7.50	4.00	1.65	1.371	2.738
15	7.50	4.00	2.11	1.483	3.215
16	7.50	8.00	1.27	1.440	2.620
17	7.50	8.00	1.65	1.548	3.066
18	7.50	8.00	2.11	1.680	3.652
19	7.50	12.00	1.27	1.478	2.575
20	7.50	12.00	1.65	1.622	3.097
21	7.50	12.00	2.11	1.777	3.732
22	7.50	16.00	1.27	1.379	2.423
23	7.50	16.00	1.65	1.511	2.886
24	7.50	16.00	2.11	1.660	3.462
25	10.00	4.00	1.27	1.596	3.087
26	10.00	4.00	1.65	1.718	3.628
27	10.00	4.00	2.11	1.850	4.253
28	10.00	8.00	1.27	1.764	3.368
29	10.00	8.00	1.65	1.901	3.973
30	10.00	8.00	2.11	2.037	4.640

FIG. 48A

31	10.00	12.00	1.27	1.809	3.319
32	10.00	12.00	1.65	1.972	3.974
33	10.00	12.00	2.11	2.139	4.733
34	10.00	16.00	1.27	1.694	3.123
35	10.00	16.00	1.65	1.848	3.708
36	10.00	16.00	2.11	2.015	4.386
37	12.50	4.00	1.27	1.922	3.868
38	12.50	4.00	1.65	2.049	4.475
39	12.50	4.00	2.11	2.199	5.228
40	12.50	8.00	1.27	2.087	4.130
41	12.50	8.00	1.65	2.234	4.824
42	12.50	8.00	2.11	2.383	5.611
43	12.50	12.00	1.27	2.132	4.059
44	12.50	12.00	1.65	2.303	4.793
45	12.50	12.00	2.11	2.484	5.680
46	12.50	16.00	1.27	1.998	3.796
47	12.50	16.00	1.65	2.169	4.474
48	12.50	16.00	2.11	2.354	5.297
<b>49</b>	<b>15.00</b>	<b>4.00</b>	<b>1.27</b>	<b>2.242</b>	<b>4.626</b>
50	15.00	4.00	1.65	2.382	5.324
51	15.00	4.00	2.11	2.537	6.164
52	15.00	8.00	1.27	2.399	4.855
53	15.00	8.00	1.65	2.569	5.693
54	15.00	8.00	2.11	2.720	6.533
55	15.00	12.00	1.27	2.444	4.767
56	15.00	12.00	1.65	2.642	5.661
57	15.00	12.00	2.11	2.816	6.580
58	15.00	16.00	1.27	2.317	4.528
59	15.00	16.00	1.65	2.499	5.288
<b>60</b>	<b>15.00</b>	<b>16.00</b>	<b>2.11</b>	<b>2.705</b>	<b>6.232</b>

FIG. 48B

Parametric study on bipolar electrode configuration as a function of applied voltage and pulse number in the resulting IRE area and volume.

Run	Voltage (V)	Pulse Number	IRE Area (cm <sup>2</sup> )	IRE Volume (cm <sup>3</sup> )	IRE Area > 670.1 V/cm (cm <sup>2</sup> )	IRE Volume > 670.1 V/cm (cm <sup>3</sup> )
1	2000	0	0.00000	0.00000	0.96961	1.57498
2	2000	20	0.21547	0.35000	0.96961	1.57498
<b>3</b>	<b>2000</b>	<b>40</b>	<b>0.43094</b>	<b>0.69999</b>	<b>0.96961</b>	<b>1.57498</b>
4	2000	60	0.64641	1.04999	0.96961	1.57498
5	2000	80	0.86188	1.39998	0.96961	1.57498
<b>6</b>	<b>2000</b>	<b>100</b>	<b>1.07734</b>	<b>1.74998</b>	<b>0.96961</b>	<b>1.57498</b>
7	2250	0	0.00000	0.00000	1.12614	2.07358
8	2250	20	0.25025	0.46080	1.12614	2.07358
9	2250	40	0.50051	0.92159	1.12614	2.07358
10	2250	60	0.75076	1.38239	1.12614	2.07358
11	2250	80	1.00101	1.84318	1.12614	2.07358
12	2250	100	1.25127	2.30398	1.12614	2.07358
13	2500	0	0.00000	0.00000	1.23823	2.32864
14	2500	20	0.27516	0.51748	1.23823	2.32864
15	2500	40	0.55032	1.03495	1.23823	2.32864
16	2500	60	0.82549	1.55243	1.23823	2.32864
17	2500	80	1.10065	2.06990	1.23823	2.32864
18	2500	100	1.37581	2.58738	1.23823	2.32864
19	2750	0	0.00000	0.00000	1.34103	2.67481
20	2750	20	0.29801	0.59440	1.34103	2.67481
21	2750	40	0.59601	1.18880	1.34103	2.67481
22	2750	60	0.89402	1.78321	1.34103	2.67481
23	2750	80	1.19203	2.37761	1.34103	2.67481
24	2750	100	1.49003	2.97201	1.34103	2.67481
25	3000	0	0.00000	0.00000	1.49312	3.17126
26	3000	20	0.33180	0.70472	1.49312	3.17126
<b>27</b>	<b>3000</b>	<b>40</b>	<b>0.66361</b>	<b>1.40945</b>	<b>1.49312</b>	<b>3.17126</b>
28	3000	60	0.99541	2.11417	1.49312	3.17126
29	3000	80	1.32722	2.81890	1.49312	3.17126
<b>30</b>	<b>3000</b>	<b>100</b>	<b>1.65902</b>	<b>3.52362</b>	<b>1.49312</b>	<b>3.17126</b>

FIG. 49

Parametric study on bipolar electrode configuration as a function of pulse number in the resulting IRE area and volume with an applied voltage of 3000 V.

Run	Voltage (V)	Pulse Number	IRE Area (cm <sup>2</sup> )	IRE Volume (cm <sup>3</sup> )	IRE Area > 670.1 V/cm (cm <sup>2</sup> )	IRE Volume > 670.1 V/cm (cm <sup>3</sup> )
1	3000	0	0.00000	0.00000	1.49312	3.17126
2	3000	20	0.33180	0.70472	1.49312	3.17126
3	3000	40	0.66361	1.40945	1.49312	3.17126
4	3000	60	0.99541	2.11417	1.49312	3.17126
5	3000	80	1.32722	2.81890	1.49312	3.17126
6	3000	100	1.65902	3.52362	1.49312	3.17126
7	3000	120	1.99083	4.22835	1.49312	3.17126
8	3000	140	2.32263	4.93307	1.49312	3.17126
9	3000	160	2.65444	5.63780	1.49312	3.17126
10	3000	180	2.98624	6.34252	1.49312	3.17126
11	3000	200	3.31804	7.04724	1.49312	3.17126
12	3000	220	3.64985	7.75197	1.49312	3.17126
13	3000	240	3.98165	8.45669	1.49312	3.17126
14	3000	260	4.31346	9.16142	1.49312	3.17126
15	3000	280	4.64526	9.86614	1.49312	3.17126
<b>16</b>	<b>3000</b>	<b>300</b>	<b>4.97707</b>	<b>10.57087</b>	<b>1.49312</b>	<b>3.17126</b>
17	3000	320	5.30887	11.27559	1.49312	3.17126
18	3000	340	5.64068	11.98032	1.49312	3.17126
<b>19</b>	<b>3000</b>	<b>360</b>	<b>5.97248</b>	<b>12.68504</b>	<b>1.49312</b>	<b>3.17126</b>

FIG. 50

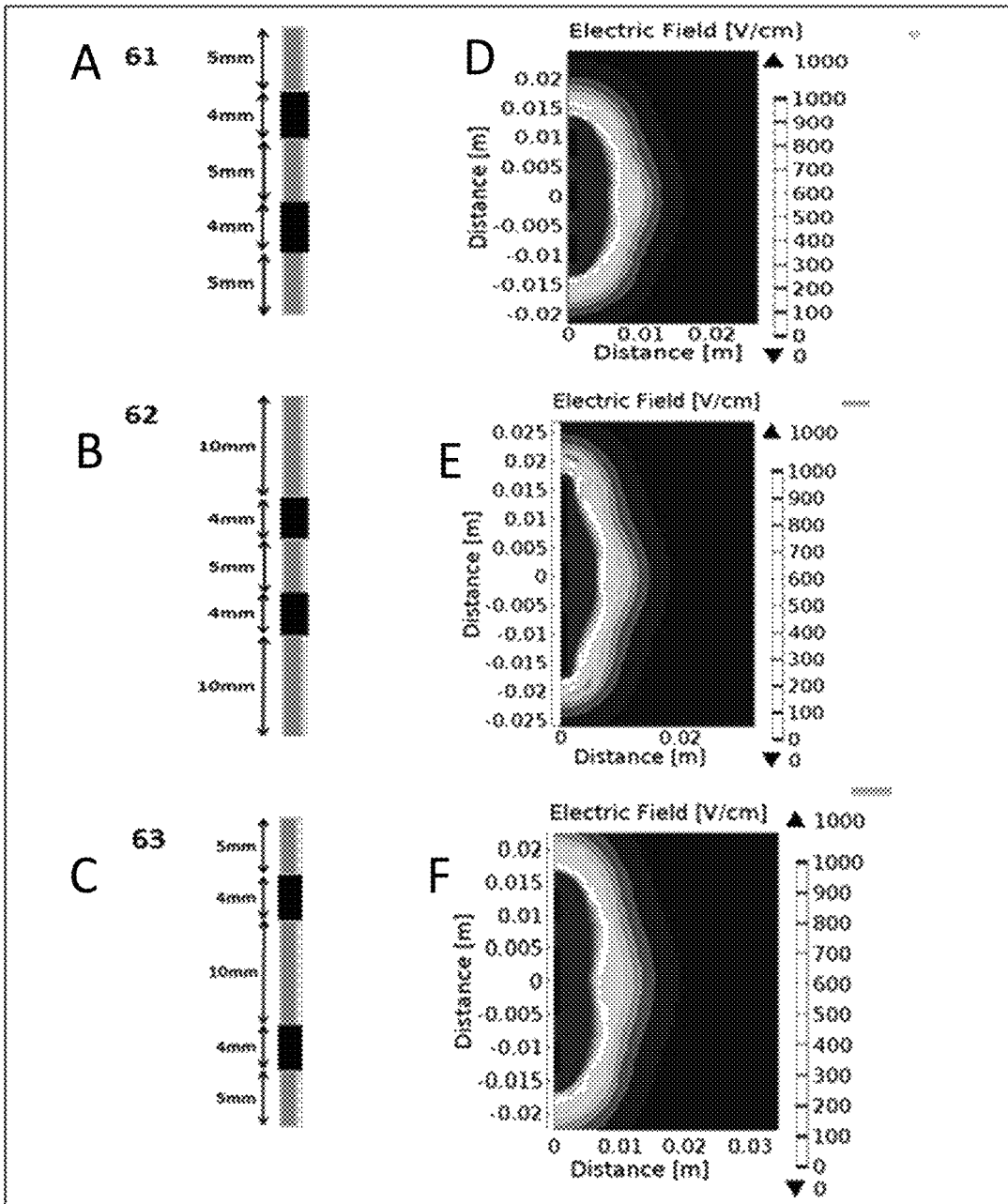


FIG. 51A-F

**SYSTEM AND METHOD FOR ESTIMATING  
TISSUE HEATING OF A TARGET ABLATION  
ZONE FOR ELECTRICAL-ENERGY BASED  
THERAPIES**

CROSS-REFERENCE TO RELATED  
APPLICATIONS

The present application is a Continuation-in-Part (CIP) of U.S. patent application Ser. No. 14/012,832, filed on Aug. 28, 2013, which published as U.S. Pat. No. 9,283,051,832, which CIP relies on and claims the benefit of the filing date of U.S. Provisional Application No. 61/694,144, filed on Aug. 28, 2012. Application Ser. No. 14/012,832 is a CIP of U.S. application Ser. No. 12/491,151, filed on Jun. 24, 2009, which published as U.S. Pat. No. 8,992,517, which relies on and claims the benefit of the filing dates of U.S. Provisional Patent Application Nos. 61/171,564, filed on Apr. 22, 2009, 61/167,997, filed on Apr. 9, 2009, and 61/075,216, filed on Jun. 24, 2008. Application Ser. No. 12/491,151 is also a CIP of U.S. patent application Ser. No. 12/432,295, filed on Apr. 29, 2009, now U.S. Pat. No. 9,598,691, which relies on and claims the benefit of the filing date of U.S. Provisional Patent Application No. 61/125,840, filed on Apr. 29, 2008. The present application also relies on and claims priority to and the benefit of the filing date of U.S. Provisional Application No. 61/910,655, filed Dec. 2, 2013. The disclosures of these patent applications are hereby incorporated by reference herein in their entireties.

FIELD OF THE INVENTION

The present invention is related to medical therapies involving the administering of electrical treatment energy. More particularly, embodiments of the present invention provide systems and methods for modeling and providing a graphical representation of tissue heating and electric field for a medical treatment device that applies electrical treatment energy through a plurality of electrodes defining a target treatment area. Embodiments of the present invention also provide systems and methods providing a graphical representation of a target ablation zone based on one or more electrical conductivity parameters that are specific for the tissue to be treated.

DESCRIPTION OF RELATED ART

Electroporation-based therapies (EBTs) are clinical procedures that utilize pulsed electric fields to induce nanoscale defects in cell membranes. Typically, pulses are applied through minimally invasive needle electrodes inserted directly into the target tissue, and the pulse parameters are tuned to create either reversible or irreversible defects. Reversible electroporation facilitates the transport of molecules into cells without directly compromising cell viability. This has shown great promise for treating cancer when used in combination with chemotherapeutic agents or plasmid DNA (M. Marty et al., "Electrochemotherapy—An easy, highly effective and safe treatment of cutaneous and subcutaneous metastases: Results of ESOPE (European Standard Operating Procedures of Electrochemotherapy) study," *European Journal of Cancer Supplements*, 4, 3-13, 2006; A. I. Daud et al., "Phase I Trial of Interleukin-12 Plasmid Electroporation in Patients With Metastatic Melanoma," *Journal of Clinical Oncology*, 26, 5896-5903, Dec. 20, 2008). Alternatively, irreversible electroporation (IRE) has been recognized as a non-thermal tissue ablation modal-

ity that produces a tissue lesion, which is visible in real-time on multiple imaging platforms (R. V. Davalos, L. M. Mir, and B. Rubinsky, "Tissue ablation with irreversible electroporation," *Ann Biomed Eng*, 33, 223-31, February 2005; R. V. Davalos, D. M. Otten, L. M. Mir, and B. Rubinsky, "Electrical impedance tomography for imaging tissue electroporation," *IEEE Transactions on Biomedical Engineering*, 51, 761-767, 2004; L. Appelbaum, E. Ben-David, J. Sosna, Y. Nissenbaum, and S. N. Goldberg, "US Findings after Irreversible Electroporation Ablation: Radiologic-Pathologic Correlation," *Radiology*, 262, 117-125, Jan. 1, 2012). Because the mechanism of cell death does not rely on thermal processes, IRE spares major nerve and blood vessel architecture and is not subject to local heat sink effects when using a specific protocol that does not exceed the thermal damage threshold. (B. Al-Sakere, F. Andre, C. Bernat, E. Connault, P. Opolon, R. V. Davalos, B. Rubinsky, and L. M. Mir, "Tumor ablation with irreversible electroporation," *PLoS ONE*, 2, e1135, 2007). These unique benefits have translated to the successful treatment of several surgically "inoperable" tumors (K. R. Thomson et al., "Investigation of the safety of irreversible electroporation in humans," *J Vasc Intery Radiol*, 22, 611-21, May 2011; R. E. Neal II et al., "A Case Report on the Successful Treatment of a Large Soft-Tissue Sarcoma with Irreversible Electroporation," *Journal of Clinical Oncology*, 29, 1-6, 2011; P. A. Garcia et al., "Non-thermal irreversible electroporation (N-TIRE) and adjuvant fractionated radiotherapeutic multimodal therapy for intracranial malignant glioma in a canine patient," *Technol Cancer Res Treat*, 10, 73-83, 2011).

In EBTs, the electric field distribution is the primary factor for dictating defect formation and the resulting volume of treated tissue (J. F. Edd and R. V. Davalos, "Mathematical modeling of irreversible electroporation for treatment planning," *Technology in Cancer Research and Treatment*, 6, 275-286, 2007 ("Edd and Davalos, 2007"); D. Miklavcic, D. Semrov, H. Mekid, and L. M. Mir, "A validated model of in vivo electric field distribution in tissues for electrochemotherapy and for DNA electrotransfer for gene therapy," *Biochimica et Biophysica Acta*, 1523, 73-83, 2000). The electric field is influenced by both the geometry and positioning of the electrodes as well as the dielectric tissue properties. Because the pulse duration is typically much longer than the pulse rise/fall time, static solutions of the Laplace's equation incorporating only electric conductivity are sufficient for predicting the electric field distribution. In tissues with uniform conductivity, solutions can be obtained analytically for various needle electrode configurations if the exposure length is much larger than the separation distance (S. Corovic, M. Pavlin, and D. Miklavcic, "Analytical and numerical quantification and comparison of the local electric field in the tissue for different electrode configurations," *Biomed Eng Online*, 6, 2007; R. Neal II et al., "Experimental Characterization and Numerical Modeling of Tissue Electrical Conductivity during Pulsed Electric Fields for Irreversible Electroporation Treatment Planning," *Biomedical Engineering, IEEE Transactions on*, PP, 1-1, 2012 ("Neal et al., 2012")). This is not often the case in clinical applications where aberrant masses with a diameter on the order of 1 cm are treated with an electrode exposure length of similar dimensions. Additionally, altered membrane permeability due to electroporation influences the tissue conductivity in a non-linear manner. Therefore numerical techniques may be used to account for any electrode configuration and incorporate a tissue-specific function relating the electrical conductivity to the electric field distribution (i.e. extent of electroporation).



Conventional devices for delivering therapeutic energy such as electrical pulses to tissue include a handle and one or more electrodes coupled to the handle. Each electrode is connected to an electrical power source. The power source allows the electrodes to deliver the therapeutic energy to a targeted tissue, thereby causing ablation of the tissue.

Once a target treatment area is located within a patient, the electrodes of the device are placed in such a way as to create a treatment zone that surrounds the treatment target area. In some cases, each electrode is placed by hand into a patient to create a treatment zone that surrounds a lesion. The medical professional who is placing the electrodes typically watches an imaging monitor while placing the electrodes to approximate the most efficient and accurate placement.

However, if the electrodes are placed by hand in this fashion, it is very difficult to predict whether the locations selected will ablate the entire treatment target area because the treatment region defined by the electrodes vary greatly depending on such parameters as the electric field density, the voltage level of the pulses being applied, size of the electrode and the type of tissue being treated. Further, it is often difficult or sometimes not possible to place the electrodes in the correct location of the tissue to be ablated because the placement involves human error and avoidance of obstructions such as nerves, blood vessels and the like.

Conventionally, to assist the medical professional in visualizing a treatment region defined by the electrodes, an estimated treatment region is generated using a numerical model analysis such as complex finite element analysis. One problem with such a method is that even a modest two dimensional treatment region may take at least 30 minutes to several hours to complete even in a relatively fast personal computer. This means that it would be virtually impossible to try to obtain on a real time basis different treatment regions based on different electrode positions.

In IRE treatments, the electric field distribution is the primary factor for dictating defect formation and the resulting volume of treated tissue (See J. F. Edd and R. V. Davalos, "Mathematical modeling of irreversible electroporation for treatment planning," *Technol Cancer Res Treat*, vol. 6, pp. 275-286, 2007; D. Sel, et al., "Sequential finite element model of tissue electroporation," *IEEE Trans Biomed Eng*, vol. 52, pp. 816-27, May 2005). The electric field is influenced by both the geometry and positioning of the electrodes as well as the dielectric tissue properties. The application of an electric field across any conductive media will result in some degree of resistive losses in which energy is dissipated as heat. Though cell death in IRE is attributed to non-thermal mechanisms, it is possible to inadvertently elevate tissue temperatures above thermal damage thresholds if parameters are not chosen carefully. Since a major advantage of IRE is the ablation of tissue without deleterious thermal effects and the therapy is often applied in regions which cannot clinically sustain thermal injury, it is important to identify safe operating parameters. Transient heating of tissue in proximity to the electrode can result in the denaturing of the extracellular matrix, scar formation, or damage to local blood vessels and nerves. To avoid these effects, it is important to understand the extent and geometry of tissue heating.

Therefore, it would be desirable to provide an improved system and method to predict a treatment region that avoids electrical and thermal overexposure and damage in order to determine safe and effective pulse protocols for administering electrical energy based therapies, such IRE.

#### SUMMARY OF THE INVENTION

In one embodiment, the invention provides a system for treating a tissue, which system applies electrical treatment

energy through one or more electrodes, such as a plurality of electrodes, defining a target treatment area of the tissue. The system comprises a memory, a display device, a processor coupled to the memory and the display device, and a treatment planning module stored in the memory and executable by the processor. In one embodiment, the treatment planning module is adapted to generate an estimated heat distribution and/or electrical field distribution in the display device based on one or more parameters for an electrical energy based protocol, such as an irreversible electroporation (IRE) protocol. In another embodiment, the treatment planning module is adapted to generate an estimated target ablation zone based on a combination of one or more parameters for an electrical energy based protocol, such as an IRE-based protocol, and one or more tissue-specific conductivity parameters.

In another embodiment, the invention provides a method of treating a tissue with a medical treatment device that applies electrical treatment energy through a one or more or a plurality of electrodes defining a target treatment area of the tissue and comprises a display device. The method may be executed partially or completely using the system of the invention. In a specific embodiment, one or more steps are executed through the treatment planning module.

In embodiments, the treatment planning module can be used to determine a temperature distribution to determine tissue heating at or around a target ablation zone prior to or during treatment. The treatment planning module can be used to graphically display contour lines which represent a specific temperature of tissue heating. In one embodiment, the treatment planning module estimates the temperature rise within tissue due to Joule heating effects, and plots a contour line according to a temperature specified by a user. Further, the treatment planning module may further plot a contour line representing an electric field intensity such that temperature and electric field intensity can be correlated. The treatment planning module may plot the temperature distribution and electric field distribution for a bipolar and single needle electrodes. This capability may allow a user (e.g. treating physician) to determine heating to surrounding tissues during treatment planning and adjust parameters to prevent thermal damage to critical surrounding structures such as nerves and blood vessels. In one embodiment, the contour lines are Cassini oval approximations performed according to the equations and procedure in Example 7.

In embodiments, the treatment planning module can be used to provide the electric field distributions using different configurations of bipolar probes and include the dynamic change in electrical conductivity from the non-electroporated baseline tissue electrical conductivity. The treatment planning module may plot contour lines representing electric field distributions based on a specific combination of electrode length, separation distance, and applied voltage. The treatment planning module may incorporate the dynamic change in electrical conductivity from the baseline during treatment to account for treatment-related changes in conductivity for particular tissues such as liver, kidney, brain, etc. This capability may allow the treating physician to determine electric field distributions and zones of ablation based on the capacity for a specific target tissue to change in conductivity during treatment. In one embodiment, the contour lines are Cassini oval approximations performed according to the equations and procedure in Example 7.

In embodiments, the treatment planning module can be based on a parametric study of the dynamic conductivity curve so that variables related to the dynamic conductivity could be used to fit tissue specific behavior. In embodiments,

the treatment planning module may provide input for one or more electrical conductivity parameters such as the baseline (e.g., non-electroporated) conductivity, change in conductivity, the transition zone (how rapidly the conductivity increases), the electric field at which the change in conductivity occurs, and the electric field at which irreversible electroporation occurs. These parameters may be experimentally derived for different tissues and stored in a database. This capability may allow the treating physician to account for different conductivity parameters as they apply to different target tissues when designing a treatment protocol. Thus, when considering a specific tissue, the treating physician may optimize the calculation of an ablation zone for that tissue by inputting one or more of the tissue-specific conductivity parameters for the tissue of interest.

**BRIEF DESCRIPTION OF THE DRAWINGS** The accompanying drawings illustrate certain aspects of embodiments of the present invention, and should not be used to limit or define the invention. Together with the written description the drawings serve to explain certain principles of the invention.

FIG. 1 is a schematic diagram of a representative system of the invention.

FIG. 2 is a schematic diagram of a representative treatment control computer of the invention.

FIG. 3 is schematic diagram illustrating details of the generator shown in the system of FIG. 1, including elements for detecting an over-current condition.

FIG. 4 is a schematic diagram showing IRE zones of ablation nomenclature (see E. Ben-David, et al., "Characterization of Irreversible Electroporation Ablation in In Vivo Porcine Liver," Am J Roentgenol, vol. 198, pp. W62-W68, January 2012).

FIG. 5 is a graph of the asymmetrical Gompertz function showing tissue electric conductivity as a function of electric field.

FIG. 6 is a graph showing a representative 3D plot of current [A] as a function of  $Z$  ( $\sigma_{max}/\sigma_0$ ) and voltage-to-distance ratio ( $W$ ) for a separation distance of 1.5 cm and an electrode exposure length of 2.0 cm as used by Ben-David et al.

FIGS. 7A and 7B are graphs showing representative contour plots of current [A] as a function of electrode exposure and separation distance using 1500 V/cm for  $Z=1$  (FIG. 7A) and  $Z=4$  (FIG. 7B).

FIGS. 8A and 8B are tables showing Whole Model Parameter Estimates and Effect Tests, respectively.

FIG. 8C is a graph showing a plot of Actual Current vs. Predicted Current.

FIGS. 9A-9E are graphs showing the representative (15 mm gap) correlation between current vs. exposure length and electrode radius for maximum electrical conductivities (1x-6x, respectively).

FIG. 10A is a table showing experimental validation of the code for determining the tissue/potato dynamic from in vitro measurements, referred to as potato experiment #1.

FIG. 10B is a table showing experimental validation of the code for determining the tissue/potato dynamic from in vitro measurements, referred to as potato experiment #2.

FIGS. 11A and 11B are graphs plotting residual current versus data point for analytical shape factor (FIG. 11A) and statistical (numerical) non-linear conductivity (FIG. 11B).

FIGS. 12A-12C are graphs showing representative contour plots of the electric field strength at 1.0 cm from the origin using an edge-to-edge voltage-to-distance ratio of

1500 V/cm assuming  $z=1$ , wherein FIG. 12A is a plot of the x-direction, FIG. 12B is a plot of the y-direction, and FIG. 12C is a plot of the z-direction.

FIGS. 13A-13C are 3D plots representing zones of ablation for a 1500 V/cm ratio, electrode exposure of 2 cm, and electrode separation of 1.5 cm, at respectively a 1000 V/cm IRE threshold (FIG. 13A), 750 V/cm IRE threshold (FIG. 13B), and 500 V/cm IRE threshold (FIG. 13C) using the equation for an ellipsoid.

FIG. 14A is a schematic diagram showing an experimental setup of an embodiment of the invention.

FIG. 14B is a schematic diagram showing dimension labeling conventions.

FIG. 14C is a waveform showing 50 V pre-pulse electrical current at 1 cm separation, grid=0.25 A, where the lack of rise in intrapulse conductivity suggests no significant membrane electroporation during pre-pulse delivery.

FIG. 14D is a waveform showing electrical current for pulses 40-50 of 1750 V at 1 cm separation, grid=5 A, where progressive intrapulse current rise suggests continued conductivity increase and electroporation.

FIGS. 15A and 15B are electric field [V/cm] isocontours for non-electroporated tissue (FIG. 15A) and electroporated tissue (FIG. 15B) maps assuming a maximum conductivity to baseline conductivity ratio of 7.0x.

FIGS. 16A and 16B are representative Cassini Oval shapes when varying the 'a=0.5 (red), 0.6 (orange), 0.7 (green), 0.8 (blue), 0.9 (purple), 1.0 (black)' or 'b=1.0 (red), 1.05 (orange), 1.1 (green), 1.15 (blue), 1.2 (purple), 1.25 (black)' parameters individually. Note: If  $a>1.0$  or  $b<1.0$  the lemniscate of Bernoulli (the point where the two ellipses first connect ( $a=b=1$ ) forming " $\infty$ ") disconnects forming non-contiguous shapes.

FIG. 17 is a graph showing NonlinearModelFit results for the 'a' and 'b' parameters used to generate the Cassini curves that represent the experimental IRE zones of ablation in porcine liver.

FIG. 18 shows Cassini curves from a ninety 100- $\mu$ s pulse IRE treatment that represent the average zone of ablation (blue dashed), +SD (red solid), and -SD (black solid) according to  $a=0.821\pm 0.062$  and  $b=1.256\pm 0.079$  using two single needle electrodes.

FIG. 19 is a representation of the Finite Element Analysis (FEA) model for a 3D Electric Field [V/cm] Distribution in Non-Electroporated (Baseline) Tissue with 1.5-cm Single Needle Electrodes at a Separation of 2.0 cm and with 3000 V applied.

FIGS. 20A-D are representations of the Electric Field [V/cm] Distributions from the 3D Non-Electroporated (Baseline) Models of FIG. 19, wherein FIG. 20A represents the x-y plane mid-electrode length, FIG. 20B represents the x-z plane mid-electrode diameter, FIG. 20C represents the y-z plane mid-electrode diameter, and FIG. 20D represents the y-z plane between electrodes.

FIG. 21 is a representation of the Finite Element Analysis (FEA) model for a 3D Electric Field [V/cm] Distribution in Electroporated Tissue with 1.5-cm Single Needle Electrodes at a Separation of 2.0 cm and 3000 V applied assuming  $\sigma_{max}/\sigma_0=3.6$ .

FIGS. 22A-22D are representations of the Electric Field [V/cm] Distributions from the 3D Electroporated Models with 1.5-cm Electrodes at a Separation of 2.0 cm and 3000 V (cross-sections) assuming  $\sigma_{max}/\sigma_0=3.6$ , wherein FIG. 22A represents the x-y plane mid-electrode length, FIG. 22B represents the x-z plane mid-electrode diameter, FIG. 22C represents the y-z plane mid-electrode diameter, and FIG. 22D represents the y-z plane between electrodes.

FIG. 23 is a representative Cassini curve showing zones of ablation derived using two single needle electrodes and the pre-pulse procedure to determine the ratio of maximum conductivity to baseline conductivity. For comparison purposes the baseline electric field isocontour is also presented in which no electroporation is taken into account.

FIGS. 24A-24D are representative surface plots showing finite element temperature calculations at different electrode spacings. The surface plots show temperature distributions at  $t=90$  seconds (Ninety pulses of  $100\ \mu\text{s}$  each) for 3000 V treatments with (A) 1.0 cm, (B) 1.5 cm, (C) 2.0 cm, and (D) 2.5 cm electrode spacing. Contour lines show approximate electric field correlating to  $T=45^\circ\text{C}$ . (A) 900 V/cm, (B) 1075 V/cm, (C) 1100 V/cm, and (D) 1080 V/cm.

FIGS. 25A-25D are representative surface plots showing Cassini Oval Approximations at different electrode spacings. The surface plots show the temperature distribution at  $t=90$  seconds (Ninety pulses of  $100\ \mu\text{s}$  each) for 3000 V treatments with (A) 1.0 cm, (B) 1.5 cm, (C) 2.0 cm, and (D) 2.5 cm electrode spacing. Red dashed lines show the Cassini oval correlating to  $T=45^\circ\text{C}$ . and the black dotted lines show the Cassini oval correlating to 500 V/cm.

FIGS. 26A-26D are representative surface plots showing Cassini Oval Approximations at different times. The surface plots show the temperature distribution at (A)  $t=10$  seconds, (B)  $t=40$  seconds, (C)  $t=90$  seconds, and (D)  $t=200$  seconds. Treatment parameters were held constant at 3000 V, 1.5 cm exposure, and 2.5 cm electrode spacing. Red dashed lines show the Cassini oval correlating to  $T=45^\circ\text{C}$ . and the black dotted lines show the Cassini oval correlating to 500 V/cm. The pulses were programmed with  $100\ \mu\text{s}$  duration.

FIGS. 27A-27D are representative surface plots showing Cassini Oval Approximations at different temperatures. The surface plots show the temperature distribution at (A)  $T=37.2^\circ\text{C}$ ., (B)  $T=40^\circ\text{C}$ ., (C)  $T=45^\circ\text{C}$ ., and (D)  $T=50^\circ\text{C}$ .. Treatment parameters were held constant at 3000V, 1.5 cm exposure, and 2.5 cm electrode spacing at a time= $90$  seconds (Ninety pulses of  $100\ \mu\text{s}$  each). Red dashed lines show the Cassini oval correlating to the specified temperatures and the black dotted lines show the Cassini oval correlating to 500 V/cm.

FIG. 28 is a screenshot of the Cassini Oval Approximation Tool using the following parameters: Voltage= $3000\text{ V}$ , Gap= $10\text{ mm}$ , Time= $90$  seconds (Ninety pulses of  $100\ \mu\text{s}$  each), Temperature= $50^\circ\text{C}$ ., and Electric Field= $500\text{ V/cm}$ . The red dashed line shows the Cassini oval correlating to  $50^\circ\text{C}$ . and the black dotted lines show the Cassini oval correlating to 500 V/cm.

FIG. 29 is a screenshot of the Cassini Oval Approximation Tool using the following parameters: Voltage= $3000\text{ V}$ , Gap= $10\text{ mm}$ , Time= $90$  seconds (Ninety pulses of  $100\ \mu\text{s}$  each), Temperature= $40^\circ\text{C}$ ., and Electric Field= $500\text{ V/cm}$ . The red dashed lines show the Cassini oval correlating to  $40^\circ\text{C}$ . and the black dotted line show the Cassini oval correlating to 500 V/cm.

FIGS. 30A-30D are representative surface plots showing Cassini Oval Approximations at different temperature thresholds. The surface plots show the temperature and electric field distribution at (A)  $T=40^\circ\text{C}$ ., (B)  $T=45^\circ\text{C}$ ., (C)  $T=50^\circ\text{C}$ ., and (D)  $T=55^\circ\text{C}$ .. The other parameters are the same as those for FIGS. 28 and 29. The red dashed lines show the Cassini oval correlating to the specified temperatures and the black dotted lines show the Cassini oval correlating to 500 V/cm.

FIGS. 31A-31D are representative surface plots showing Cassini Oval Approximations at different voltages. The surface plots show the temperature and electric field distribution

at (A) 3000 V, (B) 2000 V, (C) 1500 V and (D) 1000 V. Other parameters were Gap= $10\text{ mm}$ , Time= $90$  seconds (Ninety pulses of  $100\ \mu\text{s}$  each), Temperature= $40^\circ\text{C}$ ., and Electric Field= $500\text{ V/cm}$ . The red dashed lines show the Cassini oval correlating to  $40^\circ\text{C}$ . and the black dotted lines show the Cassini oval correlating to 500 V/cm.

FIGS. 32A-32D are representative surface plots showing Cassini Oval Approximations at different electric field thresholds. The surface plots show the temperature and electric field distribution at (A) 500 V/cm, (B) 1000 V/cm, (C) 1500 V/cm, and (D) 2000 V/cm. Other parameters were Voltage= $3000\text{ V}$ , Gap= $10\text{ mm}$ , Time= $90$  seconds (Ninety pulses of  $100\ \mu\text{s}$  each), Temperature= $40^\circ\text{C}$ .. The red dashed lines show the Cassini oval correlating to  $40^\circ\text{C}$ . and the black dotted lines show the Cassini oval correlating to the specified electric field thresholds.

FIGS. 33A-33D are representative surface plots showing Cassini Oval Approximations at different electrode spacings. The surface plots show the temperature and electric field distribution at an electrode spacing of 5 mm, 10 mm, 15 mm, and 20 mm. Other parameters were Voltage= $3000\text{ V}$ , Time= $90$  seconds (Ninety pulses of  $100\ \mu\text{s}$  each), Temperature= $40^\circ\text{C}$ ., and Electric Field= $500\text{ V/cm}$ . The red dashed lines show the Cassini oval correlating to  $40^\circ\text{C}$ . and the black dotted lines show the Cassini oval correlating to 500 V/cm.

FIGS. 34A-34D are representative surface plots showing Cassini Oval Approximations at different times. The surface plots show the temperature and electric field distribution at (A) 90 seconds (Ninety pulses of  $100\ \mu\text{s}$  each), (B) 60 seconds (Sixty pulses of  $100\ \mu\text{s}$  each), (C) 30 seconds (Thirty pulses of  $100\ \mu\text{s}$  each), and (D) 10 seconds (Ten pulses of  $100\ \mu\text{s}$  each). Other parameters were Voltage= $3000\text{ V}$ , Gap= $10\text{ mm}$ , Temperature= $40^\circ\text{C}$ ., and Electric Field= $500\text{ V/cm}$ . The red dashed lines show the Cassini oval correlating to  $40^\circ\text{C}$ . and the black dotted lines show the Cassini oval correlating to 500 V/cm.

FIG. 35 is a representation of the COMSOL three-dimensional finite element domain and mesh used to calculate Cassini Oval values for the electric and thermal curves.

FIGS. 36A-36C show a representation of a visualization tool providing the 650 V/cm electric field distributions using different configurations of bipolar probes and includes dynamic change (3.6x) in electrical conductivity from the non-electroporated baseline for runs 7, 8, and 9 of the visualization.

FIG. 36D is a table showing parameters of runs 7, 8, and 9 including electrode length, separation distance (insulation), and applied voltage.

FIG. 36E is a table showing lesion dimensions for runs 7, 8, and 9. The results show that as the length of the bipolar electrode increases the size of the zone of ablation increases.

FIG. 37 is a graph showing electrical conductivity (S/m, y-axis) plotted against electric field strength (V/cm, x-axis). FIG. 37 shows the conductivity changes from 0.1 to 0.35 at an electric field centered at 500 V/cm.

FIG. 38A is a representative contour plot showing the "Goldberg" data (red dashed line) vs a calculated threshold (solid black line) based on the parameters shown in FIG. 38C. The x and y axes represent distance [cm].

FIG. 38B is a representative contour plot showing the conductivity (blue dotted line) vs. a calculated threshold (solid black line) based on the parameters shown in FIG. 38C. The x and y axes represent distance [cm].

FIG. 38C is a table showing the parameters used to generate the contour plots of FIGS. 38A and 38B.

FIGS. 39A-39C are representative contour plots showing the “Goldberg” data (red dashed line) and calculated threshold (solid black line) and FIGS. 39D-39F are contour plots showing the conductivity (blue dotted line) and calculated threshold (solid black line) for conductivities of 2, 3, and 4, respectively. The other parameters are the same as those in the table of FIG. 38C. The x and y axes represent distance [cm].

FIGS. 40A-40C are representative contour plots showing the “Goldberg” data (red dashed line) and calculated threshold (solid black line) and FIGS. 40D-40F are contour plots showing the conductivity (blue dotted line) and calculated threshold (solid black line) for conductivity multipliers of 2, 3, and 4, respectively. Other parameters used to generate the plots of FIGS. 40A-40F include an IRE Threshold of 600 V/cm, a transition zone of 0.4, a Voltage of 700 V, an E-Field of 700 V/cm, and a Sigma (baseline electrical conductivity) of 0.20 S/m. The x and y axes represent distance [cm].

FIGS. 41A-41C are representative contour plots showing the “Goldberg” data (red dashed line) and calculated threshold (solid black line) and FIGS. 41D-41F are contour plots showing the conductivity (blue dotted line) and calculated threshold (solid black line) for conductivity multipliers of 2, 3, and 4, respectively. Other parameters used to generate the plots of FIGS. 41A-41F include an IRE Threshold of 1000 V/cm, transition zone of 0.2, Voltage of 2700 V, E-Field of 700 V/cm, and Sigma (baseline electrical conductivity) of 0.20 S/m. The x and y axes represent distance [cm].

FIG. 42 is a representative contour plot of the electric field distribution assuming a static electrical conductivity using a bipolar probe. The model assumes an applied voltage of 2700 V with 7 mm long electrodes separated by an 8 mm insulation shaft.

FIGS. 43A-43D are representative contour plots of post-IRE cell viability predictions with the colored curves illustrating different cell viability levels. The model assumes using ninety 100- $\mu$ s pulses at a rate of one pulse per second with 2700 V, and a viability value of 0.1% ( $S=0.001$ ) as the complete cell death due to IRE exposure.

FIG. 44 is a graph showing the dynamic electric conductivity function of liver tissue undergoing electroporation. The sigmoid function includes a baseline of 0.067 S/m and maximum conductivity of 0.241 S/m.

FIG. 45 is a representative contour plot showing the electric field distribution assuming a dynamic electrical conductivity using the bipolar probe with 3000 V with 7 mm long electrodes separated by an 8 mm insulation shaft.

FIGS. 46A-D are representative contour plots showing post-IRE cell viability, wherein A) corresponds to 20 pulses at 2000 volts, B) corresponds to 20 pulses at 3000 volts, C) corresponds to 100 pulses at 2000 volts, and D) corresponds to 100 pulses at 3000 volts.

FIGS. 47A and 47B are representative contour plots showing post-IRE cell viability after three hundred (FIG. 47A) and three hundred and sixty (FIG. 47B) 100- $\mu$ s pulses at a rate of one pulse per second with an applied voltage of 3000 V.

FIGS. 48A and 48B are a table showing the results of a parametric study on bipolar electrode configuration as a function of electrode length, separation distance, and diameter in the resulting IRE area and volume.

FIG. 49 is a table showing the results of a parametric study on bipolar electrode configuration as a function of applied voltage and pulse number in the resulting IRE area and volume with 7 mm long electrodes separated by an 8 mm insulation shaft.

FIG. 50 is a table showing the results of a parametric study on bipolar electrode configuration as a function of pulse number in the resulting IRE area and volume with an applied voltage of 3000 V with 7 mm long electrodes separated by an 8 mm insulation shaft.

FIGS. 51A-C are schematics of representative electrode geometries.

FIGS. 51D-F are representative contour plots showing the resulting electric field distribution corresponding to the electrode geometries of FIGS. 51A-C.

#### DETAILED DESCRIPTION OF VARIOUS EMBODIMENTS OF THE INVENTION

Reference will now be made in detail to various exemplary embodiments of the invention. Embodiments described in the description and shown in the figures are illustrative only and are not intended to limit the scope of the invention. Changes may be made in the specific embodiments described in this specification and accompanying drawings that a person of ordinary skill in the art will recognize are within the scope and spirit of the invention.

Throughout the present teachings, any and all of the features and/or components disclosed or suggested herein, explicitly or implicitly, may be practiced and/or implemented in any combination, whenever and wherever appropriate as understood by one of ordinary skill in the art. The various features and/or components disclosed herein are all illustrative for the underlying concepts, and thus are non-limiting to their actual descriptions. Any means for achieving substantially the same functions are considered as foreseeable alternatives and equivalents, and are thus fully described in writing and fully enabled. The various examples, illustrations, and embodiments described herein are by no means, in any degree or extent, limiting the broadest scopes of the claimed inventions presented herein or in any future applications claiming priority to the instant application.

Embodiments of the invention include a method for visualization of heat and electric field distribution within a target treatment area, the method comprising: selecting as inputs an applied voltage, electrode spacing, and treatment duration corresponding to a desired treatment protocol for a target treatment area; using the inputs in a Cassini approximation of data, wherein the data comprises measured voltage, electrode spacing, and time of actual treatment protocols, and determining an expected temperature distribution and expected electric field distribution of the target treatment area; and displaying a graphical representation of a selected temperature and a selected electric field of the expected temperature and electric field distributions. Such methods can further comprise as inputs one or more of a baseline conductivity for the target treatment area, a change in conductivity for the target treatment area, or a conductivity for a specific tissue type.

Such methods can include a method of treatment planning for medical therapies involving administering electrical treatment energy, the method comprising: providing one or more parameters of a treatment protocol for delivering one or more electrical pulses to tissue through one or more or a plurality of electrodes; modeling heat distribution in the tissue based on the parameters; and displaying a graphical representation of the modeled heat distribution.

One embodiment of the present invention is illustrated in FIGS. 1 and 2. Representative components that can be used with the present invention can include one or more of those that are illustrated in FIG. 1. For example, in embodiments,

11

one or more probes **22** can be used to deliver therapeutic energy and are powered by a voltage pulse generator **10** that generates high voltage pulses as therapeutic energy such as pulses capable of irreversibly electroporating the tissue cells. In the embodiment shown, the voltage pulse generator **10** includes six separate receptacles for receiving up to six individual probes **22** which are adapted to be plugged into the respective receptacle. The receptacles are each labeled with a number in consecutive order. In other embodiments, the voltage pulse generator can have any number of receptacles for receiving more or less than six probes.

For example, a treatment protocol according to the invention could include a one or more or a plurality of electrodes. According to the desired treatment pattern, the plurality of electrodes can be disposed in various positions relative to one another. In a particular example, a plurality of electrodes can be disposed in a relatively circular pattern with a single electrode disposed in the interior of the circle, such as at approximately the center. Any configuration of electrodes is possible and the arrangement need not be circular but any shape periphery can be used depending on the area to be treated, including any regular or irregular polygon shape, including convex or concave polygon shapes. The single centrally located electrode can be a ground electrode while the other electrodes in the plurality can be energized. Any number of electrodes can be in the plurality such as from about 1 to 20. Indeed, even 3 electrodes can form a plurality of electrodes where one ground electrode is disposed between two electrodes capable of being energized, or 4 electrodes can be disposed in a manner to provide two electrode pairs (each pair comprising one ground and one electrode capable of being energized). During treatment, methods of treating can involve energizing the electrodes in any sequence, such as energizing one or more electrode simultaneously, and/or energizing one or more electrode in a particular sequence, such as sequentially, in an alternating pattern, in a skipping pattern, and/or energizing multiple electrodes but less than all electrodes simultaneously, for example.

In the embodiment shown, each probe **22** includes either a monopolar electrode or bipolar electrodes having two electrodes separated by an insulating sleeve. In one embodiment, if the probe includes a monopolar electrode, the amount of exposure of the active portion of the electrode can be adjusted by retracting or advancing an insulating sleeve relative to the electrode. See, for example, U.S. Pat. No. 7,344,533, which is incorporated by reference herein in its entirety. The pulse generator **10** is connected to a treatment control computer **40** having input devices such as keyboard **12** and a pointing device **14**, and an output device such as a display device **11** for viewing an image of a target treatment area such as a lesion **300** surrounded by a safety margin **301**. The therapeutic energy delivery device **22** is used to treat a lesion **300** inside a patient **15**. An imaging device **30** includes a monitor **31** for viewing the lesion **300** inside the patient **15** in real time. Examples of imaging devices **30** include ultrasonic, CT, MRI and fluoroscopic devices as are known in the art.

The present invention includes computer software (treatment planning module **54**) which assists a user to plan for, execute, and review the results of a medical treatment procedure, as will be discussed in more detail below. For example, the treatment planning module **54** assists a user to plan for a medical treatment procedure by enabling a user to more accurately position each of the probes **22** of the therapeutic energy delivery device **20** in relation to the lesion **300** in a way that will generate the most effective

12

treatment zone. The treatment planning module **54** can display the anticipated treatment zone based on the position of the probes and the treatment parameters. The treatment planning module **54** may also display a zone of temperature heating according to cutoff values inputted by the treating physician and correlate this with a value for the electric field distribution. The treatment planning module may also allow the treating physician to display the anticipated treatment zone, or target ablation zone, according to one or more tissue-specific conductivity parameters inputted by the treating physician. The conductivity parameters may include the baseline conductivity of the tissue to be treated, the ratio of the baseline conductivity to the maximum conductivity of the tissue that is reached during treatment, the rate at which the conductivity increases from the baseline to the maximum conductivity, and/or the electric field at which the conductivity changes during treatment.

The treatment planning module **54** can display the progress of the treatment in real time and can display the results of the treatment procedure after it is completed. This information can be displayed in a manner such that it can be used for example by a treating physician to determine whether the treatment was successful and/or whether it is necessary or desirable to re-treat the patient.

For purposes of this application, the terms “code”, “software”, “program”, “application”, “software code”, “computer readable code”, “software module”, “module” and “software program” are used interchangeably to mean software instructions that are executable by a processor. The “user” can be a physician or other medical professional. The treatment planning module **54** executed by a processor outputs various data including text and graphical data to the monitor **11** associated with the generator **10**.

Referring now to FIG. 2, the treatment control computer **40** of the present invention manages planning of treatment for a patient. The computer **40** is connected to the communication link **52** through an I/O interface **42** such as a USB (universal serial bus) interface, which receives information from and sends information over the communication link **52** to the voltage generator **10**. The computer **40** includes memory storage **44** such as RAM, processor (CPU) **46**, program storage **48** such as ROM or EEPROM, and data storage **50** such as a hard disk, all commonly connected to each other through a bus **53**. The program storage **48** stores, among others, a treatment planning module **54** which includes a user interface module that interacts with the user in planning for, executing and reviewing the result of a treatment. Any of the software program modules in the program storage **48** and data from the data storage **50** can be transferred to the memory **44** as needed and is executed by the CPU **46**.

In one embodiment, the computer **40** is built into the voltage generator **10**. In another embodiment, the computer **40** is a separate unit which is connected to the voltage generator through the communications link **52**. In a preferred embodiment, the communication link **52** is a USB link. In one embodiment, the imaging device **30** is a stand-alone device which is not connected to the computer **40**. In the embodiment as shown in FIG. 1, the computer **40** is connected to the imaging device **30** through a communications link **53**. As shown, the communication link **53** is a USB link. In this embodiment, the computer can determine the size and orientation of the lesion **300** by analyzing the data such as the image data received from the imaging device **30**, and the computer **40** can display this information on the monitor **11**. In this embodiment, the lesion image generated by the imaging device **30** can be directly displayed on the

grid (not shown) of the display device (monitor) **11** of the computer running the treatment planning module **54**. This embodiment would provide an accurate representation of the lesion image on the grid, and may eliminate the step of manually inputting the dimensions of the lesion in order to create the lesion image on the grid. This embodiment would also be useful to provide an accurate representation of the lesion image if the lesion has an irregular shape.

It should be noted that the software can be used independently of the pulse generator **10**. For example, the user can plan the treatment in a different computer as will be explained below and then save the treatment parameters to an external memory device, such as a USB flash drive (not shown). The data from the memory device relating to the treatment parameters can then be downloaded into the computer **40** to be used with the generator **10** for treatment. Additionally, the software can be used for hypothetical illustration of zones of ablation, temperature thresholds or cutoffs, and electrical field thresholds or cutoffs for training purposes to the user on therapies that deliver electrical energy. For example, the data can be evaluated by a human to determine or estimate favorable treatment protocols for a particular patient rather than programmed into a device for implementing the particular protocol.

FIG. 3 illustrates one embodiment of a circuitry to detect an abnormality in the applied pulses such as a high current, low current, high voltage or low voltage condition. This circuitry is located within the generator **10** (see FIG. 1). A USB connection **52** carries instructions from the user computer **40** to a controller **71**. The controller can be a computer similar to the computer **40** as shown in FIG. 2. The controller **71** can include a processor, ASIC (application-specific integrated circuit), microcontroller or wired logic. The controller **71** then sends the instructions to a pulse generation circuit **72**. The pulse generation circuit **72** generates the pulses and sends electrical energy to the probes. For clarity, only one pair of probes/electrodes are shown. However, the generator **10** can accommodate any number of probes/electrodes (e.g., from 1-10, such as 6 probes) and energizing multiple electrodes simultaneously for customizing the shape of the ablation zone. In the embodiment shown, the pulses are applied one pair of electrodes at a time, and then switched to another pair. The pulse generation circuit **72** includes a switch, preferably an electronic switch, that switches the probe pairs based on the instructions received from the computer **40**. A sensor **73** such as a sensor can sense the current or voltage between each pair of the probes in real time and communicate such information to the controller **71**, which in turn, communicates the information to the computer **40**. If the sensor **73** detects an abnormal condition during treatment such as a high current or low current condition, then it will communicate with the controller **71** and the computer **40** which may cause the controller to send a signal to the pulse generation circuit **72** to discontinue the pulses for that particular pair of probes. The treatment planning module **54** can further include a feature that tracks the treatment progress and provides the user with an option to automatically retreat for low or missing pulses, or over-current pulses (see discussion below). Also, if the generator stops prematurely for any reason, the treatment planning module **54** can restart at the same point where it terminated, and administer the missing treatment pulses as part of the same treatment. In other embodiments, the treatment planning module **54** is able to detect certain errors during treatment, which include, but are not limited to, "charge failure", "hardware failure", "high current failure", and "low current failure".

General treatment protocols for the destruction (ablation) of undesirable tissue through electroporation are known. They involve the insertion (bringing) electroporation electrodes to the vicinity of the undesirable tissue and in good electrical contact with the tissue and the application of electrical pulses that cause irreversible electroporation of the cells throughout the entire area of the undesirable tissue. The cells whose membrane was irreversibly permeabilized may be removed or left in situ (not removed) and as such may be gradually removed by the body's immune system. Cell death is produced by inducing the electrical parameters of irreversible electroporation in the undesirable area.

Electroporation protocols involve the generation of electrical fields in tissue and are affected by the Joule heating of the electrical pulses. When designing tissue electroporation protocols it is important to determine the appropriate electrical parameters that will maximize tissue permeabilization without inducing deleterious thermal effects. It has been shown that substantial volumes of tissue can be electroporated with reversible electroporation without inducing damaging thermal effects to cells and has quantified these volumes (Davalos, R. V., B. Rubinsky, and L. M. Mir, Theoretical analysis of the thermal effects during in vivo tissue electroporation. *Bioelectrochemistry*, 2003. Vol. 61(1-2): p. 99-107).

The electrical pulses used to induce irreversible electroporation in tissue are typically larger in magnitude and duration from the electrical pulses required for reversible electroporation. Further, the duration and strength of the pulses for irreversible electroporation are different from other methodologies using electrical pulses such as for intracellular electro-manipulation or thermal ablation. The methods are very different even when the intracellular (nano-seconds) electro-manipulation is used to cause cell death, e.g. ablate the tissue of a tumor or when the thermal effects produce damage to cells causing cell death.

Typical values for pulse length for irreversible electroporation are in a range of from about 5 microseconds to about 62,000 milliseconds or about 75 microseconds to about 20,000 milliseconds or about 100 microseconds $\pm$ 10 microseconds. This is significantly longer than the pulse length generally used in intracellular (nano-seconds) electro-manipulation which is 1 microsecond or less—see published U.S. application 2002/0010491 published Jan. 24, 2002.

The pulse is typically administered at voltage of about 100 V/cm to 7,000 V/cm or 200 V/cm to 2000 V/cm or 300V/cm to 1000 V/cm about 600 V/cm for irreversible electroporation. This is substantially lower than that used for intracellular electro-manipulation which is about 10,000 V/cm, see U.S. application 2002/0010491 published Jan. 24, 2002.

The voltage expressed above is the voltage gradient (voltage per centimeter). The electrodes may be different shapes and sizes and be positioned at different distances from each other. The shape may be circular, oval, square, rectangular or irregular etc. The distance of one electrode to another may be 0.5 to 10 cm, 1 to 5 cm, or 2-3 cm. The electrode may have a surface area of 0.1-5 sq. cm or 1-2 sq. cm.

The size, shape and distances of the electrodes can vary and such can change the voltage and pulse duration used. Those skilled in the art will adjust the parameters in accordance with this disclosure to obtain the desired degree of electroporation and avoid thermal damage to surrounding cells.

Additional features of protocols for electroporation therapy are provided in U.S. Patent Application Publication

No. US 2007/0043345 A1, the disclosure of which is hereby incorporated by reference in its entirety.

In one aspect, the systems and methods may have the capability for estimating a volume of tissue that will be heated at or above a cutoff value and a volume of tissue that will receive an electric field at or above a cutoff value for the above medical treatment device. The cut-off values may be user-specified values determined by a treating physician or technician. The systems and methods are provided so that the treating physician may recognize treatments that produce overheating in the vicinity of the electrodes of the treatment device. This additional capability of the treatment device may be based on the Joule heating equations of Example 8. The values may be plotted as contour lines which may be displayed with a graphical representation of the estimated treatment volume above. In one embodiment, the contour lines are Cassini oval approximations performed according to the equations and procedure in Example 7.

In another aspect, the systems and methods may have the additional capability for providing the electric field distributions using different configurations of bipolar probes and include the dynamic change in electrical conductivity from the baseline non-electroporated tissue. The systems and methods may allow a user to incorporate tissue-specific values for the dynamic change in conductivity in estimating a treatment volume. This additional capability is further described in Example 9. In one embodiment, the contour lines are Cassini oval approximations performed according to the equations and procedure in Example 7.

In another aspect, the systems and methods may have the additional capability for inputting or adjusting one or more variables related to the dynamic conductivity so that tissue-specific behavior can be accounted for when estimating a treatment volume. In embodiments, the treatment planning module may provide input for parameters such as the baseline conductivity, change in conductivity, the transition zone (how rapidly the conductivity increases), the electric field at which the change in conductivity occurs, and the electric field at which irreversible electroporation occurs. These parameters may allow the treating physician to fine-tune the ablation zone based on the conductivity characteristics of the target tissue. The present inventors have recognized that the conductivity characteristics of the tissue, such as baseline and maximum conductivities, should be determined before the therapy in order to determine safe and effective pulse protocols. This additional capability is further described in Example 10.

The numerical models and algorithms of the invention, as provided in the Examples, such as Cassini Oval equations of Example 7 and the Joule Heating Model equations of Example 8, can be implemented in a system for estimating a 3-dimensional treatment volume for a medical treatment device that applies treatment energy through one or more or a plurality of electrodes defining a treatment area. In one embodiment, the numerical models and algorithms are implemented in an appropriate computer readable code as part of the treatment planning module 54 of the system of the invention. Computing languages available to the skilled artisan for programming the treatment planning module 54 include general purpose computing languages such as the C and related languages, and statistical programming languages such as the "S" family of languages, including R and S-Plus. The computer readable code may be stored in a memory 44 of the system of the invention. A processor 46 is coupled to the memory 44 and a display device 11 and the treatment planning module 54 stored in the memory 44 is executable by the processor 46. Treatment planning module

54, through the implemented numerical models, is adapted to generate a graphical display of an estimated temperature or electric field or target ablation zone in the display device 11.

In one embodiment, the invention provides for a system for estimating and graphically displaying a thermal and/or electric field value for a medical treatment device that applies treatment energy through one or more or a plurality of electrodes 22 defining a treatment area, the system comprising a memory 44, a display device 11, a processor 46 coupled to the memory 44 and the display device 11, and a treatment planning module 54 stored in the memory 44 and executable by the processor 46, the treatment planning module 54 adapted to generate one or more isocontours representing a value of a temperature and/or electric field for display in the display device 11 based on modeling of the temperature distributions or electrical field distributions according to one or more parameters defining an electrical energy based protocol (e.g., irreversible electroporation). The results of modeling the temperature distributions and electrical field distributions may be stored in a database or calculated in real-time. The treatment planning module may generate the isocontours based on the modeling results.

In another embodiment, the invention provides for a system for estimating a target ablation zone for a medical treatment device that applies treatment energy through one or more or a plurality of electrodes 22 defining a treatment area, the system comprising a memory 44, a display device 11, a processor 46 coupled to the memory 44 and the display device 11, and a treatment planning module 54 stored in the memory 44 and executable by the processor 46, the treatment planning module 54 adapted to generate a target ablation zone in the display device 11 based on a combination of one or more parameters for a treatment protocol for irreversible electroporation and one or more tissue-specific conductivity parameters.

The foregoing description provides additional instructions and algorithms for a computer programmer to implement in computer readable code a treatment planning module 54 that may be executable through a processor 46 to generate an estimated temperature or electrical field for display in the display device 11 based on modeling of a tissue according to one or more parameters for electroporation, such as IRE. The computer readable code may also estimate a temperature value and an electric field value according to equations described in Example 8 and graphically display these value as contour lines in the display device. In one embodiment, the contour lines are Cassini oval approximations performed according to the equations and procedure in Example 7. The computer readable code may also provide for input on one or more conductivity parameters for estimating the target ablation zone as described in Examples 9 and 10.

FIG. 4 is a schematic diagram showing a three-dimensional zone of ablation occurring during irreversible electroporation. The width and depth of this zone of ablation may be modeled two-dimensionally using the Cassini oval equation. Further, the mathematical fit of the zone of ablation has similar shape characteristics as the actual and simulated electric field and temperature values. For example, a typical single bi-polar probe will be configured to have a first and second electrode spaced apart from each other at the distal end of the single probe. Since the lesion formed by this bi-polar arrangement closely resembles the 8-like shape of the electric field, the method of the invention can be used to accurately predict the electric field and temperature contours. FIGS. 16A and 16B show variations

of 'a' and 'b' parameters that will closely resemble the 8-like shape of the electric field according to the Cassini Equation.

The method of the invention fits data extracted from numerical simulations to both the 'a' and 'b' parameters from the Cassini Equation, providing the flexibility to match potentially any shape of electric field created by the specific pulse parameters employed. Also, as illustrated in FIGS. 16A and 16B since the 'a' or 'b' parameters are not related to the separation distance or geometry of the electrodes, the electric field and temperature contours of the bi-polar probe can be captured according to the techniques described above.

Additionally, by adding the cumulative effects of electrode pairs, the electric field and thermal contours of alternative multi-electrode arrangements of three or more probes can be determined. For example, a four single probe electrode box can be captured by calculating treatment regions based on each combination of electrode pairs for the fit according to the techniques described above. Thus, for example, if the four probe electrode box is configured for treatment using pulses that cycle through probe combinations 1-2, 3-4, 1-3, 2-4, 2-3 and 1-4 the approximation tool can find electric field and temperature contours for each probe combination, then superimpose the results to display the cumulative effect of that particular pulse protocol in the treatment region.

In one embodiment, the treatment planning module 54 provides for a method for modeling and graphical display of tissue heating according to a set of parameters defining a treatment protocol. In a specific embodiment, the set of parameters correspond to a treatment protocol for inducing irreversible electroporation in a tissue.

The treatment planning module 54 may provide one or more parameters of a treatment protocol for delivering one or more electrical pulses to a tissue through one or more or a plurality of electrodes.

The treatment planning module 54 may model a heat distribution in a tissue surrounding the one or more or the plurality of electrodes based on the one or more parameters.

The treatment planning module 54 may provide a graphical representation of the heat distribution based on the modeled heat distribution.

The treatment planning module 54 may allow a user to optionally modify one or more of the parameters of the treatment protocol through input devices 12, 14 based on the graphical representation of the heat distribution.

The treatment planning module 54 may be in operable connection with a controller 71 capable of delivering one or more electrical pulses to the tissue based on the one or more parameters stored in the treatment planning module 54.

The treatment planning module 54 may model the heat distribution in the tissue based on the Joule heating in the tissue.

The treatment planning module 54 may calculate the heat distribution as:

$$\rho C_p \frac{\partial T}{\partial t} = \nabla \cdot (k \nabla T) + Q_{jh} \left[ \frac{W}{m^3} \right]$$

where  $\rho$  is the density,  $C_p$  is the heat capacity,  $k$  is the thermal conductivity, and  $Q_{jh}$  are the resistive losses

$$Q_{jh} = J \cdot E \left[ \frac{W}{m^3} \right]$$

where  $J$  is the induced current density

$$J = \sigma E \left[ \frac{A}{m^2} \right]$$

and  $\sigma$  is the tissue conductivity and  $E$  is the electric field

$$E = -\nabla \phi \left[ \frac{V}{m} \right]$$

The treatment planning module may further calculate the resistive losses as

$$jh \cdot Q_{jh} = ((jh \cdot J_{ix} + jh \cdot J_{ex}) * \text{duty\_cycle} * jh \cdot Ex + (jh \cdot J_{iy} + jh \cdot J_{ey}) * \text{duty\_cycle} * jh \cdot Ey + (jh \cdot J_{iz} + jh \cdot J_{ez}) * \text{duty\_cycle} * jh \cdot Ez) * (t <= 90) + 0 * (t > 90)$$

according to the Joule Heating Model described in Example 8.

The treatment planning module 54 may allow a user to specify a heat distribution value (i.e. temperature) and may provide a graphical representation of the temperature as an isocontour line.

The treatment planning module 54 may model an electric field distribution in a tissue surrounding the one or more or a plurality of electrodes based on the one or more parameters of the treatment protocol.

The treatment planning module 54 may provide a graphical representation of the electric field distribution based on the modeled electrical field distribution.

The treatment planning module may calculate the electric field distribution as:

$$\nabla^2 \phi = 0$$

where  $\phi$  is the electric potential, this equation is solved with boundary conditions:

$$\vec{n} \cdot \vec{J} = 0 \text{ at the boundaries}$$

$$\phi = V_m \text{ at the boundary of the first electrode}$$

$$\phi = 0 \text{ at the boundary of the second electrode}$$

wherein  $\vec{n}$  is the normal vector to the surface,  $\vec{J}$  is the electrical current and  $V_m$  is the electrical potential applied.

The treatment planning module 54 may allow a user to specify a value for an electrical field distribution and provide a graphical representation of the electrical field distribution value as an isocontour line.

The treatment planning module 54 may display isocontour lines representing the heat and electrical field distributions by calculating a Cassini oval according to Example 7. The Cassini oval may be calculated by first modeling the temperature and electrical field distributions, storing the values in a database, and then calculating the specific Cassini oval based on parameters chosen by the user.

The treatment planning module 54 may allow a user to specify the one or more parameters of a treatment protocol including voltage, gap between electrodes, duration, pulse width, and electric field intensity.

Alternatively, or in addition, the treatment planning module 54 may allow a user to input one or more of the tissue-specific conductivity parameters described herein and model the electric field distribution and tissue heating. The treatment planning module 54 may then provide graphical representations of one or more values of the electrical field intensity and tissue temperature.

The treatment planning module 54 may provide a graphical representation of an electrical field distribution and a



heat distribution through a variety of modes of operation. First, the treatment planning module 54 may model the electrical field distribution and heat distribution for each set of parameters that are entered through input devices 12, 14. Thus, every time the treating physician altered one or more parameters of the treatment protocol, the treatment planning module 54 software would model the electrical field and heat distributions according to those parameters and then graphically display them on the display device 11. In a second approach, the software would first run the modeling of the heat and electrical field distributions for a wide range of parameter combinations and store the resulting distributions in the database stored in memory 44. In this approach, when the treating physician enters a particular combination of parameters, the treatment planning module 54 retrieves the heat distribution and electrical field distribution from values stored in the database. These values are then used as a basis for Cassini oval calculations to determine specific contours for the particular combination of parameters. The Cassini oval calculations are performed according to the equations and procedure described in Example 7. The Cassini ovals are then graphically displayed on the display device 11 in real time. In embodiments, specific contours are provided according to values for temperature or electrical field intensity set by the user.

The treatment planning module 54 may model the heat and electric field distributions according to mathematical formulas. In a specific embodiment, the treatment planning module 54 may model the heat distribution and the electrical field distribution according to the formulas in Example 8.

In another embodiment, the invention provides a system for treating a tissue, which system applies electrical treatment energy through one or more or a plurality of electrodes defining a target treatment area of the tissue. The system comprises a computer 40 comprising: a memory 44, a display device 11, a processor 46 coupled to the memory 44 and the display device 11; and a treatment planning module 54 stored in the memory 44 and executable by the processor 46. In this embodiment, the treatment planning module 54 is adapted to: provide one or more parameters of a treatment protocol for delivering one or more electrical pulses to a tissue through one or more or a plurality of electrodes; model a heat distribution in a tissue surrounding the at least electrode based on the one or more parameters; provide a graphical representation of the heat distribution on the display device 11 based on the modeled heat distribution. The system further comprises input devices 12, 14 in operable connection with computer 40, which input devices are capable of modifying the one or more parameters of the treatment protocol in the treatment planning module 54. The system further comprises a generator 10 in operable connection with the computer through a controller 71, which controller 71 is capable of instructing the generator 10 to deliver the one or more electrical pulses to the target tissue through the one or more or the plurality of electrodes 22 based on the one or more parameters of the treatment protocol stored in the treatment planning module 54. The system may further comprise one or more databases stored in the memory 44 for storing the modeled heat distributions or modeled electric field distributions for a plurality of sets of parameters for a treatment protocol.

In another embodiment, the treatment planning module 54, in addition to providing one or more parameters of a treatment protocol for delivering one or more electrical pulses to a tissue through one or more or a plurality of electrodes, may also provide one or more conductivity parameters specific for the tissue to be treated.

The treatment planning module 54 may estimate the target ablation zone based on the one or more parameters of the treatment protocol and the one or more electrical flow characteristics. The treatment planning module may also display a graphical representation of the estimation in the display device 11.

The treatment planning module 54 may optionally allow for modification of one or more of the parameters of the treatment protocol through input devices 12, 14 based on the graphical representation of the target ablation zone.

Additionally, the treatment planning module 54 may be in operable communication with a controller 77 and provide one or more parameters to the controller for delivering one or more electrical pulses to the tissue.

The treatment planning module 54 may provide one or more parameters of a treatment protocol comprise voltage, gap between electrodes, duration, pulse width, and electric field intensity.

Additionally, the one or more conductivity parameters provided by the treatment planning module 54 may comprise the baseline conductivity of the tissue to be treated, the ratio of the baseline conductivity to the maximum conductivity of the tissue that is reached during treatment, the rate at which the conductivity increases from the baseline to the maximum conductivity, or the electric field at which the conductivity changes during treatment.

Additionally, one or more conductivity parameters for a plurality of tissues may be provided in a database stored in memory 44.

In another embodiment, the invention provides a system for treating a tissue, which system applies electrical treatment energy through one or more or a plurality of electrodes 22 defining a target treatment area of the tissue. The system may comprise a computer 40 comprising a memory 44, a display device 11, a processor 46 coupled to memory 44 and the display device 11, and a treatment planning module 54 stored in the memory 44 and executable by the processor 46. The treatment planning module 54 may be adapted to provide one or more parameters of a treatment protocol for delivering one or more electrical pulses to a tissue through one or more or a plurality of electrodes, provide one or more conductivity parameters specific for the tissue to be treated, estimate the target ablation zone and display a graphical representation of the estimation in the display device based on the one or more parameters of the treatment protocol and the one or more conductivity parameters. The system may further comprise input devices 12, 14 in operable connection with the computer 40, which input devices 12, 14 are capable of allowing a user to modify the one or more parameters of the treatment protocol in the treatment planning module 54. The system may further comprise a generator 10 in operable connection with the computer 40 through a controller 71, which controller 71 is capable of instructing the generator 10 to deliver the one or more electrical pulses to a tissue through the one or more or the plurality of electrodes 22 based on the one or more parameters of the treatment protocol stored in the treatment planning module 54. Additionally, the system may comprise a database of conductivity parameters for a plurality of tissues stored in the memory 44.

The systems of the invention may be further configured to include software for displaying a Graphical User Interface in the display device with various screens for input and display of information, including those for inputting various parameters or display of graphical representations of zones of temperature, electrical field, and ablation. Additionally, the Graphical User Interface (GUI) may allow a user to input

one or more values related to an irreversible electroporation protocol and tissue-specific conductivity measurements through the use of text fields, check boxes, pull-downs, sliders, command buttons, tabs, and the like.

In one embodiment, the invention provides a method of treating a tissue with a medical treatment device that applies electrical treatment energy through one or more or a plurality of electrodes defining a target treatment area of the tissue and that comprises a display device. The method may comprise providing one or more parameters of a treatment protocol for delivering one or more electrical pulses to a tissue through one or more or a plurality of electrodes, modeling a heat distribution in a tissue surrounding the at least electrode based on the one or more parameters, displaying a graphical representation of the heat distribution based on the modeled heat distribution in the display device, modifying one or more of the parameters of the treatment protocol based on the graphical representation of the heat distribution, and implanting one or a plurality of electrodes in the tissue and delivering one or more electrical pulses to the tissue through the electrodes based on the one or more modified parameters.

In an exemplary implementation of the method, a treating physician identifies a target treatment area in a tissue of a patient. For example, the target treatment area may be a tumor that is unresectable by conventional surgical methods. The treating physician then uses input devices **12**, **14** such as a keyboard or mouse to interact with the treatment planning module **54** to select and input one or more parameters for designing an irreversible electroporation treatment protocol for ablating the tumor. The treating physician then selects a temperature value to graphically display a temperature contour profile in the target treatment area on the display device **11**. For example, the treating physician may select a value of 50° C. The treating physician then may correlate this temperature contour with imaging from the treatment area, by overlaying the temperature contour with the imaging on the display device **11**. By visualizing the temperature contour relative to the imaging, the treating physician then may identify structures surrounding the treatment area such as nerves and blood vessels that may be subject to thermal damage. The treating physician then may modify the irreversible electroporation parameters so that the temperature contour no longer indicates that critical structures may be subject to overheating. Irreversible electroporation parameters that may be modified include the voltage, distance between electrodes, electrode diameter, period of treatment, pulse width, number of pulses, and electric field. Similarly, the treatment planning module **54** may allow the treating physician to visualize a temperature contour relative to an electric field contour. Through one or more iterations of adjustment of the irreversible electroporation parameters and visualization of the temperature contour and electric field contour on the display device, the treating physician may ultimately select a final set of irreversible electroporation parameters to be used for treatment. The treating physician may then implant a pair of electrodes at the target treatment area in the tissue and deliver a plurality of electrical pulses to the treatment area based on the final set of irreversible electroporation parameters.

Thus, one embodiment of the method may comprise one or more of: 1. identifying a target treatment area in a tissue of a patient; 2. selecting and inputting one or more parameters for designing an irreversible electroporation treatment protocol for the target treatment area; 3. selecting a temperature value to graphically display a temperature contour in a simulation of the target treatment area; 4. correlating the

temperature contour with imaging from the treatment area; 5. Identifying structures within or surrounding the target treatment area such as nerves and blood vessels that may be subject to thermal damage based on the temperature contour; 6. modifying the irreversible electroporation parameters through one or more iterations so that the temperature contour no longer indicates that critical structures may be subject to overheating; 7. selecting a final set of irreversible electroporation parameters to be used for treatment; and 8. implanting a pair of electrodes at the target treatment area in the tissue and delivering a plurality of electrical pulses to the treatment area based on the final set of irreversible electroporation parameters.

The target treatment area may be imaged through a variety of imaging modalities including Computed Tomography (CT), Magnetic Resonance Imaging (MRI), Ultrasound, Positron Emission Tomography (PET), and the like. The imaging devices may be operably connected with the display device **11** so that results of the imaging may overlap or otherwise be available for comparison with the graphical display of the temperature and electric field contours.

In another embodiment, the invention provides a method of treating a tissue with a medical treatment device that applies electrical treatment energy through one or more or a plurality of electrodes defining a target treatment area of the tissue, which medical treatment device comprises a display device. The method may comprise providing one or more parameters of a treatment protocol for delivering one or more electrical pulses to a tissue through one or a plurality of electrodes, and one or more conductivity parameters specific for the tissue to be treated, estimating the target ablation zone and displaying a graphical representation of the estimation in the display device based on the one or more parameters of the treatment protocol and the one or more conductivity parameters, modifying one or more of the parameters of the treatment protocol based on the graphical representation of the target ablation zone, and implanting one or a plurality of electrodes in the tissue and delivering one or more electrical pulses to the tissue through the electrodes based on the one or more modified parameters. In the context of this specification, when referring to implanting an electrode, one or more of the electrode(s) can alternatively or in addition be placed near, or contact, or otherwise be operably disposed in a manner to administer electrical energy to the tissue.

In an exemplary implementation of the method, a treating physician identifies a target treatment area in a tissue of a patient. For example, the target treatment area may be a tumor that is unresectable by conventional surgical methods. The treating physician then uses input devices **12**, **14** such as a keyboard or mouse to interact with the treatment planning module **54** to select and input one or more parameters for designing an irreversible electroporation treatment protocol for ablating the tumor. The treatment planning module **54** then graphically displays an ablation zone on the display device **11** based on the one or more parameters of the irreversible electroporation treatment protocol. The treating physician then selects one or more conductivity parameters based on the type of tissue to be treated. The one or more conductivity parameters may be tissue-specific values based on experimental data that is stored in a database in memory **44** or may be obtained by the physician and entered into the treatment planning module **54** using the keyboard or other input, such as a hands-free input. In embodiments, tissue-specific conductivity values may be provided for heart, kidney, liver, lung, spleen, pancreas, brain, prostate, breast, small intestine, large intestine, and stomach.

The one or more conductivity parameters may include the baseline conductivity, change in conductivity, the transition zone (how rapidly the conductivity increases), the electric field at which the change in conductivity occurs, and the electric field at which irreversible electroporation occurs. After selecting the one or more conductivity parameters, the treatment planning module 54 may display a modified ablation zone on the display device 11 based on the tissue-specific conductivity characteristics inputted by the physician. The treating physician then may alter the one or more parameters of the irreversible electroporation protocol to modify the target ablation zone on the display device 11 to fit a desired area of treatment. The treating physician may then strategically place (e.g., implant) a pair of electrodes at the target treatment area in the tissue and deliver a plurality of electrical pulses to the treatment area based on the final set of irreversible electroporation parameters.

Thus, one embodiment of the method may comprise one or more of: 1. identifying a target treatment area in a tissue of a patient; 2. selecting and inputting one or more parameters for designing an irreversible electroporation treatment protocol for the target treatment area; 3. displaying a graphical representation of a target ablation zone on a display device; 4. selecting and inputting one or more conductivity characteristics based on the specific tissue to be treated; 5. displaying a modified graphical representation of the target ablation zone based on the tissue-specific conductivity characteristics; 6. modifying the one or more parameters of the irreversible electroporation protocol to fit a desired area of treatment; and 7. disposing/implanting a pair of electrodes at the target treatment area in the tissue and delivering a plurality of electrical pulses to the treatment area based on the modified IRE parameters.

As will be apparent to a skilled artisan, the systems and methods described above may be compatible with a variety of bi-polar and mono-polar probe combinations and configurations. Additionally, the calculations may be extended to not only display an electric field and temperature but also using that information to calculate an electrical damage and thermal damage component which take into account the time of exposure to the electric field and temperatures and can be tissue-specific such as for liver, kidney, etc. The systems and methods may be capable of displaying information such as "electric damage" or "thermal damage" once the electric field and temperature contours are determined, based on predetermined values for electric damage and thermal damage in the given tissue type. "Electric damage" and "thermal damage" regions can be visualized in place of or in combination with electric field and temperature as isocontour lines, shaded or highlighted areas, or other forms of graphical representation. In addition, the inclusion of tissue-specific in-vivo derived data including blood flow, metabolic heat generation, and one or more conductivity parameters such as tissue conductivity and ratios of changing conductivity can be included to reflect dynamic changes within a specific tissue type.

Additional details of the algorithms and numerical models disclosed herein will be provided in the following Examples, which are intended to further illustrate rather than limit the invention.

In Example 1, the present inventors provide a numerical model that uses an asymmetrical Gompertz function to describe the response of porcine renal tissue to electroporation pulses. However, other functions could be used to represent the electrical response of tissue under exposure to pulsed electric fields such as a sigmoid function, ramp, and/or interpolation table. This model can be used to deter-

mine baseline conductivity of tissue based on any combination of electrode exposure length, separation distance, and non-electroporating electric pulses. In addition, the model can be scaled to the baseline conductivity and used to determine the maximum electric conductivity after the electroporation-based treatment. By determining the ratio of conductivities pre- and post-treatment, it is possible to predict the shape of the electric field distribution and thus the treatment volume based on electrical measurements. An advantage of this numerical model is that it is easy to implement in computer software code in the system of the invention and no additional electronics or numerical simulations are needed to determine the electric conductivities. The system and method of the invention can also be adapted for other electrode geometries (sharp electrodes, bipolar probes), electrode diameter, and other tissues/tumors once their response to different electric fields has been fully characterized.

The present inventors provide further details of this numerical modeling as well as experiments that confirm this numerical modeling in Example 2. In developing this work, the present inventors were motivated to develop an IRE treatment planning method and system that accounts for real-time voltage/current measurements. As a result of this work, the system and method of the invention requires no electronics or electrodes in addition to the NANOKNIFE® System, a commercial embodiment of a system for electroporation-based therapies. The work shown in Example 2 is based on parametric study using blunt tip electrodes, but can be customized to any other geometry (sharp, plate, bipolar). The numerical modeling in Example 2 provides the ability to determine a baseline tissue conductivity based on a low voltage pre-IRE pulse (non-electroporating ~50 V/cm), as well as the maximum tissue conductivity based on high voltage IRE pulses (during electroporation) and low voltage post-IRE pulse (non-electroporating ~50 V/cm). Two numerical models were developed that examined 720 or 1440 parameter combinations. Results on IRE lesion were based on in vitro measurements. A major finding of the modeling in Example 2 is that the electric field distribution depends on conductivity ratio pre- and post-IRE. Experimental and clinical IRE studies may be used to determine this ratio. As a result, one can determine e-field thresholds for tissue and tumor based on measurements. The 3-D model of Example 2 captures depth, width, and height e-field distributions.

In Example 3, as a further extension of the inventors work, the inventors show prediction of IRE treatment volume based on 1000 V/cm, 750 v/cm, and 500 V/cm IRE thresholds as well as other factors as a representative case of the numerical modeling of the invention.

In Example 4, the inventors describe features of the Specific Conductivity and procedures for implementing it in the invention.

In Example 5, the inventors describe in vivo experiments as a reduction to practice of the invention.

In Example 6, the inventors describe how to use the ratio of maximum conductivity to baseline conductivity in modifying the electric field distribution and thus the Cassini oval equation.

In Example 7, the inventors describe the Cassini oval equation and its implementation in the invention.

In Example 8, the inventors describe mapping of electric field and thermal contours using a simplified data cross-referencing approach.

In Example 9, the inventors describe visualization of electric field distributions using different configurations of bipolar probes.

In Example 10, the inventors describe a method for determining the IRE threshold for different tissues according to one or more conductivity parameters.

In Example 11, the inventors describe correlating experimental and numerical IRE lesions using the bipolar probe.

EXAMPLES

Example 1

Materials and Methods

The tissue was modeled as a 10-cm diameter spherical domain using a finite element package (Comsol 4.2a, Stockholm, Sweden). Electrodes were modeled as two 1.0-mm diameter blunt tip needles with exposure lengths (Y) and edge-to-edge separation distances (X) given in Table 1. The electrode domains were subtracted from the tissue domain, effectively modeling the electrodes as boundary conditions.

TABLE 1

Electrode configuration and relevant electroporation-based treatment values used in study.		
	PARAMETER VALUES	MEAN
W [V/cm]	500, 1000, 1500, 2000, 2500, 3000	1750
X [cm]	0.5, 1.0, 1.5, 2.0, 2.5	1.5
Y [cm]	0.5, 1.0, 1.5, 2.0, 2.5, 3.0	1.75
Z [cm]	1.0, 1.25, 1.5, 2.0, 3.0, 4.0, 5.0, 6.0	2.968 75

The electric field distribution associated with the applied pulse is given by solving the Laplace equation:

$$\nabla \cdot (\sigma(E)\nabla\varphi)=0 \tag{1}$$

where  $\sigma$  is the electrical conductivity of the tissue, E is the electric field in V/cm, and  $\varphi$  is the electrical potential (Edd and Davalos, 2007). Boundaries along the tissue in contact with the energized electrode were defined as  $\varphi=V_o$ , and boundaries at the interface of the other electrode were set to ground. The applied voltages were manipulated to ensure that the voltage-to-distance ratios (VV) corresponded to those in Table 1. The remaining boundaries were treated as electrically insulating,  $\partial\varphi/\partial n=0$ .

The analyzed domain extends far enough from the area of interest (i.e. the area near the electrodes) that the electrically insulating boundaries at the edges of the domain do not significantly influence the results in the treatment zone. The physics-controlled finer mesh with ~100,000 elements was used. The numerical models have been adapted to account for a dynamic tissue conductivity that occurs as a result of electroporation, which is described by an asymmetrical Gompertz curve for renal porcine tissue (Neal et al., 2012):

$$\sigma(E)=\sigma_o+(\sigma_{max}-\sigma_o)\exp[-A\cdot\exp[-B\cdot E]] \tag{2}$$

where  $\sigma_o$  is the non-electroporated tissue conductivity and  $\sigma_{max}$  is the maximum conductivity for thoroughly permeabilized cells, A and B are coefficients for the displacement and growth rate of the curve, respectively. Here, it is assumed that  $\sigma_o=0.1$  S/m but this value can be scaled by a factor to match any other non-electroporated tissue conductivity or material as determined by a pre-treatment pulse. In this work the effect of the ratio of maximum conductivity to

baseline conductivity in the resulting electric current was examined using the 50- $\mu$ s pulse parameters ( $A=3.05271$ ;  $B=0.00233$ ) reported by Neal et al. (Neal et. al., 2012). The asymmetrical Gompertz function showing the tissue electric conductivity as a function of electric field is, for example, shown in FIG. 5.

The current density was integrated over the surface of the ground electrode to determine the total current delivered. A regression analysis on the resulting current was performed to determine the effect of the parameters investigated and their interactions using the NonlinearModelFit function in Wolfram Mathematica 8.0. Current data from the numerical simulations were fit to a mathematical expression that accounted for all possible interactions between the parameters:

$$I=\text{factor}[aW+bX+cY+dZ+e(W-\bar{W})(X-\bar{X})+f(W-\bar{W})(Y-\bar{Y})+g(W-\bar{W})(Z-\bar{Z})+h(X-\bar{X})(Y-\bar{Y})+i(X-\bar{X})(Z-\bar{Z})+j(Y-\bar{Y})(Z-\bar{Z})+k(W-\bar{W})(X-\bar{X})(Y-\bar{Y})+l(X-\bar{X})(Y-\bar{Y})(Z-\bar{Z})+m(W-\bar{W})(Y-\bar{Y})(Z-\bar{Z})+n(W-\bar{W})(X-\bar{X})(Z-\bar{Z})+o(W-\bar{W})(X-\bar{X})(Y-\bar{Y})(Z-\bar{Z})+p] \tag{3}$$

where I is the current in amps, W is the voltage-to-distance ratio [V/cm], X is the edge-to-edge distance [cm], Y is the exposure length [cm], and Z is the unitless ratio  $\sigma_{max}/\sigma_o$ . The  $\bar{W}$ ,  $\bar{X}$ ,  $\bar{Y}$ , and  $\bar{Z}$  are means for each of their corresponding parameters (Table 1) and the coefficients (a, b, c, . . . , n, o, p) were determined from the regression analysis (Table 2).

Results.

A method to determine electric conductivity change following treatment based on current measurements and electrode configuration is provided. The best-fit statistical (numerical) model between the W, X, Y, and Z parameters resulted in Eqn. 3 with the coefficients in Table 2 ( $R^2=0.999646$ ). Every coefficient and their interactions had statistical significant effects on the resulting current ( $P<0.0001^*$ ). With this equation one can predict the current for any combination of the W, Y, X, Z parameters studied within their ranges ( $500 \text{ V/cm} \leq W \leq 3000 \text{ V/cm}$ ,  $0.5 \text{ cm} \leq X \leq 2.5 \text{ cm}$ ,  $0.5 \text{ cm} \leq Y \leq 3.0 \text{ cm}$ , and  $1.0 \leq Z \leq 6.0$ ). Additionally, by using the linear results ( $Z=1$ ), the baseline tissue conductivity can be extrapolated for any blunt-tip electrode configuration by delivering and measuring the current of a non-electroporating pre-treatment pulse. The techniques described in this specification could also be used to determine the conductivity of other materials, such as non-biological materials, or phantoms.

TABLE 2

Coefficients ( $P < 0.0001^*$ ) from the Least Square analysis using the NonlinearModelFit function in Mathematica.	
	ESTIMATE
a $\rightarrow$	0.00820
b $\rightarrow$	7.18533
c $\rightarrow$	5.80997
d $\rightarrow$	3.73939
e $\rightarrow$	0.00459
f $\rightarrow$	0.00390
g $\rightarrow$	0.00271
h $\rightarrow$	3.05537
i $\rightarrow$	2.18763
j $\rightarrow$	1.73269
k $\rightarrow$	0.00201
l $\rightarrow$	0.92272
m $\rightarrow$	0.00129
n $\rightarrow$	0.00152
o $\rightarrow$	0.00067
p $\rightarrow$	-33.92640

FIG. 6 shows a representative case in which the effect of the W and Z are studied for electroporation-based therapies with 2.0 cm electrodes separated by 1.5 cm. The 3D plot corroborates the quality of the model which shows every data point from the numerical simulation (green spheres) being intersected by the best-fit statistical (numerical) model. This 3D plot also shows that when Z is kept constant, the current increases linearly with the voltage-to-distance ratio (W). Similarly, the current increases linearly with Z when the voltage-to-distance ratio is constant. However, for all the other scenarios there is a non-linear response in the current that becomes more drastic with simultaneous increases in Wand Z

In order to fully understand the predictive capability of the statistical (numerical) model, two cases in which the current is presented as a function of the exposure length and electrode separation are provided. FIG. 7A shows the linear case (Z=1) in which the current can be scaled to predict any other combination of pulse parameters as long as the pulses do not achieve electroporation. For example, one can deliver a non-electroporation pulse (~50 V/cm) and measure current. The current can then be scaled to match one of the W values investigated in this study. By using Eqn. 3 and solving for the factor, the baseline electric conductivity of the tissue can be determined and used for treatment planning. FIG. 7B is the case in which the maximum electric conductivity was 0.4 S/m (Z=4) after electroporation. The trends are similar to the ones described in FIG. 5 in that if exposure length is constant, the current increases linearly with increasing electrode separation and vice versa. However, even though the conductivity within the treated region increases by a factor of 4, the current increases non-linearly only by a factor of 3. This can be seen by comparing the contours in FIG. 7A with those in FIG. 7B which consistently show that the curves are increased by a factor of 3.

Example 2

Determining the Relationship between Blunt Tip Electrode Configuration and Resulting Current after IRE Treatment

Model Assumptions:  
 Gompertz Conductivity: Pulse duration=50 μs, Ex-vivo kidney tissue  
 Baseline Conductivity: σ=0.1 S/m  
 Spherical Domain: diameter=10 cm  
 Applied Voltage: Voltage=1000 V  
 Parametric Study:  
 Total Combinations: 720 models  
 Maximum Conductivity: 1.0x, 1.25x, 1.5x, 2x, 3x, 4x, 5x, 6x the baseline  
 Edge-to-edge Distance: 5, 10, 15, 20, 25 mm  
 Electrode Exposure: 5, 10, 15, 20, 25, 30 mm  
 Electrode Radius: 0.5, 0.75, 1.0 mm  
 The output of statistical analysis software (JMP 9.0) used to fit model and determine the coefficients for all parameter combinations is shown in the tables of FIGS. 8A and 8B and the plot of FIG. 8C.

Parameters of Best Fit for Dynamic Conductivity Changes between 1x-6x the Baseline Conductivity (R<sup>2</sup>=0.96):

- a=-1.428057; (\*Intercept Estimate\*)
- b=-0.168944; (\*Gap Estimate\*)
- c=2.1250608; (\*Radius Estimate\*)
- d=0.2101464; (\*Exposure Estimate\*)
- e=1.1114726; (\*Factor Estimate\*)

- f=-0.115352; (\*Gap-Radius Estimate\*)
- g=-0.010131; (\*Gap-Exposure Estimate\*)
- h=-0.067208; (\*Gap-Factor\*)
- i=0.0822932; (\*Radius-Exposure Estimate\*)
- j=0.4364513; (\*Radius-Factor Estimate\*)
- k=0.0493234; (\*Exposure-Factor Estimate\*)
- l=-0.006104; (\*Gap-Radius-Exposure Estimate\*)
- m=0.0165237; (\*Radius-Exposure-Factor Estimate\*)
- n=-0.003861; (\*Gap-Exposure-Factor Estimate\*)
- o=-0.041303; (\*Gap-Radius-Factor Estimate\*)
- p=-0.002042; (\*Gap-Radius-Exposure-Factor Estimate\*)

Analytical Function for Dynamic Conductivity Changes Between 1x-6x the Baseline Conductivity (R<sup>2</sup>=0.96):

$$5 \text{ mm} < \text{gap} = x < 25 \text{ mm}, 0.5 \text{ mm} < \text{radius} = y < 1.0 \text{ mm}, \\ 5 \text{ mm} < \text{exposure} = z < 30 \text{ mm}, 1 < \text{factor} = w < 6$$

Default conductivity of 0.1 S/m and 1000 V which can be scaled for dynamic conductivities. The function is a linear combination of all iterations examined in the parametric study:

$$\text{Current}(w,x,y,z) = a + bx + cy + dz + ew + f(x+bb)(y+cc) + g(x+bb)(z+dd) + h(x+bb)(w+ee) + i(y+cc)(z+dd) + j(y+cc)(w+ee) + k(z+dd)(w+ee) + l(x+bb)(y+cc) + m(y+cc)(z+dd)(w+ee) + n(x+bb)(z+dd)(w+ee) + o(x+bb)(y+cc)(w+ee) + p(x+bb)(y+cc)(z+dd)(w+ee)$$

FIGS. 9A-9E show the representative (15 mm gap) correlation between current vs. exposure length and electrode radius for maximum conductivities (1x-6x, respectively).

FIGS. 10A and 10B are tables showing experimental validation of the code for determining the tissue/potato dynamic conductivity from in vitro measurements.

Determining the Relationship Between Blunt Tip Electrode Configuration and e-Field Distribution after IRE Treatment

Model Assumptions:

- Gompertz Conductivity: Pulse duration=50 μs, Ex-vivo kidney tissue
- Baseline Conductivity: σ=0.1 S/m
- Spherical Domain: diameter=10 cm
- Electrode Radius: r=0.5 mm
- Parametric Study:  
 Total Combinations: 1440 models  
 Maximum Conductivity: 1.0x, 1.25x, 1.5x, 2x, 3x, 4x, 5x, 6x the baseline  
 Edge-to-edge Distance: 5, 10, 15, 20, 25 mm  
 Electrode Exposure: 5, 10, 15, 20, 25, 30 mm  
 Voltage-to-distance Ratio: 500, 1000, 1500, 2000, 2500, 3000 V/cm

Example 3

Comparison of analytical solutions with statistical (numerical) model to calculate current and explanation of procedure that results in 3D IRE volume.

The process of backing-out the electrical conductivity using the analytical solutions and the one proposed in the "Towards a Predictive Model of Electroporation-Based Therapies using Pre-Pulse Electrical Measurements" abstract presented in the IEEE Engineering in Medicine and Biology Conference in Aug. 28, 2012 in San Diego, Calif. were compared. A method to determine the predictive power of the equations to calculate current is analyzing the residuals of the 1440 combinations of parameters examined. In the context of this specification, a residual is the difference between the predicted current and the actual current. As can be seen in FIGS. 11A and 11B with increasing non-linear change in conductivity due to electroporation and increasing applied electric field there is an increase in the residual for

both cases. The main message though is that using the shape factor (analytical) method the maximum residual is 11.3502 A and with the statistical (numerical) model the maximum is 1.55583 A. This analysis suggests that the shape factor method may be inadequate to predict the non-linear changes in current that occur during electroporation and for reliable predictions the statistical (numerical) method may be better.

In terms of the prediction of the volume treated a representative method is to map out the electric field 5 cm in the directions along the (x,0,0), (0,y,0), and (0,0,z) axes from the origin. In addition, the electric field can be extracted along a line that starts at the origin and ends at 3 cm along each of the axes. These plots contain the information for determining the distances at which a particular IRE threshold occurs. In embodiments, 1440 different parameter combinations were simulated that resulted in data sets of 28,692 (x-direction), 20,538 (y-direction), 27,306 (z-direction), and 25,116 (xyz-direction) for homogeneous conductivity. Even though these simulations only include dynamic conductivity changes due to electroporation, it is believed that an identical analysis for simulations that also include the changes in conductivity due to temperature could also be performed. In this manner, it would be possible to determine irreversible electroporation thresholds as a function of temperature and electroporation. Manipulating these large data sets is challenging but it provides all the necessary information to study the effect of electrode separation, electrode length, dynamic conductivity factor, and voltage-to-distance ratio for any position along the described paths. In order to be able to manipulate the data and extract the distance for different IRE thresholds, the function NonlinearModelFit (Mathematica) was used in order to come up with analytical expressions that would closely match the electric field. A different function was used for each of the directions studied in the positive directions along the Cartesian coordinate system. The Micheilis Menten function was used along the x-direction ( $R^2=0.978978$ ), the analytical solution to the Laplace equation along the y-direction ( $R^2=0.993262$ ), and the Logistic equation in the z-direction ( $R^2=0.983204$ ). Each of those functions was scaled by a 3rd order polynomial function that enabled the fit to incorporate the electrode separation and electrode exposure as well. Even though the described functions were used to fit the data from the numerical data, there might be other functions that are also appropriate and this will be explored further in order to use the most reliable fit. In FIGS. 12A-12C provided are representative contour plots of the electric field strength at 1.0 cm from the origin using an edge-to-edge voltage-to-distance ratio of 1500 V/cm assuming a  $z=1$  which is the case for non-electroporated electrical conductivity. It is important to note that in this case the y and z data are starting from (0, 0, 0) and the x-data starts outside the external electrode-tissue boundary. One representative case is presented, but any of the 1440 parameters combinations that were disclosed in the conference proceeding could be plotted as well.

The following functions describe the electric field [V/cm] distributions along the x-axis ( $E_x$ ), y-axis ( $E_y$ ), and z-axis ( $E_z$ ) as a function of voltage-to-distance (W), edge-to-edge separation between the electrodes (X), exposure length (Y), maximum conductivity to baseline conductivity (Z), and distance in the x-direction (xx), y-direction (yy), and z-direction (zz).

$$E_x(W,X,Y,Z,xx)=W*(a*Exp[-b*xx]+c)* \\ (dX^3+eX^2+fX+gY^2+hY^2+iY+j)+k$$

Micheilis Menten  
Equation (electric field  
in the x-direction)

The coefficients for the NonlinearModelFit are given below:

$a=-0.447392$ ,  $b=8.98279$ ,  $c=-0.0156167$ ,  $d=-0.0654974$ ,  
 $e=0.468234$ ,  $f=-6.17716$ ,  $g=0.326307$ ,  $h=-2.33953$ ,  
 $I=5.90586$ ,  $j=-4.83018$ ,  $k=-9.44083$

Laplace Equation (Electric Field in the y-Direction)

$$E_y(W, X, Y, Z, yy) = a + (X^3 + X^2 + bX + cY^3 + dY^2 + eY + f) *$$

$$\left( h + \frac{(gWYZ)}{2} * \left( \frac{1}{\text{Log}\left[\frac{X+0.1}{0.05}\right]} \right) * \right.$$

$$\left. \text{Abs}\left[ \frac{1}{\left[ \frac{1}{\text{Log}\left[\frac{X}{0.05}\right]} - \frac{1}{\text{Log}\left[\frac{X}{0.05}\right]} \right]} - \frac{1}{\left[ \frac{1}{\text{Log}\left[\frac{X}{0.05}\right]} + \frac{1}{\text{Log}\left[\frac{X}{0.05}\right]} \right]} \right] \right)$$

The coefficients for the NonlinearModelFit are given below:

$a=-56.6597$ ,  $b=-42.9322$ ,  $c=6.66389$ ,  $d=-50.8391$ ,  
 $e=141.263$ ,  $f=138.934$ ,  $g=0.00417123$ ,  $h=0.184109$

Logistic Equation (electric field in the z-direction)

$$E_z(W, X, Y, Z, zz) = a +$$

$$\frac{bWZ}{1 + c \cdot \text{Exp}\left[d \cdot \left(\frac{2zz}{y} - e\right)\right]} \cdot (fX^3 + gX^2 + hX + i) \cdot (jY^3 + kY^2 + lY + m)$$

The coefficients for the NonlinearModelFit are given below:

$a=49.0995$ ,  $b=-0.00309563$ ,  $c=1.39341$ ,  $d=4.02546$ ,  
 $e=1.24714$ ,  $f=0.276404$ ,  $g=-1.84076$ ,  $h=4.93473$ ,  
 $I=-9.13219$ ,  $j=0.699588$ ,  $k=-5.0242$ ,  $l=12.8624$ ,  
 $m=19.9113$ .

In order to visualize the predicted IRE shape the equation of an ellipsoid was used and the semi-axes were forced to intersect with the locations at which the IRE threshold wants to be examined. Therefore, the provided functions can be adjusted in real-time to display the IRE volume for any electric field threshold. This is important since different tissues have different IRE thresholds that depend on the temperature, dielectric properties of the tissue, the electrode configuration, and the pulse parameters used. Once again, even though the equation for an ellipsoid is used to represent the IRE volume, other functions may be evaluated that may also be appropriate to replicate the morphology of the zones of ablation being achieved experimentally such as the Cassini curve. A 1500 V/cm was used as the voltage-to-distance ratio, electrode exposure 2 cm, and electrode separation 1.5 cm to generate 3 different IRE zones using 1000 V/cm, 750 V/cm, and 500 V/cm as the IRE thresholds with  $z=1$ .

From the 3D plots representing the zones of ablation shown in FIGS. 13A-13C it can be seen that if the IRE threshold is reduced from 1000 V/cm to either 750 V/cm or 500 V/cm, the volume becomes larger. This is representative of how different tissues may have different thresholds and this code may provide the ability to simulate the fields in a broad/generic manner that can then be applied to any tissue. Incorporating the xyz-data that was extracted from the parametric study will help modify the "roundness" of the current depictions of the zone of IRE ablation in order to more realistically replicate the experimental results. However, to the best of the inventors' knowledge there is no such adaptable code currently available to provide a 3D IRE volume as a function of measured current, electrode length,

electrode exposure, applied voltage-to-distance ratio, and customizable electric field threshold so it is believed that this will greatly help the medical community in planning and verifying the clinical treatments of patients being treated with the IRE technology.

Example 4

Specific Conductivity

Specific conductivity can be important in embodiments for treatment planning of irreversible electroporation (IRE). For many applications, especially when treating tumors in the brain, the volume (area) of IRE should be predicted to maximize the ablation of the tumorous tissue while minimizing the damage to surrounding healthy tissue. The specific electrical conductivity of tissue during an irreversible electroporation (IRE) procedure allows the physicians to: determine the current threshold; minimize the electric current dose; decrease the Joule heating; and reduce damage to surrounding healthy tissue. To measure the specific conductivity of tissue prior to an IRE procedure the physician typically performs one or more of the following: establishes the electrode geometry (shape factor); determines the physical dimensions of the tissue; applies a small excitation AC voltage signal (1 to 10 mV); measures the AC current response; calculates the specific conductivity ( $\sigma$ ) using results from the prior steps. This procedure tends to not generate tissue damage (low amplitude AC signals) and will supply the physician (software) with the required information to optimize IRE treatment planning, especially in sensitive organs like the brain which is susceptible to high electrical currents and temperatures. Thus, the IRE procedure is well monitored and can also serve as a feedback system in between series of pulses and even after the treatment to evaluate the area of ablation.

Special Cases for electrode geometry

Nomenclature (units in brackets):

$V_e$ =voltage on the hot electrode (the highest voltage), [V]

$G$ =electroporation voltage gradient (required for electroporation), [V/m]

$R_1$ =radius of electrode with highest voltage (inner radius), [m]

$R_2$ =radius at which the outer electrodes are arranged (outer radius), [m]

$i$ =total current, [A]

$L$ =length of cylindrical electrode, [m]

$A$ =area of plate electrode, [m<sup>2</sup>]

$\sigma$ =electrical conductivity of tissue, [S/m]

$\rho$ =density

$c$ =heat capacity

Case 1

Electrical conduction between a two-cylinder (needle) arrangement of length  $L$  in an infinite medium (tissue). It is important to note that this formulation is most accurate when  $L \gg R_1, R_2$  and  $L \gg w$ . The electrical conductivity can be calculated from,

$$\sigma = \frac{i \cdot S}{V_e}$$

where the shape factor ( $S$ ) corresponding to the electrode dimensions and configuration is given by,

$$\frac{2 \cdot \pi \cdot L}{\cosh^{-1}\left(\frac{4 \cdot w^2 - (2 \cdot R_1)^2 - (2 \cdot R_2)^2}{8 \cdot R_1 \cdot R_2}\right)}$$

Case 2

Cylindrical arrangement in which the central electrode is a cylinder (needle) with radius  $R_1$  and the outer electrodes are arranged in a cylindrical shell with a shell radius of  $R_2$  (not the radius of the electrodes). The voltage on the central electrode is  $V_e$ . The voltage distribution in the tissue may be determined as a function of radius,  $r$ :

$$V = V_e \frac{\ln \frac{r}{R_2}}{\ln \frac{R_2}{R_1}}$$

The required voltage on the central electrode to achieve IRE:

$$V_e = GR_2 \ln \frac{R_2}{R_1}$$

The required current on the central electrode:

$$i = \frac{2\pi L \sigma V_e}{\ln \frac{R_2}{R_1}}$$

The specific conductivity ( $\sigma$ ) of the tissue can be calculated since the voltage signal ( $V_e$ ) and the current responses (i) are known.

Explanation of Electrical Concepts.

By using the bipolar electrode described previously in US Patent Application Publication No. 2010/0030211A1, one can apply a small excitation AC voltage signal (for example from about 1 to 10 mV),

$$V(t) = V_0 \sin(\omega t)$$

where  $V(t)$  is the potential at time  $t$ ,  $V_0$  is the amplitude of the excitation signal and  $\omega$  is the frequency in radians/s. The reason for using a small excitation signal is to get a response that is pseudo-linear since in this manner the value for the impedance can be determined indicating the ability of a system (tissue) to resist the flow of electrical current. The measured AC current (response) that is generated by the excitation signal is described by

$$I(t) = I_0 \sin(\omega t + \theta)$$

where  $I(t)$  is the response signal,  $I_0$  is the amplitude of the response ( $I_0 \neq V_0$ ) and  $\theta$  is the phase shift of the signal. The impedance ( $Z$ ) of the system (tissue) is described by,

$$Z = \frac{V(t)}{I(t)} = \frac{V_0 \sin(\omega t)}{I_0 \sin(\omega t + \theta)} = Z_0 \frac{\sin(\omega t)}{\sin(\omega t + \theta)}$$

It is important to note that the measurement of the response is at the same excitation frequency as the AC voltage signal to prevent interfering signals that could compromise the results. The magnitude of the impedance  $|Z_0|$  is the electrical resistance of the tissue. The electrical resistivity ( $\Omega m$ ) can be determined from the resistance and the physical dimensions of the tissue in addition to the

electrode geometry (shape factor). The reciprocal of the electrical resistivity is the electrical conductivity (S/m). Therefore, after deriving the electrical resistivity from the methods described above, the conductivity may be determined.

As described in U.S. Patent Application No. 61/694,144 the analytical solution (Table 4) assumes that the length of the electrodes is much larger than the electrode radius or separation distance between the electrodes. Additionally, the analytical solution is not capable of capturing the non-linear electrical response of the tissue during electroporation procedures. The proposed statistical algorithm (Table 3) is preferably used in order to capture the response in treatments that are being conducted clinically and show how the analytical overestimates the baseline and maximum current that uses the experimental data.

TABLE 3

Determination of conductivity using the statistical model and in vivo data from pre-pulse and IRE pulses in canine kidney tissue using identical electrode configuration that the experimental one described below.

	Current [A]	Voltage [V]	Volt-2-Dist [V/cm]	Conductivity [S/m]	Z = $\sigma_{max}/\sigma_{min}$
Pre-Pulse	0.258	48	53	0.365	—
IRE-Pulse	20.6	1758	1953	1.037	2.841
IRE-Pulse	23.7	1758	1953	1.212	3.320
IRE-Pulse	23.6	1758	1953	1.207	3.305
Avg. IRE	22.6	1758	1953	1.150	3.150
IRE-Pulse	10.4	1259	1399	0.727	1.990
IRE-Pulse	11.1	1257	1397	0.789	2.162
IRE-Pulse	11	1257	1397	0.781	2.138
Avg. IRE	10.8	1257	1397	0.763	2.090
Pre-Pulse	0.343	73.3	52	0.341	—
IRE-Pulse	23.6	2262	1616	1.007	2.952
IRE-Pulse	24.3	2262	1616	1.041	3.051
IRE-Pulse	25.4	2262	1616	1.094	3.207
Avg. IRE	24.5	2262	1616	1.050	3.080

TABLE 4

Determination of conductivity using the analytical model and in vivo data from pre-pulse and IRE pulses in canine kidney tissue using identical electrode configuration than the experimental one described below. Assumption: Length >> radius, Length >> width, 2 cylindrical electrodes in an infinite medium.

	Current [A]	Voltage [V]	Volt-2-Dist [V/cm]	Shape Factor [m]	Conductivity [S/m]
Pre-Pulse	0.258	48	53	0.01050	0.512
IRE-Pulse	20.6	1758	1953	0.01050	1.116
IRE-Pulse	23.7	1758	1953	0.01050	1.284
IRE-Pulse	23.6	1758	1953	0.01050	1.279
Avg. IRE	22.6	1758	1953	0.01050	1.225
IRE-Pulse	10.4	1259	1399	0.01050	0.787
IRE-Pulse	11.1	1257	1397	0.01050	0.841
IRE-Pulse	11	1257	1397	0.01050	0.834
Avg. IRE	10.8	1257	1397	0.01050	0.819
Pre-Pulse	0.343	73.3	52	0.00924	0.506
IRE-Pulse	23.6	2262	1616	0.00924	1.129
IRE-Pulse	24.3	2262	1616	0.00924	1.163
IRE-Pulse	25.4	2262	1616	0.00924	1.215
Avg. IRE	24.5	2262	1616	0.00924	1.172

In Vivo Experiments

1) Animals.

IRE ablations were performed in canine kidneys in a procedure approved by the local animal ethics committee. Male canines weighing approximately 30 kg were premedicated with acetylpromazine (0.1 mg/kg), atropine (0.05 mg/kg), and morphine (0.2 mg/kg) prior to general anesthesia induced with propofol (6 mg/kg, then 0.5 mg/kg/min) and maintained with inhaled isoflurane (1-2%). Anesthetic depth was monitored by bispectral index monitoring (Covidien, Dublin, Ireland) of EEG brain activity. After ensuring adequate anesthesia, a midline incision was made and mesenchymal tissue was maneuvered to access the kidney. Pancuronium was delivered intravenously to mitigate electrically mediated muscle contraction, with an initial dose of 0.2 mg/kg, and adjusted if contractions increased.

2) Experimental Procedure.

Two modified 18 gauge needle electrodes (1.0 mm diameter and 1.0 cm in exposure) were inserted as pairs into the superior, middle, or inferior lobe of the kidney, with lobes being randomly selected. A BTX ECM830 pulse generator (Harvard Apparatus, Cambridge, Mass.) was used to deliver an initial 100  $\mu$ s pre-pulse of 50 V/cm voltage-to-distance ratio (center-to-center) between the electrodes to get an initial current able to be used to determine baseline conductivity. Electrical current was measured with a Tektronix TCP305 electromagnetic induction current probe connected to a TCPA300 amplifier (both Tektronix, Beaverton, Ore.). A Protek DSO-2090 USB computer-interface oscilloscope provided current measurements on a laptop using the included DSO-2090 software (both GS Instruments, Incheon, Korea). A schematic of the experimental setup can be found in FIG. 14A. Following the pre-pulse, a series of 100 pulses, each 100  $\mu$ s long, at a rate of 1 pulse per second was delivered, reversing polarity after 50 pulses. A five second pause was encountered after pulses 10 and 50 to save data. A schematic diagram showing dimension labeling conventions is shown in FIG. 14B. Representative current waveforms from a pre-pulse and experimental pulse can be found in FIGS. 14C and 14D, respectively. Electrode exposure lengths were set to 1 cm for all trials. The separation distance between electrodes and applied voltage may be found in Table 5. After completing pulse delivery, the electrodes were removed. Two additional ablations were performed in the remaining lobes before repeating the procedure on the contralateral kidney, resulting in a total of three ablations per kidney and six per canine.

TABLE 5

KIDNEY EXPERIMENT PROTOCOLS IN CANINE SUBJECTS

Setup	Separation, cm	Voltage, V	Voltage-Distance Ratio, V/cm	n
1	1	1250	1250	4
2	1	1750	1750	4
3	1.5	2250	1500	6

3) Kidney Segmentation and 3D Reconstruction.

Numerical models provide an advantageous platform for predicting electroporation treatment effects by simulating electric field, electrical conductivity, and temperature distributions. By understanding the electric field distribution, one can apply an effective lethal electric field threshold for IRE,



$E_{IRE}$ , to predict ablation lesion dimensions under varying pulse protocols (electrode arrangements and applied voltages). However, in order to do so, these models should first be calibrated with experimental data. Here, the numerical simulation algorithm developed from porcine kidneys was expanded that accounts for conductivity changes using an asymmetrical sigmoid function (R. E. Neal, 2nd, et al., "Experimental characterization and numerical modeling of tissue electrical conductivity during pulsed electric fields for irreversible electroporation treatment planning," IEEE Trans Biomed Eng., vol. 59, pp. 1076-85. Epub 2012 Jan. 6, 2012 ("R. E. Neal, 2<sup>nd</sup>, et al., 2012"). The model is calibrated to the experimental lesions to determine an effective electric field threshold under the three experimental setups used. In addition, static and linear conductivity functions are also correlated to the lesion dimensions. The three functions are used to evaluate which numerical technique will result in better accuracy in matching lesion shapes and resulting current from actual IRE ablations in mammalian tissue, particularly for kidney.

The imaging-based computational model domains were constructed from a magnetic resonance imaging (MRI) scan of a kidney from a canine subject of similar size to those in the study. The scans were scaled by 1.21 times in all directions to better match the experimental kidney dimensions while maintaining the anatomical characteristics. Mimics 14.1 image analysis software (Materialise, Leuven, BG) was used to segment the kidney geometry from the surrounding tissues. The kidney was traced in each of the two-dimensional (2D) MRI axial slices, which were then integrated into a three-dimensional (3D) solid representation of the kidney volume which was refined and exported to 3-matic version 6.1 (Materialise, Leuven, BG) to generate a volumetric mesh compatible with Comsol Multiphysics finite element modeling software (Comsol Multiphysics, v.4.2a, Stockholm, Sweden).

Electrodes were simulated as paired cylinders, each 1 cm long and 1 mm in diameter, and separated by 1 or 1.5 cm to represent the two experimental conditions. The pairs were inserted into the 3D kidney mesh in two configurations, representing both experimental approaches that used either the superior/inferior (vertical) or middle (horizontal) lobe of the kidney, both with tips 1.5 cm deep. The finite element model simulated the electric field distribution in the kidney, which was used to determine cell death EIRE by correlating the electric field values with the average in vivo lesion height and width dimensions.

4) Electric Field Distribution and Lethal  $E_{IRE}$  Determination.

The electric field distribution is determined according to

$$-\nabla \cdot (\sigma(E) \nabla \phi) = 0 \tag{1}$$

where  $\sigma$  is the electrical conductivity of the tissue,  $E$  is the electric field in V/cm, and  $\phi$  is the electrical potential. Tissue-electrode boundaries for the cathode and anode were defined as  $\phi = V_0$  and ground, respectively. The remaining boundaries were treated as electrically insulating,  $d\phi/dn = 0$ , since the kidneys were isolated from the surrounding mesenchymal tissue during the experimental procedures. The current density was integrated over a mid-plane parallel to both electrodes to determine simulated electric current.

The model was solved for the vertical and horizontal electrode configurations, each considering three electrical conductivity tissue responses. These responses included a homogeneous static conductivity ( $\sigma_0$ ) as well as two that

dynamic models are based on a relationship between a minimum baseline and a maximum conductivity. The static conductivity model was used to determine the baseline conductivity,  $\sigma_0$ , by matching simulated electrical current with the pre-pulse experimental data, where the field strength should be below that able to permeabilize any cells in the tissue. The maximum conductivity,  $\sigma_{max}$ , occurs when the number of cells electroporated in the tissue has saturated, and the cellular membranes no longer restrict the extent of interstitial electrolyte mobility. The statistical model discussed in (P. A. Garcia, et al., "Towards a predictive model of electroporation-based therapies using pre-pulse electrical measurements," Conf Proc IEEE Eng Med Biol Soc, vol. 2012, pp. 2575-8, 2012 ("P. A. Garcia, et al., 2012")) was used to predict  $\sigma_{max}$  from previously characterized tissue response to pre-pulse  $\sigma_0$  and electrical data.

The  $\sigma_0$  and  $\sigma_{max}$  values provide the required parameters to define the electric field-dependent conductivity,  $\sigma(E)$ , of renal tissue in vivo. One model assumed a linear relationship that grew between the minimum and maximum conductivities over a range from 200 to 2000 V/cm,  $\sigma_L(E)$ , and the second used an asymmetrical sigmoid Gompertz curve,  $\sigma_S(E)$ , derived from the work described in (R. E. Neal, 2nd, et al., 2012) using the equation:

$$\sigma_S(E) = \sigma_0 + (\sigma_{max} - \sigma_0) \exp[-A \exp(-B \cdot E)] \tag{2}$$

where  $A$  and  $B$  are unitless coefficients that vary with pulse length,  $t(s)$ . This function was fit using curve parameters for a 100  $\mu s$  long pulse, where  $A=3.053$  and  $B = 0.00233$  (R. E. Neal, 2<sup>nd</sup>, et al., 2012)

The electric field distribution along a width and height projection based at the midpoint length of the electrodes was used to determine the electric field magnitude that matched experimental lesion dimensions. This was performed for all three conductivity scenarios in all three experimental protocol setups in order to determine which model best matched the IRE ablations, providing the optimum conductivity modeling technique for mammalian tissue.

5) Results: In Vivo Experiments.

Electrical Currents.

All animals survived the procedures without adverse event until euthanasia. Electrical pre-pulse currents were  $0.258 \pm 0.036$  A (mean  $\pm$  SD) for the 1 cm electrode separation trials and  $0.343 \pm 0.050$  A for the 1.5 cm separation trials. Electrical currents from the trials for pulses 1-10, 40-50, and 90-100 are reported in Table 6. Although currents are typically reported to increase with consecutive pulses, there is no statistically significant correlation between pulse number and measured current. Therefore, all numerical calibrations to match electrical current and determine  $\sigma_{max}$  used the average current from all captured pulses for each experimental setup.

TABLE 6

EXPERIMENTAL ELECTRIC CURRENTS TO CALIBRATE NUMERICAL MODELS				
Setup	Separation, cm	Average Delivered Voltage, V	Pulse Number	Average Electric Current, A*
Pre 1	1	48	1750	0.258 (0.036)
Pre 2	1.5	73	1250	0.343 (0.050)
1	1	1258	1-10	10.4 (1.7)
			40-50	11.1 (1.1)
			90-100	11.0 (1.7)
2	2	1758	1-10	20.6 (3.2)
			40-50	23.7 (5.1)
			90-100	23.6 (3.8)
3	1.5	2262	1-10	23.6 (1.47)
			40-50	24.3 (3.25)
			90-100	25.4 (3.27)

\*Currents given as "average (standard deviation)"

6) Determination of Dynamic Conductivity Function.

Pre-pulse electrical current was used to calculate the baseline conductivity,  $\sigma_0$ , used in the static numerical simulation. In addition, the baseline and maximum,  $\sigma_{max}$ , electrical conductivities required for generating the asymmetrical sigmoid and linear dynamic conductivity functions were calculated according to the procedure outlined in (P. A. Garcia, et al., 2012) and are provided in Table 7. The ratio between these conductivities was calculated and demonstrates an increase in conductivity between 2.09 and 3.15 times, consistent with values determined in the literature for other organs (N. Pavselj, et al., "The course of tissue permeabilization studied on a mathematical model of a subcutaneous tumor in small animals," IEEE Trans Biomed Eng, vol. 52, pp. 1373-81, August 2005).

TABLE 7

BASELINE AND MAXIMUM ELECTRIC CONDUCTIVITIES					
Setup	Gap, cm	V/d Ratio, V/cm	$\sigma_0$	$\sigma_{max}$	$\sigma_{max}/\sigma_0$
1	1	1250	0.365	0.763	2.09
2	1	1750	0.365	1.150	3.15
3	1.5	1500	0.341	1.050	3.08

Example 6

How to Use the Ratio of Maximum Conductivity to Baseline Conductivity in Modifying the Electric Field Distribution and Thus the Cassini Oval Equation

Irreversible electroporation (IRE) is a promising new method for the focal ablation of undesirable tissue and tumors. The minimally invasive procedure involves placing electrodes into the region of interest and delivering a series of low energy electric pulses to induce irrecoverable structural changes in cell membranes, thus achieving tissue death. To achieve IRE, the electric field in the region of interest needs to be above a critical threshold, which is dependent on a variety of conditions such as the physical properties of the tissue, electrode geometry and pulse parameters. Additionally, the electric conductivity of the tissue changes as a result of the pulses, redistributing the electric field and thus the treatment area. The effect of a dynamic conductivity around the electrodes where the highest electric fields are generated was investigated in order to better predict the IRE treatment for clinical use.

The electric field distribution associated with the electric pulse is given by solving the governing Laplace equation,  $\nabla \cdot (\sigma \nabla \varphi) = 0$ , where  $\sigma$  is the tissue electrical conductivity (baseline 0.2 S/m) and  $\varphi$  the electrical potential (3000 V). The dynamic changes in electrical conductivity due to electroporation were modeled with the *flc2hs* Heaviside function within the finite element modeling software used in the study (Comsol Multiphysics 3.5a, Stockholm, Sweden). The dynamic conductivity factor ranged between 2.0-7.0 times the baseline value in the regions exceeding 3000 V/cm. The total electrical current, volumes, and lesion shapes from the IRE treatment were evaluated.

FIGS. 15A and 15B display the electric field distributions for the non-electroporated (baseline conductivity) and electroporated (maximum/baseline conductivity) maps, respectively. The electric field from using the baseline conductivity resulted in a "peanut" shape distribution (FIG. 15A). By

incorporating the conductivity ratio between  $\sigma_{max}/\sigma_0$ , there is a redistribution of the electric field and thus the volumes, currents and lesion shapes are modified as well. The electric field distribution for a 7.0x factor (FIG. 15B), shows a more gradual dissipation of the electric field and a rounder predicted IRE lesion.

A method to predict IRE lesions and incorporate the dynamic changes in conductivity due to electroporation around the electrodes is presented in this example. This procedure provides additional tools to better approximate the electric field distributions in tissue and thus help to generate more reliable IRE treatment planning for clinical use using Finite Element Analysis (FEA) models.

Specifically in order to adapt the Cassini Oval to match experimental lesions or electric field distributions the following procedure should be used:

In IRE treatments, the electric field distribution is the primary factor for dictating defect formation and the resulting volume of treated tissue (J. F. Edd and R. V. Davalos, "Mathematical modeling of irreversible electroporation for treatment planning," Technol Cancer Res Treat, vol. 6, pp. 275-286, 2007; D. Sel, et al., "Sequential finite element model of tissue electroporation," IEEE Trans Biomed Eng, vol. 52, pp. 816-27, May 2005; S. Mahnic-Kalamiza, et al., "Educational application for visualization and analysis of electric field strength in multiple electrode electroporation," BMC Med Educ, vol. 12, p. 102, 2012 ("S. Mahnic-Kalamiza, et al., 2012")). The electric field is influenced by both the geometry and positioning of the electrodes as well as the dielectric tissue properties. Additionally, altered membrane permeability due to electroporation influences the tissue conductivity in a non-linear manner. Therefore numerical techniques are preferably used to account for different electrode configurations and incorporate tissue-specific functions relating the electrical conductivity to the electric field distribution (i.e. extent of electroporation). The inventors are currently using imaging-based computational models for IRE treatment planning that use the physical properties of the tissue and patient-specific 3D anatomical reconstructions to generate electric field distributions (P. A. Garcia, et al., "Non-thermal irreversible electroporation (N-TIRE) and adjuvant fractionated radiotherapeutic multimodal therapy for intracranial malignant glioma in a canine patient," Technol Cancer Res Treat, vol. 10, pp. 73-83, 2011 ("P. A. Garcia, et al, 2011")).

Oftentimes in clinical practice, there is need to rapidly visualize the estimated zone of ablation without relying on complex and time consuming numerical simulations. As an alternative, analytical solutions are powerful techniques that provide valuable insight and offer the ability to rapidly visualize electric field distributions (S. Mahnic-Kalamiza, et al., 2012). However, these analytical solutions assume infinitely long electrodes which are not the case in clinical practice and do not incorporate the non-linear changes in tissue conductivity due to electroporation. Therefore, there is a need for simple, quick, and accurate methods to provide physicians with predicted IRE zones of ablation during surgery when one of the pulse parameters needs to be adjusted. To this end, the inventors have adapted the Cassini curve in an effort to provide researchers and physicians with a graphical representation of IRE zones of ablation, for example, in in vivo porcine liver. The goal of this work is to provide a correlation between experimentally produced zones of ablations in in vivo porcine liver tissue with the corresponding IRE pulse parameters and electrode configuration. These Cassini curves are calibrated to experimental

IRE ablations, and incorporate the dynamic changes in tissue conductivity, a limitation of the analytical approach.

The Cassini oval is a plane curve that derives its set of values based on the distance of any given point,  $a$ , from the fixed location of two foci,  $q_1$  and  $q_2$ , located at  $(x_1, y_1)$  and  $(x_2, y_2)$ . The equation is similar to that of an ellipse, except that it is based on the product of distances from the foci, rather than the sum. This makes the equation for such an oval

$$[(x_1-a)^2+(y_1-a)^2][(x_2-a)^2+(y_2-a)^2]=b^4 \quad (3)$$

where  $b^4$  is a scaling factor to determine the value at any given point. For incorporation of this equation into shapes that mimic the electric field distribution, it is assumed that the two foci were equidistantly located on the x-axis at  $(\pm x, 0)$ . The flexibility of the Cassini curve is crucial since it allows for fitting a wide range of shapes by adjusting the 'a' and/or 'b' parameters from Equation 3 simultaneously and fitting them to the experimental lesion dimensions or the locations at which a particular electric field value results from the computational simulations. The new approach in this analysis is that it is not assumed that the parameter 'a' is related to the separation distance between the electrodes used in IRE treatments for example but will be a second parameter to match the width/depth of any distribution thus allowing for more flexibility between the shapes achieved with the Cassini Oval as can be seen in FIGS. 16A and 16B.

The in vivo experimental data in porcine liver was provided from published studies performed at the Applied Radiology Laboratory of Hadassah Hebrew University Medical Center (P. A. Garcia, et al., 2011). All experiments were performed with Institutional Animal Care and Use Committee approval from the Hebrew University Medical Center. The treatments were performed with a two-needle electrode configuration, 1.5 cm center-to-center separation, 2.0 cm electrode exposure, and an applied voltage of 2250 V. In this paper we only evaluate the effect of pulse number and pulse duration on the resulting 'a' and 'b' parameters required to fit the IRE zones of ablation with the Cassini curve. The NonlinearModelFit function in Wolfram Mathematica 9 was used to determine the 'a' and 'b' parameters (average±standard deviation) for each pulse parameter resulting in three curves for each condition. This same technique can be used to fit the 'a' and 'b' parameters to match the electric field shape at any particular electric field value as well thus providing an avenue to capture the shape for any IRE lesion independent of the tissue or patient.

The NonlinearModelFit results for the 'a' and 'b' parameters to generate the Cassini curves are provided in FIG. 17. The 'a' parameter ranged from 0.75-1.04 and the 'b' from 1.06-1.35 for the average IRE zones of ablation in the in vivo porcine liver. From these data it can be seen that each pulse parameter used results in a unique 'a' and 'b' combination except for the twenty 100-μs pulses and ninety 20-μs pulses which overlap since they had identical IRE ablations. Therefore, consideration should be given to pulse length and total number of pulses when planning treatments to ensure maximum accuracy when using Cassini curves to rapidly predict treatment zones.

FIG. 18 provides a representation of the average IRE zone of ablation and also includes the experimentally achieved standard deviations. This Cassini curve is the most clinically relevant as ninety 100-μs pulses is the recommended setting by the manufacturer that is currently being used by physicians to treat several types of cancer. The Cassini curves in FIG. 18 were generated using two single needle electrodes with  $a=0.821\pm 0.062$  and  $b=1.256\pm 0.079$  that corresponded

to IRE ablations that were  $3.0\pm 0.2$  cm in width and  $1.9\pm 0.1$  cm in depth (P. A. Garcia, et al., 2011). The results suggest that the Cassini curve is a viable method to represent experimentally achieved IRE zones of ablation. These curves can be used to provide physicians with simple, quick, and accurate prediction of IRE treatments. The parameters generated in this study were achieved from porcine liver ablations data. The parameters for other tissues and/or tumors can be determined in a similar manner. Cassini curve parameters should be re-calibrated if the pulse parameters or electrode configuration (i.e. separation or exposure) deviate from the typical protocols in Ben-David et al. Additionally, there is a need to calibrate these Cassini curves to electric and temperature distributions in order to take advantage of the relatively simple curves in representing simulated solutions that account for other pulse parameters and electrode configuration including different electrode separations, diameter, exposure, and voltages. A method to represent IRE zones of ablation in a computationally efficient manner and based on experimental data is thus presented. Such methods can be used to predict IRE ablation in liver in order to provide physicians with an immediate tool for treatment planning.

FIG. 19 is a representation of the 3D Electric Field [V/cm] Distribution in Non-Electroporated (Baseline) Tissue with 1.5-cm Single Needle Electrodes at a Separation of 2.0 cm and 3000 V applied.

FIGS. 20A-D are representations of the Electric Field [V/cm] Distributions from the 3D Non-Electroporated (Baseline) Models with 1.5-cm Electrodes at a Separation of 2.0 cm and 3000 V (cross-sections), wherein FIG. 20A is a representation of the x-y plane mid-electrode length, FIG. 20B is a representation of the x-z plane mid-electrode diameter, FIG. 20C is a representation of the y-z plane mid electrode diameter, and FIG. 20D is a representation of the y-z plane between electrodes.

FIG. 21 is a representation of the 3D Electric Field [V/cm] Distribution in Electroporated Tissue with 1.5-cm Single Needle Electrodes at a Separation of 2.0 cm and 3000 V applied assuming  $\sigma_{max}/\sigma_0=3.6$ .

FIGS. 22A-22D are representations of the Electric Field [V/cm] Distributions from the 3D Electroporated Models with 1.5-cm Electrodes at a Separation of 2.0 cm and 3000 V (cross-sections) assuming a  $\sigma_{max}/\sigma_0=3.6$ , wherein FIG. 22A is a representation of the x-y plane mid-electrode length, FIG. 22B is a representation of the x-z plane mid-electrode diameter, FIG. 22C is a representation of the y-z plane mid electrode diameter, and FIG. 22D is a representation of the y-z plane between electrodes.

### Example 7

#### The Cassini Oval Equation

In mathematics, a Cassini oval is a set (or locus) of points in the plane such that each point  $p$  on the oval bears a special relation to two other, fixed points  $q_1$  and  $q_2$ : the product of the distance from  $p$  to  $q_1$  and the distance from  $p$  to  $q_2$  is constant. That is, if the function  $\text{dist}(x,y)$  is defined to be the distance from a point  $x$  to a point  $y$ , then all points  $p$  on a Cassini oval satisfy the equation:

$$\text{dist}(q_1,p)\times\text{dist}(q_2,p)=b^2 \quad (2)$$

where  $b$  is a constant.

Nevertheless, in embodiments the 'b' parameter can be modified to manipulate the shape of the Cassini curve and illustrate the desired electric field distribution. Therefore, the

'b' is a variable parameter that is determined based on the specific location (distance) of a particular electric field threshold to be displayed.

The points q<sub>1</sub> and q<sub>2</sub> are called the foci of the oval.

Suppose q<sub>1</sub> is the point (a,0), and q<sub>2</sub> is the point (-a,0). Then the points on the curve satisfy the equation:

$$((x-a)^2+y^2)((x+a)^2+y^2)=b^4 \tag{3}$$

The equivalent polar equation is:

$$r^4-2a^2r^2 \cos 2\theta=b^4-a^4 \tag{4}$$

The shape of the oval depends on the ratio b/a. When b/a is greater than 1, the locus is a single, connected loop. When b/a is less than 1, the locus comprises two disconnected loops. When b/a is equal to 1, the locus is a lemniscate of Bernoulli.

The Cassini equation provides a very efficient algorithm for plotting the boundary line of the treatment zone that was created between two probes on grid 200. By taking pairs of probes for each firing sequence, the first probe is set as q<sub>1</sub> being the point (a,0) and the second probe is set as q<sub>2</sub> being the point (-a,0). This original Cassini oval formulation was revised by modifying the assumption of the 'a' parameter being related to the position of the electrodes. In the revised formulation the 'a' is a variable parameter that is adjusted depending on the width and length of the Cassini oval in order to intercept the zone of ablation in the x- and y-directions.

In summary, the 'a' and 'b' variable parameters should be determined in order to have the ability to generate a Cassini curve that could fit the shape of any electric field isocontour. Specifically from the electric field simulations or experimental irreversible electroporation zones of ablation the user should determine the distance along the x-axis and y-axis that the Cassini curve should intersect.

For example in the case of a Finite Element Analysis (FEA) simulation using two 1-mm in diameter electrodes, separated by a center-to-center distance of 2.0 cm, 1.5 cm in exposure, and an applied voltage of 3000 V to one electrode and ground to the other electrode the distances from the point in between the electrodes to a specific electric field contour is given below (Table 8 for the baseline (non-electroporated) and  $\sigma_{max}/\sigma_0=3.6$  (electroporated) models.

TABLE 8

E-field [V/cm]	Baseline (p <sub>1x</sub> , 0) [cm]	Baseline (0, p <sub>2y</sub> ) [cm]	$\sigma_{max}/\sigma_0 = 3.6$ (p <sub>3x</sub> , 0) [cm]	$\sigma_{max}/\sigma_0 = 3.6$ (0, p <sub>4y</sub> ) [cm]
300	1.97	0.92	2.38	1.39
400	1.81	0.69	2.17	1.18
500	1.70	0.49	1.99	1.01

Using the 500 V/cm electric field isocontour as an example it can be determined that the Cassini oval using the baseline model will intersect the points (1.70,0) and (0,0.49) and the model using  $\sigma_{max}/\sigma_0=3.6$  will intersect the point (1.99,0) and (0,1.01). Using the two points that will be intersected by the Cassini oval of each specific model type (non-electroporated vs. electroporated) allows for determination of the 'a' and 'b' variable parameter and still satisfy the mathematical condition outlined above in the first paragraph of this section by way of least square fits such as the NonlinearModelFit function in Mathematica or via interpolation tables as the one presented below.

The interpolation method involves assuming values for the 'a' parameter from 0.00 cm to 3.00 cm in steps of 0.01 cm and calculating the 'b' parameter using the specific

points from the previous paragraph. The distance and steps were arbitrarily chosen and can vary depending on the specific Cassini oval that is being developed. In the case of Table 9 the point p<sub>1x</sub>=(1.70 cm, 0 cm) and the point p<sub>2y</sub>=(0 cm, 0.49 cm) and the corresponding distances to either q<sub>1</sub> (-a,0) or q<sub>2</sub> (a,0) are calculated.

TABLE 9

'a'	d(q <sub>1</sub> , p <sub>1x</sub> ) = d1	d(q <sub>2</sub> , p <sub>1x</sub> ) = d2	d(q <sub>1</sub> , p <sub>2y</sub> ) = d3	d(q <sub>2</sub> , p <sub>2y</sub> ) = d4	d1*d2	d3*d4	d1*d2/d3*d4
1.04	0.66	2.74	1.808	1.150	1.150	1.322	1.37
1.05	0.65	2.75	1.788	1.159	1.159	1.343	1.33
1.06	0.64	2.76	1.766	1.168	1.168	1.364	1.30
1.07	0.63	2.77	1.745	1.177	1.177	1.385	1.26
1.08	0.62	2.78	1.724	1.186	1.186	1.407	1.23
1.09	0.61	2.79	1.702	1.195	1.195	1.428	1.19
1.1	0.60	2.80	1.680	1.204	1.204	1.450	1.16
1.11	0.59	2.81	1.658	1.213	1.213	1.472	1.13
1.12	0.58	2.82	1.636	1.222	1.222	1.495	1.09
1.13	0.57	2.83	1.613	1.232	1.232	1.517	1.06
1.14	0.56	2.84	1.590	1.241	1.241	1.540	1.03
1.15	0.55	2.85	1.568	1.250	1.250	1.563	1.00
1.16	0.54	2.86	1.544	1.259	1.259	1.586	0.97
1.17	0.53	2.87	1.521	1.268	1.268	1.609	0.95
1.18	0.52	2.88	1.498	1.278	1.278	1.633	0.92
1.19	0.51	2.89	1.474	1.287	1.287	1.656	0.89
1.2	0.50	2.90	1.450	1.296	1.296	1.680	0.86
1.21	0.49	2.91	1.426	1.305	1.305	1.704	0.84
1.22	0.48	2.92	1.402	1.315	1.315	1.729	0.81
1.23	0.47	2.93	1.377	1.324	1.324	1.753	0.79
1.24	0.46	2.94	1.352	1.333	1.333	1.778	0.76

In the baseline case analyzed above when the variable parameter 'a' was 1.15 cm the calculated b<sup>2</sup> were 1.568 and 1.563 for the d<sub>1</sub>\*d<sub>2</sub> and d<sub>3</sub>\*d<sub>4</sub>, respectively. The last column calculates the ratio of both b<sup>2</sup> values in order to determine the location at which they are the same (or closest) which happens when (d<sub>1</sub>\*d<sub>2</sub>)/(d<sub>3</sub>\*d<sub>4</sub>)=1.00.

Once it is determined that 'a'=1.15 cm provides the closest ratio to one, the average of the d<sub>1</sub>\*d<sub>2</sub> (1.568) and d<sub>3</sub>\*d<sub>4</sub> (1.563) quantities is calculated and used to determine the corresponding 'b' parameter by taking the square root as shown in the equation below.

$$b = \sqrt{\frac{(d1 * d2) + (d3 * d4)}{2}} = \sqrt{\frac{1.568 + 1.563}{2}} = \sqrt{1.5655} = 1.2512 \tag{5}$$

Once the 'a' and 'b' parameters are determined then any plotting software can be used to illustrate the Cassini curve in Cartesian coordinates using the modified equation

$$y = \pm \sqrt{-a^2 - x^2 \pm \sqrt{b^4 + 4a^2x^2}} \tag{6}$$

The steps outlined in the previous paragraphs just above can also be used to determine the 'a' and 'b' parameters using the same methodology and with points p<sub>3x</sub>=(1.99 cm, 0 cm) and p<sub>4y</sub>=(0 cm, 1.01 cm) and results in 'a'=1.21 cm and 'b'=1.578 cm as the Cassini parameters for the electroporated model when  $\sigma_{max}/\sigma_0=3.6$ .

TABLE 10

'a'	d(q1, p3x) = d5	d(q2, p3x) = d6	d5*d6	d(q1, p4y) = d7	d(q2, p4y) = d8	d7*d8	d5*d6/ d7*d8
1.1	0.89	3.09	2.750	1.493	1.493	2.230	1.23
1.11	0.88	3.10	2.728	1.501	1.501	2.252	1.21
1.12	0.87	3.11	2.706	1.508	1.508	2.275	1.19
1.13	0.86	3.12	2.683	1.516	1.516	2.297	1.17
1.14	0.85	3.13	2.661	1.523	1.523	2.320	1.15
1.15	0.84	3.14	2.638	1.531	1.531	2.343	1.13
1.16	0.83	3.15	2.615	1.538	1.538	2.366	1.11
1.17	0.82	3.16	2.591	1.546	1.546	2.389	1.08
1.18	0.81	3.17	2.568	1.553	1.553	2.413	1.06
1.19	0.80	3.18	2.544	1.561	1.561	2.436	1.04
1.2	0.79	3.19	2.520	1.568	1.568	2.460	1.02
1.21	0.78	3.20	2.496	1.576	1.576	2.484	1.00
1.22	0.77	3.21	2.472	1.584	1.584	2.509	0.99
1.23	0.76	3.22	2.447	1.592	1.592	2.533	0.97
1.24	0.75	3.23	2.423	1.599	1.599	2.558	0.95
1.25	0.74	3.24	2.398	1.607	1.607	2.583	0.93
1.26	0.73	3.25	2.373	1.615	1.615	2.608	0.91
1.27	0.72	3.26	2.347	1.623	1.623	2.633	0.89
1.28	0.71	3.27	2.322	1.630	1.630	2.659	0.87
1.29	0.70	3.28	2.296	1.638	1.638	2.684	0.86
1.3	0.69	3.29	2.270	1.646	1.646	2.710	0.84

In FIG. 23, it can be seen that with the implementation of the pre-pulse concept to determine the ratio of maximum conductivity to baseline conductivity one can derive a Cassini curve representing zones of ablation. In this case the 500 V/cm isocontour was specified but this technique could be used for any other isocontour that perhaps could represent the lethal IRE threshold for any other tissue/tumor type.

The polar equation for the Cassini curve could also be used because since it provides an alternate method for computation. The current Cartesian coordinate algorithm can work equally as well by using the polar equation of the Cassini curve. By solving for  $r^2$  from eq. (4) above, the following polar equation was developed:

$$r^2 = a^2 \cos(2*\theta) + \sqrt{b^4 - a^4 \sin^2(2*\theta)} \quad (5)$$

and the 'a' and 'b' parameters should be determined as previously described in this application.

### Example 8

#### Mapping of Electric Field and Thermal Contours Using a Simplified Data Cross-Referencing Approach

This method can be used to identify the volume of tissue which will be elevated above a specific temperature (e.g. 45° C.) for specific treatment parameters. This contour can then be correlated with electric field intensity. This data in turn can be used to fit a contour using the Cassini oval software in the NANOKNIFE® System.

Methods: A mathematical model was built with COMSOL Multiphysics (Version 4.2a, Comsol Inc., Burlington, Mass., USA) to estimate the temperature rise within tissue due to Joule heating effects. The electric field distribution within the simulation domain was solved using the Joule Heating module, as described by the Laplace Equation:

$$\nabla^2 \phi = 0$$

where  $\phi$  is the electric potential, this equation is solved with boundary conditions:

$$\vec{n} \cdot \vec{J} = 0 \text{ at the boundaries}$$

$$\phi = V_m \text{ at the boundary of the first electrode}$$

$$\phi = 0 \text{ at the boundary of the second electrode}$$

wherein  $\vec{n}$  is the normal vector to the surface,  $\vec{J}$  is the electrical current and  $V_m$  is the electrical potential applied. Heat transfer in the solid domain was calculated as:

$$\rho C_p \frac{\partial T}{\partial t} = \nabla \cdot (k \nabla T) + Q_{jh} \left[ \frac{W}{m^3} \right]$$

where  $\rho$  is the density,  $C_p$  is the heat capacity,  $k$  is the thermal conductivity, and  $Q_{jh}$  are the resistive losses

$$Q_{jh} = J \cdot E \left[ \frac{W}{m^3} \right]$$

where  $J$  is the induced current density

$$J = \sigma E \left[ \frac{A}{m^2} \right]$$

and  $\sigma$  is the tissue conductivity and  $E$  is the electric field

$$E = -\nabla \phi \left[ \frac{V}{m} \right]$$

To account for the pulsed nature of the applied electric field, the Joule heating term in COMSOL was adjusted by adding in a duty cycle term equal to  $100 \times 10^{-6}$ , the pulse duration (100  $\mu$ s) (See P. A. Garcia, et al., "A Parametric Study Delineating Irreversible Electroporation from Thermal Damage Based on a Minimally Invasive Intracranial Procedure," *Biomed Eng Online*, vol. 10, p. 34, Apr. 30, 2011).

In the Joule Heating Model equation view, the equation for resistive losses was modified to:

$$jh \cdot Q_{rh} = ((jh \cdot J_{ix} + jh \cdot J_{ex}) * \text{duty\_cycle} * jh \cdot E_x + (jh \cdot J_{iy} + jh \cdot J_{ey}) * \text{duty\_cycle} * jh \cdot E_y + (jh \cdot J_{iz} + jh \cdot J_{ez}) * \text{duty\_cycle} * jh \cdot E_z) * (t < 90) + 0 * (t > 90)$$

The resulting behavior was to calculate Joule heating only for the first 90 seconds (Ninety pulses of 100  $\mu$ s each) of the simulation, after which, heat was allowed to dissipate within the tissue domain without additional heating. The parameters used in the simulations are provided in Table 11 below.

TABLE 11

Parameters used in COMSOL finite element model			
Parameter	Value	Unit	Description
r_e	0.0005	[m]	electrode radius
l_e	0.15	[m]	electrode length
l_t	0.15	[m]	tissue radius
h_t	0.1	[m]	tissue thickness
gap	0.015	[m]	center-to-center spacing
epsi_e	0	—	electrode permittivity
epsi_i	0	—	insulation permittivity
epsi_t	0	—	tissue permittivity
sigma_e	2.22E+06	[S/m]	electrode conductivity
sigma_i	6.66E-16	[S/m]	insulation conductivity
sigma_t	0.2	[S/m]	tissue conductivity
rho	1080	[kg/m3]	tissue density
Cp	3890	[J/(kg * K)]	tissue heat capacity
k	0.547	[W/(m * K)]	tissue thermal conductivity
duty_cycle	1.00E-04	—	pulse duty cycle

Results: The COMSOL model was used to solve for temperature distributions at times between 0 and 900 seconds (10 second increment 0-100s, 100 second increment 100-900 seconds). Electric Field and Temperature distributions were exported along lines on the x-(width) and y-axis (depth) with 100 micrometer spacing between data points. These values were imported into Excel and used as the basis for the Cassini oval calculations. FIGS. 24A-D shows the temperature distributions determined in COMSOL at 90 seconds (Ninety pulses of 100  $\mu$ s each) for 3000 V treatments with 1.0 cm, 1.5 cm, 2.0 cm, and 2.5 cm electrode spacing and an electrode exposure of 1.5 cm. Contours on this figure show an approximate electric field which corresponds to tissue temperatures greater than 45° C. Simulations of each parameter required approximately 30 minutes to complete for a total computational duration of 15 hours.

FIGS. 25A-D shows the Cassini oval approximations for the temperature and electric field distributions based on the finite element simulation results. Iso-contour lines correspond to the tissue with temperature elevated above 45° C. and electric field above 500 V/cm, at the end of a 90 second IRE treatment (Ninety pulses of 100  $\mu$ s).

The Cassini oval spreadsheet has been programmed so that the user can plot contour lines for specified voltages (500, 1000, 1500, 2000, 2500, 3000 V), electrode separations (0.5, 1.0, 1.5, 2.0, 2.5 cm), Simulation times (0-900 seconds), Temperatures (37-Tmax ° C.), and electric field intensities (0-infinity V/cm). FIGS. 26A-D shows the temperature distributions for a 3000 V, 2.5 cm spacing treatment at 10, 40, 90, and 200 seconds. The simulation accounts for Joule heating up to 90 seconds. After 90 seconds, Joule heating is no longer calculated and the temperature dissipates over time since the ninety-pulse delivery is completed.

The Cassini oval approximation can also be used to investigate the contours of any temperature. FIG. 27A-D shows the volumes of tissue that have been heated by at least 0.2, 3.0, 8.0, and 13.0° C. At 3000V, 1.5 cm exposure, and 2.5 cm electrode spacing at a time=90 seconds (Ninety pulses of 100  $\mu$ s each), only a very small volume of tissue outside the ablation zone (500 V/cm) experiences any temperature increase.

The Cassini oval approximation tool provides a rapid method for determining the temperature distribution expected for a given set of treatment parameters (FIGS. 28 and 29). Voltage, Electrode Spacing (Gap), Time, Temperature, and Electric Field can be selected by moving the slider or editing values in the green boxes. In embodiments, baseline conductivity of the target treatment area, and/or a conductivity for a specific tissue type, and/or a change in conductivity for the target treatment area can also, and/or alternatively, be selected. Voltage is selectable in 500 V discrete steps between 500 and 3000 V. Electrode Spacing (Gap) is selectable in 5.0 mm discrete steps between 5.0 mm and 25 mm. Time is selectable in 10 second discrete steps between 0 and 100 seconds and 100 second discrete steps between 100 and 900 seconds. The temperature contour line is selectable for any value between 37° C. and  $T_{max}$ , where  $T_{max}$  is the maximum temperature in the tissue at a given treatment time. Additionally, the electric field distribution within the tissue can be set for any value.

Additional examples of usage of the Cassini oval approximation tool are shown in the following figures. FIGS. 30A-D show temperature contour lines for 40° C. (FIG. 30A), 45° C. (FIG. 30B), 50° C. (FIG. 30C), and 55° C. (FIG. 30D) for a 90 second IRE treatment (Ninety pulses of 100  $\mu$ s each) with a voltage of 3000 V and electrode spacing of 10 mm. An electric field contour line of 500 V/cm is

shown for comparison. As can be seen, the figures show a temperature gradient that expectedly increases from the 500 V/cm contour line toward the electrodes.

FIGS. 31A-D show contour lines representing a 40° C. temperature and a 500 V/cm electric field for a 90 second IRE treatment (Ninety pulses of 100  $\mu$ s each) and electrode spacing of 10 mm at different voltages (3000V (FIG. 31A), 2000V (FIG. 31B), 1500V (FIG. 31C), and 1000V (FIG. 31D)). The figures show that the size of the electric field and heated area decreases in proportion to the decrease in voltage.

FIGS. 32A-D show electric field contour lines for 500 V/cm (FIG. 32A), 1000 V/cm (FIG. 32B), 1500 V/cm (FIG. 32C), and 2000 V/cm (FIG. 32D) for a 90 second IRE treatment (Ninety pulses of 100  $\mu$ s each) with a voltage of 3000 V and electrode spacing of 10 mm. As can be seen, the figures show an electric field gradient that expectedly increases from the 40° C. contour line toward the electrodes.

FIGS. 33A-D show contour lines representing a 40° C. temperature and a 500 V/cm electric field for a 90 second IRE treatment (Ninety pulses of 100  $\mu$ s each) and voltage of 3000V at different electrode spacings (5 mm (FIG. 33A), 10 mm (FIG. 33B), 15 mm (FIG. 33C), 20 mm (FIG. 33D)). As can be seen, increasing the electrode distance up to 15 mm widens the electric field and temperature contour. At an electrode distance of 20 mm, the electric field contour line widens and narrows, but the area heated to at least 40° C. is limited to a radius around each electrode.

FIGS. 34A-D show contour lines representing a 40° C. temperature and a 500 V/cm electric field for an IRE treatment of 3000V and an electrode spacing of 10 mm at different durations of treatment (90 seconds (Ninety pulses of 100  $\mu$ s each) (FIG. 34A), 60 seconds (Sixty pulses of 100  $\mu$ s each) (FIG. 34B), 30 seconds (Thirty pulses of 100  $\mu$ s each) (FIG. 34C), 10 seconds (Ten pulses of 100  $\mu$ s each) (FIG. 34D)). The graphs show that decreasing the durations of treatment reduces the area heated at least 40° C., but not the area of the electric field.

Model Limitations: This model was designed to give a rapid approximation for the temperature distribution within a volume of tissue without the need for complex finite element simulations. The data used to fit the Cassini oval curves uses values calculated assuming a constant conductivity of 0.2 S/m. This represents an approximate conductivity of human tissue, though conductivities of tissue vary between patients, tissue types, locations, and pathologies. Changing conductivity due to temperature increases or electroporation effects were not included. FIG. 35 shows the COMSOL three-dimensional finite element domain mesh used to calculate the electric field and temperature information to create the Cassini Oval values and curves.

The effects of blood flow and perfusion through the tissue, metabolic heat generation, or diffusion of heat at the tissue domain boundaries were not considered. It is anticipated that these effects will result in lower temperatures. Therefore, the visualization tool provides a conservative (worst case scenario) estimate as to the zones exposed to critical temperatures. The effects of changing conductivity and conductivities other than 0.2 S/m were not considered. Elevated conductivities are anticipated to result in higher temperatures within the tissue. Blood flow, metabolic heat generation, tissue conductivity, and ratios of changing conductivity are tissue type specific and will require the inclusion of in-vivo derived data.

Conclusions: In this Example, a real time visualization package plots the isocontour lines for an arbitrary temperature and electric field based on applied voltage, electrode

spacing, and time. This data can be used to build intuition and instruct clinicians on reasonable expectations of temperature increases to prevent damage to critical structures of organs in the proximity of the treatment.

#### Example 9

##### Visualization of Electric Field Distributions Using Different Configurations of Bipolar Probes

FIGS. 36A-36C show a representation of a visualization tool providing the 650 V/cm electric field distributions using different configurations of bipolar probes and includes dynamic change (3.6×) in electrical conductivity from the non-electroporated baseline for runs 7, 8, and 9 of the visualization. FIG. 36D is a table showing parameters of each run including electrode length, separation distance (insulation), and applied voltage. FIG. 36E is a table showing lesion dimensions for runs 7, 8, and 9. The results show that as the length of the bipolar electrode increases, the size of the zone of ablation increases.

#### Example 10

##### Determining the IRE Threshold for Different Tissues According to Conductivity

In this Example, as shown in the following figures, the “Goldberg” data (red-dashed line), is from pre-clinical data for a particular treatment (2700V, 90 pulses, 100 μs energized per pulse). By adjusting one or more treatment parameters, a user can determine the electric field threshold for these types of tissues (black-solid line).

An important aspect of this model is that the tissue conductivity is allowed to change as a function of electric field to simulate what happens when the tissue becomes irreversibly electroporated. This function is ‘sigmoidal’ or ‘S’ shaped and increases from a baseline (non-electroporated) to a conductivity multiplier (electroporated). This transition happens at a specific electric field intensity.

In FIG. 37, the conductivity changes from 0.1 to 0.35 at an electric field centered at 500 V/cm. A user can change/shift all of the values in this curve to fit the experimental data. FIG. 38A is a contour plot comparing the “Goldberg” data (red dashed line) with a calculated threshold (solid black line) based on the parameters shown in FIG. 38C, explained below. FIG. 38B is a contour plot comparing the conductivity (blue dotted line) with a calculated threshold (solid black line) based on the parameters shown in FIG. 38C.

**IRE Threshold [V/cm]:** This parameter is the electric field at which the change in conductivity occurs for the sigmoidal curve. By changing this value, the sigmoidal curve shifts to the left or right. A value of 500 V/cm has been found to fit the data best.

**Transition zone:** This is the ‘width’ of the transition zone. By changing this value, the rate at which the conductivity increase changes. In FIG. 37, this value is set to 0.49, the widest transition possible. It has been found that a transition of 0.2 matches the experimental data best.

**Sigma:** This is the baseline conductivity before treatment. It has been found that a value of 0.067 (or 0.1) works well.

**Conductivity Multiplier:** This is how much the conductivity increases by when the tissue has been irreversibly electroporated. A 3.6× increase has been found experimentally for liver and fits the data well.

**E-Field:** This is the parameter that is adjusted to find the in-vivo irreversible electroporation threshold. With the values set for the other parameters above, it has been found that IRE should occur at a threshold of 580 V/cm to match the lesions found in-vivo.

The following figures show how modifying the conductivity of the tissue changes the calculated zone of ablation. FIGS. 39A-39F were performed according to the parameters in FIG. 38C, except the conductivity of the tissue was modified. FIGS. 39A-39C show the “Goldberg” data and calculated threshold and FIGS. 39D-39F show the conductivity and calculated threshold for conductivity multipliers of 2, 3, and 4, respectively. As can be seen, the calculated ablation zone increases in comparison to the Goldberg preclinical data as conductivity increases.

FIGS. 40A-40F were performed for an IRE Threshold of 600 V/cm, a transition zone of 0.4, a Voltage of 700 V, an E-Field of 700 V/cm, and a Sigma (electrical conductivity) of 0.20 S/m. FIGS. 40A-40C show the “Goldberg” data and calculated threshold and FIGS. 40D-40F show the conductivity and calculated threshold for conductivity multipliers of 2, 3, and 4, respectively.

FIGS. 41A-41F were performed for an IRE Threshold of 1000 V/cm, a transition zone of 0.2, a Voltage of 2700 V, an E-Field of 700 V/cm, and a Sigma (electrical conductivity) of 0.20 S/m. FIGS. 41A-41C show the “Goldberg” data and calculated threshold and FIGS. 41D-41F show the conductivity and calculated threshold for conductivity multipliers of 2, 3, and 4, respectively.

As can be seen, the calculated ablation zone increases in comparison to the Goldberg preclinical data as the conductivity multiplier increases.

#### Example 11

##### Correlating Experimental and Numerical IRE Lesions Using the Bipolar Probe

**Purpose:** To establish a function that correlates experimentally produced zones of ablations in in vivo porcine tissue with the corresponding IRE pulse parameters (duration, number, strength) and single needle electrode configuration.

A mathematical function was developed that captures the IRE response in liver tissue as a function of applied voltage, pulse number, and pulse duration for the bipolar electrode configuration. It is important to note that the inventors used a rate equation that was fit to the 1.5 cm×2.9 cm IRE zone of ablation but this has not been validated experimentally (See Golberg, A. and B. Rubinsky, *A statistical model for multidimensional irreversible electroporation cell death in tissue*. Biomed Eng Online, 2010. 9(1): p. 13). The results below provide insight as to the effect of different pulse parameters and electrode/insulation dimensions in the resulting zone of IRE ablation in order to optimize the bipolar probe electrode for clinical use. In order to perform a computationally efficient study, the models were constructed in a 2-D axis-symmetric platform which generates results that are representative of the 3-D space.

**Part 1:** The work from Part 1 determined the electric field threshold for 0.7 cm electrodes with a 0.8 cm insulation to be 572.8 V/cm assuming a static electric conductivity (Table 12). This threshold is the average between the width (349.5 V/cm) and length (795.1V/cm) electric field thresholds that matched the experimental lesion of 1.5 cm (width) by 2.9 cm (length). It is important to note that due to the mismatch between the electric field thresholds, the predicted width

will be underestimated and the predicted length will be overestimated when using the average value of 572.8 V/cm. The model assumes an applied voltage of 2700 V, ninety 100- $\mu$ s pulses, at a repetition rate of 1 pulse per second, and a viability value of 0.1% (S=0.001) as the complete cell death due to IRE exposure (FIG. 42). The rate equation used in the analysis is given by  $S=e^{-kE \cdot t}$  where S is the cell viability post-IRE, E is the electric field, t is the cumulative exposure time, and k is the rate constant that dictates cell death. Specifically during this Part, it was determined that  $k=1.33996$  assuming an  $E=572.8$  V/cm,  $S=0.001$ , and  $t=0.009$  s (90 $\times$ 100- $\mu$ s). The k parameter was scaled by the duty cycle of the pulses (0.0001 s) in order to reflect the cell viability in the time scale in which the pulses were delivered (i.e. one pulse per second).

TABLE 12

Electric field thresholds for the static modeling approach from experimental IRE lesions in liver.				
Conductivity	Lesion Dimensions	E-field [V/cm]	Average [V/cm]	Threshold [V/cm]
Static- $\sigma_0$	x = 1.5 cm	349.5	349.5	572.8
Static- $\sigma_0$	y = 2.9 cm (distal)	796.2	795.1	
Static- $\sigma_0$	y = 2.9 cm (proximal)	795.6		

A parametric study was constructed in order to explore the effect of electrode diameter (18G=1.27 mm, 16G=1.65 mm, 14G=2.11 mm), electrode spacing (0.4 cm, 0.8 cm, 1.2 cm, 1.6 cm), and electrode length (0.5 cm, 0.75 cm, 1.0 cm, 1.25 cm, and 1.5 cm). In order to provide a comprehensive analysis of all iterations we computed the volumes of tissue that would achieve a cell viability,  $S<0.001$ , and these results are reported in the table of FIG. 48A-B. The results with the specific minimum and maximum parameters from Part 1 are presented in Table 13 and demonstrate that with increasing probe diameter and electrode length a larger area/volume of IRE ablation is achieved for ninety 100- $\mu$ s pulses delivered at 2700 V at a repetition rate of one pulse per second. FIGS. 43A-D shows the predicted regions of post-IRE cell viability isocontour levels with the solid white curve illustrating the 0.1%, 1.0%, and 10% cell viability levels. Of importance is the fact that if the electrodes are spaced too far apart, the resulting IRE zone of ablation is not contiguous and the treatment would fail between the electrodes as shown with Runs 60 and 10, respectively.

TABLE 13

Predicted IRE lesion dimensions for the min. and max. parameters investigated in Part 1.									
Run	Diameter (cm)	Spacing (cm)	Length (cm)	Area (cm <sup>2</sup> )	Volume (cm <sup>3</sup> )	x(cm)	y(cm)	x:y	
60	14 G = 2.11 mm	1.6	1.5	2.705	6.232	0.311	5.550	0.056	
10	18 G = 1.27 mm	1.6	0.5	1.042	1.689	0.227	3.390	0.067	
49	18 G = 1.27 mm	0.4	1.5	2.242	4.626	1.257	4.210	0.299	
3	14 G = 2.11 mm	0.4	0.5	1.120	2.241	1.221	2.190	0.558	

In an effort to better understand the effects of the electrode geometry on the ablation region an extra set of values (Table 14) was generated. The closest outputs to a 1.5 cm $\times$ 2.9 cm

lesion size from parameters in Table 13 were modified to better approximate the targeted lesion. Considering all 60 different runs, number 15 is closest to the targeted values with a lesion geometry of 1.301 cm $\times$ 2.84 cm.

TABLE 14

Predicted IRE lesion dimensions for parameters approximating a 1.5 cm $\times$ 2.9 cm ablation region.								
Run	Diameter (cm)	Spacing (cm)	Length (cm)	Area (cm <sup>2</sup> )	Volume (cm <sup>3</sup> )	x(cm)	y(cm)	x:y
3	14 G = 2.11 mm	0.4	0.5	1.120	2.241	1.221	2.190	0.558
1	18 G = 1.27 mm	0.4	0.5	0.943	1.590	1.037	2.170	0.478
15	14 G = 2.11 mm	0.4	0.75	1.483	3.215	1.301	2.840	0.458
18	14 G = 2.11 mm	0.8	0.75	1.680	3.652	1.181	3.250	0.363

Part 2: In Part 2 the electric field distribution assuming a dynamic electric conductivity was used to determine the threshold of cell death due to IRE exposure. Specifically during this Part, a sigmoid function (FIG. 44) with a baseline (0.067 S/m) and maximum (0.241 S/m) conductivity values was used (see Sel, D., et al., *Sequential finite element model of tissue electroporation*. IEEE Trans Biomed Eng, 2005. 52(5): p. 816-27). This published function assumes that reversible electroporation starts at 460 V/cm and is irreversible at 700 V/cm as reported by Sel. et al. Using the dynamic conductivity function resulted in a more consistent electric field threshold between the width (615.7 V/cm) and the length (727.4 V/cm); therefore, using the average (670.1V/cm) provides a better prediction of the IRE lesions being achieved in vivo versus the ones predicted in Part 1 that assume a static conductivity (Table 15). The electric field threshold for IRE using the dynamic conductivity approach resulted in a revised  $k=1.14539$  assuming an  $E=670.1$ V/cm,  $S=0.001$ , and  $t=0.009$  s (90 $\times$ 100  $\mu$ s). The k parameter was scaled by the duty cycle of the pulses (0.0001s) in order to reflect the cell viability in the time scale in which the pulses were delivered (i.e. one pulse per second).

TABLE 15

Electric field thresholds for the dynamic modeling approach from experimental IRE lesions in liver.				
Conductivity	IRE Dimension	E-field [V/cm]	Average	Threshold [V/cm]
Dynamic- $\sigma(E)$	x = 1.5 cm	615.7	615.7	670.1
Dynamic- $\sigma(E)$	y = 2.9 cm (distal)	720.7	727.4	
Dynamic- $\sigma(E)$	y = 2.9 cm (proximal)	734.0		

In Part 2, the effect of pulse strength (2000 V, 2250 V, 2500 V, 2750 V, 3000 V) and pulse number (20, 40, 60, 80, 100) was explicitly investigated and the results of the parametric study are provided in the table of FIG. 49 and a representative plot provided in FIG. 45. The results with the specific minimum and maximum parameters from Part 2 are presented in

Table 16 and demonstrate that with increasing pulse strength and pulse number a larger volume of IRE ablation is achieved at a repetition rate of one pulse per second



(FIGS. 46A-D). In order to compare the results to the electric field threshold, both areas/volumes were computed and are provided as well. Similar to the results from Part 1, the white solid curve represents the 0.1%, 1.0%, and 10% cell viability isocontour levels due to IRE. For all voltages investigated, delivering one hundred 100- $\mu$ s pulses covers a greater area/volume than the prediction by the 670.1 V/cm electric field threshold assumed with the dynamic conductivity function.

TABLE 16

Predicted lesion dimensions for the minimum and maximum parameters investigated in Part 2.									
Run	Voltage (V)	Number	Area (cm <sup>2</sup> )	Volume (cm <sup>3</sup> )	E-Field (cm <sup>2</sup> )	E-Field (cm <sup>3</sup> )	x(cm)	y(cm)	x:y
3	2000	20	0.080	0.050	0.970	1.575	0.216	2.350	0.092
6	2000	100	1.209	2.238	0.970	1.575	0.646	1.630	0.396
27	3000	20	0.209	0.170	1.493	3.171	0.221	1.800	0.123
30	3000	100	1.900	4.604	1.493	3.171	0.946	1.130	0.837

Part 3: In this Part the exposure of liver tissue to 300 (5x60) and 360 (4x90) pulses were simulated at an applied voltage of 3000 V, 100- $\mu$ s pulses, at a repetition rate of one pulse per second. From the cell viability plots in FIG. 47A-B it can be seen that with increasing number of pulses, larger zones of IRE ablation are achieved with the corresponding areas and volumes included in Table 17 and the table of FIG. 50. It is important to note that in this case the simulation assumes that there is sufficient thermal relaxation time between sets of pulses; thus preventing any potential thermal damage from Joule heating which is not simulated in this work.

TABLE 17

Predicted lesion dimensions for the 5 x 60 and 4 x 90 IRE pulses investigated in Part 3.									
Run	Voltage (V)	Number	Area (cm <sup>2</sup> )	Volume (cm <sup>3</sup> )	E-Field (cm <sup>2</sup> )	E-Field (cm <sup>3</sup> )	x(cm)	y(cm)	x:y
16	3000	5 x 60	6.135	27.282	1.493	3.171	2.877	4.900	0.587
19	3000	4 x 90	6.950	33.202	1.493	3.171	3.287	5.540	0.593

Models with exploratory geometries were developed that include multiple voltage sources and current diffusers (balloons). FIGS. 51A-C present images of the raw geometries being tested and FIGS. 51D-F show the corresponding electric field distribution. In general, the most influential parameter remains the size of the electrodes and insulation. According to the values generated from these simulations, it seems like substantial helps to achieve more spherical lesions.

TABLE 18

Predicted IRE lesion dimensions for exploratory models in Appendix D.									
Run	Diameter	Spacing (cm)	Length (cm)	Area (cm <sup>2</sup> )	Volume (cm <sup>3</sup> )	x(cm)	y(cm)	x:y	
61	0.211	0.4	0.5	1.453	1.807	1.201	2.850	0.421	
62	0.211	0.4	1	1.617	2.129	1.321	3.670	0.360	

TABLE 18-continued

Predicted IRE lesion dimensions for exploratory models in Appendix D.									
Run	Diameter	Spacing (cm)	Length (cm)	Area (cm <sup>2</sup> )	Volume (cm <sup>3</sup> )	x(cm)	y(cm)	x:y	
63	0.211	0.4	1	2.008	3.041	1.241	2.955	0.420	
64	0.211	0.4	0.5	1.389	1.929	1.261	2.810	0.449	
65	0.211	0.4	0.5	0.976	1.142	1.421	2.000	0.711	

The present invention has been described with reference to particular embodiments having various features. In light of the disclosure provided, it will be apparent to those skilled in the art that various modifications and variations can be made in the practice of the present invention without departing from the scope or spirit of the invention. One skilled in the art will recognize that the disclosed features may be used singularly, in any combination, or omitted based on the requirements and specifications of a given application or design. Other embodiments of the invention will be apparent to those skilled in the art from consideration of the specification and practice of the invention.

It is noted in particular that where a range of values is provided in this specification, each value between the upper and lower limits of that range is also specifically disclosed. The upper and lower limits of these smaller ranges may independently be included or excluded in the range as well. The singular forms "a," "an," and "the" include plural referents unless the context clearly dictates otherwise. It is intended that the specification and examples be considered as exemplary in nature and that variations that do not depart from the essence of the invention fall within the scope of the invention. In particular, for method embodiments, the order of steps is merely exemplary and variations appreciated by a skilled artisan are included in the scope of the invention. Further, all of the references cited in this disclosure are each individually incorporated by reference herein in their entireties and as such are intended to provide an efficient way of supplementing the enabling disclosure of this invention as well as provide background detailing the level of ordinary skill in the art.

The invention claimed is:

1. A method of treating a tissue with a medical treatment device that applies electrical treatment energy through one or more electrodes defining a target treatment area of the tissue and comprises a display device, the method comprising:

- providing one or more parameters of a treatment protocol for delivering one or more electrical pulses to a tissue through one or more electrodes;
- modeling heat distribution and/or the electric field distribution in a tissue surrounding the electrodes based on the one or more parameters and a treatment protocol-related change in electrical conductivity for the target treatment area, which is a ratio of a maximum electrical conductivity that is reached during treatment to a baseline, non-electroporated, tissue-specific electrical conductivity;
- displaying a graphical representation of the heat and/or electric field distribution based on the modeled heat and/or electric field distribution in the display device;
- modifying one or more of the parameters of the treatment protocol based on the graphical representation of the heat and/or electric field distribution; and

53

implanting the electrodes in the tissue and delivering one or more electrical pulses to the tissue through the electrodes by way of a voltage pulse generator based on the one or more modified parameters.

2. The method of claim 1, wherein the one or more parameters are chosen from one or more of voltage, electrode spacing, electrode length, treatment duration, number of pulses, pulse width, electric field intensity, electrode diameter, a baseline conductivity for the target treatment area, or a conductivity for a specific tissue type.

3. The method of claim 1, wherein the treatment protocol-related change in electrical conductivity is calculated in real time based on measured voltages and currents before, during, and/or after pulse delivery.

4. A method of treatment planning for medical therapies involving administering electrical treatment energy, the method comprising:

providing one or more parameters of a treatment protocol for delivering one or more electrical pulses to tissue through one or more electrodes;

modeling heat and/or electric field distribution in the tissue based on the parameters and a treatment protocol-related change in electrical conductivity for the target treatment area, which is a ratio of a maximum electrical conductivity that is reached during treatment to a baseline, non-electroporated, tissue-specific electrical conductivity; and

displaying a graphical representation of the modeled heat and/or electric field distribution.

5. The method of claim 4, wherein the heat distribution is modeled to estimate the Joule heating in the tissue and is calculated as:

$$\rho C_p \frac{\partial T}{\partial t} = \nabla \cdot (k \nabla T) + Q_{jh} \left[ \frac{W}{m^3} \right]$$

where  $\rho$  is the density,  $C_p$  is the heat capacity,  $k$  is the thermal conductivity, and  $Q_{jh}$  are the resistive losses

$$Q_{jh} = J \cdot E \left[ \frac{W}{m^3} \right]$$

where  $J$  is the induced current density

$$J = \sigma E \left[ \frac{A}{m^2} \right]$$

and  $\sigma$  is the tissue conductivity and  $E$  is the electric field

$$E = -\nabla \phi \left[ \frac{V}{m} \right].$$

6. The method of claim 4, further comprising specifying a cutoff heat distribution value and providing a graphical representation of the heat and/or electric field distribution curve as an isocontour line.

7. The method of claim 4, further comprising: modeling an electrical damage and/or a thermal damage in the tissue based on the parameters; displaying a graphical representation of the modeled electrical damage and/or thermal damage.

54

8. The method of claim 7, wherein the electric field distribution is calculated as:

$$\nabla^2 \phi = 0$$

where  $\phi$  is the electric potential, this equation is solved with boundary conditions:

$\vec{n} \cdot \vec{J} = 0$  at the boundaries

$\phi = V_m$  at the boundary of the first electrode

$\phi = 0$  at the boundary of the second electrode

wherein  $\vec{n}$  is the normal vector to the surface,  $\vec{J}$  is the electrical current and  $V_m$  is the electrical potential applied.

9. The method of claim 7, further comprising specifying a cutoff electrical field distribution value and providing a graphical representation of the electrical field distribution value as an isocontour line.

10. The method of claim 9, further comprising one or more databases comprising a plurality of sets of parameters for treatment protocols stored in the database.

11. The method of claim 10, wherein the graphical representations of the modeled heat and electrical field distributions are derived from Cassini oval calculations.

12. The method of claim 7, wherein the graphical representation of the modeled thermal damage and/or electrical damage is derived from Cassini oval calculations.

13. The method of claim 4, wherein the parameters are chosen from one or more of voltage, electrode spacing, electrode diameter, electrode length, number of pulses, treatment duration, pulse width, electric field intensity, a baseline conductivity for the target treatment area, or a conductivity for a specific tissue type.

14. The method of claim 4, further comprising: modeling one or more of a thermally damaged region, IRE necrotic region, IRE apoptotic region, reversible electroporation region, and region where there is no effect in the tissue based on the parameters; and displaying a graphical representation of the modeled regions.

15. The method of claim 4, further comprising: modeling one or more of a thermally damaged region, an electroporation region, and a region where there is no effect in the tissue based on the parameters; and displaying a graphical representation of the modeled regions.

16. A system for treatment planning for medical therapies involving administering electrical treatment energy, the system comprising:

a computer comprising:

a memory;

a display device;

a processor coupled to the memory and the display device; and

a treatment planning module stored in the memory and executable by the processor, the treatment planning module adapted to:

receive as input one or more parameters of a treatment protocol for delivering one or more electrical pulses to tissue through one or more electrodes; model heat and/or electric field distribution in the tissue based on the parameters and a treatment protocol-related change in electrical conductivity for the target treatment area, which is a ratio of a maximum electrical conductivity that is reached during treatment to a baseline, non-electroporated, tissue-specific electrical conductivity;

display a graphical representation of the modeled heat and/or electric field distribution on the display device.

17. The system of claim 16, further comprising one or more databases comprising a plurality of sets of parameters for treatment protocols stored in the databases. 5

18. The system of claim 16, wherein the inputs are chosen from one or more of voltage, electrode spacing, treatment duration, pulse width, electric field intensity, a baseline conductivity for the target treatment area, or a conductivity for a specific tissue type. 10

19. The system of claim 18, wherein the conductivity for a specific tissue type is provided in a database for a plurality of tissues.

20. The system of claim 16, wherein the one or more electrodes is provided by one or more bipolar probes. 15

21. The system of claim 16, wherein the one or more electrodes are provided by one or more single needle electrodes.

\* \* \* \* \*